Surface melting of mountain glaciers: aerodynamic roughness estimates for distributed surface energy balance models

Joshua Robert Chambers

Submitted in accordance with the requirements for the degree of Doctor of Philosophy

School of Geography

University of Leeds

August 2021

Intellectual Property and Publication Statements

Declaration

The candidate confirms that the work submitted is his/her/their own, except where work which has formed part of jointly authored publications has been included. The contribution of the candidate and the other authors to this work has been explicitly indicated below. The candidate confirms that appropriate credit has been given within the thesis where reference has been made to the work of others.

Attribution of work to others

Work creditable to others is included in the following Chapters:

Chapter 4: Glacial Aerodynamic Roughness Estimates: Uncertainty, Sensitivity, and Precision in Field Measurements

Based on the published paper:

Chambers, J. R., Smith, M. W., Quincey, D. J., Carrivick, J. L., Ross, A. N. & James, M. R. (2019). Glacial aerodynamic roughness estimates: uncertainty, sensitivity, and precision in field measurements. *Journal of Geophysical Research: Earth Surface*, 125(2). DOI: 10.1029/2019JF005167.

Work attribution:

Mark Smith, Jonathan Carrivick and Duncan Quincey collected the data. I performed data processing and analysis and wrote the manuscript. All other authors provided discussion of the results and feedback on the manuscript.

Chapter 5: Correcting for systematic underestimation of topographic glacier aerodynamic roughness values from Hintereisferner, Austria

Based on the published paper:

Chambers, J. R., Smith, M. W., Smith, T., Sailer, R., Quincey, D. J., Carrivick, J. L., Nicholson, L., Mertes, J., Stiperski, I. & James, M. R. (2021). Correcting for Systematic Underestimation of Topographic Glacier Aerodynamic Roughness Values from Hintereisferner, Austria, *Frontiers in Earth Science*, 9, pp. 1–16. DOI: 10.3389/feart.2021.691195.

Work attribution:

Fieldwork was carried out during the HEFEX campaign (2018). Tom Smith, Mark Smith and I collected UAV, pole, ground and wind tower data. Turbulence tower data was collected by Ivana Stiperski, Lindsey Nicholson and Jordan Mertes, and TLS data by Rudolf Sailer. I performed data analysis and wrote the manuscript with supervision from Mark Smith and Duncan Quincey. Ivana Stiperski processed the turbulence data and all authors provided manuscript feedback.

Chapter 6: Incorporating fully spatially and temporally distributed aerodynamic roughness in a distributed glacier surface energy balance model

Based on the submitted paper:

Chambers, J. R., Smith, M. W., Bravo, C. & Quincey, D. J., Nicholson, L., Stiperski, I., Prinz, R., Sailer, R. and Mertes, J. [Submitted]. Incorporating fully spatially and temporally distributed aerodynamic roughness in a distributed glacier surface energy balance model. Submitted to: *Journal of Glaciology*

Work attribution:

Field data collection during the HEFEX campaign (2018) was carried out by me, Tom Smith and Mark Smith. Rudolf Sailer provided the TLS data, and AWS data are freely available from the University of Innsbruck, collected by Rainer Prinz. Claudio Bravo provided the SEB code and guidance on the SEB modelling. I processed and analysed the data and wrote the manuscript, with supervision and feedback from Mark Smith and Duncan Quincey, with additional feedback from all other authors.

Rationale for submission using alternative thesis style:

The structure of this thesis is such that the work was completed in three distinct stages, each of which built of the findings of the previous stage. Each stage provided a dataset, results and findings that warranted publication as it was completed. The first publication explores the uncertainties, precision and sensitivities of past methods and features detailed introductory and background sections. The second publication builds on the analysis of the first in order to develop a new method, then the third paper demonstrates the use and effects of the new method.

The background section of each publication contains overlap in themes which is necessary to give the reader the proper context. Chapter 2 gives an overall background, encapsulating

all three publications but avoiding repetition where possible, and providing signposts to relevant sections; however, some overlap is unavoidable due to the closely linked themes of the publications.

Briefly, the thesis has been structured as follows: overall introduction with statement of research aim and objectives; background, covering the glacier surface energy balance, turbulent fluxes, aerodynamic roughness, structure from motion photogrammetry, and airborne and terrestrial laser scanning; three results chapters as listed above; overall discussion of findings and implications, followed by conclusions.

Copyright statement

Assertion of moral rights

Acknowledgements

First and foremost, I would like to thank my supervisors, who I think of as my main victims and who are probably as weary as me by this point. Thanks to Mark Smith, who, from the first time we spoke when I applied to undertake the project, has maintained a level of enthusiasm and optimism that verges on being suspicious. I would still be working on that first paper to this day if it hadn't been for your encouragement, support and good humour. I would also like to thank Duncan Quincey for his 'humour'. And for also being very supportive and making me feel as though I was working on something that could pass as a half decent PhD project. Your friendship, and the time you've both put into reading my work, talking through ideas and ordering rounds at the pub are very much appreciated. Thanks also to my supervisor-at-a-distance, Mike James, who provided invaluable SfM guidance and offered insightful perspectives on any work I sent him, despite finding himself in unfamiliar, icy territory. Others within the School of Geography who merit a special mention include: Jonathan Carrivick, for his friendship and interest in my project; Claudio Bravo, for supplying Matlab code and assistance with energy balance modelling; Dave Roe, for making every trip to the field store memorable with his stories, and Tom Smith, for providing unparalleled entertainment and great companionship during our cohabitation at Station Hintereis (along with the Hintermice, RIP). For their extensive help in the field and contributions to journal articles, I'm particularly grateful to Lindsey Nicholson, Iva Stiperski and Jordan Mertes. Thanks also to Rudy Sailer, for literally climbing mountains to collect TLS data, to Rainer Prinz, for his work on the AWS network on Hintereisferner, and to Andrew Ross, for his expert knowledge and assistance with wind tower data processing and theory

I am indescribably lucky to have had the support of my boyfriend, Emyr Williams, who has been an absolute foundation on the worst days, popped the champagne on the best days, and made sure the journey has had much more to it than this project. Adam Hepburn has been (and is) a beacon of joy, providing unquestioning encouragement, valuable perspective (it could be worse, you could be in Aber) and lovely holidays to Aber, so thank you (to him)(from me)(for that). Thanks also to Benj Stoker and Will Smith for Czeching up on me. Zuzka, Teo and Steve have provided continued friendship, laughter and Christmas dinners, and I'm very grateful to Liam Taylor for his company on many walks, for all the cups of tea and for giving me a reason to run around Cusco hunting for solar panels. I'm not grateful to him for any hotels he books, ever. For their friendship, pub trips and runs (even when I got lazy) I'd like to thank Tom Sim, Will Barker and Olly Roberts, and Victoria Yuskaitis for providing distraction with entertaining (and long) stories. Many other postgrads and staff have contributed kind words, tea breaks, pub trips and cakes, which are all appreciated. Last, but by no means least, I would like to thank my Mum, Dad and Seth. Firstly, for all the time and effort it took getting me to the point where I was able to go to University, and then for continuing to support me without really being sure what I'm doing (despite me sending PDFs of my papers) and for being proud anyway.

I'd like to acknowledge: the efforts of *most* of the reviewers who have provided feedback on manuscripts; Sci-Hub; and the various individuals and organisations without whose code, software or data this project would not have been possible. Finally: this work was carried out by a grateful and proud member of the LGBTQIA+ community, for others who don't share the privilege of being able to pursue their interests that has been afforded me.

Abstract

Parameterisation of glacier aerodynamic roughness (z_0) is a key uncertainty in calculation of the turbulent fluxes using the bulk aerodynamic approach. z_0 represents the effect of glacier surface roughness on the turbulent fluxes (comprising the sensible and latent heat fluxes), which are an important source of energy in the surface energy balance. However, z_0 is often oversimplified by the use of point-scale measurements or assumed to be constant, potentially leading to the calculation of inaccurate turbulent flux contributions to the surface energy balance and modelled ablation. In this thesis, an exploration of the current methods of estimating z_0 shows that microtopographic estimates of z_0 derived from 3D data can be similar to those obtained from aerodynamic profiles, but are dependent on the measurement scale and data resolution. A multi-scale analysis of data from Hintereisferner, Austria, shows that these sensitivities display consistency across sites, allowing systematic underestimation at coarser resolutions to be corrected to within an order of magnitude of previously validated values. Robust spatially distributed maps of z_0 are created, and temporal evolution of corrected topographic z_0 is then modelled and incorporated into a surface energy balance model. Model run comparisons show that seasonal importance of the turbulent fluxes changes when modelled with fully distributed z_0 in contrast to fixed z_0. With fully distributed z_0, 30% more energy was contributed by the turbulent fluxes to the energy balance during the ablation season, 19% more energy was available for melting and ~23% more ablation was modelled. The work presented in this thesis shows not only that it is possible to fully distribute z_0 and incorporate it into a distributed energy balance model, but also that doing so provides important constraints on the spatial and temporal distribution of the turbulent fluxes, which could lead to more robust surface energy balance and melt modelling.

Table of Contents

List of Figures

List of Tables

Abbreviations

ALS – Airborne laser scanning/scanner

DEM – Digital elevation model

dGPS – differential Global Positioning System

HEF – Hintereisferner (a glacier in Austria)

HEFEX – Hintereisferner experiment

LiDAR – Light detection and ranging

MO – Monin-Obukhov (similarity theory)

SEB – Surface energy balance

SfM – Structure-from-motion photogrammetry

SK - Sydöstra Kaskasatjäkkaglaciären (a glacier in Tarfala, Sweden)

Stor – Storglaciären (a glacier in Tarfala, Sweden)

TLS – Terrestrial laser scanning/scanner

UAV – Un-crewed aerial vehicle

Chapter 1 : Introduction

1.1 Introduction

Melting glaciers and ice sheets are commonly used as a striking metaphor for the changes happening to Earth's climate. Evocative time-lapse imagery shows shrinking glaciers and large icebergs detaching from ice shelves (Davis, 2017; Balog, 2020), while quantitative evidence irrefutably shows that ice-loss is accelerating and that human activity is responsible (Hugonnet *et al.*, 2021; Roe *et al.*, 2021; Slater *et al.*, 2021). The impacts of glacier ice loss will be profound, and affect water, energy supplies and ecosystems. From studies that observe and monitor glacier changes, it is possible to model the possible effects, although current models still have assumptions that need to be better understood. The need to understand and communicate the results of modelling is urgent, for their ability to help us prepare for the impacts that are likely to affect humans, such as landscape change, natural hazards and water security (Hock *et al.*, 2019).

Several methods exist for the task of quantifying current volumes of ice melt, which also allow future melt to be predicted. The mass balance approach uses measurements of changes in ice area, volume or gravitational effects to calculate changes in mass, and thus melt (Østrem and Brugman, 1966; Hagen and Liestøl, 1990; Braithwaite, 2002; Zemp *et al.*, 2009). Degree day models use empirical relationships between positive near-surface air temperature and ice melt to predict how much melt will occur (Braithwaite, 1984; Braithwaite & Raper, 2007; Hock, 2003); while effective, they over-simplify the processes involved (Hock, 2003). Finally, surface energy balance (SEB) models use measurements of all energy inputs and outputs to produce a more faithful representation of melt processes and calculate the energy available for melt, and subsequent rate and volume of melt (Hock, 2005). As well as quantifying glacier ice melt and contribution to stream flow at a given time, a SEB model can also be used to make predictions of melt under forecasted climate scenarios (Hock, 2005).

At local and regional scales, the amount of energy available for melt (M; all units are W m^{-2}) is given as,

$$M = Q_R + Q_S + Q_L + G + R \tag{1.1}$$

where Q_R is the net radiative heat flux, comprising incoming/outgoing shortwave and longwave radiation, Q_S and Q_L are the sensible and latent heat fluxes (together known as the turbulent fluxes), G is the ground (subsurface) energy flux and R is the sensible heat flux supplied by rain. While the radiative fluxes are the dominant form of energy transfer over time scales of weeks or longer (Morris, 1982; Harding *et al.*, 1989; Munro, 1989; Hock and

Holmgren, 1996; Brock *et al.*, 2006; Sicart *et al.*, 2014; Fitzpatrick *et al.*, 2017), the contribution of the turbulent fluxes can be greater over shorter time scales (hour/days) and in favourable conditions found in warmer, windier and more moisture-rich mid-latitude maritime environments (Anderson *et al.*, 2010; Cuffey and Paterson, 2010; Conway and Cullen, 2013). Of particular note for this thesis is the fact that the significance of turbulent fluxes is likely to increase as parts of the climate become wetter and windier (Stull, 1988; Garratt, 1994; Fausto *et al.*, 2016).

SEB modelling is usually performed at the point scale and extrapolated to the rest of the glacier, with data from a single automatic weather station (AWS) at a location that is assumed to be representative (Oerlemans and Klok, 2002; Giesen *et al.*, 2014). With AWS data from more than one location and some additional parameterisation, the components of the energy balance can be distributed onto a grid covering an entire glacier or region, thus accounting for the spatial variability of the energy fluxes (e.g. Arnold *et al.*, 2006; Ayala *et al.*, 2017; Hock & Holmgren, 2005).

The process of distributing each flux has received varying degrees of attention (see Hock, 2005). For example, distribution of incoming shortwave radiation accounts for direct and diffuse components, the effects of topography and the relationship between observed and potential radiation (Fu and Rich, 2002; Hock and Holmgren, 2005; Sicart *et al.*, 2010). Parameterisation of albedo incorporates the influence of precipitation and subsequent changes in surface characteristics (Oerlemans and Knap, 1998; Hock and Holmgren, 2005). Distribution of the turbulent fluxes relies on successful distribution of meteorological variables, often based on elevation gradients (Braun and Hock, 2004; Fyffe *et al.*, 2014; Molg *et al.*, 2020), and modelling using the bulk aerodynamic method (Hay and Fitzharris, 1988; Brock *et al.*, 2000).

The bulk aerodynamic method uses an integrated form of the gradient-flux relationship (Stull, 1988), requiring measurements of meteorological characteristics including air temperature, wind velocity, wind direction and specific humidity from at least one level in the atmosphere above a surface. To calculate gradients, surface values of each variable are assumed (temperature = 0°C, vapour pressure = 6.11 hPa), and a value for the roughness lengths of momentum and temperature must be known. The roughness length is defined as the height above a surface at which the variable reaches its surface value. The research presented in this thesis is focussed on the roughness length of momentum, which is also known as the **aerodynamic roughness length** and will herein be referred to by the notation z_0 to avoid ambiguity.

Past work has shown that the turbulent fluxes are sensitive to changes in z_0, with an order of magnitude increase in z_0 leading to a doubling of the turbulent fluxes (Munro, 1989). Additionally, the sensitivity of the SEB to the turbulent fluxes is well documented in mid-latitude and maritime climates (Ishikawa *et al.*, 1992; Conway and Cullen, 2013; Giesen *et al.*, 2014) and over hourly/daily timescales (Fausto *et al.*, 2016). Despite this, it is common in point-based and distributed energy balance studies to assume a spatially and temporally constant value of z_0, owing to the difficulty of obtaining measurements *in situ* (e.g. Arnold *et al.*, 2006; Oerlemans & Klok, 2002). In other cases, z_0 is used as a tuning parameter to force models to fit observed melt volumes (e.g. Braun & Hock, 2004). Empirical studies have shown, however, that z_0 is spatially variable by several orders of magnitude across individual glaciers and ice masses, and is dynamic throughout the melt season (Brock *et al.*, 2006; Smith *et al.*, 2020). Thus, z_0 represents a key uncertainty in the calculation of the turbulent fluxes and overall energy balance.

Traditional methods of estimating z_0 include using extrapolated log-linear wind speed profiles (the aerodynamic profile method; Brock *et al.*, 2006; Denby and Smeets, 2000) or 2D microtopographic transects (the 2D transect method; Munro, 1989). The aerodynamic profile and 2D transect methods have been used mainly for collecting point data and are ill-suited to collecting distributed z_0 values, but recent work has considered how estimates of z_0 can be derived from 3D topographic data (Irvine-Fynn *et al.*, 2014; Smith *et al.*, 2016b). Topographic data derived from structure from motion photogrammetry (SfM; Smith *et al.*, 2016a) or terrestrial laser scanning (TLS; Lemmens, 2011; Telling *et al.*, 2017) have been successfully used to generate z_0 values that are similar to those obtained from aerodynamic profiles (Miles *et al.*, 2017; Quincey *et al.*, 2017; Fitzpatrick *et al.*, 2019), although these are limited to the plot scale (tens of metres, centimetres per pixel). Attempts to produce glacier-scale maps of z_0 have so far required site-specific validation or not been otherwise transferable to other glaciers (Smith *et al.*, 2016b; Fitzpatrick *et al.*, 2019). Scale- and resolution-dependence inherent to microtopographic methods (Rees and Arnold, 2006; Quincey *et al.*, 2017) has also impeded the development of methods for obtaining robust z_0 estimates that can be incorporated into distributed SEB models. This clear need forms the rationale of this thesis.

1.2 Research aim and objectives

The overarching aim of this research is to investigate the impact of fully distributed estimates of z_0 on calculations of the turbulent fluxes, energy balance and ablation. To achieve this, I

sought to develop a method to allow spatially and temporally distributed z_0 estimates to be included in distributed SEB models, and to bridge the gap between the plot and glacier scale domains so that useful and robust distributed estimates of z_0 can be obtained from satellite or other widely available remotely sensed datasets. Three objectives have been devised to enable fulfilment of this aim and inform the structure of this thesis:

O1. Interrogate and compare the sensitivities, precision and uncertainty of current methods of calculating z_0. This objective (Chapter 4) provides a timely and much needed synthesis of methods, along with context for development of new methods.

O2. Develop a method to upscale plot-scale z_0 estimates so that they can be acquired from coarse resolution, glacier-scale data. Informed by the previous objective, this objective is central to obtaining distributed estimates of z_0 (Chapter 5).

O3. Implement fully distributed z_0 in a glacier SEB model. This final objective will elucidate the possible effects that incorporating spatially and temporally variable z_0 has on the turbulent fluxes and overall SEB, and what the implications may be for melt estimates (Chapter 6).

1.3 Thesis structure

This thesis is organised into four parts. In Part I, the background of the main research themes is provided, including the theory behind SEB and turbulent flux calculations, followed by a review of the role and calculation of z_0 (Chapter 2). The principles and applications of the topographic survey techniques used within the thesis are then reviewed (Chapter 3). Next, in Part II, the three results chapters present the main findings of the thesis: an investigation of the sensitivities, precision and uncertainty in z_0 estimation methods (Chapter 4), the development of a method for obtaining robust glacier-scale estimates of z_0 from topographic data (Chapter 5), and the implementation of spatially and temporally distributed z_0 in a distributed glacier SEB model (Chapter 6). These three chapters relate to each of the objectives above and are based on published papers (Chambers, *et al.*, In press; Chambers *et al.*, 2019; 2021). Contributions are detailed on pages ii - iii. Each results chapter contains its own location, data and methods, discussion of results and reference list. Part III draws together the results from all three results chapters to provide an overall discussion of the work presented in this thesis, indications of what remains to be considered in future work, and the conclusions that can be drawn (Chapter 7). Finally, Part IV (Appendices A-C) includes the supporting information for the results chapters.

References

Anderson, B., Mackintosh, A., Stumm, D., George, L., Kerr, T., Winter-Billington, A. & Fitzimons, S. (2010) 'Climate sensitivity of a high-precipitation glacier in New-Zealand', *Journal of Glaciology*, 56(195), pp. 114-128(15). doi: 10.3189/002214310791190929.

Arnold, N. S., Rees, W. G., Hodson, A. J. & Kohler, J. (2006) 'Topographic controls on the surface energy balance of a high Arctic valley glacier', *Journal of Geophysical Research: Earth Surface*, 111(2). doi: 10.1029/2005JF000426.

Ayala, A., Pellicciotti, F., Peleg, N. & Burlando, P. (2017) 'Melt and surface sublimation across a glacier in a dry environment: Distributed energy-balance modelling of Juncal Norte Glacier, Chile', *Journal of Glaciology*, 63(241), pp. 803–822. doi: 10.1017/jog.2017.46.

Balog, J. (2020) *Extreme Ice Survey*. Available at: http://extremeicesurvey.org/ (Accessed: 5 January 2021).

Braithwaite, R. J. (2002) 'Glacier mass balance: The first 50 years of international monitoring', *Progress in Physical Geography*, 26(1), pp. 76–95. doi: 10.1191/0309133302pp326ra.

Braun, M. & Hock, R. (2004) 'Spatially distributed surface energy balance and ablation modelling on the ice cap of King George Island (Antarctica)', *Global and Planetary Change*, 42(1–4), pp. 45–58. doi: 10.1016/j.gloplacha.2003.11.010.

Brock, B. W., Willis, I. C. & Sharp, M. J. (2006) 'Measurement and parameterization of aerodynamic roughness length variations at Haut Glacier d'Arolla, Switzerland', *Journal of Glaciology*, 52(177), pp. 281–297. doi: 10.3189/172756506781828746.

Brock, B. W., Willis, I. C., Sharp, M. J. & Arnold, N. S. (2000) 'Modelling seasonal and spatial variations in the surface energy balance of Haut Glacier d'Arolla, Switzerland', *Annals of Glaciology*, 31(January 2016), pp. 53–62. doi: 10.3189/172756400781820183.

Chambers, J. R., Smith, M. W., Bravo, C., Quincey, D. J., Nicholson, L., Stiperski, I., Prinz, R., Sailer, R. & Mertes, J. (In press) 'Incorporating fully spatially and temporally distributed aerodynamic roughness in a distributed glacier surface energy balance model', *Journal of Glaciology*.

Chambers, J. R., Smith, M. W., Quincey, D. J., Carrivick, J. L., Ross, A. N. & James, M. R. (2019) 'Glacial Aerodynamic Roughness Estimates: Uncertainty, Sensitivity, and Precision in Field Measurements', *Journal of Geophysical Research: Earth Surface*, 125(2). doi: 10.1029/2019JF005167.

Chambers, J. R., Smith, M. W., Smith, T., Sailer, R., Quincey, D. J., Carrivick, J. L., Nicholson, L., Mertes, J., Stiperski, I. & James, M. R. (2021) 'Correcting for Systematic Underestimation of Topographic Glacier Aerodynamic Roughness Values From Hintereisferner, Austria', *Frontiers in Earth Science*, 9, pp. 1–16. doi: 10.3389/feart.2021.691195.

Conway, J. P. & Cullen, N. J. (2013) 'Constraining turbulent heat flux parameterization over a temperate maritime glacier in New Zealand', *Annals of Glaciology*, 54(63), pp. 41–51. doi: 10.3189/2013AoG63A604.

Cuffey, K. M. & Paterson, W. S. B. (2010) *The Physics of Glaciers*. Fourth. Oxford: Elsevier. doi: 10.1063/1.2915138.

Davis, N. (2017) 'Iceberg twice size of Luxembourg breaks off Antarctic ice shelf', *The*

Guardian, 12 July.

Denby, B. & Smeets, C. J. P. P. (2000) 'Derivation of Turbulent Flux Profiles and Roughness Lengths from Katabatic Flow Dynamics', *Journal of Applied Meteorology*, 39(9), pp. 1601–1612. doi: 10.1175/1520-0450(2000)039<1601:DOTFPA>2.0.CO;2.

Fausto, R. S., Van As, D., Box, J. E., Colgan, W., Langen, P. L. & Mottram, R. H. (2016) 'The implication of nonradiative energy fluxes dominating Greenland ice sheet exceptional ablation area surface melt in 2012', *Geophysical Research Letters*, 43(6), pp. 2649–2658. doi: 10.1002/2016GL067720.

Fitzpatrick, N., Radić, V. & Menounos, B. (2017) 'Surface Energy Balance Closure and Turbulent Flux Parameterization on a Mid-Latitude Mountain Glacier, Purcell Mountains, Canada', *Frontiers in Earth Science*, 5(September), pp. 1–20. doi: 10.3389/feart.2017.00067.

Fitzpatrick, N., Radić, V. & Menounos, B. (2019) 'A multi-season investigation of glacier surface roughness lengths through in situ and remote observation', *The Cryosphere*, 13, pp. 1051–1071. doi: https://doi.org/10.5194/tc-13-1051-2019.

Fu, P. & Rich, P. M. (2002) *A geometric solar radiation model with applications in agriculture and forestry*, *Computers and Electronics in Agriculture*. Available at: www.elsevier.com/locate/compag.

Fyffe, C. L., Reid, T. D., Brock, B. W., Kirkbride, M. P., Diolaiuti, G., Smiraglia, C. & Diotri, F. (2014) 'A distributed energy-balance melt model of an alpine debris-covered glacier', *Journal of Glaciology*, 60(221), pp. 587–602. doi: 10.3189/2014JoG13J148.

Garratt, J. R. (1994) 'The atmospheric boundary layer - review', *Earth Science Reviews*, 37(1–2), pp. 89–134. doi: 10.1016/0012-8252(94)90026-4.

Giesen, R. H., Andreassen, L. M., Oerlemans, J. & Van Den Broeke, M. R. (2014) 'Surface energy balance in the ablation zone of Langfjordjøkelen, an arctic, maritime glacier in northern Norway', *Journal of Glaciology*, 60(219), pp. 57–70. doi: 10.3189/2014JoG13J063.

Gusain, H. S., Singh, K. K., Mishra, V. D., Srivastava, P. K. & Ganju, A. (2009) 'Study of surface energy and mass balance at the edge of the antarctic ice sheet during summer in dronning maud land, east antarctica', *Antarctic Science*, 21(4), pp. 401–409. doi: 10.1017/S0954102009001989.

Hagen, J. O. & Liestøl, O. (1990) 'Long-term glacier mass balance investigations in Svalbard, 1950-88', *Annals of Glaciology*, 14, pp. 102–106. doi: https://doi.org/10.3189/S0260305500008351.

Harding, R. J., Entrasser, N., Escher-Vetter, H., Jenkins, A., Kaser, G., Kuhn, M., Morris, E. M. & Tanzer, G. (1989) 'Energy and Mass Balance Studies in the Firn Area of the Hintereisferner', in Oerlemans, J. (ed.) *Glacier Fluctuations and Climatic Chang*. doi: 10.1007/978-94-015-7823-3_21.

Hay, J. E. & Fitzharris, B. B. (1988) 'A Comparison of the Energy-Balance and Bulk-aerodynamic Approaches for Estimating Glacier Melt', *Journal of Glaciology*, 34(117), pp. 145–153. doi: https://doi.org/10.3189/S0022143000032172.

Hock, R. (2005) 'Glacier melt: a review of processes and their modelling', *Progress in Physical Geography*, 29(3), pp. 362–391. doi: 10.1191/0309133305pp453ra.

Hock, R. & Holmgren, B. (1996) 'Some Aspects of Energy Balance and Ablation of

Storglaciären , Northern Sweden', *Geografiska Annaler Series A-Physical Geography*, 78(2), pp. 121–131.

Hock, R. & Holmgren, B. (2005) 'A distributed surface energy-balance model for complex topography and its application to Storglaciären, Sweden', *Journal of Glaciology*, 51(172), pp. 25–36. doi: https://doi.org/10.3189/172756505781829566.

Hock, R., Rasul, G., Adler, C., Cáceres, B., Gruber, S., Hirabayashi, Y., Jackson, M., Kääb, A., Kang, S. & Kutuzov, S. (2019) 'High Mountain Areas', in *IPCC Special Report on the Ocean and Cryosphere in a Changing Climate*. Geneva, Switzerland, pp. 131–202.

Hugonnet, R., McNabb, R., Berthier, E., Menounos, B., Nuth, C., Girod, L., Farinotti, D., Huss, M., Dussaillant, I., Brun, F. & Kääb, A. (2021) 'Accelerated global glacier mass loss in the early twenty-first century', *Nature*, 592(7856), pp. 726–731. doi: 10.1038/s41586-021-03436-z.

Irvine-Fynn, T. D. L., Sanz-Ablanedo, E., Rutter, N., Smith, M. W. & Chandler, J. H. (2014) 'Measuring glacier surface roughness using plot-scale, close-range digital photogrammetry', *Journal of Glaciology*, 60(223), pp. 957–969. doi: 10.3189/2014JoG14J032.

Ishikawa, N., Owens, I. F. & Sturman, A. P. (1992) 'Heat balance characteristics during fine periods on the lower parts of the Franz Josef Glacier, South Westland, New Zealand', *International Journal of Climatology*, 12(4), pp. 397–410. doi: 10.1002/joc.3370120407.

Lemmens, M. (2011) 'Terrestrial Laser Scanning', in *Geo-information*, pp. 101–121. doi: 10.1007/978-94-007-1667-4.

Liu, J., Chen, R. & Han, C. (2020) 'Spatial and temporal variations in glacier aerodynamic surface roughness during the melting season, as estimated at the August-one ice cap, Qilian mountains, China', *Cryosphere*, 14(3), pp. 967–984. doi: 10.5194/tc-14-967-2020.

Miles, E. S., Steiner, J. F. & Brun, F. (2017) 'Highly variable aerodynamic roughness length (z0) for a hummocky debris-covered glacier', *Journal of Geophysical Research: Atmospheres*, 122(16), pp. 8447–8466. doi: 10.1002/2017JD026510.

Molg, T., R. Hardy, D., Collier, E., Kropač, E., Schmid, C., J. Cullen, N., Kaser, G., Prinz, R. & Winkler, M. (2020) 'Mesoscale atmospheric circulation controls of local meteorological elevation gradients on Kersten Glacier near Kilimanjaro summit', *Earth System Dynamics*, 11(3), pp. 653–672. doi: 10.5194/esd-11-653-2020.

Morris, E. M. (1982) 'Sensitivity of the European Hydrological System snow models', in *Hydrological Aspects of Alpine and High Mountain Areas, Proceedings of the Symposium International Association of Hydrological Sciences*. Exeter, pp. 221–231.

Munro, D. S. (1989) 'Surface roughness and bulk heat transfer on a glacier: comparison with eddy correlation', *Journal of Glaciology*, 35(121), pp. 343–348.

Oerlemans, J. & Klok, E. J. (2002) 'Energy Balance of a Glacier Surface: Analysis of Automatic Weather Station Data from the Morteratschgletscher, Switzerland', *Arctic, Antarctic, and Alpine Research*, 34(4), pp. 477–485. doi: 10.1080/15230430.2002.12003519.

Oerlemans, J. & Knap, W. (1998) 'A 1 year record of global radiation and albedo in the ablation zone of Morteratschgletscher, Switzerland', *Journal of Glaciology*, 44(147), pp. 231–238. doi: https://doi.org/10.3189/S0022143000002574.

Østrem, G. & Brugman, M. (1966) *Glacier Mass Balance Measurements: A manual for field work*.

Quincey, D. J., Smith, M. W., Rounce, D. R., Ross, A. N., King, O. & Watson, C. S. (2017) 'Evaluating morphological estimates of the aerodynamic roughness of debris covered glacier ice', *Earth Surface Processes and Landforms*. doi: 10.1002/esp.4198.

Rees, W. G. & Arnold, N. S. (2006) 'Scale-dependent roughness of a glacier surface: Implications for radar backscatter and aerodynamic roughness modelling', *Journal of Glaciology*, 52(177), pp. 214–222. doi: 10.3189/172756506781828665.

Roe, G. H., Christian, J. E. & Marzeion, B. (2021) 'On the attribution of industrial-era glacier mass loss to anthropogenic climate change', *The Cryosphere*, 15(4), pp. 1889–1905. doi: 10.5194/tc-15-1889-2021.

Sicart, J. E., Hock, R., Ribstein, P. & Chazarin, J. P. (2010) 'Sky longwave radiation on tropical Andean glaciers: parameterization and sensitivity to atmospheric variables', *Journal of Glaciology*, 56(199), pp. 854–860. doi: https://doi.org/10.3189/002214310794457182.

Sicart, J. E., Litt, M., Helgason, W., Tahar, V. Ben & Chaperon, T. (2014) 'A study of the atmospheric surface layer and roughness lengths on the high-altitude tropical Zongo glacier, Bolivia', *Journal of Geophysical Research*, 119(7), pp. 3793–3808. doi: 10.1002/2013JD020615.

Slater, T., Lawrence, I. R., Otosaka, I. N., Shepherd, A., Gourmelen, N., Jakob, L., Tepes, P., Gilbert, L. & Nienow, P. (2021) 'Review article: Earth's ice imbalance', *Cryosphere*, 15(1), pp. 233–246. doi: 10.5194/tc-15-233-2021.

Smith, M. W., Carrivick, J. L. & Quincey, D. J. (2016a) 'Structure from motion photogrammetry in physical geography', *Progress in Physical Geography*, 40(2), pp. 247–275. doi: 10.1177/0309133315615805.

Smith, M. W., Quincey, D. J., Dixon, T., Bingham, R. G., Carrivick, J. L., Irvine-Fynn, T. D. L. & Rippin, D. M. (2016b) 'Aerodynamic roughness of glacial ice surfaces derived from high-resolution topographic data', *Journal of Geophysical Research: Earth Surface*, 121(4), pp. 748–766. doi: 10.1002/2015JF003759.

Stull, R. (1988) *An introduction to boundary layer meteorology*. London: Kluwer.

Telling, J., Lyda, A., Hartzell, P. & Glennie, C. (2017) 'Review of Earth science research using terrestrial laser scanning', *Earth-Science Reviews*, 169(April), pp. 35–68. doi: 10.1016/j.earscirev.2017.04.007.

Zemp, M., Hoelzle, M. & Haeberli, W. (2009) 'Six decades of glacier mass-balance observations: a review of the worldwide monitoring network', *Annals of Glaciology*, 50(50), pp. 101–111. doi: https://doi.org/10.3189/172756409787769591.

Part I: Background

Chapter 2 : Glacier surface energy balance modelling and aerodynamic roughness

2.1 Introduction

In this section, more detailed context is given for the work carried out in the thesis, highlighting the need and rationale for its completion and for the data collection methods used. First, the importance of the aerodynamic roughness length, z_0, and its key role within the SEB are outlined (Section 2.2). Then, a more general background is given for the glacier SEB, its components and approaches to SEB modelling including distributed models (Sections 2.3 and 2.4), followed by the mechanisms, calculation and importance of the turbulent fluxes (Section 2.5), leading into the different approaches to calculating z_0 including using secondary values, wind profiles (Section 2.6) and microtopographic data (Section 2.7 and 2.8). Elements of this chapter overlap with the content in later chapters, specifically Section 4.2 of Chapter 4 which gives background for methods of finding z_0 and reviews previous work, and Section 6.1 of Chapter 6, which briefly discusses point-scale and distributed SEB models. Chapter 3 gives an introduction to the topographic data collection methods used in this thesis, and reviews the background and applications of each.

2.2 The role of z_0 in glacial melt modelling

The aerodynamic roughness length (z_0), also known as the roughness length of momentum, is the height above the mean surface at which horizontal wind speed is zero (Stull, 1988; Greuell and Genthon, 2004; Cuffey and Paterson, 2010). Additional roughness lengths of temperature and humidity are sometimes used and while evidence exists that these differ to z_0 (Andreas, 1987; Smeets *et al.*, 1998; Hock and Holmgren, 2005; Giesen *et al.*, 2014), it is common to assume that they are equal (Munro, 1989; Gillett and Cullen, 2011; Dadic *et al.*, 2013). The focus of this thesis is the parameterisation and calculation of z_0; roughness lengths of temperature and humidity are not considered.

A value for z_0 is required when the turbulent flux components of the SEB are calculated using the bulk aerodynamic method (Cuffey and Paterson, 2010), which is explained in Section 2.5. The z_0 term is used in the integration of log-linear wind speed profiles in the bulk aerodynamic equations using flux-gradient theory, and depends on wind speed and the geometry of the surface (Fig. 2.1; Greuell and Genthon, 2004). Since z_0 is not an actual physical property of a surface, but rather is a property arising from the interaction of wind speed and surface topography, it is difficult to measure. As a result, values that are available for particular glacier surfaces are widely adopted as representative of all similar glacier surfaces. Yet evidence shows that the turbulent fluxes, and indeed the overall SEB and ablation quantities, are sensitive to fluctuations in z_0 (e.g. Hock and Holmgren, 1996); indeed,

it is often recognised that an order of magnitude increase in z_0 can lead to a doubling of the turbulent fluxes (Munro, 1989). This sensitivity is demonstrated in Chapter 6 (Section 6.5.1). Spatial differences in z_0 spanning at least three orders of magnitude have been observed across individual glaciers (Fig. 2.2; Brock *et al.*, 2006; Fitzpatrick *et al.*, 2019), but such variability is unrepresented in SEB models. Spatial differences translate into temporal differences when areas of a glacier surface have different geometric properties at different times of the year, yet this is usually represented by simply implementing one value for ice and another for snow.

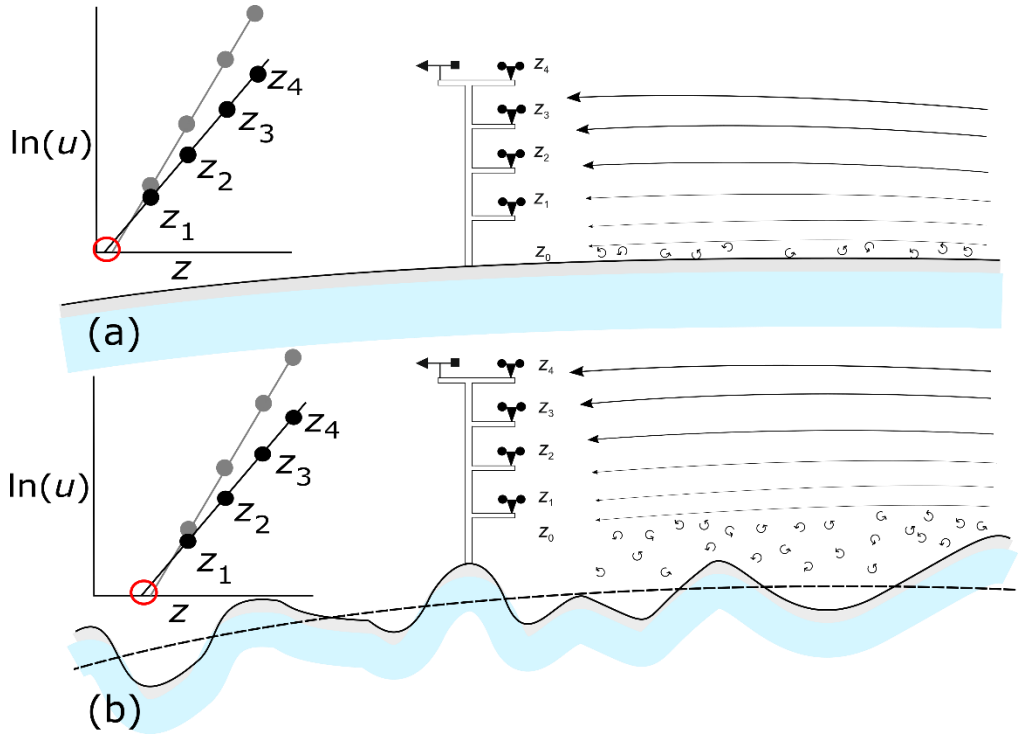

Fig. 2.1 Sketch of log-linear wind speed profiles. This diagram gives a simplified representation of how wind speed (u) and glacier topography influence z_0. In the upper panel (a) the glacier surface is much smoother, so the wind profile measured by the wind tower reaches zero closer to the surface and the turbulent exchange of energy is inhibited. In the lower panel (b), a rougher surface interrupts the horizontal movement of air, promoting the turbulent exchange of energy between the surface and atmosphere. The sketched plots in each panel show idealised examples of log-linear wind speed profiles from the wind towers (black lines/points), and how z_0 can be altered by faster wind speeds (grey lines/points).

Distributed, or gridded, SEB models have been shown to provide greater detail than point-based models (Hock, 2005; Ayala *et al.*, 2017). They show how the SEB varies spatially and enable more accurate simulations of glacier melt, despite uncertainties arising from the extrapolation methods used to distribute the various elements of the SEB (Chapter 6; Hock and Holmgren, 2005; Arnold *et al.*, 2006). While the use of microtopographic data has shown

potential for distributed z_0 estimates to be obtained, work in this area has lagged and, consequently, single, static values are still widely used (Hock and Holmgren, 2005; Ayala *et al.*, 2017; Bravo *et al.*, 2021). Obtaining and implementing robust distributed (or gridded) estimates of z_0 represents the current frontier of research into glacier z_0, as well as being the aim underpinning this research.

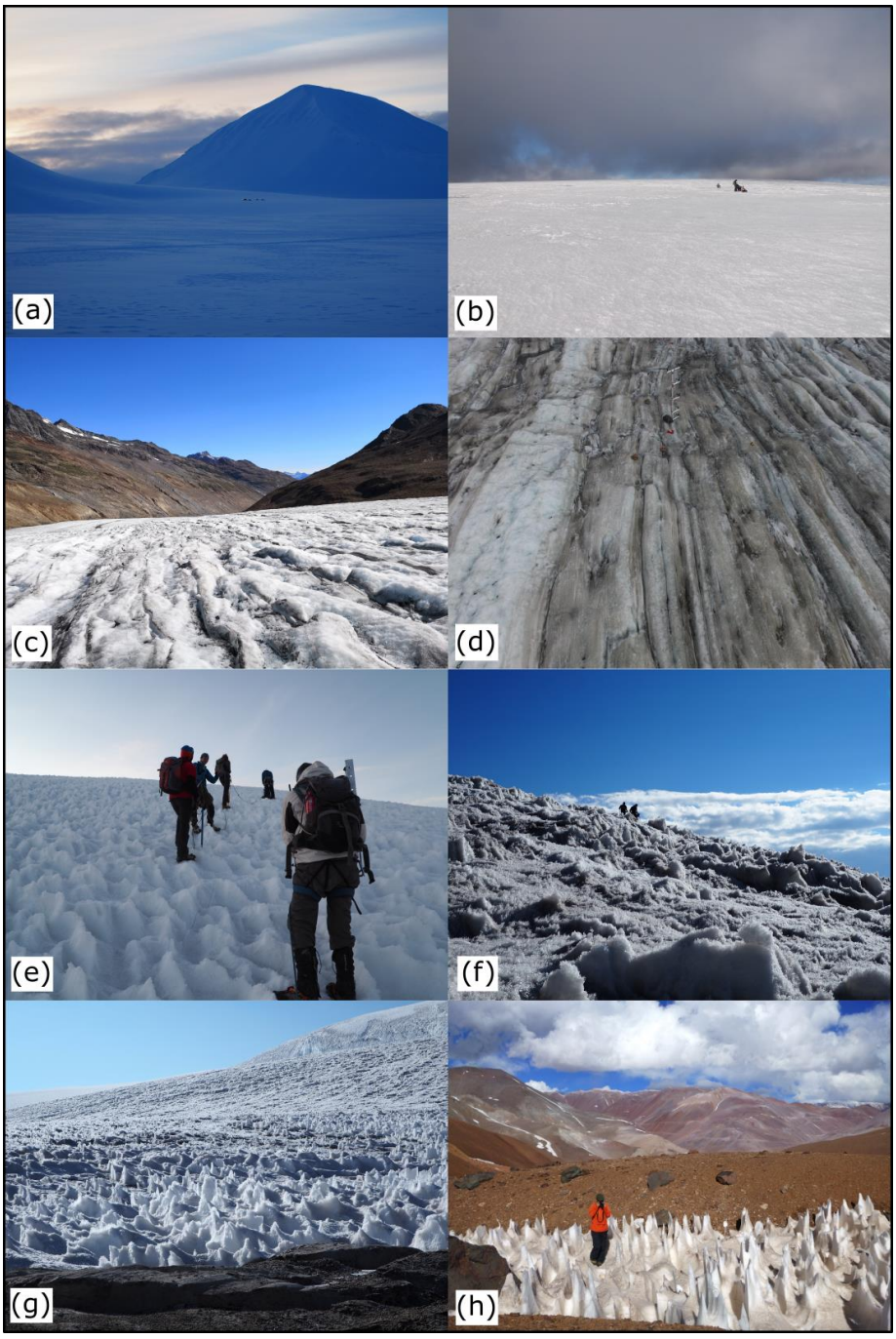

Fig. 2.2 Examples of ice surface types. (a) shows a snow-covered glacier and (b) shows a smooth ice cap, both in Svalbard. (c) and (d) both show bare ice surfaces with linear, streamlined roughness following the glacier flow direction and prevailing wind direction at Hintereisferner, Austria. (e), (f) and (g) show ice with increasingly rough characteristics at Quelccaya ice cap in Peru, and finally (h) shows a field of ice penitents at Tapado glacier, Chile. The diversity of surfaces demonstrates the argument that z_0 cannot be adequately represented by a single value. (Photo (h) by Lindsey Nicholson, all others by the author).

2.3 The glacier surface energy balance

Monitoring and predicting the melt of glaciers is critical to understanding some of the impacts of climate change (Hock *et al.*, 2019; Roe *et al.*, 2021). Global sea levels, heat budgets and fresh water availability are all affected by the retreat of ice sheets, ice caps and glaciers (Hock *et al.*, 2019). Observation of interactions at the boundary between the glacier surface and atmosphere can help quantify short-term runoff estimates, as well as longer-term mass balance predictions. While simple empirical relationships between air temperature and melt can give good runoff estimates, such as with a temperature-index model, they are unreliable under climate change scenarios. A SEB model is transferrable in space and time, and can provide a more complete picture of the processes causing melt (Hock, 2005). In a SEB model, all energy inputs and outputs are calculated separately and combined; any surplus energy (M, W m^{-2}) is assumed to be used to melt ice (or snow). The energy balance usually expressed as in equation (1.1), comprising Q_R, the net radiative short- and longwave heat flux, Q_S and Q_L, the sensible and latent heat fluxes (turbulent fluxes), the ground energy flux (G) and the sensible heat flux supplied by rain (R). The latter two components are often considered to be negligible, and are usually left out of SEB calculations (e.g. Bravo *et al.*, 2017; Litt *et al.*, 2017). These exclusions are quite restrictive: excluding G only really applies when the surface is predominantly at melting point, and G becomes more significant as elevation increases; R is important in some maritime locations. Generally, the custom within glaciology is that positive flux values represent energy gain at the surface, contributing to ablation, whereas negative flux values characterise energy loss (Hock, 2005).

Shortwave radiation comprises wavelengths 0.15-4 µm and is supplied directly from the sun, commonly accounting for > 60% of the SEB (Giesen *et al.*, 2014). At the point that it reaches the ground it is known as global radiation and has three components: direct solar beam, diffuse light from scattering in the atmosphere and light reflected from surrounding terrain (Cuffey and Paterson, 2010). The amount of incoming shortwave radiation depends on the elevation of the measurement point, cloud cover, the solar zenith angle, latitude and aspect (Oke, 1987). Generally, the most solar radiation is received at high elevation locations at low latitudes, with clear skies and a sun-facing aspect; hence, in the northern hemisphere north-eastern aspects are most favourable for glacier formation (Evans, 1977; Barr and Spagnolo, 2015).

Reflected, or outgoing, shortwave radiation is accounted for by the albedo, which is the proportion of all incoming shortwave radiation that is reflected by a surface. Due to the reflectivity of ice and snow, glacier albedo is usually high, such that much of the radiation

that reaches large ice masses is reflected back into space. Albedo is often acknowledged to be a driving factor in a glacier SEB (Hock, 2005; Sicart *et al.*, 2008; Dumont *et al.*, 2012); yet, glacier albedo is variable depending on the age and composition of snow and ice, as well as any coverings of debris, dust or biological matter (Ming *et al.*, 2009; Box *et al.*, 2012; Fyffe *et al.*, 2014; Gabbi *et al.*, 2015; Davaze *et al.*, 2018). The albedo of a typical mountain glacier increases in line with the elevation of the glacier, with fresh, clean snow tending to dominate in the accumulation area and more dirty or debris-covered ice being found near the glacier terminus (Van De Wal *et al.*, 1992; Oerlemans and Knap, 1998; Naegeli *et al.*, 2019).

Longwave radiation is characterised as energy with wavelengths of 4-120 µm and radiates from the Earth surface and atmosphere (Kondratyev, 1965). The amount of incoming longwave radiation at a glacier surface is dependent on humidity, air temperature and the temperature of water vapour, so tends to be less at higher elevations where temperatures are lower (Hock, 2005). To quantify incoming longwave radiation, most glacier SEB models use an expression that is based on clear-sky emissivity and incorporates the Stefan-Boltzmann constant, which relates radiation intensity increases to temperature increases, air temperature and a cloud factor (Hock, 2005; Mölg *et al.*, 2009; Sicart *et al.*, 2010; Juszak and Pellicciotti, 2013). Outgoing longwave radiation is calculated in a similar fashion, using the emissivity and temperature of the surface. At infrared longwave wavelengths ice, snow and liquid water behave as black body radiators, meaning they have near-perfect emissivity (Cuffey and Paterson, 2010). Therefore, the longwave radiation flux is often an energy sink, transferring more energy away from the surface than to it (Favier *et al.*, 2004; Giesen *et al.*, 2014; Fitzpatrick *et al.*, 2017).

The heat fluxes due to rain and subsurface heating are often discounted in SEB studies of glaciers (Hock, 2005). For alpine glaciers comprising temperate ice, they contribute little as a heat source or sink (Giesen *et al.*, 2014; Fitzpatrick *et al.*, 2017). There are exceptions, however – Arctic, or cold, glaciers like those found in Svalbard can experience significant subsurface warming due to the refreezing of meltwater beneath the firn layer, which releases latent heat (Wilson and Flowers, 2013; van Pelt *et al.*, 2016). In addition, evidence suggests that substantial quantities of energy transferred to a glacier surface at the start of the melt season can be used to raise subsurface temperatures, potentially altering the duration and magnitude of the ablation season (Sauter *et al.*, 2020). Rain can also indirectly affect the SEB by refreezing after percolating through the firn layer. For rain to directly impact the SEB significantly a warm, heavy, sustained rainfall event is required, in which conditions the rain heat flux can contribute as much as 37% of daily ablation (Hay and

Fitzharris, 1988; Hock, 2005).

Named for their turbulent energy transfer mechanisms, the turbulent fluxes are induced by a temperature or moisture gradient near the boundary between the atmosphere and surface of a glacier (Cuffey & Paterson, 2010). Heat exchanged between the surface and atmosphere through conduction and/or convection via turbulent eddies makes up the sensible heat flux (Q_S). For example, when the atmosphere near the surface is warmer than the surface, energy is transferred to the ice (Fig. 2.3a), and vice versa in the opposite conditions (Fig. 2.3b). Similarly, the latent heat flux (Q_L) refers to the exchange of energy via evaporation/condensation in the presence of a moisture gradient (Fig. 2.3c and 2.3d). Sublimation can occur when a very steep moisture gradient exists, acting as a form of ablation without melt usually at high elevations (e.g. Sicart *et al.*, 2005). These turbulent mechanisms are more efficient in strong winds (when energy can be quickly carried towards/away from the surface) and when a rough glacier surface promotes turbulent mixing of the air near the surface/atmosphere boundary (Stull, 1988; Garratt, 1992); however, direct measurement of the turbulent fluxes is difficult (see Section 2.5).

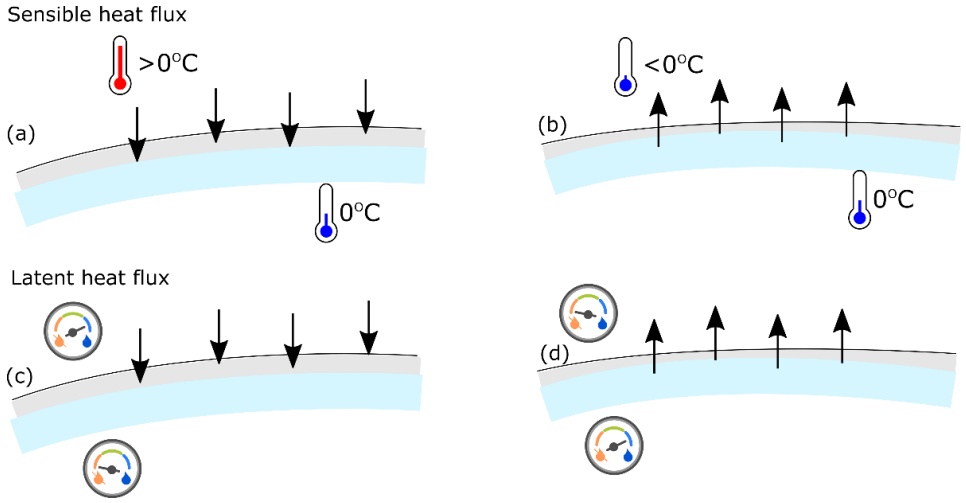

Fig. 2.3 Sketch of temperature and moisture gradients. The sensible heat flux is induced by a temperature gradient: when the surface is cooler than the air, energy is transferred to the surface via conduction and convection (a) and when the air is cooler than the surface, energy is transferred away from the surface (b). Likewise with the latent heat flux, when the surface is drier than the air, energy is transferred to the surface via condensation (c) and away from the surface via evaporation when the air is drier than the surface (d).

Q_S and Q_L can contribute between ~35% to ~50% of the SEB over hourly to daily timescales, and more in cloudy and windy conditions (Giesen *et al.*, 2014). In extreme cases, the turbulent fluxes comprise >75% of the SEB (Fausto *et al.*, 2016b, a). Fig. 2.4 summarises the roles of radiant and turbulent energy fluxes globally, showing areas with higher contributions from turbulent fluxes are preferentially located in maritime climates (Anderson *et al.*, 2010).

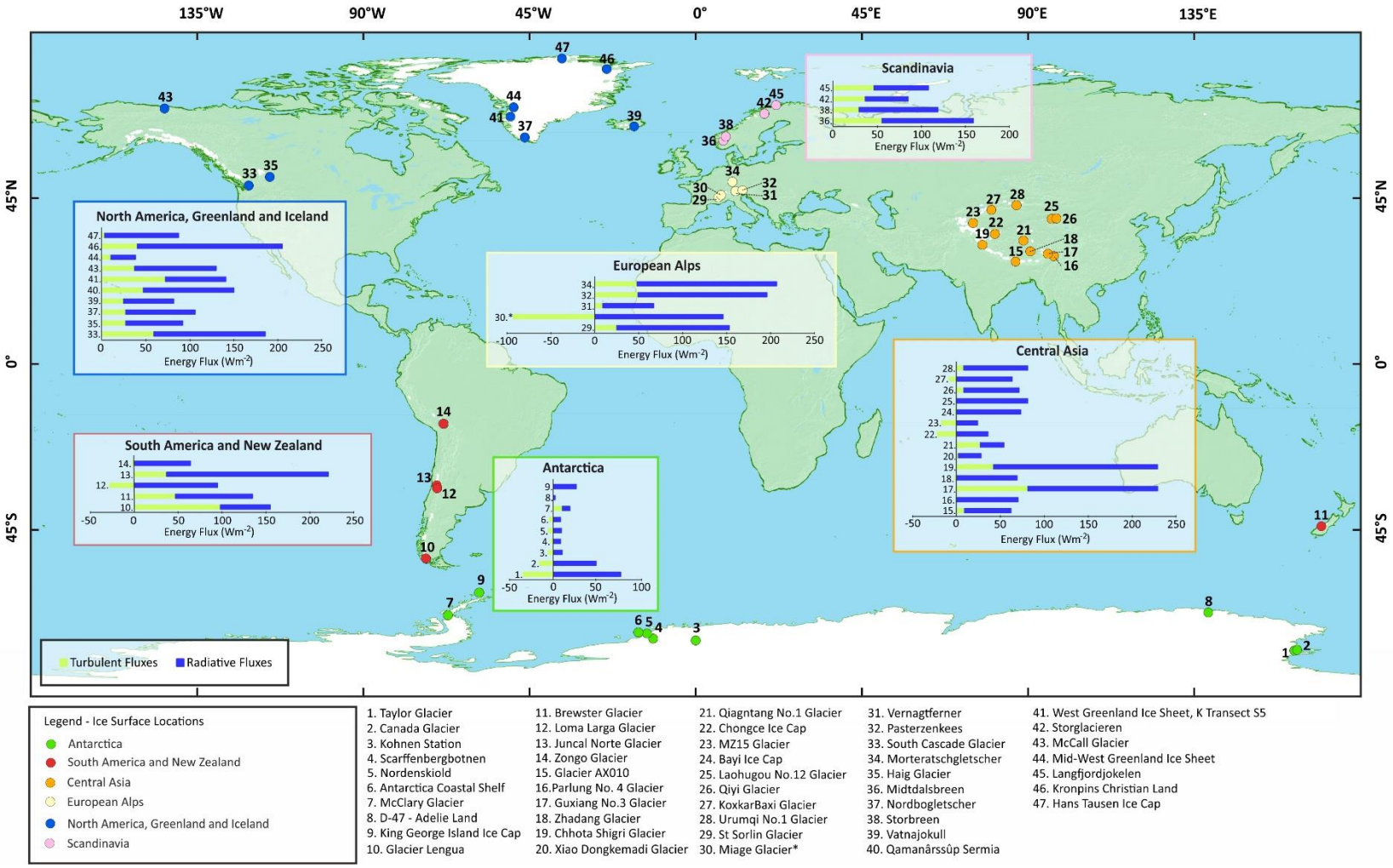

Fig. 2.4 Role of turbulent fluxes globally. Data summarised from studies over permanent snow or ice surfaces for longer than two weeks during the ablation season. The Miage Glacier* is debris covered. References for each point are available from Appendix C. Values over ice sheets indicated by an asterisk. Reproduced from Smith *et al.* (2020).

2.4 Distributed surface energy balance models

Most commonly, a SEB model is calculated from point-based data, from which melt values are assumed to be representative for the given study area (e.g. Giesen *et al.*, 2014b; Oerlemans *et al.*, 1999; Radić *et al.*, 2017a; Sicart *et al.*, 2005). Distributed data can also be used to inform a SEB, but this approach is less common owing to the additional data requirements for model parameterisation (e.g. Arnold *et al.*, 2006; Bravo *et al.*, 2017; Shaw *et al.*, 2017). Distributed SEB models are gaining popularity as the quality and availability of digital elevation models (DEMs) improves, including regional datasets such as the ArcticDEM, the Reference Elevation Model for Antarctica and the High Mountain Asia DEM (Shean, 2017; Porter *et al.*, 2018; Howat *et al.*, 2019). Distribution of SEB model components has garnered substantial research interest through endeavours to reflect the spatial and temporal heterogeneity of the different components. For each component there are several approaches, which are summarised briefly here.

Incoming shortwave radiation is split into direct and diffuse components, so that the differing effect that local topography has on each can be taken into account (Hock, 2005; Hock and Holmgren, 2005). Whether for a point or a grid, the amount of incoming shortwave radiation is influenced by the surrounding topography, as well as the angle and elevation of the sun and the cloud-cover. Several different radiation models exist; using a DEM and an algorithm incorporated into a Geographical Information System (GIS) is common practice (Fu and Rich, 2002).

Distributed albedo is used to account for the shortwave radiation that is reflected by the surface, but correctly calculating it is challenging. Many factors influence changes in albedo, such as snow depth and density, melt rate, sun altitude, air temperature and precipitation (Willis *et al.*, 2002). The extent to which these factors are included in albedo models varies. Regardless of which factors are included, most albedo models attempt to recreate the degradation of a surface over time since the last snowfall (Oerlemans and Knap, 1998; Hock and Holmgren, 2005; Arnold *et al.*, 2006). Temporal models require observations of snow-depth, snow-density or precipitation data from which to calculate albedo. When these are not available an alternative method is to derive albedo from remotely sensed satellite imagery. Different bands of data from Landsat scenes, for example, can be combined once corrected for the solar angle to give an accurate estimate (±0.01 compared to validation data) of the albedo of ice, snow and mountain glaciers (Liang, 2000; Wang *et al.*, 2016; Naegeli *et al.*, 2019).

The distribution of incoming longwave radiation is also dependent on several factors and

becomes more complex in mountain terrain. Accurate distribution of air temperature, relative humidity and pressure are essential, as is a calculation of the potential incoming longwave radiation at each point over the glacier, itself dependent on how much sky is visible, cloud cover and the proximity of terrain like valley sides (Mölg *et al.*, 2009). Outgoing longwave radiation is usually much simpler to model, being dependent on the emissivity of the surface and the surface temperature.

Accurate distribution of meteorological variables is also fundamental for calculations of the turbulent fluxes. For wind speed, approaches vary from simply assuming a constant speed over the study area (e.g. Arnold *et al.*, 2006; Hock and Holmgren, 2005), to elevation gradient-based distribution (Bravo *et al.*, 2021; Fyffe *et al.*, 2014), to complex models incorporating logarithmic wind profiles that depend on surface roughness, atmospheric stability and overall regional wind direction (Ayala *et al.*, 2017). Similarly, there are various methods for distributing air temperatures. Extrapolating temperatures using average lapse rates is a common technique (e.g. Fyffe *et al.*, 2014; Hock and Holmgren, 2005; Schaefer *et al.*, 2015), although some studies incorporate variable lapse rates (Ayala *et al.*, 2017; Bravo *et al.*, 2019). Another approach is to model air temperature distribution from the morphometry of a glacier and the surrounding topography along with the ambient air temperature of the region (Shea and Moore, 2010; Shaw *et al.*, 2017). Distributed values of the dew point temperature are often used as a proxy for surface temperature; dew point temperature is calculated using air temperature and relative humidity (Murray, 1967; Raleigh *et al.*, 2013). Generally, when air temperature is positive it is assumed that the surface temperature is 0°C (Oerlemans and Klok, 2002). Distribution of these variables then allows other relevant meteorological variables to be distributed, such as air vapour pressure, air saturation vapour pressure and relative humidity (Bravo *et al.*, 2021; Bolton, 1980; Shea and Moore, 2010), rather than assuming fixed values (e.g. Braun and Hock, 2004; Fyffe *et al.*, 2014; Hock and Holmgren, 2005).

It is worth noting that these parameterisations oversimplify the processes involved and the distribution of meteorological variables is much more complex in reality. Air temperature, wind speed and humidity are all sensitive to the condition of the surface-atmosphere boundary layer, which alters the profiles of each depending on the presence of katabatic or disturbed conditions (Mott *et al.*, 2020), and to the presence of supraglacial debris which changes the radiative and thermal properties of the glacier surface (Nicholson and Stiperski, 2020).

Finally, calculations of the turbulent fluxes often require the effect of surface roughness to

be accounted for. The effects of surface roughness are represented by the aerodynamic roughness length parameter, z_0, which is often assumed to be spatially and temporally constant (Lewis *et al.*, 1998; Oerlemans and Klok, 2002; Gusain *et al.*, 2009; Giesen *et al.*, 2014; Bravo *et al.*, 2017), and thus overlooked or underestimated. While distribution of most of the inputs to the SEB have received much attention, as summarised here, incorporating distributed estimates of z_0 remains a key uncertainty in the quantification of distributed SEB models. Recent advances in topographic surveying techniques (see Chapter 3) now offer the opportunity to incorporate distributed estimates of z_0 but progress thus far has been limited. An overview of methods for calculation of the turbulent fluxes and parameterising z_0 follows in the next sections.

2.5 Turbulent fluxes

Eddy covariance (EC) techniques offer the closest equivalent to direct observation of the turbulent fluxes, combining observations and modelling of the movements of turbulent eddies (Burba, 2013). A sonic anemometer can be used to measure the three-dimensional (3D) movement of gas particles at a particular location, and thus calculate the overall vertical flux of eddies for a given time period. Q_S can be estimated by observing the thermal properties of the gas particles, and Q_L by observing their water content. While the number of studies employing sonic anemometers and EC is increasing (e.g. Fitzpatrick *et al.*, 2017; Mott *et al.*, 2020; Nicholson and Stiperski, 2020; Radić *et al.*, 2017), issues of site accessibility, challenging terrain and weather conditions mean that they are still relatively sparse (Munro, 1989; Denby and Smeets, 2000; Sicart *et al.*, 2014; Litt *et al.*, 2017). The fragility of sensors, their typical cost of > £10,000 per sensor, significant power demands and unsuitability for harsh conditions found in Arctic and Alpine climates, necessitate almost constant supervision and mean that they are impractical for long observational periods (Fig. 2.5).

Fig. 2.5 Damaged sonic anemometer station on Hintereisferner, Austria. Differential ablation beneath the feet of the tripod caused it to fall, causing potentially expensive damage to the instruments and loss of hard-won data. Note the wind tower in the background is still vertical.

Lack of direct observation has led to turbulent fluxes being calculated through parameterisation and modelling, based on the idea that the fluxes are proportional to the difference in temperature and moisture between the surface and atmosphere (Moore, 1983; Hay and Fitzharris, 1988; Garratt, 1992; Cuffey and Paterson, 2010). Three factors control the fluxes in the turbulent exchange of air: 1) wind speed, 2) surface roughness and 3) atmospheric stability (the structure of the pressure gradient above the surface, and whether this allows for vertical turbulent mixing). Atmospheric measurements (subscript a; surface measurements have subscript s) of wind speed (u, m s^{-1}), air temperature (T, °C) and vapour pressure (q, hPa) are assumed to be representative of a well-mixed boundary layer, informing the name the 'bulk aerodynamic approach' (Garratt, 1992). The bulk exchange formulae take the form:

$$Q_S = \rho_a c_a C_H u(T_a - T_s) \tag{2.1}$$

$$Q_L = \rho_a L_{v/s} C_E u(q_a - q_s) \tag{2.2}$$

where ρ_a is the density of air (kg m^{-3}), c_a its specific heat capacity (J kg^{-1} K^{-1}), $L_{v/s}$ the latent heat of vaporisation or sublimation. In finding the bulk exchange parameters C_H and C_E using flux-gradient theory, an important step is finding the friction velocity (u_*) using

$$u(z) = \frac{1}{k_0} u_* \ln\left(\frac{z}{z_0}\right) \tag{2.3}$$

as u is related to the logarithm of measurement height (z, m). k_0 is the dimensionless von Karman's constant, 0.4, and z_0 is the surface roughness parameter, defined as the height (m) above the surface at which horizontal wind speed is zero. Integrating into (2.1), the bulk equation for the sensible heat flux becomes

$$Q_S = \rho_a c_a k_0 u_* \frac{T_a - T_s}{\ln(z/z_0)}. \tag{2.4}$$

The bulk method assumes that the atmospheric boundary layer is statically neutral; that is, the wind speed profile above the surface is logarithmic (Stull, 1988). As in Fig. 2.6, this appears as a straight line on a semi-log plot. In non-neutral conditions, the profile deviates from logarithmic. Statically neutral surface layers are commonly found, in theory and experimentally, over flat homogeneous terrain and allow a constant flux layer and stationarity (Stull, 1988; Garratt, 1992). Over the sloping, inhomogeneous surface of a glacier, however, the surface layer can be stable as warmer air overrides cooler air, or even strongly stable as density driven, down-glacier (katabatic) winds develop, creating a wind speed maximum within the first few metres above the surface. This means that the wind speed profile would not be logarithmic, the constant flux layer is suppressed and advection is non-negligible (Denby and Greuell, 2000; Denby and Smeets, 2000).

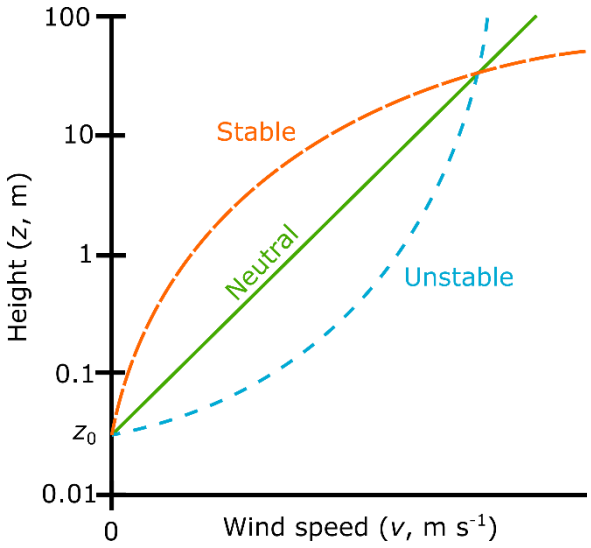

Fig. 2.6 Examples of stable vs. unstable boundary layer wind profiles.

In neutral conditions, $\frac{z}{L}$ is equal to zero, where *L* is the Obukhov length (the height at which buoyant production of turbulent kinetic energy equals shear production [Foken, 2008]).

Stable conditions, when $\frac{z}{L} > 0$, are common over glaciers during katabatic conditions so two types of correction are often used to account for this and extend the validity of the bulk approach: 1) a correction that uses the bulk Richardson number as a proxy for stability (e.g. Sicart *et al.*, 2005; Mölg *et al.*, 2008; Anderson *et al.*, 2010), and 2) one that uses the Monin-Obukhov stability parameter $\frac{z}{L}$ (e.g. Braithwaite, 1995; Klok *et al.*, 2005; Van den Broeke *et al.*, 2005). The use of a stability correction has been criticised because it ignores the unsuitability of the bulk method for sloping glacier surfaces; yet, the lack of an alternative means it is still widely used (Denby and Greuell, 2000).

2.6 Calculating z_0 from meteorological data

It is possible to derive z_0 from two or more levels of wind speed measurements over a glacier by incorporating a correction factor into (2.3), which then becomes:

$$u(z) = \frac{u_*}{\kappa_0}\left(\ln\frac{z}{z_0} + \alpha_m\frac{z}{L}\right), \tag{2.5}$$

if α_m is a stability function (α_m = 5). Since (2.3) or (2.5) is used to find u_*, z_0 is often parameterised using other methods. It is common practice to assign values to z_0 based on those obtained from similar surfaces, i.e. 0.001 m for snow and 0.01 m for ice (e.g. Bravo *et al.*, 2017). This has been shown to be unrepresentative of reality, as z_0 can span several orders of magnitude across a glacier surface and through time (Brock *et al.*, 2006; Smith *et al.*, 2020).

The same shortcomings apply when z_0 is used as a model tuning parameter to force model outcomes to agree with observed turbulent fluxes and melt volumes (Anderson *et al.*, 2010; Fausto *et al.*, 2016b). Adopting a z_0 value from another study, or using it as a tuning parameter, are approaches often resorted to because of the added complexity that measuring or estimating z_0 introduces to a study. While the bulk method requires measurement of meteorological variables from just one level above the surface, the commonly used profile method for estimating z_0 requires at least three measurement levels (Denby and Smeets, 2000). A value for z_0 can be extrapolated from profiles of wind speed and temperature above the surface (Fig. 2.7), which are assumed to be log-linear in near-neutral conditions (Garratt, 1992).

The drawbacks of the profile method (further detailed in Chapter 4 [Section 4.2.1]), broadly fall into two categories:

1. Those due to instrument height: instrument height is important because all

parameters are dependent upon it (Cuffey and Paterson, 2010), and because it can be difficult to measure on an ablating surface (Smeets *et al.*, 1999). Additionally, the height of the instruments determines the size of the aerodynamically-important upwind area (fetch), which, for Monin-Obukhov similarity theory, should be homogeneous for 100-200 m upwind of any instruments (Bradley, 1968; Wieringa, 1993; Fitzpatrick *et al.*, 2019).

2. Those due to the incompatibility of glacier surfaces with the assumptions of Monin-Obukhov similarity theory. These include: a neutral atmosphere, constant flux layer and negligible advection (Fitzpatrick *et al.*, 2017). Aggressive data filters are required to isolate profiles which do conform to the theory but up to 90% of collected data can be discarded, making the profile method extremely low-yield (e.g. Miles *et al.*, 2017).

2.7 Calculating z_0 from microtopographic data

As an alternative to the technical and theoretical difficulties inherent to deriving z_0 from aerodynamic methods, the geometric properties of a surface can be used to assess aerodynamic roughness (Elliott, 1958; Bandyopadhyay, 1987; Smith, 2014). Estimating z_0 from glacier surface geometry has provided deeper insights into the influence that surface roughness may have on the turbulent fluxes by showing spatial and temporal variability across the surface of a glacier throughout the year (e.g. Brock *et al.*, 2006). The merits and drawbacks of microtopographic approaches are further described in Chapter 4 (Section 4.2.2), but are outlined here to provide a comprehensive background.

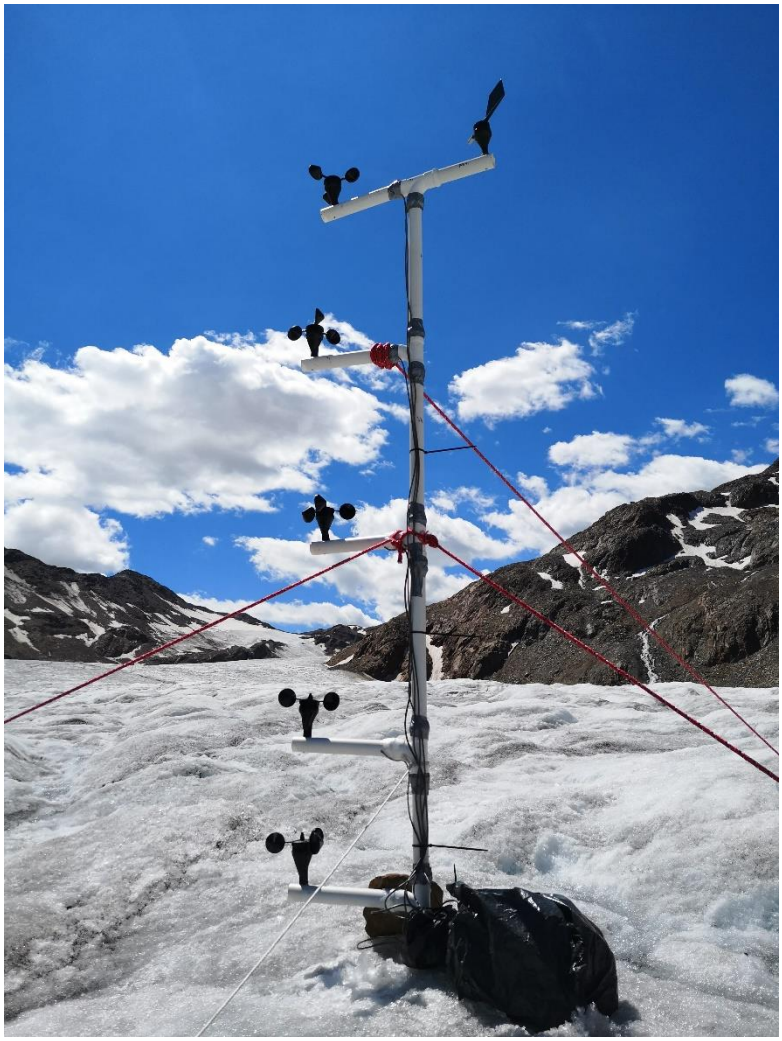

Fig. 2.7 Aerodynamic profile instrument set-up. Wind tower used to collect wind speed (cup anemometers), wind direction (wind vane), air temperature and relative humidity (sensors housed in arms) data over Hintereisferner, Austria. Data were recorded onto a data logger stored in a weather-resistant bin bag and lunch box system at the base of the tower.

Roughness metrics that include some measure of surface element height provide the best estimates of z_0 (Nield *et al.*, 2013), and the most widely used of those builds on the work of Kutzbach (1961) and Lettau (1969). From empirical experiments involving arrangements of bushel baskets on an ice lake, Lettau (1969) showed that

$$z_0 = 0.5h^* \frac{s}{S_A}, \tag{2.6}$$

where h^* is the effective (average) obstacle height (m), s is the silhouette (exposed frontal area, m^2) of an average roughness element, S_A is the area in the horizontal plane of the site of interest (m^2), and 0.5 represents an average drag coefficient (dimensionless). This empirical approach represents a significant reduction in data required from the field, and Lettau (1969) found results matched those of Kutzbach's (1961) experiment to within ± 25%.

While the use of 0.5 as an average drag coefficient has become the norm (used by practically all glaciological studies that estimate z_0 from microtopography), it has been recognised in several studies that, depending on the surface, 0.5 could be an overestimate or an underestimate (Banke and Smith, 1973; Wieringa, 1993; Quincey *et al.*, 2017) yet no improvement has been made.

Subsequently, Munro (1989) applied (2.6) to a glacier surface and introduced a method for obtaining each parameter from simplified horizontal microtopographic transects (Fig. 2.8a). Roughness elements are modelled using regularly-sized and spaced rectangles arranged perpendicular to the prevailing wind direction. For a transect of length *X*, twice the standard deviation of detrended elevations ($2\sigma_d$) is used as h^*,

$$s = \frac{2\sigma_d X}{2f} \tag{2.7}$$

when *f* is the number of times the transect crosses from negative to positive, and

$$S_A = \left(\frac{X}{f}\right)^2. \tag{2.8}$$

Therefore,

$$z_0 = \frac{f}{X}(\sigma_d)^2. \tag{2.9}$$

While data collection using the Munro transect method is relatively rapid, several key assumptions are imposed (Smith *et al.*, 2016): (i) that all roughness elements are uniform in spacing and size, (ii) there is no difference in the silhouette of elements when seen from different directions (Fig. 2.8b), and (iii) that downwind roughness elements are not sheltered by upwind elements.

Adapting (2.6) to work with 3D data relaxes assumptions (i) – (iii) (Smith *et al.*, 2016). S_A becomes the horizontal area of a plot, and *s* becomes the sum of the heights of cells above preceding "upwind" cells (where the cell behind is taller, or 'visible'), multiplied by cell width. This allows z_0 to be calculated for each of the four cardinal wind directions, or just the prevailing wind direction. It also opens up the possibility of estimating distributed geometric z_0 at a range of scales, from plot scale to glacier scale, and even regional scales (e.g. Fitzpatrick *et al.*, 2019).

One key issue with microtopographically derived z_0, common to both 2D and 3D methods, is that z_0 is a function of sampling resolution and scale, i.e. transect length or plot area (Rees and Arnold, 2006). Sampling a surface at greater intervals (coarser resolution) over a set area loses surface detail and makes the surface artificially smooth, and has been compared to

running a smoothing filter over the data (Quincey *et al.*, 2017). Conversely, sampling at smaller intervals (finer resolution) increases the surface detail included in calculations, inflating h^* or s, and giving a greater z_0 value. Calculating z_0 from a longer transect or larger plot increases S_A, which also inflates z_0. Various studies have referred to Rees and Arnold (2006) for guidelines on the appropriate sampling resolution and scale for adequate representation of z_0 (Smith *et al.*, 2016; 2020; Miles *et al.*, 2017; Quincey *et al.*, 2017). Rees and Arnold (2006) proposed that a sampling interval of ~10 cm and a transect length of a few metres is sufficient to capture z_0 based on their multiscale analysis, while acknowledging that additional data was required to bridge to gap between two observed scale domains, and that their z_0 values were not validated against *in situ* aerodynamic data. Such a multiscale analysis has not been performed on 3D data, and as such, using these guidelines to acquire glacier-wide distributed z_0 values is beyond their original scope. The scale/resolution dependence aspect of microtopographic z_0 is considered further in Chapter 4 (Sections 4.2.2 and 4.4.2) and Chapter 5 (Section 5.3.1).

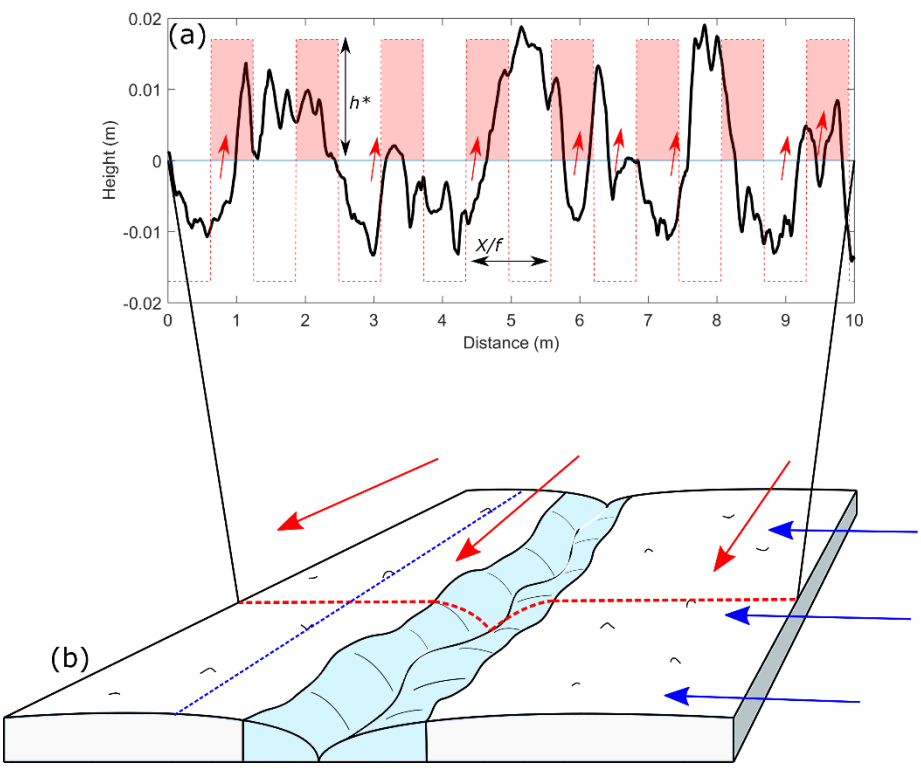

Fig. 2.8 Schematic representation of Munro's (1989) 2D transect method for calculating z_0 (a). The solid black line is a 10 m (X) detrended transect from Storglaciären. The dashed red line shows the modelled roughness corresponding to the number of negative-positive upcrossings (f), where h^* is twice the standard deviation of elevations. In (b), the issue with using 2D transects is illustrated. The transect shown by the red dashed line would give a higher z_0 value than the blue dashed line because of the channel/crevasse feature. However, if the wind was following the red arrows, the channel would be streamlined to the airflow and provide less of an obstacle than it would were the wind following the blue arrows.

A second key issue concerns the detrending of topographic data as part of z_0 calculations. It is clear from examination of each of the assumptions attached to equation (2.6) that the size of obstacles is a key control on z_0. The scale of topographic variation which constitutes an obstacle to air flow is determined somewhat qualitatively, by deciding on the upper and lower topographic partition scale for the surface in question (Smith, 2014). Variability below the lower measurement scale is considered indistinguishable from instrument noise, and above the partition scale is classed as topography. The definition of partition scales is dependent on the surface being studied; over bare ice (e.g. Brock *et al.*, 2006; Rippin *et al.*, 2015) the range of scales is often smaller than over debris-covered ice (e.g. Rounce *et al.*, 2015; Miles *et al.*, 2017; Quincey *et al.*, 2017). The issue is more complex over debris-covered ice; even though z_0 is predominantly controlled by roughness on the scale of cobbles/boulders, Quincey *et al.* (2017) found that a covering of snow significantly reduced z_0, demonstrating the breadth of scales that require consideration. Different scales of topography can be separated for analysis by detrending (Smith, 2014). With smaller plots or transects (<10 m), planar or linear detrending is sufficient, whereby the best-fit plane or line is subtracted and the mean elevation set to zero (Lettau, 1969; Munro, 1989; Smith *et al.*, 2016). This level of detrending is ineffective for removing larger scale topographic trends, making sloping glacier surfaces more problematic (Miles *et al.*, 2017). Perhaps the most straightforward solution is to remove the overall coarse elevation trends prior to planar or linear detrending using a moving mean, median filter or fitting a spline (Miles *et al.*, 2017; Quincey *et al.*, 2017); however, these steps require a qualitative interpretation of the appropriate topographic partition scales, which can lead to quite different z_0 values if not considered carefully (Grohmann *et al.*, 2011). The effects of different levels of detrending are considered in Chapter 4 (Section 4.4.2). A more robust, yet complex approach is to apply a 1D or 2D fast fourier transformation, which can isolate low frequency topographic wavelengths for removal (Smith, 2014; Fitzpatrick *et al.*, 2019), but the extra steps can be counterproductive when seeking to minimise the calculation complexities of finding z_0 compared to aerodynamic methods.

2.8 Estimating distributed z_0 for glacier-scale maps

An initial attempt at glacier-scale mapping by Smith *et al.* (2016) used a regression relationship between plot-scale 3D microtopographic z_0 and the standard deviation of elevations from a terrestrial laser scan of Kärsaglaciaren, Sweden (Fig. 2.9a). This was also the first known study to derive z_0 directly from 3D data. Plots of 2 m x 2 m were detrended

by removing the best-fit plane, before assigning values to the terms in equation (2.7) to estimate z_0 for each plot. A total of 27 plots were used to develop the regression model, which provides a simplification of the information used and gained from 3D estimation of z_0. The model approach requires either validation data from the glacier surface, or the assumption that the model developed within the study is applicable to other glaciers. Additionally, it assumes that the scale and resolution at which plot-scale z_0 was calculated is appropriate for providing the most robust estimate.

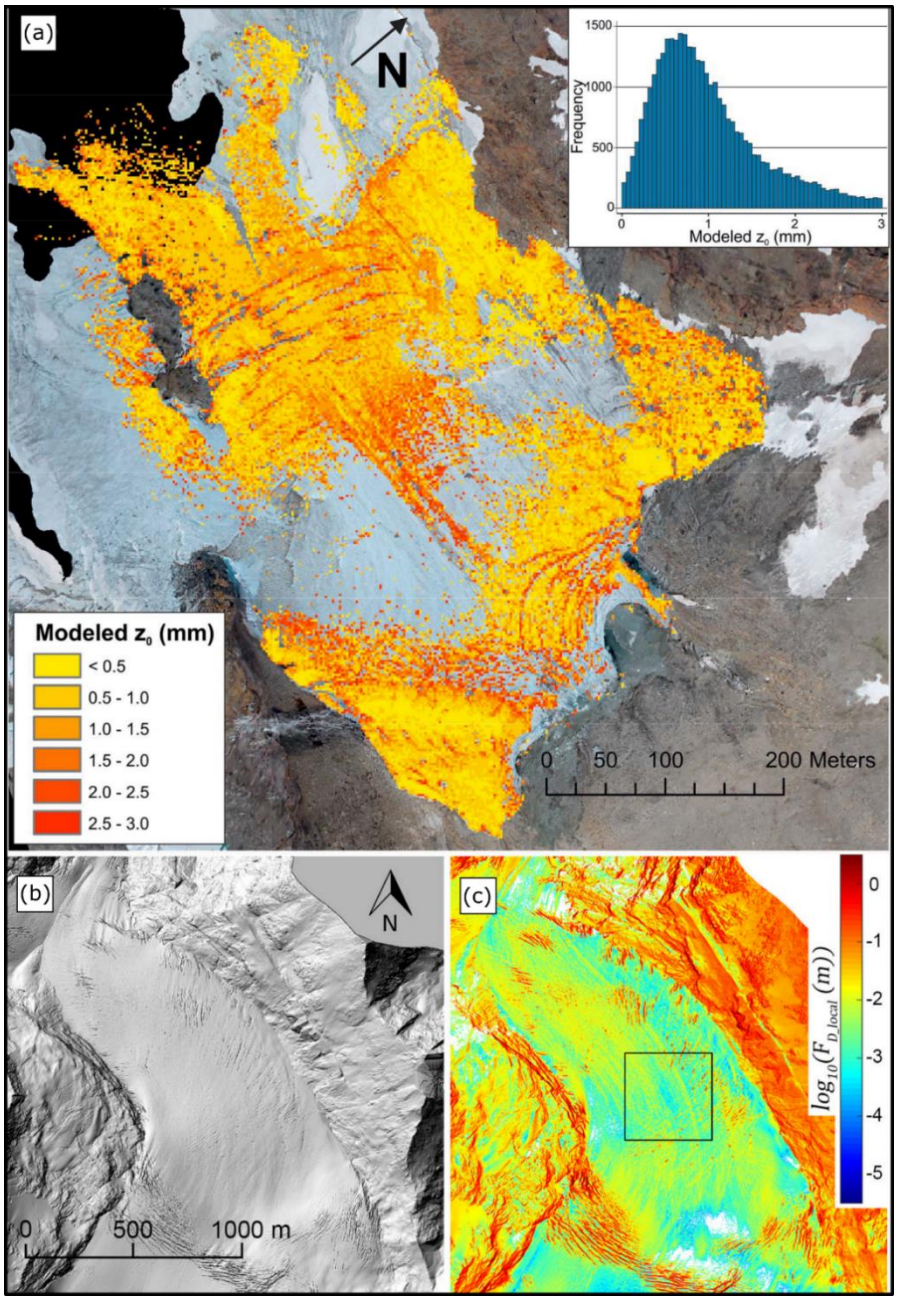

Fig. 2.9 Previous glacier scale maps of z_0. (a) shows a z_0 map created using a regression relationship between plot-scale z_0 and TLS surface roughness, with data gaps where the wet glacier surface provided poor TLS reflections. (b) shows a hillshaded DEM which was used to calculate a "drag parameter" (FD_{local}) shown in (c). From (b), an area of interested was selected (the inset box in (c)) with the sum of all cells (given equal weighting) used as z_0. (a) reproduced from Smith *et al.* (2016), (b) and (c) reproduced from Fitzpatrick *et al.* (2019).

A subsequent glacier-scale z_0 map was created by Fitzpatrick *et al.* (2019). In this case, z_0 was estimated for each grid cell of elevation data based on the geometry of the cells in the immediate proximity (Fig. 2.9b & 2.9c). Using a moving window (or sliding neighbourhood) algorithm, an estimate of z_0 was calculated for the central cell of 9 m x 9 m windows (at 1 m resolution). Fitzpatrick *et al.* (2019) estimated z_0 building on the 3D method of Smith *et al.* (2016); they maintained the planar detrending step but eliminated the regression model by deriving z_0 directly from elevation data, and validated their geometric estimates with z_0 derived from eddy covariance data. While these changes made more robust z_0 estimates, they still require input topographic data of 1 m resolution which is relatively uncommon at regional scales and do not account for temporal changes through the ablation season. The effects of different resolutions and input data from a full range of surfaces were not investigated, which undermines the applicability of Fitzpatrick *et al.*'s (2019) method to other locations.

Other attempts at distributing z_0 have been made, using two main approaches. First, Irvine-Fynn *et al.* (2014) aggregated z_0 estimates from transects of all rows and columns of a grid to give an overall estimate for a plot. This approach was also tested by Miles *et al.* (2017), who additionally employed best-fit relations devised by Nield *et al.* (2013) and applied them to fine-resolution grids that had been subdivided into smaller grids (a distinct-block approach, as opposed to a sliding neighbourhood). Scale and resolution dependence are common to these alternative approaches, as is the inability for them to be deployed rapidly over glacier or regional scales.

Each of the outlined approaches is underpinned by the availability of topographic data. Laser scanning (terrestrial or airborne) and Structure-from-Motion with Multi-View Stereo (abbreviated herein to SfM) are topographic survey techniques that have seen rapid expansion over the recent decades. These methods were also employed in data collection for this thesis, and are explored in the next section.

2.9 Summary

The aerodynamic roughness length (z_0) is a key uncertainty in calculations of turbulent energy fluxes. The turbulent fluxes are calculated as part of a glacier surface energy balance (SEB), which can be used to model the inputs and outputs of energy to a glacier surface, provide estimates of melt and runoff. The SEB comprises the net radiative energy fluxes, which are usually the dominant source of melt energy, the turbulent fluxes, which can be a

major source of melt energy over short timescales, the sensible feat flux due to rain and the ground energy flux, both of which are considered negligible. The SEB is usually calculated at the point-scale, but inputs can be distributed onto a grid and used to investigate spatial variability in each of the fluxes. The turbulent fluxes are often parameterised from meteorological data using the bulk aerodynamic approach, which requires z_0 to be known; however, values from the direct observation of turbulent eddies (eddy covariance) and values derived from wind speed profiles are rare, and provide only point-scale values. Distributed values of z_0 can be obtained from topographic data, yet these are most common at the plot-scale and attempts to map z_0 at the glacier scale have been limited. Topographic z_0 estimates are known to be dependent on measurement scale and data resolution, but a full analysis of these effects at different scales has yet to be carried out. Existing methods of producing distributed maps of z_0 require site-specific validation or are not transferrable to other locations.

References

Anderson, B., Mackintosh, A., Stumm, D., George, L., Kerr, T., Winter-Billington, A. & Fitzimons, S. (2010) 'Climate sensitivity of a high-precipitation glacier in New-Zealand', *Journal of Glaciology*, 56(195), pp. 114-128(15). doi: 10.3189/002214310791190929.

Andreas, E. L. (1987) 'A theory for the scalar roughness and the scalar transfer coefficients over snow and sea ice.', *Boundary-Layer Meteorology*, 38, pp. 159–184. doi: https://doi.org/10.1007/BF00121562.

Arnold, N. S., Rees, W. G., Hodson, A. J. & Kohler, J. (2006) 'Topographic controls on the surface energy balance of a high Arctic valley glacier', *Journal of Geophysical Research: Earth Surface*, 111(2). doi: 10.1029/2005JF000426.

Ayala, A., Pellicciotti, F., Peleg, N. & Burlando, P. (2017) 'Melt and surface sublimation across a glacier in a dry environment: Distributed energy-balance modelling of Juncal Norte Glacier, Chile', *Journal of Glaciology*, 63(241), pp. 803–822. doi: 10.1017/jog.2017.46.

Bandyopadhyay, P. R. (1987) 'Rough-wall turbulent boundary layers in the transition regime', *Journal of Fluid Mechanics*, 180(1), p. 231. doi: 10.1017/S0022112087001794.

Banke, E. G. & Smith, S. D. (1973) 'Wind stress on Arctic sea ice', *Journal of Geophysical Research*, 78(33), pp. 7871–7883. doi: 10.1029/jc078i033p07871.

Barr, I. D. & Spagnolo, M. (2015) 'Glacial cirques as palaeoenvironmental indicators: Their potential and limitations', *Earth-Science Reviews*, 151, pp. 48–78. doi: 10.1016/j.earscirev.2015.10.004.

Bolton, D. (1980) 'The Computation of Equivalent Potential Temperature', *Monthly Weather Review*, 108(7), pp. 1046–1053. doi: https://doi.org/10.1175/1520-0493(1980)108<1046:TCOEPT>2.0.CO;2.

Box, J. E., Fettweis, X., Stroeve, J. C., Tedesco, M., Hall, D. K. & Steffen, K. (2012) 'Greenland ice sheet albedo feedback: Thermodynamics and atmospheric drivers', *Cryosphere*. doi: 10.5194/tc-6-821-2012.

Bradley, E. F. (1968) 'A micrometeorological study of velocity profiles and surface drag in the region modified by a change in surface roughness', *Quarterly Journal of the Royal Meteorological Society*, 94(401), pp. 361–379. doi: 10.1002/qj.49709440111.

Braithwaite, R. J. (1995) 'Aerodynamic stability and turbulent sensible-heat flux over a melting ice surface, the Greenland ice sheet', *Journal of Glaciology*, 41(139), pp. 562–571. doi: 10.1017/S0022143000034882.

Braun, M. & Hock, R. (2004) 'Spatially distributed surface energy balance and ablation modelling on the ice cap of King George Island (Antarctica)', *Global and Planetary Change*, 42(1–4), pp. 45–58. doi: 10.1016/j.gloplacha.2003.11.010.

Bravo, C., Loriaux, T., Rivera, A. & Brock, B. W. (2017) 'Assessing glacier melt contribution to streamflow at Universidad Glacier, central Andes of Chile', *Hydrology and Earth System Sciences*, 21(7), pp. 3249–3266. doi: 10.5194/hess-21-3249-2017.

Bravo, C., Quincey, D. J., Ross, A. N., Rivera, A., Brock, B., Miles, E. & Silva, A. (2019) 'Air Temperature Characteristics, Distribution, and Impact on Modeled Ablation for the South Patagonia Icefield', *Journal of Geophysical Research: Atmospheres*, 124(2), pp. 907–925. doi: 10.1029/2018JD028857.

Bravo, C., Ross, A. N., Quincey, D. J., Cisternas, S. & Rivera, A. (2021) 'Surface ablation and its drivers along a west–east transect of the Southern Patagonia Icefield', *Journal of Glaciology*, pp. 1–14. doi: 10.1017/jog.2021.92.

Brock, B. W., Willis, I. C. & Sharp, M. J. (2006) 'Measurement and parameterization of aerodynamic roughness length variations at Haut Glacier d'Arolla, Switzerland', *Journal of Glaciology*, 52(177), pp. 281–297. doi: 10.3189/172756506781828746.

Van den Broeke, M. R., Reijmer, C., Van As, D., Van de Wal, R. & Oerlemans, J. (2005) 'Seasonal cycles of Antarctic surface energy balance from automatic weather stations', *Annals of Glaciology*, 41(Aws 4), pp. 131–139. doi: 10.3189/172756405781813168.

Burba, G. (2013) *Eddy Covariance Method-for Scientific, Industrial, Agricultural, and Regulatory Applications*. Lincoln, Nebraska: LI-COR Biosciences. doi: 10.1007/s00704-004-0095-y.

Cuffey, K. M. & Paterson, W. S. B. (2010) *The Physics of Glaciers*. Fourth. Oxford: Elsevier. doi: 10.1063/1.2915138.

Dadic, R., Mott, R., Lehning, M., Carenzo, M., Anderson, B. & Mackintosh, A. (2013) 'Sensitivity of turbulent fluxes to wind speed over snow surfaces in different climatic settings', *Advances in Water Resources*, 55, pp. 178–189. doi: 10.1016/j.advwatres.2012.06.010.

Davaze, L., Rabatel, A., Arnaud, Y., Sirguey, P., Six, D., Letreguilly, A. & Dumont, M. (2018) 'Monitoring glacier albedo as a proxy to derive summer and annual surface mass balances from optical remote-sensing data', *Cryosphere*, 12(1), pp. 271–286. doi: 10.5194/tc-12-271-2018.

Denby, B. & Greuell, W. (2000) 'The Use of Bulk and Profile Methods for Determining Surface Heat Fluxes in the Presence of Glacier Winds', *Journal of Glaciology*, 46(154), pp. 445–452.

Denby, B. & Smeets, C. J. P. P. (2000) 'Derivation of Turbulent Flux Profiles and Roughness Lengths from Katabatic Flow Dynamics', *Journal of Applied Meteorology*, 39(9), pp. 1601–1612. doi: 10.1175/1520-0450(2000)039<1601:DOTFPA>2.0.CO;2.

Dumont, M., Gardelle, J., Sirguey, P., Guillot, A., Six, D., Rabatel, A. & Arnaud, Y. (2012) 'Linking glacier annual mass balance and glacier albedo retrieved from MODIS data', *The Cryosphere*, 6, pp. 1527–1539. doi: 10.5194/tc-6-1527-2012ï.

Elliott, W. P. (1958) 'The growth of the atmospheric internal boundary layer', *Eos, Transactions of the American Geophysical Union*, 39(6), pp. 1048–1054. doi: 10.1029/TR039i006p01048.

Evans, I. S. (1977) 'World-Wide Variations in the Direction and Concentration of Cirque and Glacier Aspects', *Source: Geografiska Annaler. Series A, Physical Geography*, 59(4), pp. 151–175. doi: https://doi.org/10.1080/04353676.1977.11879949.

Fausto, R. S., Van As, D., Box, J. E., Colgan, W. & Langen, P. L. (2016a) 'Quantifying the surface energy fluxes in South Greenland during the 2012 high melt episodes using in-situ observations', *Frontiers in Earth Science*, 4. doi: 10.3389/feart.2016.00082.

Fausto, R. S., Van As, D., Box, J. E., Colgan, W., Langen, P. L. & Mottram, R. H. (2016b) 'The implication of nonradiative energy fluxes dominating Greenland ice sheet exceptional ablation area surface melt in 2012', *Geophysical Research Letters*, 43(6), pp. 2649–2658. doi: 10.1002/2016GL067720.

Favier, V., Wagnon, P., Chazarin, J. P., Maisincho, L. & Coudrain, A. (2004) 'One-year measurements of surface heat budget on the ablation zone of Antizana Glacier 15, Ecuadorian Andes', *Journal of Geophysical Research Atmospheres*, 109(18), pp. 1–15. doi: 10.1029/2003JD004359.

Fitzpatrick, N., Radić, V. & Menounos, B. (2017) 'Surface Energy Balance Closure and Turbulent Flux Parameterization on a Mid-Latitude Mountain Glacier, Purcell Mountains, Canada', *Frontiers in Earth Science*, 5(September), pp. 1–20. doi: 10.3389/feart.2017.00067.

Fitzpatrick, N., Radić, V. & Menounos, B. (2019) 'A multi-season investigation of glacier surface roughness lengths through in situ and remote observation', *The Cryosphere*, 13, pp. 1051–1071. doi: https://doi.org/10.5194/tc-13-1051-2019.

Foken, T. (2008) *Micrometeorology*. Berlin: Springer.

Fu, P. & Rich, P. M. (2002) *A geometric solar radiation model with applications in agriculture and forestry*, *Computers and Electronics in Agriculture*. Available at: www.elsevier.com/locate/compag.

Fyffe, C. L., Reid, T. D., Brock, B. W., Kirkbride, M. P., Diolaiuti, G., Smiraglia, C. & Diotri, F. (2014) 'A distributed energy-balance melt model of an alpine debris-covered glacier', *Journal of Glaciology*, 60(221), pp. 587–602. doi: 10.3189/2014JoG13J148.

Gabbi, J., Huss, M., Bauder, A., Cao, F. & Schwikowski, M. (2015) 'The impact of Saharan dust and black carbon on albedo and long-term mass balance of an Alpine glacier', *Cryosphere*, 9(4), pp. 1385–1400. doi: 10.5194/tc-9-1385-2015.

Garratt, J. R. (1992) *The Atmospheric Boundary Layer*. Cambridge: Cambridge University Press.

Giesen, R. H., Andreassen, L. M., Oerlemans, J. & Van Den Broeke, M. R. (2014) 'Surface energy balance in the ablation zone of Langfjordjøkelen, an arctic, maritime glacier in northern Norway', *Journal of Glaciology*, 60(219), pp. 57–70. doi: 10.3189/2014JoG13J063.

Gillett, S. & Cullen, N. J. (2011) 'Atmospheric controls on summer ablation over Brewster Glacier, New Zealand', *International Journal of Climatology*, 31(13), pp. 2033–2048. doi: 10.1002/joc.2216.

Greuell, W. & Genthon, C. (2004) 'Modelling land-ice surface mass balance', in *Mass Balance of the Cryosphere*, pp. 117–168. doi: 10.1017/CBO9780511535659.007.

Grohmann, C. H., Smith, M. J. & Riccomini, C. (2011) 'Multiscale analysis of topographic surface roughness in the Midland Valley, Scotland', *IEEE Transactions on Geoscience and Remote Sensing*. doi: 10.1109/TGRS.2010.2053546.

Gusain, H. S., Singh, K. K., Mishra, V. D., Srivastava, P. K. & Ganju, A. (2009) 'Study of surface energy and mass balance at the edge of the antarctic ice sheet during summer in dronning maud land, east antarctica', *Antarctic Science*, 21(4), pp. 401–409. doi: 10.1017/S0954102009001989.

Hay, J. E. & Fitzharris, B. B. (1988) 'A Comparison of the Energy-Balance and Bulk-aerodynamic Approaches for Estimating Glacier Melt', *Journal of Glaciology*, 34(117), pp. 145–153. doi: https://doi.org/10.3189/S0022143000032172.

Hock, R. (2005) 'Glacier melt: a review of processes and their modelling', *Progress in Physical Geography*, 29(3), pp. 362–391. doi: 10.1191/0309133305pp453ra.

Hock, R. & Holmgren, B. (1996) 'Some Aspects of Energy Balance and Ablation of Storglaciären , Northern Sweden', *Geografiska Annaler Series A-Physical Geography*, 78(2), pp. 121–131.

Hock, R. & Holmgren, B. (2005) 'A distributed surface energy-balance model for complex topography and its application to Storglaciären, Sweden', *Journal of Glaciology*, 51(172), pp. 25–36. doi: https://doi.org/10.3189/172756505781829566.

Hock, R., Rasul, G., Adler, C., Cáceres, B., Gruber, S., Hirabayashi, Y., Jackson, M., Kääb, A., Kang, S. & Kutuzov, S. (2019) 'High Mountain Areas', in *IPCC Special Report on the Ocean and Cryosphere in a Changing Climate*. Geneva, Switzerland, pp. 131–202.

Howat, I. M., Porter, C., Smith, B. E., Noh, M. J. & Morin, P. (2019) 'The reference elevation model of antarctica', *Cryosphere*, 13(2), pp. 665–674. doi: 10.5194/tc-13-665-2019.

Irvine-Fynn, T. D. L., Sanz-Ablanedo, E., Rutter, N., Smith, M. W. & Chandler, J. H. (2014) 'Measuring glacier surface roughness using plot-scale, close-range digital photogrammetry', *Journal of Glaciology*, 60(223), pp. 957–969. doi: 10.3189/2014JoG14J032.

Juszak, I. & Pellicciotti, F. (2013) 'A comparison of parameterizations of incoming longwave radiation over melting glaciers: Model robustness and seasonal variability', *Journal of Geophysical Research Atmospheres*, 118(8), pp. 3066–3084. doi: 10.1002/jgrd.50277.

Klok, E. J., Nolan, M. & Van Den Broeke, M. R. (2005) 'Analysis of meteorological data and the surface energy balance of McCall Glacier, Alaska, USA', *Journal of Glaciology*, 51(174), pp. 451–461. doi: 10.3189/172756505781829241.

Kondratyev, K. Y. (1965) *Radiative Heat Exchange in the Atmosphere*, *Radiative Heat Exchange in the Atmosphere*. London: Pergamon Press. doi: 10.1016/b978-0-08-010107-1.50012-0.

Kutzbach, J. (1961) 'Investigations of the modification of wind profiles by artificially controlled surface roughness', in Lettau, H. (ed.) *Studies of the Three-Dimensional Structure of the Planetary Boundary Layer*. University of Wisconsin--Madison, pp. 71–115.

Lettau, H. (1969) 'Note on Aerodynamic Roughness-Parameter Estimation on the Basis of Roughness-Element Description', *Journal of Applied Meteorology*, 8(5), pp. 828–832. doi: http://dx.doi.org/10.1175/1520-0450(1969)008<0828:NOARPE>2.0.CO;2.

Lewis, K. J., Fountain, A. G. & Dana, G. L. (1998) 'Surface energy balance and meltwater production for a Dry Valley glacier, Taylor Valley, Antarctica', *Annals of Glaciology*, 27, pp. 603–609. doi: 10.3189/1998AoG27-1-603-609.

Liang, S. (2000) 'Narrowband to broadband conversions of land surface albedo I Algorithms', *Remote Sensing of Environment*, 76(2), pp. 213–238. doi: https://doi.org/10.1016/S0034-4257(00)00205-4.

Litt, M., Sicart, J. E., Six, D., Wagnon, P. & Helgason, W. D. (2017) 'Surface-layer turbulence, energy balance and links to atmospheric circulations over a mountain glacier in the French Alps', *Cryosphere*, 11(2), pp. 971–987. doi: 10.5194/tc-11-971-2017.

Miles, E. S., Steiner, J. F. & Brun, F. (2017) 'Highly variable aerodynamic roughness length (z0) for a hummocky debris-covered glacier', *Journal of Geophysical Research: Atmospheres*, 122(16), pp. 8447–8466. doi: 10.1002/2017JD026510.

Ming, J., Xiao, C., Cachier, H., Qin, D., Qin, X., Li, Z. & Pu, J. (2009) 'Black Carbon (BC) in the snow of glaciers in west China and its potential effects on albedos', *Atmospheric Research*,

92(1), pp. 114–123. doi: 10.1016/j.atmosres.2008.09.007.

Mölg, T., Cullen, N. J., Hardy, D. R., Kaser, G. & Klok, L. (2008) 'Mass balance of a slope glacier on Kilimanjaro and its sensitivity to climate', *International Journal of Climatology*, 28, pp. 881–892. doi: 10.1002/joc.

Mölg, T., Cullen, N. J. & Kaser, G. (2009) 'Solar radiation, cloudiness and longwave radiation over low-latitude glaciers: implications for mass-balance modelling', *Journal of Glaciology*, 55(190), pp. 292–302. doi: https://doi.org/10.3189/002214309788608822.

Moore, R. D. (1983) 'On the Use of Bulk Aerodynamic Formulae Over Melting Snow', *Nordic Hydrology*, pp. 193–206.

Mott, R., Stiperski, I. & Nicholson, L. (2020) 'Spatio-temporal flow variations driving heat exchange processes at a mountain glacier', *Cryosphere*, 14(12), pp. 4699–4718. doi: 10.5194/tc-14-4699-2020.

Munro, D. S. (1989) 'Surface roughness and bulk heat transfer on a glacier: comparison with eddy correlation', *Journal of Glaciology*, 35(121), pp. 343–348.

Murray, F. W. (1967) 'On the Computation of Saturation Vapor Pressure', *Journal of Applied Meteorology and Climatology*, pp. 203–204. doi: https://doi.org/10.1175/1520-0450(1967)006<0203:OTCOSV>2.0.CO;2.

Naegeli, K., Huss, M. & Hoelzle, M. (2019) 'Change detection of bare-ice albedo in the Swiss Alps', *Cryosphere*, 13(1), pp. 397–412. doi: 10.5194/tc-13-397-2019.

Nicholson, L. & Stiperski, I. (2020) 'Comparison of turbulent structures and energy fluxes over exposed and debris-covered glacier ice', *Journal of Glaciology*, 66(258). doi: https://doi.org/10.1017/jog.2020.23.

Nield, J. M., King, J., Wiggs, G. F. S., Leyland, J., Bryant, R. G., Chiverrell, R. C., Darby, S. E., Eckardt, F. D., Thomas, D. S. G., Vircavs, L. H. & Washington, R. (2013) 'Estimating aerodynamic roughness over complex surface terrain', *Journal of Geophysical Research Atmospheres*, 118(23), pp. 12948–12961. doi: 10.1002/2013JD020632.

Oerlemans, J., Björnsson, H., Kuhn, M., Obleitner, F., Palsson, F., Smeets, C. J. P. P., Vugts, H. F. & De Wolde, J. (1999) 'Glacio-meteorological investigations on Vatnajokull, Iceland, Summer 1996: An overview', *Boundary-Layer Meteorology*, 92(1), pp. 3–26. doi: 10.1023/A:1001856114941.

Oerlemans, J. & Klok, E. J. (2002) 'Energy Balance of a Glacier Surface: Analysis of Automatic Weather Station Data from the Morteratschgletscher, Switzerland', *Arctic, Antarctic, and Alpine Research*, 34(4), pp. 477–485. doi: 10.1080/15230430.2002.12003519.

Oerlemans, J. & Knap, W. (1998) 'A 1 year record of global radiation and albedo in the ablation zone of Morteratschgletscher, Switzerland', *Journal of Glaciology*, 44(147), pp. 231–238. doi: https://doi.org/10.3189/S0022143000002574.

Oke, T. R. (1987) *Bundary Layer Climates*. Second. Routledge.

van Pelt, W. J. J. Van, Pohjola, V. A. & Reijmer, C. H. (2016) 'The Changing Impact of Snow Conditions and Refreezing on the Mass Balance of an Idealized Svalbard Glacier', *Frontiers in Earth Science*, 4(102), pp. 1–15. doi: 10.3389/feart.2016.00102.

Porter, C. *et al.* (2018) *ArcticDEM*. doi: https://doi.org/10.7910/DVN/OHHUKH.

Quincey, D. J., Smith, M. W., Rounce, D. R., Ross, A. N., King, O. & Watson, C. S. (2017)

'Evaluating morphological estimates of the aerodynamic roughness of debris covered glacier ice', *Earth Surface Processes and Landforms*. doi: 10.1002/esp.4198.

Radić, V., Menounos, B., Shea, J., Fitzpatrick, N., Tessema, M. A. & Déry, S. J. (2017) 'Evaluation of different methods to model near-surface turbulent fluxes for a mountain glacier in the Cariboo Mountains, BC, Canada', *Cryosphere*, 11(6), pp. 2897–2918. doi: 10.5194/tc-11-2897-2017.

Raleigh, M. S., Landry, C. C., Hayashi, M., Quinton, W. L. & Lundquist, J. D. (2013) 'Approximating snow surface temperature from standard temperature and humidity data: New possibilities for snow model and remote sensing evaluation', *Water Resources Research*, 49(12), pp. 8053–8069. doi: 10.1002/2013WR013958.

Rees, W. G. & Arnold, N. S. (2006) 'Scale-dependent roughness of a glacier surface: Implications for radar backscatter and aerodynamic roughness modelling', *Journal of Glaciology*, 52(177), pp. 214–222. doi: 10.3189/172756506781828665.

Rippin, D. M., Pomfret, A. & King, N. (2015) 'High resolution mapping of supra-glacial drainage pathways reveals link between micro-channel drainage density, surface roughness and surface reflectance', *Earth Surface Processes and Landforms*, 40(10), pp. 1279–1290. doi: 10.1002/esp.3719.

Roe, G. H., Christian, J. E. & Marzeion, B. (2021) 'On the attribution of industrial-era glacier mass loss to anthropogenic climate change', *The Cryosphere*, 15(4), pp. 1889–1905. doi: 10.5194/tc-15-1889-2021.

Rounce, D. R., Quincey, D. J. & McKinney, D. C. (2015) 'Debris-covered glacier energy balance model for Imja-Lhotse Shar Glacier in the Everest region of Nepal', *Cryosphere*, 9(6), pp. 2295–2310. doi: 10.5194/tc-9-2295-2015.

Sauter, T., Arndt, A. & Schneider, C. (2020) 'COSIPY v1.3 – an open-source coupled snowpack and ice surface energy and mass balance model', *Geoscientific Model Development*, 13(11), pp. 5645–5662. doi: 10.5194/gmd-13-5645-2020.

Schaefer, M., MacHguth, H., Falvey, M., Casassa, G. & Rignot, E. (2015) 'Quantifying mass balance processes on the Southern Patagonia Icefield', *Cryosphere*, 9(1), pp. 25–35. doi: 10.5194/tc-9-25-2015.

Shaw, T. E., Brock, B. W., Ayala, Á., Rutter, N. & Pellicciotti, F. (2017) 'Centreline and cross-glacier air temperature variability on an Alpine glacier: Assessing temperature distribution methods and their influence on melt model calculations', *Journal of Glaciology*, 63(242), pp. 973–988. doi: 10.1017/jog.2017.65.

Shea, J. M. & Moore, R. D. (2010) 'Prediction of spatially distributed regional-scale fields of air temperature and vapor pressure over mountain glaciers', *Journal of Geophysical Research Atmospheres*, 115(23). doi: 10.1029/2010JD014351.

Shean, D. (2017) *High Mountain Asia 8-meter DEM Mosaics Derived from Optical Imagery, Version 1*, *NASA National Snow and Ice Data Center Distributed Active Archive Center*. doi: https://doi.org/10.5067/KXOVQ9L172S2.

Sicart, J. E., Hock, R., Ribstein, P. & Chazarin, J. P. (2010) 'Sky longwave radiation on tropical Andean glaciers: parameterization and sensitivity to atmospheric variables', *Journal of Glaciology*, 56(199), pp. 854–860. doi: https://doi.org/10.3189/002214310794457182.

Sicart, J. E., Hock, R. & Six, D. (2008) 'Glacier melt, air temperature, and energy balance in different climates: The Bolivian Tropics, the French Alps, and northern Sweden', *Journal of*

Geophysical Research Atmospheres, 113(24). doi: 10.1029/2008JD010406.

Sicart, J. E., Litt, M., Helgason, W., Tahar, V. Ben & Chaperon, T. (2014) 'A study of the atmospheric surface layer and roughness lengths on the high-altitude tropical Zongo glacier, Bolivia', *Journal of Geophysical Research*, 119(7), pp. 3793–3808. doi: 10.1002/2013JD020615.

Sicart, J. E., Wagnon, P. & Ribstein, P. (2005) 'Atmospheric controls of the heat balance of Zongo Glacier (16°S, Bolivia)', *Journal of Geophysical Research D: Atmospheres*, 110(12), pp. 1–17. doi: 10.1029/2004JD005732.

Smeets, C. J. P. P., Duynkerke, P. G. & Vugts, H. F. (1998) 'Turbulence characteristics of the stable boundary layer over a mid-latitude glacier. Part I: a combination of katabatic and large-scale forcing', *Boundary-Layer Meteorology*, 87(1), pp. 117–145. doi: 10.1023/A:1000860406093.

Smeets, C. J. P. P., Duynkerke, P. G. & Vugts, H. F. (1999) 'Observed wind profiles and turbulent fluxes over an ice surface with changing surface roughness', *Boundary-Layer Meteorology*, 92(1994), pp. 101–123. doi: 10.1023/A:1001899015849.

Smith, M. W. (2014) 'Roughness in the Earth Sciences', *Earth-Science Reviews*, 136, pp. 202–225. doi: 10.1016/j.earscirev.2014.05.016.

Smith, M. W., Quincey, D. J., Dixon, T., Bingham, R. G., Carrivick, J. L., Irvine-Fynn, T. D. L. & Rippin, D. M. (2016) 'Aerodynamic roughness of glacial ice surfaces derived from high-resolution topographic data', *Journal of Geophysical Research F: Earth Surface*, 121(4), pp. 748–766. doi: 10.1002/2015JF003759.

Smith, T. I., Smith, M. W., Chambers, J. R., Sailer, R., Nicholson, L., Mertes, J., Quincey, D. J., Carrivick, J. L. & Stiperski, I. (2020) 'A scale-dependent model to represent changing aerodynamic roughness of ablating glacier ice based on repeat topographic surveys', *Journal of Glaciology*, pp. 1–15. doi: 10.1017/jog.2020.56.

Stull, R. (1988) *An introduction to boundary layer meteorology*. London: Kluwer.

Van De Wal, R. S. W., Oerlemans, J. & Van Der Rage, J. C. (1992) 'A study of ablation variations on the tongue of Hintereisferner , Austrian Alps', *Journal of Glaciology*, 38(130), pp. 319–324. doi: https://doi.org/10.3189/S0022143000002203.

Wang, Z., Erb, A. M., Schaaf, C. B., Sun, Q., Liu, Y., Yang, Y., Shuai, Y., Casey, K. A. & Román, M. O. (2016) 'Early spring post-fire snow albedo dynamics in high latitude boreal forests using Landsat-8 OLI data', *Remote Sensing of Environment*, 185, pp. 71–83. doi: 10.1016/j.rse.2016.02.059.

Wieringa, J. (1993) 'Representative roughness parameters for homogeneous terrain', *Boundary-Layer Meteorology*, 63(4), pp. 323–363. doi: 10.1007/BF00705357.

Willis, I. C., Arnold, N. S. & Brock, B. W. (2002) 'Effect of snowpack removal on energy balance, melt and runoff in a small supraglacial catchment', *Hydrological Processes*. doi: 10.1002/hyp.1067.

Wilson, N. J. & Flowers, G. E. (2013) 'Environmental controls on the thermal structure of alpine glaciers', *The Cryosphere*, 7(1), pp. 167–182. doi: 10.5194/tc-7-167-2013.

Chapter 3 : Topographic Survey Methods

3.1 Introduction

The ability to survey landscapes and the character of the Earth's surface accurately is central to almost every branch of physical geography. In glaciology, topographic data has many applications including: mapping of glacier surface features (e.g. Hodson *et al.*, 2007); mapping glacial, periglacial and proglacial landforms (e.g. Carrivick *et al.*, 2015; Sutherland *et al.*, 2019); quantifying snow depth (e.g. Nolan *et al.*, 2015); quantifying glacier mass balance and retreat (e.g. King *et al.*, 2017, 2019) and tracking ice velocity (e.g. Davison *et al.*, 2020). The diversity of applications has been bolstered by advances in technology that allow rapid data collection at fine resolutions. From simple optical levels and electronic distance measurement surveys that yield 10^1-10^2 measurements per day, recent decades have seen the progression of laser scanning and digital photographic technology to different platforms that mean terrestrial, airborne or space-borne devices can collect >>10^6 measurements in a day (Smith *et al.*, 2015). As will be outlined in this section, different technologies and platforms can be used to acquire data spanning spatial resolutions from 10^{-3} m per pixel up to 10^2 m per pixel and from plot scales (10^1 m^2) to entire regions (>10^7 m^2), with varying costs and limitations. Background will be given first for SfM, followed by some of its applications within glaciology, then the same for terrestrial laser scanning (TLS) and airborne laser scanning (ALS). Applications listed here are in addition to estimation of glacier aerodynamic roughness, which is reviewed for both methods in subsequent chapters.

3.2 Introduction to Structure-from-Motion

Structure-from-Motion with Multi-View Stereo (SfM) refers to the process of using the principles of photogrammetry to calculate the geometry of a scene and digitally reconstruct it in 3D (Ullman, 1979; Brown and Lowe, 2005; Snavely *et al.*, 2008). The process is usually called SfM for simplicity but comprises all steps in the process, from data acquisition, to feature detection, keypoint correspondence and filtering, SfM, scaling and georeferencing, and Multi-View Stereo (James and Robson, 2012). Widespread availability of digital cameras and specialist software has significantly increased the popularity and accessibility of SfM for geoscience applications in recent decades (Anderson *et al.*, 2019). SfM cannot contend with light detection and ranging (LiDAR) for accuracy over scales of hundreds to thousands of metres, but at scales of less than a metre up to hundreds of metres it has several advantages (Smith *et al.*, 2016). While the cost and size of TLS units is decreasing, equipment required for SfM remains far less expensive, less difficult to transport and easier to use in harsh environments compared to the peripheral equipment required for TLS surveys, such as

tripods, targets and batteries. Data collection from a TLS also tends to be slower, with careful survey design required to ensure that targets are seen from various scan positions. SfM, by comparison, allows rapid data acquisition with limited equipment; useful for locations with limited access or for repeat surveys within a limited amount of time.

3.3 Principles of Structure-from-Motion

As mentioned previously, the abbreviation of SfM has come to refer to a workflow rather than a single step in a process. The SfM process is complex and is explained in detail in several publications (e.g. Snavely *et al.*, 2008; Micheletti *et al.*, 2015; Smith *et al.*, 2016), so it will only be outlined briefly here. The first step of any SfM workflow is survey design, which is necessary for both efficiency and to achieve robust results. It is common to survey a plot in a regular grid pattern, with consideration given to the placement of ground control points (GCPs) for strong georeferencing (James *et al.*, 2017a). Once data have been acquired, the dataset is usually inspected for image quality before being loaded into a software package. The software begins by detecting features within images, then finds corresponding features (or keypoints) within multiple images. The matching of keypoints between image pairs is refined until it is statistically unlikely to contain outliers. Once the geometry of keypoints has been ascertained, bundle adjustment algorithms estimate the 3D coordinates of each point (structure of the scene), the locations of different cameras and their intrinsic calibrations – i.e., structure from motion. Bundle adjustment refers to the least-squares optimisation of a network of keypoints and camera positions, resulting in a sparse cloud of points with an arbitrary scale and orientation (Granshaw, 1980).

The sparse cloud (Fig. 3.1) is then given a scale and orientation within a coordinate system based on the locations of GCPs. The location of the GCPs within the coordinate system is recorded during the initial data collection survey, and James *et al.* (2017) presented ways to optimise the number and distribution of GCPs for robust georeferencing. Bundle adjustment is usually re-run incorporating the GCP coordinates and provides reprojection error and georeferencing error estimates. A Multi-View Stereo algorithm is then applied to the sparse point cloud, which creates subsets of overlapping images to reduce the demand on processors. Within each subset, the locations of points are used to identify others and increase the density of points by several orders of magnitude. Once the dense point cloud (Fig. 3.1) has been generated (this step can be extremely computationally demanding), the point cloud can be exported for further analysis, or used to construct a digital elevation model (DEM).

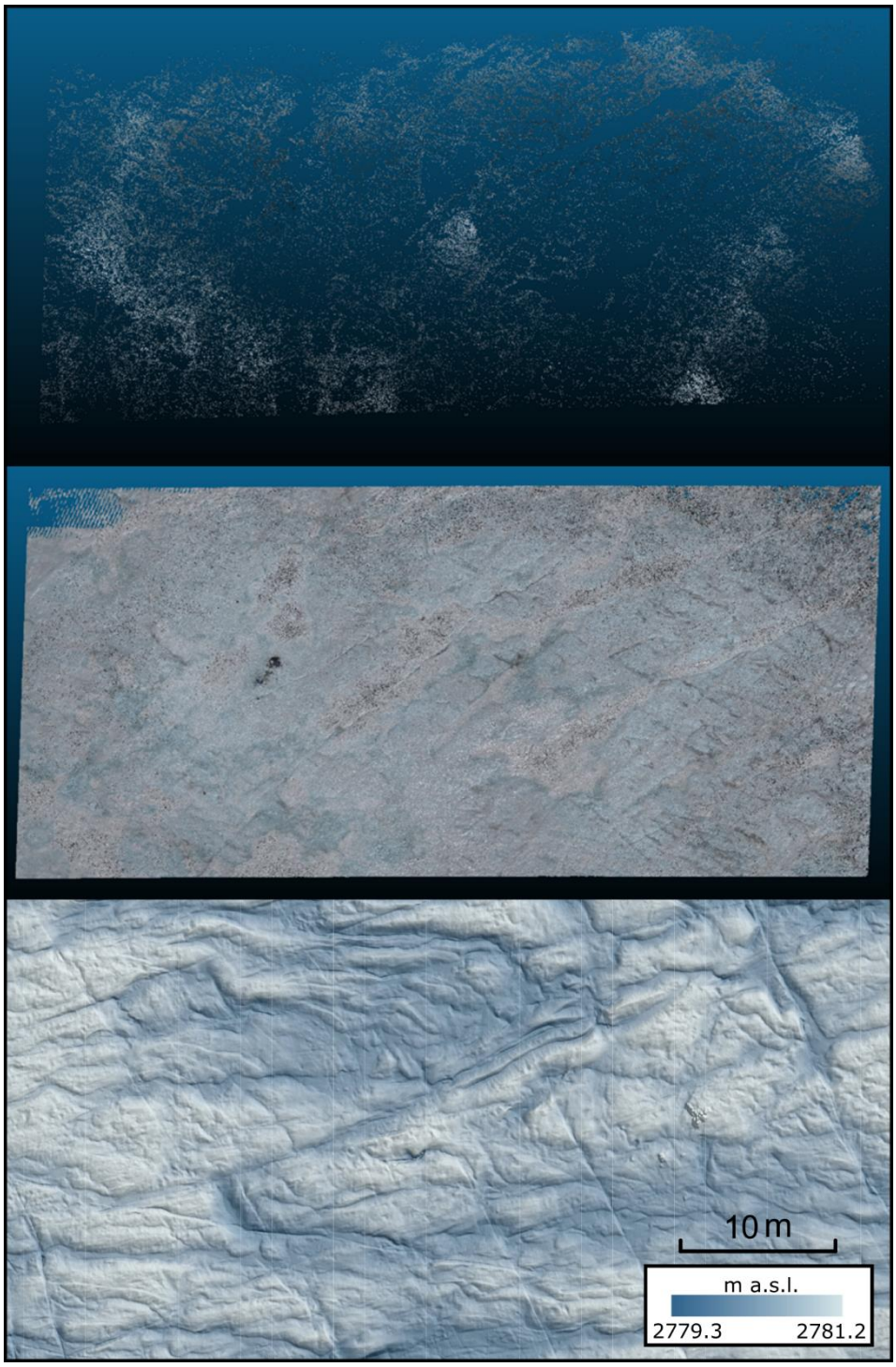

Fig. 3.1 Example outputs from SfM workflow. The top panel shows a sparse point cloud from Storglaciären, Sweden, The middle shows a dense point cloud from the same glacier. The bottom panel shows an exported and hillshaded digital elevation model from Hintereisferner, Austria.

As explored below, the number of studies employing SfM has proliferated in parallel with the availability of technology and software. In light of the increased popularity of SfM,

attention has turned to how the use and results of SfM are reported. In the past, specialist knowledge of photogrammetric principles was required to perform SfM but modern software has turned the process into a 'black box', into which the user inputs their data and is presented with a result without understanding the processes used to create it, or their limitations (Fraser and Congalton, 2018; James *et al.*, 2019). Subsequent concerns over the quality of topographic data acquired using SfM have led to investigations into the accuracy and precision of the process (James *et al.*, 2017b). With these concerns in mind, and with many studies now basing conclusions on SfM-derived topographic data, efforts have been made to ensure that users in the geosciences are aware the principles of digital photography (O'Connor *et al.*, 2017) and of best-practice guidelines for survey design, camera settings, software parameters and error reporting that should be included to facilitate reproducibility (James *et al.*, 2019).

3.4 Platforms and applications

Along with advances and access to digital cameras and SfM software, the platforms from which SfM surveys can be carried out have developed in parallel. Platforms used to elevate the position of the camera so that overhead, nadir or aerial photographs (Fig. 3.2) can be captured include survey poles (Smith and Vericat, 2015), kites (Smith *et al.*, 2009), lighter-than-air blimps (Vericat *et al.*, 2009) and Uncrewed Aerial Vehicles (UAVs; Pearce *et al.*, 2020; Ryan *et al.*, 2015; Woodget *et al.*, 2017). The latter, once the domain of enthusiastic hobbyists and military programmes, has seen marked changes in accessibility to non-experts (Pajares, 2015; Manfreda *et al.*, 2018). From small DIY rotary-wing models that cost up to £29,500 (including flight training) in 2010 (Woodget *et al.*, 2015) to bespoke fixed-wing platforms that require knowledge of programming and electronics (Ryan *et al.*, 2015), earlier work with UAVs was relatively specialist. Currently, rotary- or fixed-wing UAVs can be bought off-the-shelf fitted with HD cameras and with software that makes flight planning and photography straightforward for non-experts, with mid-range models costing <£2000 (DJI, 2020). In the UK, current legislation changes require anyone using a UAV for commercial purposes (under which scientific research is usually included) to be given permission by the Civil Aviation Authority after having passed theory and practical examinations (CAA, 2020). Despite the cost associated with this, the use of UAVs for SfM is much more affordable after just a few years since the technology started to take-off.

Fig. 3.2 Example of UAV photography. From an aerial vantage point, it is possible to capture the characteristics of a glacier surface over a broad area. This image also shows an example of a ground control point (red square with yellow dot and white number) used for georeferencing, along with the author demonstrating expert UAV piloting skills.

Recent advances in SfM and UAV availability have led to widespread uptake in almost all fields of geoscience (Anderson *et al.*, 2019). In drylands, applications have included landscape mapping (Gillan *et al.*, 2017), measuring erosion and deposition (Smith and Vericat, 2015) and hydrological modelling of slopes (Wolstenholme *et al.*, 2020). SfM has also been used for quantification of biomass in mangroves (Warfield and Leon, 2019) and for mapping temperate forests (Fraser and Congalton, 2018). In river science, SfM has been employed for a multitude of applications (Carrivick and Smith, 2019), from investigations of bank and channel morphology (Dietrich, 2016; Hamshaw *et al.*, 2017; Leduc *et al.*, 2019) to submerged topography (Woodget *et al.*, 2015), river restoration (Marteau *et al.*, 2017) and habitat mapping (Woodget *et al.*, 2017).

Glaciological uses for SfM have been almost as numerous as those in other areas. For example, pro-glacial and periglacial landscapes have been digitally reconstructed to aid in mapping the past behaviour of glaciers (Ely *et al.*, 2016), and repeat surveys of glacial

landforms have helped inform our understanding of the geomorphological processes that created them (Chandler *et al.*, 2018). Historic aerial photographs of glaciers have been used to recreate former ice extents in 3D, which provides information on past ice dynamics and mass loss (Mertes *et al.*, 2017; Holmlund and Holmlund, 2019; Holmlund, 2020). Time-lapse technology allows repeat SfM surveys to be carried out in the absence of researchers, so that infrequent morphological phenomena can be captured for later study; Mallalieu *et al.* (2017; 2020) used this approach to quantify ice mass loss through lake calving events at the margin of the Greenland ice sheet. Glacier surface features have also been studied using SfM, including UAV surveys of current and relict surface meltwater channels, giving information on their changing hydrology (Rippin *et al.*, 2015). The highly variable surface topography of debris-covered glaciers has been modelled and monitored, shedding light on the melting behaviour of the ice beneath (Watson *et al.*, 2017; 2020; King *et al.*, 2020; Westoby *et al.*, 2020).

While the use of UAVs has enabled researchers to collect data from areas which would otherwise be impractical to survey, a degree of accessibility to a site is still required in order to place and record ground control points (GCPs) so that a resulting SfM survey can be georeferenced. In addition, this restriction usually limits the size of the survey; however, Chudley *et al.* (2019) used a 'direct georeferencing' approach to record the location of each image so that GCPs are not required, and spatially accurate surveys of broad or inaccessible areas can be completed. Using this approach and repeat surveys, it is also possible to calculate the velocity of a glacier at much finer spatial and temporal resolutions than satellite data allow (Chudley *et al.*, 2019).

The use of SfM and UAVs has certainly changed how topographic surveying is approached within the geosciences. Yet, limitations to the spatial coverage that can be reasonably achieved mean that larger scale features ($>10^2$ m^2), which glaciers and other ice masses commonly are, cannot be surveyed practically. For broader, or regional scale coverage, Light Detection and Ranging (LiDAR) is commonly employed.

3.5 Introduction to LiDAR

Whether airborne or terrestrial, laser scanning technology uses the principles of LiDAR for topographic data acquisition (Petrie and Toth, 2018). LiDAR uses time-of-flight (light transit time estimation), or phase-shift , to measure the distance between a sensor and a surface (Vosselman and Maas, 2010). Like Radio Detection and Ranging (RaDAR), LiDAR is an active

remote sensing technique; a signal is sent from a source and its reflection is detected by a sensor, assuming that light travels at a finite and constant velocity in a given medium. This propagation speed and the time taken for a round trip are used to calculate the distance between source and reflector. If the location of the sensor is known then the angle from sensor to reflector can be used along with the distance to calculate the coordinates of the reflector relative to the sensor. Characteristics of the reflector surface can cause multiple return signals, or pulse echoes, to be received by the sensor. Vegetation is a good example of this, where pulse echoes can be caused by different surfaces in close proximity (Pfeifer and Briese, 2007). Most airborne systems are able to detect several pulse echoes, but the feature is not yet ubiquitous in terrestrial systems. In this section, first airborne laser scanning (ALS) then terrestrial laser scanning (TLS) will be introduced; the underlying principles are similar, so the focus will be on the differences that suit each method to its applications.

3.6 Airborne laser scanning principles

ALS systems usually consist of three time-synchronised systems carried by a piloted aircraft: a laser scanner unit that emits pulses and records their return time, a navigation system such as differential global positioning systems (dGPS) or differential global navigation satellite systems (dGNSS) and an inertial measurement unit (IMU) that logs the orientation of the aircraft (Wehr and Lohr, 1999). The laser scanner collects the light transit time estimation data, while the positioning system logs the location of the aircraft, and the IMU tracks the pitch, yaw and roll. As an aircraft is able to fly high above the landscape and travel great distances in a short amount of time, ALS is well suited to regional- or landscape-scale surveys that can achieve centimetre to decimetre accuracy (Gallay, 2013). The cost of carrying out ALS surveys is prohibitive to most individual studies, but datasets produced by national or international programmes and collaborations are becoming increasingly available to the public (e.g. Bollmann *et al.*, 2011; Open Data Austria, 2020).

The typical operational wavelength of ALS systems is around 1064 nm, in the near-infrared part of the electromagnetic spectrum (Gallay, 2013). The optimum wavelength depends on the reflective properties of the surface or terrain of interest; for example, absorption of light nearer the visible part of the spectrum (300-750 nm) by liquid water is high, yet at infrared wavelengths of ~1550 nm ice and snow are also poor reflectors (Vosselman and Maas, 2010). For glaciological applications, the wavelength is normally 1050-1064 nm. Cryospheric applications for ALS mainly take advantage of ability to collect data over broad spatial scales,

and use repeat surveys to create DEMs (Baltsavias *et al.*, 2001; Arnold *et al.*, 2006) and monitor regional changes in glacier extent, mass balance and dynamics (Bamber *et al.*, 2005; Foy *et al.*, 2011; Sisson *et al.*, 2011; Pelto *et al.*, 2019). Surveys can also be compiled into regional glacier inventories (Knoll and Kerschner, 2009), or be used to map glacial landforms (Irvine-Fynn *et al.*, 2011; Sailer *et al.*, 2012; Midgley *et al.*, 2018), investigate periglacial hazards (Lancaster *et al.*, 2012) and calculate glacier velocity (Abdalati and Krabill, 1999; Telling *et al.*, 2017a).

3.7 Terrestrial laser scanning principles

TLS systems are usually operated from multiple static scan positions, at each of which the TLS is mounted on a conventional survey tripod (Brasington *et al.*, 2012; Smith, 2015). Less commonly, an IMU can be incorporated, enabling a TLS to be mounted on terrestrial transports such as snowmobiles, boats and 4x4 vehicles (Barber and Mills, 2007; Alho *et al.*, 2009; Kaasalainen *et al.*, 2011). Like ALS, TLS primarily use time-of-flight to calculate distance. A key difference is in the planning required for TLS, which requires substantial consideration of the scanner field of view (Petrie and Toth, 2018). In terms of choosing the appropriate model of scanner, the field of view can be described as camera, hybrid or panoramic depending on the arrangement, number and motion of mirrors (Telling *et al.*, 2017b). A camera scanner has a window-like field of view, of a fixed horizontal and vertical extent. A hybrid scanner rotates its field of view through 360° about the vertical axis, and a panoramic scanner is able to do this while incorporating an upward view to collect data from the full "dome" (Telling *et al.*, 2017b).

The choice of scan location is critical in survey design and is influenced by the angle of incidence between the TLS and scan target. Highly oblique angles (>60°) can increase the beam footprint size, decrease point accuracy and reduce the power of returned signals (Lichti, 2007; Carrea *et al.*, 2016). This is a key consideration in glaciological applications where access to scan sites in high relief terrain might be impractical, limiting scan positions to those with a relatively oblique angle of incidence. Point cloud voids can be a consequence of such situations, arising when areas of the surface are occluded by another (Smith, 2015; Telling *et al.*, 2017b). Use of multiple scan locations that offer views of the scan site from different angles can mitigate the effects of occlusion. Where more than one scan location is used, scans are registered so that they are geometrically aligned within an arbitrary coordinate system using at least three common, fixed points of known location, usually reflective targets. Once registered into one coherent scan, point clouds can be

georeferenced either using real-world coordinates of the targets (Smith, 2015) or via co-registration to an independent dataset that has been previously georeferenced (e.g. Prantl *et al.*, 2017).

Fig. 3.3 Terrestrial laser scanner. This Riegl VZ-6000 unit has been permanently located near the summit of 'Im Hinterin Eis' near Hinteriesferner, Austria with a field of view over the glacier. The scanner is housed in a climate-controlled storage container and can be used to acquire repeated scans of the glacier, as demonstrated in Chapter 5. Images of scanner from riegl.com, main image from uibk.ac.at, by R. Sailer, Department of Geography, University of Innsbruck.

3.8 Applications

LiDAR has enabled advances in many areas of glaciology that require fine resolution measurements with high accuracy (Fig. 3.3). LiDAR surveys have provided data that have been used for mapping surface topography, detecting surface change and calculating mass balance, from regional-scale topographic surveys of ice sheets and mountain glaciers to repeat surveys of single glaciers (Knoll and Kerschner, 2009; Foy *et al.*, 2011; Pelto *et al.*, 2019). Repeat surveys can also be used to calculate glacier motion or velocity (Abdalati and Krabill, 1999; Telling *et al.*, 2017a). Smaller scale surface features such as penitentes have been investigated using TLS (Nicholson *et al.*, 2016), and even internal (englacial) passages and conduits have been mapped (Santagata *et al.*, 2017; Kamintzis *et al.*, 2018). LiDAR studies of periglacial and paraglacial landforms and dynamics have been just as informative, illuminating processes in the landscape around glaciers (Carrivick *et al.*, 2015) and in areas

where glaciers are currently retreating (Lancaster *et al.*, 2012; Sailer *et al.*, 2012), as well as showing how landscapes can evolve after deglaciation over much longer timescales (Fischer *et al.*, 2015).

3.9 Summary

The methods described in this chapter - SfM, TLS and ALS - are all well-established techniques within the field of glaciology. While the widespread use of SfM is a more recent trend, the falling cost of hardware and the development of best practice guidelines make it the ideal tool for many glaciological applications including this research. The fine-resolution data products are well suited to capturing the aerodynamically important details of glacier surfaces. The longer history of ALS and TLS means that they have been adopted into government and institute sponsored programmes which are able to provide useful data which is accessible to the public, and which have been instrumental to this thesis. Glacier- and regional-scale laser scanning data provides a broader, yet detailed, view of glacier surface topography. The ways in which each method introduced in this chapter were employed are described in relevant sections in each of the subsequent results chapters.

References

Abdalati, W. & Krabill, W. B. (1999) 'Calculation of Ice Velocities in the Jakobshavn Isbrae Area Using Airborne Laser Altimetry', *Remote Sensing of Environment*, 67(2), pp. 194–204. doi: https://doi.org/10.1016/S0034-4257(98)00086-8.

Alho, P., Kukko, A., Hyyppä, H., Kaartinen, H., Hyyppä, J. & Jaakkola, A. (2009) 'Application of boat-based laser scanning for river survey', *Earth Surface Processes and Landforms*, 34(13), pp. 1831–1838. doi: 10.1002/esp.1879.

Anderson, K., Westoby, M. J. & James, M. R. (2019) 'Low-budget topographic surveying comes of age: Structure from motion photogrammetry in geography and the geosciences', *Progress in Physical Geography*. SAGE Publications Ltd, pp. 163–173. doi: 10.1177/0309133319837454.

Arnold, N. S., Rees, W. G., Devereux, B. J. & Amable, G. S. (2006) 'Evaluating the potential of high-resolution airborne LiDAR data in glaciology', *International Journal of Remote Sensing*, 27(6), pp. 1233–1251. doi: 10.1080/01431160500353817.

Baltsavias, E. P., Favey, E., Bauder, A., Bosch, H. & Pateraki, M. (2001) 'Digital Surface Modelling by Airborne Laser Scanning and Digital Photogrammetry for Glacier Monitoring', *Photogrammetric Record*, 17(98), pp. 243–273. doi: https://doi.org/10.1016/S0924-2716(99)00016-7.

Bamber, J. L., Krabill, W., Raper, V., Dowdeswell, J. A. & Oerlemans, J. (2005) 'Elevation changes measured on Svalbard glaciers and ice caps from airborne laser data', *Annals of Glaciology*, 42. doi: https://doi.org/10.3189/172756405781813131.

Barber, D. M. & Mills, J. P. (2007) 'Vehicle based waveform laser scanning in a coastal environment', *International Archives of Photogrammetry, Remote Sensing and Spatial Information Sciences*, 36(C55).

Bollmann, E., Sailer, R., Briese, C., Stotter, J. & Fritzmann, P. (2011) 'Potential of airborne laser scanning for geomorphologie feature and process detection and quantifications in high alpine mountains', *Zeitschrift fur Geomorphologie*, 55(SUPPL. 2), pp. 83–104. doi: 10.1127/0372-8854/2011/0055S2-0047.

Brasington, J., Vericat, D. & Rychkov, I. (2012) 'Modeling river bed morphology, roughness, and surface sedimentology using high resolution terrestrial laser scanning', *Water Resources Research*, 48(11). doi: 10.1029/2012WR012223.

Brown, M. & Lowe, D. G. (2005) 'Unsupervised 3D Object Recognition and Reconstruction in Unordered Datasets', *Proceedings of the Fifth International Conference on 3-D Digital Imaging and Modeling*. doi: 10.1109/3DIM.2005.81.

Carrea, D., Abellan, A., Humair, F., Matasci, B., Derron, M. H. & Jaboyedoff, M. (2016) 'Correction of terrestrial LiDAR intensity channel using Oren-Nayar reflectance model: An application to lithological differentiation', *ISPRS Journal of Photogrammetry and Remote Sensing*, 113, pp. 17–29. doi: 10.1016/j.isprsjprs.2015.12.004.

Carrivick, J. L. & Smith, M. W. (2019) 'Fluvial and aquatic applications of Structure from Motion photogrammetry and unmanned aerial vehicle/drone technology', *Wiley Interdisciplinary Reviews: Water*, 6(1), pp. 405–426. doi: https://doi.org/10.1002/wat2.1328.

Carrivick, J. L., Smith, M. W. & Carrivick, D. M. (2015) 'Terrestrial laser scanning to deliver high-resolution topography of the upper Tarfala valley, arctic Sweden', *Gff*, 137(4), pp. 383–396. doi: 10.1080/11035897.2015.1037569.

Chandler, B. M. P., Lovell, H., Boston, C. M., Lukas, S., Barr, I. D., Benediktsson, Í. Ö., Benn, D. I., Clark, C. D., Darvill, C. M., Evans, D. J. A., Ewertowski, M. W., Loibl, D., Margold, M., Otto, J. C., Roberts, D. H., Stokes, C. R., Storrar, R. D. & Stroeven, A. P. (2018) 'Glacial geomorphological mapping: A review of approaches and frameworks for best practice', *Earth-Science Reviews*. Elsevier B.V., pp. 806–846. doi: 10.1016/j.earscirev.2018.07.015.

Chudley, T. R., Christoffersen, P., Doyle, S. H., Abellan, A. & Snooke, N. (2019) 'High-accuracy UAV photogrammetry of ice sheet dynamics with no ground control', *Cryosphere*, 13(3), pp. 955–968. doi: 10.5194/tc-13-955-2019.

Davison, B. J., Sole, A. J., Cowton, T. R., Lea, J. M., Slater, D. A., Fahrner, D. & Nienow, P. W. (2020) 'Subglacial Drainage Evolution Modulates Seasonal Ice Flow Variability of Three Tidewater Glaciers in Southwest Greenland', *Journal of Geophysical Research: Earth Surface*, 125(9). doi: 10.1029/2019JF005492.

Dietrich, J. T. (2016) 'Riverscape mapping with helicopter-based Structure-from-Motion photogrammetry', *Geomorphology*, 252, pp. 144–157. doi: 10.1016/j.geomorph.2015.05.008.

Ely, J. C., Graham, C., Barr, I. D., Rea, B. R., Spagnolo, M., Evans, J. & Ely, J. (2016) 'Using UAV acquired photography and structure from motion techniques for studying glacier landforms: application to the glacial flutes at Isfallsglaciären', *Earth Surface Processes and Landforms*, 42(6), pp. 877–888. doi: 10.1002/esp.4044.

Fischer, A., Seiser, B., Stocker Waldhuber, M., Mitterer, C. & Abermann, J. (2015) 'Tracing glacier changes in Austria from the Little Ice Age to the present using a lidar-based high-resolution glacier inventory in Austria', *Cryosphere*, 9(2), pp. 753–766. doi: 10.5194/tc-9-753-2015.

Foy, N., Copland, L., Zdanowicz, C., Demuth, M. & Hopkinson, C. (2011) 'Recent volume and area changes of Kaskawulsh Glacier, Yukon, Canada', *Journal of Glaciology*, 57(203). doi: https://doi.org/10.3189/002214311796905596.

Fraser, B. T. & Congalton, R. G. (2018) 'Issues in Unmanned Aerial Systems (UAS) data collection of complex forest environments', *Remote Sensing*, 10(6). doi: 10.3390/rs10060908.

Gallay, M. (2013). Section 2.1.4: 'Direct Acquisition of Data: Airborne laser scanning'. In: Cook, S.J., Clarke, L.E. & Nield, J.M. (Eds.) Geomorphological Techniques (Online Edition). British Society for Geomorphology, London. ISSN: 2047-0371

Gillan, J. K., Karl, J. W., Elaksher, A. & Duniway, M. C. (2017) 'Fine-resolution repeat topographic surveying of dryland landscapes using UAS-based structure-from-motion photogrammetry: Assessing accuracy and precision against traditional ground-based erosion measurements', *Remote Sensing*, 9(5). doi: 10.3390/rs9050437.

Granshaw, B. (1980) 'Bundle Adjustment Methods in Engineering Photogrammetry', *Photogrammetric Record*, 10(56), pp. 181–207. doi: https://doi.org/10.1111/j.1477-9730.1980.tb00020.x.

Hamshaw, S. D., Bryce, T., Rizzo, D. M., O'Neil-Dunne, J., Frolik, J. & Dewoolkar, M. M. (2017) 'Quantifying streambank movement and topography using unmanned aircraft

system photogrammetry with comparison to terrestrial laser scanning', *River Research and Applications*, 33(8), pp. 1354–1367. doi: 10.1002/rra.3183.

Hodson, A., Anesio, A. M., Ng, F., Watson, R., Quirk, J., Irvine-Fynn, T., Dye, A., Clark, C., Mccloy, P., Kohler, J. & Sattler, B. (2007) 'A glacier respires: Quantifying the distribution and respiration CO2 flux of cryoconite across an entire arctic supraglacial ecosystem', *Journal of Geophysical Research: Biogeosciences*, 112(4), pp. 1–9. doi: 10.1029/2007JG000452.

Holmlund, E. S. (2020) 'Aldegondabreen glacier change since 1910 from structure-from-motion photogrammetry of archived terrestrial and aerial photographs: utility of a historic archive to obtain century-scale Svalbard glacier mass losses', *Journal of Glaciology*, pp. 1–10. doi: 10.1017/jog.2020.89.

Holmlund, E. S. & Holmlund, P. (2019) 'Constraining 135 years of mass balance with historic structure-from-motion photogrammetry on Storglaciären, Sweden', *Geografiska Annaler, Series A: Physical Geography*, 101(3), pp. 195–210. doi: 10.1080/04353676.2019.1588543.

Irvine-Fynn, T. D. L., Barrand, N. E., Porter, P. R., Hodson, A. J. & Murray, T. (2011) 'Recent High-Arctic glacial sediment redistribution: A process perspective using airborne lidar', *Geomorphology*, 125(1), pp. 27–39. doi: 10.1016/j.geomorph.2010.08.012.

James, M. R., Chandler, J. H., Eltner, A., Fraser, C., Miller, P. E., Mills, J. P., Noble, T., Robson, S. & Lane, S. N. (2019) 'Guidelines on the use of Structure from Motion Photogrammetry in Geomorphic Research', *Earth Surface Processes and Landforms*. doi: 10.1002/esp.4637.

James, M. R. & Robson, S. (2012) 'Straightforward reconstruction of 3D surfaces and topography with a camera: Accuracy and geoscience application', *Journal of Geophysical Research: Earth Surface*, 117(F03017). doi: 10.1029/2011JF002289.

James, M. R., Robson, S., D'Oleire-Oltmanns, S. & Niethammer, U. (2017a) 'Optimising UAV topographic surveys processed with structure-from-motion: Ground control quality, quantity and bundle adjustment', *Geomorphology*, 280, pp. 51–66. doi: 10.1016/j.geomorph.2016.11.021.

James, M. R., Robson, S. & Smith, M. W. (2017b) '3-D uncertainty-based topographic change detection with structure-from-motion photogrammetry: Precision maps for ground control and directly georeferenced surveys', *Earth Surface Processes and Landforms*, 42, pp. 1769–1788. doi: 10.1002/esp.4125.

Kaasalainen, S., Kaartinen, H., Kukko, A., Anttila, K. & Krooks, A. (2011) 'Brief communication "application of mobile laser scanning in snow cover profiling"', *Cryosphere*, 5(1), pp. 135–138. doi: 10.5194/tc-5-135-2011.

Kamintzis, J. E., Jones, J. P. P., Irvine-Fynn, T. D. L., Holt, T. O., Bunting, P., Jennings, S. J. A., Porter, P. R. & Hubbard, B. (2018) 'Assessing the applicability of terrestrial laser scanning for mapping englacial conduits', *Journal of Glaciology*, 64(243), pp. 37–48. doi: 10.1017/jog.2017.81.

King, O., Bhattacharya, A., Bhambri, R. & Bolch, T. (2019) 'Glacial lakes exacerbate Himalayan glacier mass loss', *Scientific Reports*, 9(1). doi: 10.1038/s41598-019-53733-x.

King, O., Quincey, D. J., Carrivick, J. L. & Rowan, A. V. (2017) 'Spatial variability in mass loss of glaciers in the everest region, central Himalayas, between 2000 and 2015', *Cryosphere*, 11(1), pp. 407–426. doi: 10.5194/tc-11-407-2017.

King, O., Turner, A. G. D., Quincey, D. J. & Carrivick, J. L. (2020) 'Morphometric evolution of Everest region debris-covered glaciers', *Geomorphology*, 371. doi:

10.1016/j.geomorph.2020.107422.

Knoll, C. & Kerschner, H. (2009) 'A glacier inventory for South Tyrol, Italy, based on airborne laser-scanner data', *Annals of Glaciology*, 50(53), pp. 46–52. doi: https://doi.org/10.3189/172756410790595903.

Lancaster, S. T., Nolin, A. W., Copeland, E. A. & Grant, G. E. (2012) 'Periglacial debris-flow initiation and susceptibility and glacier recession from imagery, airborne LiDAR, and ground-based mapping', *Geosphere*, 8(2), pp. 417–430. doi: 10.1130/GES00713.1.

Leduc, P., Peirce, S. & Ashmore, P. (2019) 'Short communication: Challenges and applications of structure-from-motion photogrammetry in a physical model of a braided river', *Earth Surface Dynamics*, 7(1), pp. 97–106. doi: 10.5194/esurf-7-97-2019.

Lichti, D. D. (2007) 'Error modelling, calibration and analysis of an AM-CW terrestrial laser scanner system', *ISPRS Journal of Photogrammetry and Remote Sensing*, 61(5), pp. 307–324. doi: 10.1016/j.isprsjprs.2006.10.004.

Mallalieu, J., Carrivick, J. L., Quincey, D. J. & Smith, M. W. (2020) 'Calving Seasonality Associated With Melt-Undercutting and Lake Ice Cover', *Geophysical Research Letters*, 47(8). doi: 10.1029/2019GL086561.

Mallalieu, J., Carrivick, J. L., Quincey, D. J., Smith, M. W. & James, W. H. M. (2017) 'An integrated Structure-from-Motion and time-lapse technique for quantifying ice-margin dynamics', *Journal of Glaciology*, 63(242), pp. 937–949. doi: 10.1017/jog.2017.48.

Manfreda, S. *et al.* (2018) 'On the use of unmanned aerial systems for environmental monitoring', *Remote Sensing,* 10(4), 641. doi: 10.3390/rs10040641.

Marteau, B., Vericat, D., Gibbins, C., Batalla, R. J. & Green, D. R. (2017) 'Application of Structure-from-Motion photogrammetry to river restoration', in *Earth Surface Processes and Landforms*. John Wiley and Sons Ltd, pp. 503–515. doi: 10.1002/esp.4086.

Mertes, J. R., Gulley, J. D., Benn, D. I., Thompson, S. S. & Nicholson, L. I. (2017) 'Using structure-from-motion to create glacier DEMs and orthoimagery from historical terrestrial and oblique aerial imagery', *Earth Surface Processes and Landforms*, 42(14), pp. 2350–2364. doi: 10.1002/esp.4188.

Micheletti, N., Chandler, J. H. & Lane, S. N. (2015). Section 2.2.2: 'Structure from Motion (SfM) Photogrammetry'. In: Cook, S.J., Clarke, L.E. & Nield, J.M. (Eds.) Geomorphological Techniques (Online Edition). British Society for Geomorphology, London. ISSN: 2047-0371

Midgley, N. G., Tonkin, T. N., Graham, D. J. & Cook, S. J. (2018) 'Evolution of high-Arctic glacial landforms during deglaciation', *Geomorphology*, 311, pp. 63–75. doi: 10.1016/j.geomorph.2018.03.027.

Nicholson, L. I., Pętlicki, M., Partan, B. & MacDonell, S. (2016) '3-D surface properties of glacier penitentes over an ablation season, measured using a Microsoft Xbox Kinect', *Cryosphere*, 10(5), pp. 1897–1913. doi: 10.5194/tc-10-1897-2016.

Nolan, M., Larsen, C. & Sturm, M. (2015) 'Mapping snow depth from manned aircraft on landscape scales at centimeter resolution using structure-from-motion photogrammetry', *Cryosphere*, 9(4), pp. 1445–1463. doi: 10.5194/tc-9-1445-2015.

O'Connor, J., Smith, M. J. & James, M. R. (2017) 'Cameras and settings for aerial surveys in the geosciences: Optimising image data', *Progress in Physical Geography*, 41(3), pp. 325–344. doi: 10.1177/0309133317703092.

Pajares, G. (2015) ‘Overview and current status of remote sensing applications based on unmanned aerial vehicles (UAVs)’, *Photogrammetric Engineering and Remote Sensing*, 81(4), pp. 281–329. doi: 10.14358/PERS.81.4.281.

Pearce, S., Ljubicic, R., Peña-Haro, S., Perks, M., Tauro, F., Pizarro, A., Dal Sasso, S. F., Strelnikova, D., Grimaldi, S., Maddock, I., Paulus, G., Plavšic, J., Prodanovic, D. & Manfreda, S. (2020) ‘An evaluation of image velocimetry techniques under low flow conditions and high seeding densities using unmanned aerial systems’, *Remote Sensing*, 12(2), 232. doi: 10.3390/rs12020232.

Pelto, B. M., Menounos, B. & Marshall, S. J. (2019) ‘Multi-year evaluation of airborne geodetic surveys to estimate seasonal mass balance, Columbia and Rocky Mountains, Canada’, *Cryosphere*, 13(6), pp. 1709–1727. doi: 10.5194/tc-13-1709-2019.

Petrie, G. & Toth, C. (2018) ‘Introduction to laser ranging, profiling, and scanning’. In Shan, J., & Toth, C.K. (Eds.). (2009). Topographic Laser Ranging and Scanning: Principles and Processing (1st ed.). CRC Press. https://doi.org/10.1201/9781420051438

Pfeifer, N. & Briese, C. (2007) ‘Geometrical Aspects of Airborne Laser Scanning and Terrestrial Laser Scanning’, *International Archives of Photogrammetry & Remote Sensing*, 36(3/W52), pp. 311–319.

Prantl, H., Nicholson, L. & Sailer, R. (2017) ‘Glacier Snowline Determination from Terrestrial Laser Scanning Intensity Data’, *Geosciences*, 7(3), 60. doi: 10.3390/geosciences7030060.

Rippin, D. M., Pomfret, A. & King, N. (2015) ‘High resolution mapping of supra-glacial drainage pathways reveals link between micro-channel drainage density, surface roughness and surface reflectance’, *Earth Surface Processes and Landforms*, 40(10), pp. 1279–1290. doi: 10.1002/esp.3719.

Ryan, J. C., Hubbard, A. L., Box, J. E., Todd, J., Christoffersen, P., Carr, J. R., Holt, T. O. & Snooke, N. (2015) ‘UAV photogrammetry and structure from motion to assess calving dynamics at Store Glacier, a large outlet draining the Greenland ice sheet’, *Cryosphere*, 9(1), pp. 1–11. doi: 10.5194/tc-9-1-2015.

Sailer, R., Bollmann, E., Hoinkes, S., Rieg, L., Sproß, M. & Stötter, J. (2012) ‘Quantification of geomorphodynamics in glaciated and recently deglaciated terrain based on airborne laser scanning data’, *Geografiska Annaler, Series A: Physical Geography*, 94(1), pp. 17–32. doi: 10.1111/j.1468-0459.2012.00456.x.

Santagata, T., Vattano, M., Sauro, F., Spitaleri, G., Giudice, G., Bongiorno, C., Romeo, A. & Lazzaroni, M. (2017) ‘Inside The Glaciers Project: Laser Scanning Of The Grotta Del Gelo (Mount Etna, Italy)’, in *17th International Congress of Speleology*. Australian Speleological Federation Inc. Sydney, pp. 137–139.

Sisson, T. W., Robinson, J. E. & Swinney, D. D. (2011) ‘Whole-edifice ice volume change A.D. 1970 to 2007/2008 at mount rainier, washington, based on LiDAR surveying’, *Geology*, 39(7), pp. 639–642. doi: 10.1130/G31902.1.

Smith, M. J., Chandler, J. & Rose, J. (2009) ‘High spatial resolution data acquisition for the geosciences: Kite aerial photography’, *Earth Surface Processes and Landforms*, 34(1), pp. 155–161. doi: 10.1002/esp.1702.

Smith, M. W. (2015). Section 2.1.5: ‘Direct acquisition of elevation data: Terrestrial Laser Scanning’. In: Cook, S.J., Clarke, L.E. & Nield, J.M. (Eds.) Geomorphological Techniques (Online Edition). British Society for Geomorphology, London. ISSN: 2047-0371

Smith, M. W., Carrivick, J. L. & Quincey, D. J. (2015) 'Structure from motion photogrammetry in physical geography', *Progress in Physical Geography*, 40(2), pp. 247–275. doi: 10.1177/0309133315615805.

Smith, M. W., Carrivick, J. L. & Quincey, D. J. (2016) 'Structure from motion photogrammetry in physical geography', *Progress in Physical Geography*, 40(2), pp. 247–275. doi: 10.1177/0309133315615805.

Smith, M. W. & Vericat, D. (2015) 'From experimental plots to experimental landscapes: Topography, erosion and deposition in sub-humid badlands from Structure-from-Motion photogrammetry', *Earth Surface Processes and Landforms*, 40(12), pp. 1656–1671. doi: 10.1002/esp.3747.

Snavely, N., Seitz, S. M. & Szeliski, R. (2008) 'Modeling the world from Internet photo collections', *International Journal of Computer Vision*, 80(2), pp. 189–210. doi: 10.1007/s11263-007-0107-3.

Sutherland, J. L., Carrivick, J. L., Evans, D. J. A., Shulmeister, J. & Quincey, D. J. (2019) 'The Tekapo Glacier, New Zealand, during the Last Glacial Maximum: An active temperate glacier influenced by intermittent surge activity', *Geomorphology*, 343, pp. 183–210. doi: 10.1016/j.geomorph.2019.07.008.

Telling, J., Glennie, C., Fountain, A. G. & Finnegan, D. C. (2017a) 'Analyzing glacier surface motion using LiDAR data', *Remote Sensing*, 9(3), 283. doi: 10.3390/rs9030283.

Telling, J., Lyda, A., Hartzell, P. & Glennie, C. (2017b) 'Review of Earth science research using terrestrial laser scanning', *Earth-Science Reviews*, 169(April), pp. 35–68. doi: 10.1016/j.earscirev.2017.04.007.

Ullman, S. (1979) 'The interpretation of structure from motion.', *Proceedings of the Royal Society of London. Series B, Containing papers of a Biological character. Royal Society (Great Britain)*, 203(1153), pp. 405–426. doi: 10.1098/rspb.1979.0006.

Vericat, D., Brasington, J., Wheaton, J. & Cowie, M. (2009) 'Accuracy assessment of aerial photographs acquired using lighter-than-air blimps: LOW-cost tools for mapping river corridors', *River Research and Applications*, 25(8), pp. 985–1000. doi: 10.1002/rra.1198.

Vosselman, G. & Maas, H.G. (eds.) (2010) *Airborne and terrestrial laser scanning*. Whittles Publishing, Caithness

Warfield, A. D. & Leon, J. X. (2019) 'Estimating mangrove forest volume using terrestrial laser scanning and UAV-derived structure-from-motion', *Drones*, 3(2), pp. 1–17. doi: 10.3390/drones3020032.

Watson, C. S., Kargel, J. S., Shugar, D. H., Haritashya, U. K., Schiassi, E. & Furfaro, R. (2020) 'Mass Loss From Calving in Himalayan Proglacial Lakes', *Frontiers in Earth Science*, 7, 342. doi: 10.3389/feart.2019.00342.

Watson, C. S., Quincey, D. J., Smith, M. W., Carrivick, J. L., Rowan, A. V. & James, M. R. (2017) 'Quantifying ice cliff evolution with multi-temporal point clouds on the debris-covered Khumbu Glacier, Nepal', *Journal of Glaciology*, 63(241), pp. 823–837. doi: 10.1017/jog.2017.47.

Wehr, A. & Lohr, U. (1999) 'Airborne laser scanning-an introduction and overview', *ISPRS Journal of Photogrammetry & Remote Sensing*, 54, pp. 68–82. doi: https://doi.org/10.1016/S0924-2716(99)00011-8.

Westoby, M. J., Rounce, D. R., Shaw, T. E., Fyffe, C. L., Moore, P. L., Stewart, R. L. & Brock, B. W. (2020) 'Geomorphological evolution of a debris-covered glacier surface', *Earth Surface Processes and Landforms*. doi: 10.1002/esp.4973.

Wolstenholme, J. M., Smith, M. W., Baird, A. J. & Sim, T. G. (2020) 'A new approach for measuring surface hydrological connectivity', *Hydrological Processes*, 34(3), pp. 538–552. doi: 10.1002/hyp.13602.

Woodget, A. S., Austrums, R., Maddock, I. P. & Habit, E. (2017) 'Drones and digital photogrammetry: from classifications to continuums for monitoring river habitat and hydromorphology', *Wiley Interdisciplinary Reviews: Water*, 4(4), p. e1222. doi: 10.1002/wat2.1222.

Woodget, A. S., Carbonneau, P. E., Visser, F. & Maddock, I. P. (2015) 'Quantifying submerged fluvial topography using hyperspatial resolution UAS imagery and structure from motion photogrammetry', *Earth Surface Processes and Landforms*, 40(1), pp. 47–64. doi: 10.1002/esp.3613.

Part II: Results

Chapter 4 : Glacial Aerodynamic Roughness Estimates: Uncertainty, Sensitivity, and Precision in Field Measurements

Glacial Aerodynamic Roughness Estimates: Uncertainty, Sensitivity, and Precision in Field Measurements

Joshua R. Chambers[1], Mark W. Smith[1], Duncan J. Quincey[1], Jonathan L. Carrivick[1], Andrew N. Ross[2], and Mike R. James[3]

[1]School of Geography, University of Leeds, Leeds, UK,

[2]School of Earth and Environment, University of Leeds, Leeds, UK,

[3]Lancaster Environment Centre, Lancaster University, Lancaster, UK

Citation:

Chambers, J. R., Smith, M. W., Quincey, D. J., Carrivick, J. L., Ross, A. N. & James, M. R. (2019). Glacial aerodynamic roughness estimates: uncertainty, sensitivity, and precision in field measurements. *Journal of Geophysical Research: Earth Surface*, 125(2). DOI: 10.1029/2019JF005167.

Abstract

Calculation of the sensible and latent heat (turbulent) fluxes is required in order to close the surface energy budget of glaciers and model glacial melt. The aerodynamic roughness length, z_0, is a key parameter in the bulk approach to calculating sensible heat flux; yet, z_0 is commonly considered simply as a tuning parameter or generalized between surfaces and over time. Spatially and temporally distributed observations of z_0 over ice are rare. Both direct (from wind towers and sonic anemometers) and indirect (from microtopographic surveys) measurements of z_0 are subject to sensitivities and uncertainties that are often unstated or overlooked. In this study, we present a quantitative evaluation of aerodynamic profile-based and microtopographic methods and their effect on z_0 using data collected from Storglaciären and Sydöstra Kaskasatjäkkaglaciären, Tarfala Valley, Arctic Sweden. Aggressive data filters discard most of the wind tower data but still produce realistic z_0 values of 1.9 mm and 2 mm. Despite uncertainty introduced by scale and resolution dependence, microtopographic methods produced estimates of z_0 comparable to wind tower values and those found on similar surfaces. We conclude that (1) in the absence of direct turbulent flux measurements from sonic anemometers, the profile and microtopographic methods provide realistic z_0 values, (2) both 2D and 3D microtopographic methods are dependent on scale, resolution, and the chosen detrending method, and (3) careful calibration of these parameters could enable glacier-wide investigations of z_0 from remotely sensed data, including those increasingly available from satellite platforms.

4.1 Introduction

At local and regional scales, surface energy balance modelling is commonly used to calculate glacier melt and contribution to stream flow (Hock, 2005), wherein sensible and latent heat (turbulent) fluxes are usually secondary to the net radiative energy fluxes. The contribution of the turbulent fluxes is enhanced during conditions when radiative fluxes are reduced, e.g. in cloudy, windy conditions and in maritime climates (Anderson *et al.*, 2010; Giesen *et al.*, 2014), and have been recently implicated in widespread melt events on the Greenland Ice Sheet, for example, during which >98% of the ice surface experienced melt (Fausto *et al.*, 2016). As changes in cyclonic activity (Gorter *et al.*, 2014) and precipitation rates (Vavrus, 2013) are likely to increase the significance of the turbulent fluxes, it is imperative to ensure that they are calculated as accurately as possible so that current levels of melt can be quantified and future melt can be forecast confidently.

Three main methods for calculating turbulent fluxes over glacier surfaces exist: eddy correlation (EC), the profile method, and the bulk aerodynamic method (Fig. 4.1). EC uses sonic anemometers to record the three-dimensional (3D) movement of air in turbulent eddies (Burba, 2013) and, being the closest to a direct measurement of the turbulent fluxes, is often used as the benchmark for validating the two alternative theoretical model-based methods below (Munro, 1989; Greuell and Genthon, 2004). A number of aspects, including the cost of the sensors (typically > £10000) and their unsuitability for long observational periods in harsh arctic and alpine climates, make EC impractical for most glacial energy balance studies. The profile method estimates turbulent fluxes from near-surface interpolated profiles of wind speed, air temperature and specific humidity (Garratt, 1992). The bulk approach requires measurements of each from only one level, as are typically available from a standard meteorological station, assuming that the aerodynamic roughness length (z_0) and surface temperature are known. This study focuses on the parameterisation of z_0 for the bulk approach (Fig. 4.1; orange boxes), as the comparatively low requirement for data collection makes it a popular choice in energy balance studies (e.g. Favier *et al.*, 2004; Arnold *et al.*, 2006; Brock *et al.*, 2010; Bravo *et al.*, 2017; Litt *et al.*, 2017; Radić *et al.*, 2017).

The aerodynamic roughness length, z_0, is the height above a surface where wind speed becomes zero, controlled by the geometry of the surface (Stull, 1988). z_0 is difficult to measure directly (usually in the order of mm over glaciers) and several different ways of obtaining a value exist; many glacial energy balance studies following the bulk approach use values from elsewhere in the literature, or use z_0 as a parameter to tune models to fit

observed melt (e.g. Inoue and Yoshida, 1980; Braun and Hock, 2004; Arnold *et al.*, 2006; Fausto *et al.*, 2016; Bravo *et al.*, 2017). Often, z_0 is erroneously assumed to be spatially and temporally uniform, in contradiction of observations (c.f. Brock *et al.*, 2006).

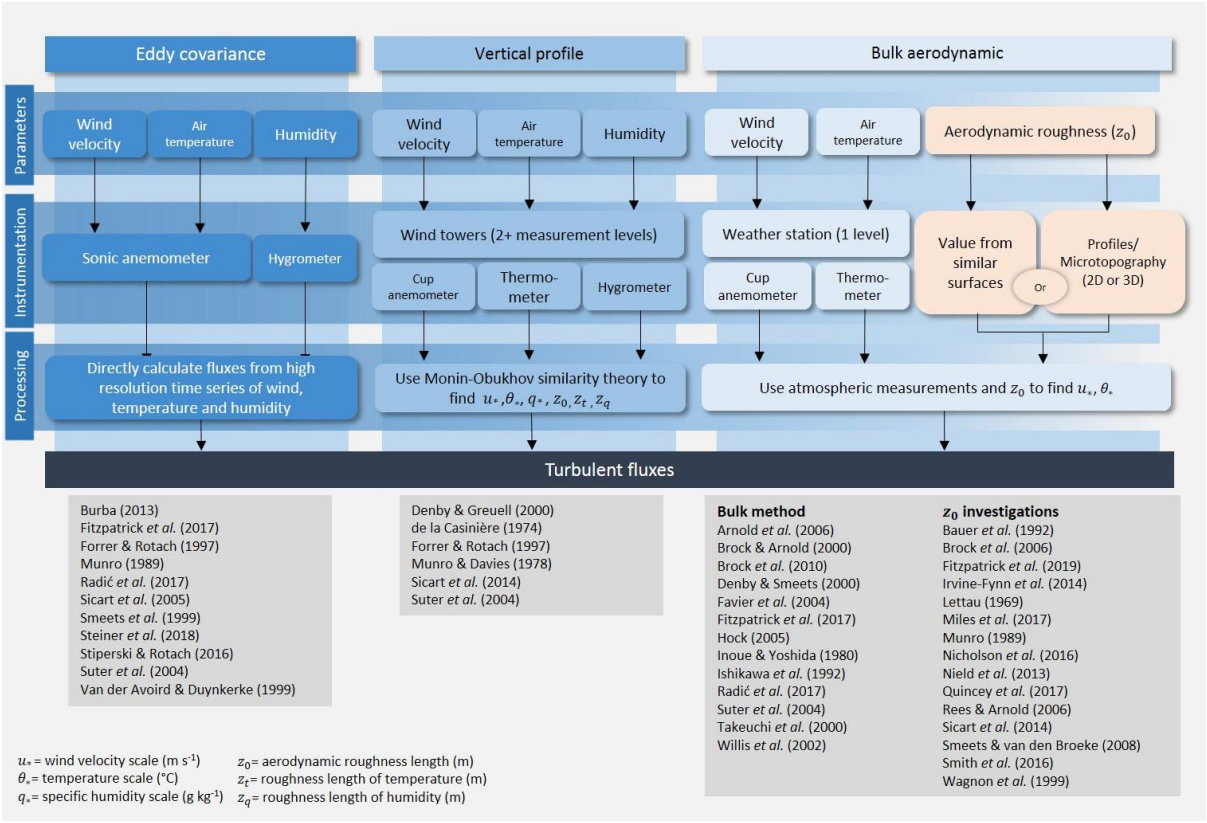

Fig. 4.1 Summary of techniques used to calculate turbulent fluxes. This research is concerned primarily with the right-hand portion of the figure (orange), where different methods can be used to obtain a value of z_0 for the bulk aerodynamic approach.

Aerodynamic profiles are traditionally used to find z_0 (Hock and Holmgren, 1996; Brock *et al.*, 2006; Sicart *et al.*, 2014; Quincey *et al.*, 2017) however, they are subject to large uncertainties and sensitivities, and provide point data. Microtopographic transects are commonly used to circumvent the need for wind towers, enabling more rapid, spatially distributed z_0 estimates (Munro, 1989; Brock *et al.*, 2006; Irvine-Fynn *et al.*, 2014; Smith *et al.*, 2016b; Miles *et al.*, 2017). However, the calculation of z_0 from microtopographic transects is subject to a number of assumptions surrounding the spacing and dimension of roughness elements, shading and sheltering and the effects of wind direction (Smith *et al.*, 2016b) which are unrealistic, but largely ignored in the absence of a more robust approach.

Recently, fine-resolution survey techniques such as Structure from Motion (SfM)

photogrammetry and terrestrial laser scanning (TLS) have been explored for their ability to enhance glacier surface microtopographic data collection. These methods have been used to collect transects rapidly and at fine resolution (Miles *et al.*, 2017), and to devise 3D geometric approaches to finding z_0 that relax the previously mentioned assumptions (see Section 4.2), including initial steps towards glacier-wide z_0 maps (Smith *et al.*, 2016b) and calculating z_0 from remotely sensed data products (Fitzpatrick *et al.*, 2019). Potential for cryosphere-wide z_0 measurements increases in line with the expansion of available fine-resolution data sources (e.g. ArcticDEM, global DEM, NASA High Mountain Asia DEM).

As a first step, we seek here to explore the existing methods for finding z_0 from wind profiles and microtopography, and to understand their sensitivities and uncertainties. The aim of this paper is to test existing methods as a foundation for the development of new methods in future work. We present a brief review of the methods that are currently available, highlighting factors that can alter z_0 unrelated to variability in the physical properties being measured. These critical uncertainties are summarized at the end of Sections 4.2.1 and 4.2.2. Then, using new data collected from two glaciers, Storglaciären and Sydöstra Kaskasatjäkkaglaciären in Arctic Sweden (Section 4.3), we present quantitative analysis of the uncertainties in Sections 4.4.1 and 4.4.2

4.2 Previous Work

4.2.1 Aerodynamic Profile z_0

In the field, the aerodynamic profile method (based on Monin-Obukhov (MO) similarity theory (Foken, 2006)) can be used to capture site specific z_0 values for use with the bulk approach. For simplicity we shorten this to the 'profile method', and use 'profile z_0' to refer to z_0 obtained in this manner. The profile method is only valid for near neutral conditions, and is used to extrapolate z_0 from linear least-squares fits of wind speed, profiles of which are assumed to be log-linear above a surface (Garratt, 1992). Wind velocity (U, m s^{-1}) at height z (m) is given by

$$U(z) = \frac{u_*}{\kappa}\left(\ln\frac{z}{z_0} + \alpha_m\frac{z}{L}\right), \tag{4.1}$$

where u^* is the wind velocity scale (m s^{-1}), k is the von Karman constant (κ = 0.4). $\alpha_m\frac{z}{L}$ is a stability function within which α_m is an empirically derived coefficient (α_m= 5) (Dyer and Hicks, 1970; Stull, 1988) and L is the Obukhov length (the height at which buoyant production of turbulent kinetic energy equals shear production (Foken, 2006)). This correction can be used to extend the validity of the method to weak-to-moderate stabilities. L can be

calculated directly from sonic anemometer measurements, or inferred by iteratively fitting wind speed and temperature profiles (e.g. Quincey *et al.*, 2017). Briefly, the method involves making an initial guess at *L* (in this case 108 m, implying effectively neutral conditions). From this, log-linear profiles can be fitted to the wind and temperature data. This gives values for z_0, u^* and T* (temperature scale, °C), from which a new (more accurate) value of *L* can be calculated. This process is repeated until the values of *L* converge or until some limit is reached, in which case it is assumed that the profiles do not fit the theory and so the profiles are not used to calculate z_0. Wind speed and temperature profiles obtained from mast-mounted cup anemometers and shielded/vented thermometers facing perpendicular to the prevailing wind are commonly used in this approach (e.g. Smeets *et al.*, 1998, 1999; Brock *et al.*, 2006; Pelletier and Field, 2016).

MO similarity theory has underpinned turbulent flux calculations in studies of the surface-atmosphere boundary layer since its conception in 1954 (Monin and Obukhov, 1954; Stull, 1988; Foken, 2008). However, the theory does not necessarily hold over glacial surfaces (Denby and Greuell, 2000; Litt *et al.*, 2014; Radić *et al.*, 2017). Low surface temperatures on glaciers cool the air near the surface, inducing density driven katabatic (glacier) winds (Denby and Greuell, 2000; Denby and Smeets, 2000) and creating strongly stable conditions with a wind speed maximum within the first few metres above the surface. These conditions therefore violate a number of key assumptions made by MO similarity theory: that there is atmospheric stationarity, low advection and a constant flux layer. This makes MO similarity theory only representative of a very thin layer above the ice surface, thus turbulent flux measurements made above the surface are disconnected from their surface values (Denby and Greuell, 2000). Nonetheless, MO similarity theory is often applied in glacier studies because of a lack of alternative (Denby, 1999; Stiperski and Rotach, 2016; Radić *et al.*, 2017).

Where the profile method is used for estimating z_0, measured wind velocity and air temperature profiles are compared with ideal log-linear profiles, and those with a coefficient of determination which is too low (e.g. $r^2 < 0.98$) are discarded. Additional filters can reject: i) data with wind speeds less than cup anemometer stall speeds; ii) non-stationary conditions; and iii) data from specific wind directions (Andreas *et al.*, 2010). These filters drastically reduce the amount of data by up to 98% (Miles *et al.*, 2017); that reduction is a reflection of how rarely the assumptions of the profile method are met.

MO breaks down in very stable or unstable conditions. In moderately stable/unstable conditions, MO similarity theory introduces an empirical stability correction to the wind (and temperature) profiles, which depends on the ratio of the height above the ground, z, to the

Obukhov length, L. The stability correction has been shown to be valid for $-5<z/L<1$ (Garratt, 1992). L can be determined iteratively as described earlier. As a result, a z_0 value is obtained for each time-step, which can then be averaged or used to examine the temporal change in z_0. Data are typically averaged over periods of up to 30 minutes to ensure an appropriate number of turbulent eddies are samples, which can mask more subtle temporal dynamics in z_0 – a restriction which is lifted with microtopographic approaches.

Regardless of the slope of the glacier surface, taking measurements over a melting ice surface is problematic (Smeets *et al.*, 1999). Profile z_0 is very sensitive to instrument height (Foken, 2008), with an offset of +0.1 m supposedly altering z_0 by an order of magnitude and doubling the estimated sensible heat flux (Munro, 1989). In micrometeorological studies, a height correction is sometimes applied to compensate for the breakdown of a log-linear wind profile due to the influence of the forest canopy (Foken, 2008). This correction is based on the difference between 'actual' ground level and the height at which extrapolated wind speed drops to zero, which is usually somewhere near the top of the canopy. This principle has been adopted in glaciology to compensate for surface slope and variable topography, which can lead to the mean surface being beneath the apparent local surface of the glacier when considering the whole surface of the glacier (Munro, 1989; Sicart *et al.*, 2005), but defining a zero reference plane on a degrading or non-planar surface is challenging. Various workarounds have been suggested to mitigate the impact of an uneven, melting surface (e.g. Brock *et al.*, 2006; Sicart *et al.*, 2014; Fitzpatrick *et al.*, 2017; Quincey *et al.*, 2017), yet the most effective method remains unclear.

MO similarity theory assumes a homogeneous fetch (upwind area) is present (i.e. with consistent aerodynamic properties), but this is rarely found on glaciers (Brock *et al.*, 2006; Miles *et al.*, 2017; Quincey *et al.*, 2017). Moreover, it is unclear over what distance the fetch should be homogeneous, and several measurement height-fetch length ratios are proposed, including 1:100 (Wieringa, 1993) and 1:200 (Bradley, 1968). Recent EC work shows that 80% of flux contribution comes from within 150-200 m upwind of the measurement point when instruments are 2 m above the surface (Fitzpatrick *et al.*, 2019) – this suggests that a ratio of c.1:100 will incorporate the aerodynamically important fetch.

The sensitivities for profile z_0 discussed in this section are summarized in Table 4.1. In subsequent sections we present the analysis of those we found to have the most severe effects on z_0.

Table 4.1 Sensitivities and uncertainties in finding glacier z_0 from aerodynamic profiles

Sensitivity	Description	Stage	Reference	Section	Severity*
Instrument height/reference level	Accounts for surface slope/topographic undulations. Can be dynamic as glacier surfaces evolve and equipment melts into the ice. Important for identifying shallow katabatic conditions.	Field/processing	Munro (1989) Garratt (1992) Foken (2008) Sicart *et al.* (2014)	**4.4.1** **Fig. 4.3c**	**High**
Stability correction	Used in near-neutral conditions commonly found over glaciers. Based on Monin-Obukhov similarity theory. Not applicable in strongly or weakly stable conditions. Reduces number of profiles which can be fitted and number of results, but important over ice where temperature gradients are strong.	Processing	Foken (2008) Radić *et al.* (2017) Fitzpatrick *et al.* (2019)	**4.4.1** **Fig. 4.3a and b**	**High**
Data filters (wind speed, stationarity, profile fitting)	Thresholds used to filter out data close to anemometer stall speed, non-stationarity and non-convergence of wind speed/temperature profiles. Can lead to majority of data being discarded.	Processing	Miles *et al.* (2017) Quincey *et al.* (2017) Radić *et al.* (2017)	**4.4.1** **Fig. 4.3d**	**Medium**
Time averaging	Period over which meteorological data are averaged. Can be applied before or after profile fitting, severely reduce the quantity of profiles and mask temporal trends.	Processing	Anderson *et al.* (2010) Cullen *et al.* (2007) Fitzpatrick *et al.* (2017)	**4.4.1** **Table. 4.3**	**Medium**
Fetch/footprint	Wind speed at increasing measurement levels affected by obstacles at increasing distance from instruments. Homogeneous fetch desirable. Height/fetch ratio recommendations vary.	Field	Garratt (1992) Wieringa (1993) Foken (2008) Fitzpatrick *et al.* (2019)		**Medium**
Regression	In addition to filtering out weaker profile fits, stricter r^2 values can decrease the statistical error introduced by assigning variables incorrectly, i.e. measurement height as the dependent variable, and wind speed as the dependent variable.	Processing	Bauer *et al.* (1992)		**Medium**
Surface slope	Partly causes katabatic winds. On steeper slopes it is difficult to identify vertical/horizontal movement of air using cup anemometers.	Field/processing	Denby and Greuell (2000) Denby and Smeets (2000) Radić *et al.* (2017)		**Low**

*****as suggested by the effect of each sensitivity on z_0 in this study

4.2.2 Microtopographic z_0

Aerodynamic roughness is a function of surface roughness, particularly in fully turbulent flow conditions (Elliott, 1958; Bandyopadhyay, 1987; Smith, 2014). Therefore, surface roughness metrics can be used to assess aerodynamic roughness. Their much simpler field data requirements make them a viable alternative that can better characterise the observed spatial and temporal variability in z_0 (Munro, 1989; MacKinnon *et al.*, 2004). Variations of the microtopographic method have been developed over a range of surfaces, based on empirical measurements of physical properties including grain size (Bagnold, 1941), average obstacle height (Sellers, 1965), plan area of roughness elements (Fryrear, 1965; Counihan, 1971) and surface roughness wavelength (Banke and Smith, 1973; Baechlin *et al.*, 1992). A study by Nield *et al.* (2013) showed that those including some height index exhibited the best relationship with aerodynamic roughness, yet all of the current, empirical approaches lack a grounding in physical theory. The most widely used approach within glacial studies is based on the work of Lettau (1969), who showed that

$$z_0 = 0.5h^* \left(\frac{s}{S_A}\right) \tag{4.2}$$

where h^* is the effective (average) obstacle height (m), s is the silhouette (exposed frontal area) of an average roughness element (m^2), S_A is area in the horizontal plane of the site of interest (m^2) and 0.5 represents an average drag coefficient (Kutzbach, 1961; Lettau, 1969). Microtopographic z_0 values derived from (4.2) appear to agree with wind profile-derived z_0 to within +/- 25% (Lettau, 1969). The relation was based on empirical experiments wherein increasing/decreasing roughness was simulated by the systematic emplacement/removal of bushel baskets upwind of an anemometer mast erected on an ice lake (Kutzbach, 1961).

Parameters in (4.2) are obtained easily in such a controlled environment, but not over glaciers where individual roughness elements are not distinct. Munro (1989) devised an influential interpretation of (4.2) based on simplified horizontal microtopographic transects perpendicular to the prevailing wind direction, and populated by modelled roughness elements of equal spacing and dimension. Terms in (4.2) were re-defined in order to find z_0 for a transect of length X (m), where h^* (m) is given by twice the standard deviation ($2\sigma_d$) of elevations after the mean elevation has been set to zero. Thereafter

$$s = \frac{2\sigma_d X}{2f}, \tag{4.3}$$

where f is the number of groups of positive elevation values, and

$$S_A = \left(\frac{X}{f}\right)^2. \tag{4.4}$$

Thus,

$$z_0 = \frac{f}{X}(\sigma_d)^2. \quad (4.5)$$

Whether collected manually, using photogrammetry-based edge detection algorithms (Rees, 1998; Rees and Arnold, 2006; Fassnacht *et al.*, 2009) or extracted from 3D digital surface models (Irvine-Fynn *et al.*, 2014; Miles *et al.*, 2017), the transect method can be used to show variation in aerodynamic roughness across a glacier and throughout the melt season (Brock *et al.*, 2006), challenging the assumption made in most energy balance studies that z_0 is spatially and temporally homogeneous (e.g. Braun and Hock, 2004; Bravo *et al.*, 2017). The simplification of microtopography in (4.5) imposes several assumptions about the surface (Smith *et al.*, 2016b): (i) that all roughness elements are equally spaced and have equal dimensions; (ii) that the silhouette of roughness features is the same under different wind directions; and (iii) that no shading of downwind elements is caused by those upwind.

Assumption (ii) becomes problematic when considering a wind-perpendicular transect, as glacial surfaces often host anisotropic roughness features (e.g. sastrugi, crevasses, supraglacial channels) that can be oriented parallel to the prevailing wind. Smith *et al.* (2016a) point out that in such cases exposed frontal area (and thus impact on flow) would appear much larger in a perpendicular transect than is realistic, resulting in erroneously high z_0. Additionally, streamlined features exhibit a small drag coefficient (Wieringa, 1993; Macdonald *et al.*, 1998), raising questions about whether Lettau's (1969) average of 0.5 is an overestimate for bare ice (Smith *et al.*, 2016b) or an underestimate for debris-covered ice (Quincey *et al.*, 2017). Lettau adopted the 0.5 value after the drag coefficient (C_d) of upturned >4 m^3 bushel baskets was given as 0.45 in experiments by Kutzbach (1961), who followed Schlichting's (1937) expression which is valid for regular arrays of geometrically similar roughness elements (Wooding *et al.*, 1973). This likely represents a simplification of the actual drag characteristics of glacier surfaces, where distinct, uniform roughness elements are rare.

A 2D wind-perpendicular transect also fails to consider the shading and sheltering of adjacent roughness elements which may be up- or down-wind of the transect (assumption (iii), Fitzpatrick *et al.*, 2019). Sheltering effects are characterized by the ratio between the exposed frontal area and ground area, or roughness density (Wooding *et al.*, 1973; Raupach, 1992). Equation (4.2) holds where the roughness density is $\lesssim$0.3, but at higher densities the wakes caused by roughness elements interfere with each other, reducing z_0 as air flow starts to skim over the top of elements rather than between and around them (Macdonald *et al.*,

1998; Smith, 2014). Alternatives to (4.2) and (4.5) account for obstacle density (Rounce *et al.*, 2015) and drag coefficient (Macdonald *et al.*, 1998), but so far lack robust testing and independent validation.

3D methods have been proposed to address the shortcomings of the transect method, coincident with the proliferation of high-resolution survey techniques such as Structure from Motion photogrammetry (SfM) (Carrivick *et al.*, 2016; Smith *et al.*, 2016a) and terrestrial laser scanning (TLS) (Smith *et al.*, 2011; Fey and Wichmann, 2017).These methods allow rapid data acquisition over much larger areas and shorter timescales than is feasible with more traditional manual surveys. Recent studies have used digital elevation models (DEMs) constructed from SfM (Irvine-Fynn *et al.*, 2014; Rounce *et al.*, 2015; Miles *et al.*, 2017) or TLS (Nield *et al.*, 2013) data, from which transects can be extracted as the grid rows and columns. Smith *et al.* (2016a) obtained terms for (4.2) from both DEMs and filtered point clouds, allowing the previous assumptions to be relaxed by accounting for the total exposed frontal area and giving a value for each cardinal wind direction.

The increasingly widespread use of SfM mandates that an assessment of the inherent uncertainties and how they relate to z_0 is carried out. Georeferencing provides an important control on the shape of the modelled surface and correctly recording the location and accuracy of ground control points (GCPs) is key. Interrogation of the bundle adjustment processing step (which minimises the overall residual error by tuning camera orientations and parameters, slightly adjusting 3D point coordinates) is made possible using a precision estimation workflow (James *et al.*, 2017a), which allows the effects of SfM precision on z_0 estimates to be quantified.

Whether 2D or 3D methods are employed, the inclusion of an average height index imposes a spatial boundary (Smith, 2014), and as such the resulting z_0 value is dependent on the length of transect or the area of the plot (Rees and Arnold, 2006; Smith *et al.*, 2016b; Quincey *et al.*, 2017; Fitzpatrick *et al.*, 2019). Further dependence is placed on the resolution of the data, with coarser resolution data effectively representing a filtered fine-resolution dataset (Quincey *et al.*, 2017); for a given transect length, a surface which is sampled every 10 cm will appear smoother than one that is sampled every millimetre, artificially reducing z_0.

The scale and resolution of the data (and thus to some extent z_0) is informed somewhat qualitatively by the allocation of an upper and lower topographic partition scale for the surface in question, larger than which is deemed overall topography and smaller than which is indistinguishable from measurement noise (Smith, 2014). That is, the chosen scale of the

study will dictate the survey technique used, which in turn can decide the resolution and impact the estimated z_0. The required scales of topography can be isolated for analysis by detrending, and transects are often detrended linearly, where the mean elevation is set to zero (Munro, 1989). With 3D data, the same effect is achieved by subtracting the fitted plane (Smith *et al.*, 2016b). This is a robust approach with smaller transects/plots; however, linear (and planar) detrending is susceptible to scale dependence (Miles *et al.*, 2017). For larger plots/transects or more complex topography, other detrending methods may be more appropriate to remove overall trends, such as coarse-DEM removal, median filtering or splines (Miles *et al.*, 2017; Quincey *et al.*, 2017). These methods necessitate careful evaluation of the topographic partition scales, as slight adjustment of the scale over which detrending is applied can give quite different roughness values (Grohmann *et al.*, 2011).

As with profile z_0 (Table 4.1), in Table 4.2 we summarise microtopographic sensitivities. A severity rating is assigned based on our analysis. Those to which z_0 is most sensitive are presented in Section 4.4.2 and others in the Supporting Information.

4.3 Location, data and methods

4.3.1 Location

Data were collected between 8th and 19th July 2017, from two glaciers in the Tarfala Valley, Sweden (Fig. 4.2). The valley, located at 67°55'N and 18°35'E, has a Sub-Arctic climate with a mean annual temperature of around -3.3°C and an average of ~1000 mm of precipitation per year (Carrivick *et al.*, 2015). The frequent precipitation, winds and cloud cover (Hock *et al.*, 1999) produce turbulent fluxes which often contribute up to 50% of local glacier surface energy balances (Carrivick and Hock, 1998). The study glaciers, Storglaciären (Stor) and Sydöstra Kaskasatjäkkaglaciären (SK), are oriented (and flow) West-East and North-South respectively. Sites were visited on alternating days with the exception of day 7 (14th July), when poor weather precluded fieldwork. At SK in particular, the surface changed throughout the study from snow-covered, through slush to bare ice.

4.3.2 Aerodynamic profile z_0 measurements

Two wind towers were erected, one at Stor and the other at SK, with instruments at five levels (Stor: 0.35, 0.72, 1.27, 1.85 and 2.39 m, SK: 0.35, 0.69, 1.30, 1.80 and 2.43 m). On each tower, wind speed was recorded using five NRG #40 cup anemometers, wind direction with one NRG 200P wind vane and air temperature with five shielded and passively-ventilated

TinyTag TGP-4017 sensors, each averaged at one-minute intervals for a total of 10 days at SK and 4 days at Stor. Instrument heights were re-measured at each repeat visit. Data were recorded on Campbell CR1000s with a 12 V battery stored at the base of each tower, and are presented in full in Fig. A.1. Raw one-minute interval data of each variable were averaged over periods of 10 and 15 minutes for processing.

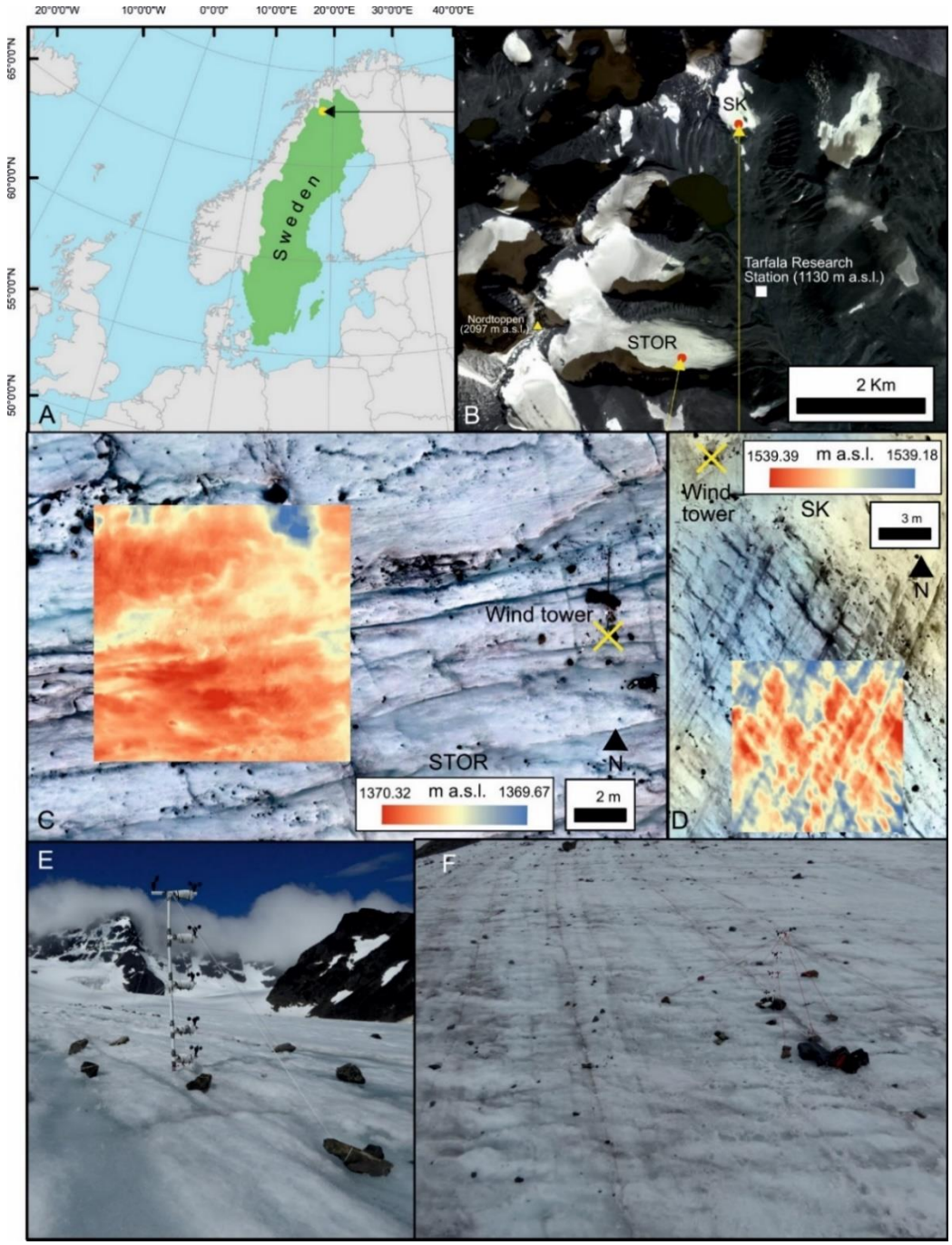

Fig. 4.2 Location of study in Tarfala Valley, Sweden (A). Satellite imagery (B) courtesy of Planet Labs (Planet Team, 2018). Lowermost images show location of wind towers on Stor (C) and SK (D), orthophotos were generated from SfM data for each site. Elevation overlays show the 10x10 m DEMs used as the base case for analysis of each site. (E) and (F) show the site around the wind towers at Stor (E) and SK (F). Both are looking roughly up-glacier.

Table 4.2 Sensitivities and uncertainties in using microtopographic methods to find glacier z_0

Sensitivity	Description	Stage	Reference	Section	Severity*
Detrending	Appropriate detrending method depends on the scale of study – linear/planar is fine for smaller scales, but not for larger plots.	Processing	Quincey *et al.* (2017)	4.4.2 Table 4.5	**High**
Scale dependence	Longer transects/larger plots cause z_0 to increase.	Field/processing	Miles *et al.* (2017) Quincey *et al.* (2017) Rees & Arnold (2006)	4.4.2 Fig. 4.6a and b	**High**
Resolution dependence	Coarser resolution data causes z_0 to decrease.	Field/processing	Miles *et al.* (2017) Quincey *et al.* (2017) Rees & Arnold (2006)	4.4.2 Fig. 4.6c and d	**High**
Drag coefficient	0.5 is used as the "average". Depends on scale and density of roughness elements, surface anisotropy and wind direction, usually two orders of magnitude smaller for ice surfaces.	Field/processing	Munro (1975) Munro (1989) Quincey *et al.* (2017)		**Medium**
Assumptions of Munro (1989) equation	Simplification of Lettau (1969) equation used with transects assumes uniform spacing/height of roughness elements, no sheltering effects, and that z_0 is not reliant on wind direction.	Processing	Smith *et al.* (2016)		**Medium**
Disruption of surface	Field methods can alter the natural glacier surface, e.g. laying down a pole for a transect, placing GCPs for SfM surveys or walking with crampons.	Field	Brock *et al.* (2006)		**Low**
SfM/TLS uncertainties	Field uncertainties can be mitigated with robust survey design. Also worth considering doming effect, bundle adjustment and ground control.	Field/processing	James *et al.* (2017a)	4.4.2 Fig. A.7	**Low**

***as suggested by the effect of each sensitivity on z_0 in this study

The resulting profiles were used along with equation (4.1) to calculate z_0 for each 10 or 15 minute time step. In so doing, wind speed is regressed against log(z), and the extrapolated model is used to find z_0. The filters listed below were then applied, either retaining or rejecting those profiles where: (a) the extrapolated model deviated more than an acceptable amount away from a log-linear profile, (b) changes in temperature over time indicate conditions were not stationary, and (c) wind speeds were too low to be reliably recorded by our instruments. Profiles of wind speed and temperature were filtered in 3 stages:

1. relaxed filters: rejected poor log-linear profile fits (r^2<0.95) and low wind speeds (<1 m s^{-1}) whilst assuming stability is valid for MO theory;
2. standard filters (as used by Quincey *et al.*, 2017) again assume valid MO stability, applying a stricter r^2 filter (rejecting r^2<0.99), a minimum wind speed filter (<1 m s^{-1}) and a stationarity filter (which identifies when mean air temperature changed by >0.25 °C min^{-1});
3. finally, a stability correction based on MO similarity theory was applied as a third step, in addition to the standard filters. We found L using an iterative approach, in which any profiles which required more than 10 iterations to converge with MO theory (and were thus unlikely to converge at all) were discarded.

An estimate of the error attached to each z_0 value was obtained by first isolating the raw one-minute interval data that had contributed to successful profile fits when averaged over a 10 or 15 minute period. Each one minute profile was then used to find z_0. The mean z_0 of the one minute profiles from each 10 or 15 minute period was then compared to the z_0 value given by the original averaged profile, and the standard deviation was used as an estimate of error, as it represents the higher and lower bounds of possible z_0 values for each time period.

Each of the data filters were varied systematically, testing whether they should be made stricter or could be relaxed. Previous studies have shown that introducing additional filters greatly reduces the number of profiles obtained (Radić *et al.*, 2017), whereas we altered the filter thresholds themselves using a Monte Carlo approach, generating n = 1000 different threshold values for each filter. Next, we tested the effect of adding several height corrections to each measured instrument height, replicating previous efforts to compensate for glacier slope and topographic undulations (Munro, 1989; Sicart *et al.*, 2014).

4.3.3 Microtopographic z_0 estimates

On each visit and when weather conditions allowed, photogrammetric surveys of each site were carried out using both a Phantom 3 UAV with gimbal-stabilized digital camera, and a Panasonic DMC-TZ60 compact digital camera mounted on an 8 m inspection pole and operated remotely via a wireless connection (see Table A.1 for further details). Sites were surveyed on alternate days, giving a total of five survey days for each, from which one for each site was selected used to produce a digital elevation model (Table A.2 to A.4) to compare with aerodynamic profile data collected during conditions favourable for MO similarity theory.

SfM data processing was carried out using Agisoft PhotoScan Professional Edition (version 1.4.0), following the procedure outlined by James *et al.* (2017b) with further point cloud processing in CloudCompare 2.10 (CloudCompare, 2018). Following recommendations in James *et al.* (2019), camera/image specifications and processing settings are included in Section A.1, and Tables A.1 and A.2. SfM precision analysis was carried out using the Monte Carlo approach of James *et al.* (2017a), in which repeated bundle adjustments are carried out with pseudo-random offsets applied to image observations. SfM and raster method precision were estimated from the Monte Carlo output using a bespoke Matlab tool called sfm_georef (James and Robson, 2012). The routine was adapted to generate a dense point cloud and interpolate a digital elevation model (DEM) for each iteration (n = 1000), from which an estimate of microtopographic z_0 error was obtained (see Section A.1 and Fig. A.7).

Microtopographic z_0 was calculated using the commonly applied Munro (1989) transect method (treating each row/column of a DEM as a separate transect), and the DEM method used by Smith *et al.* (2016b) and Quincey *et al.* (2017), with the difference that h^* was calculated from twice the standard deviation of elevations above the detrended plane rather than the mean elevation. As noted by Smith *et al.* (2016b) the choice of statistic is somewhat arbitrary; twice the standard deviation above the detrended plane was chosen as it provided the closest approximation of average roughness height as used by Lettau (1969).

Sensitivity tests depend on the perturbation of one property while all others stay constant. The standard elevation datasets were 10x10 m in extent, had a resolution of 0.005 m pixel^{-1}, and were detrended using 2D linear/3D planar detrending depending on the z_0 method in question. Initial comparisons were made between the aerodynamic profile and microtopographic methods using the standard datasets. We then looked first at the dependence of z_0 on scale (c.f. Rees and Arnold, 2006; Quincey *et al.*, 2017), varying the size

of the plot/length of transect incrementally from 1 m to the maximum that would allow the plot to remain a square; 39 m in the case of Stor and 29 m for SK. To investigate the influence of DEM resolution, we gradually degraded the grid/transect resolution from 0.005 to 0.5 m per pixel. As a final step, the standard datasets were detrended using coarse-DEM removal, with moving mean window sizes varying from 0.5 to 5 m.

4.4 Results

4.4.1 Profile z_0

The number of fitted profiles giving z_0 values acceptable to MO theory was reduced by more than 97% in all cases of filtered data (Table 4.3). Most data were discarded by the r^2 filter, as few profiles adhered to the log-linear profile required for MO theory (see Fig. A.2 for examples). Using stricter filters was found to decrease z_0 in all cases but one, where the standard filters were applied to the 10 minute averaged data on Stor, giving a higher mean z_0 (8.07 mm) than the relaxed filters (6.11 mm). Introducing the MO stability correction left even fewer profiles, but these were more in line with previously published z_0 from the same location (Hock and Holmgren, 1996). The same pattern is seen in the standard deviation of z_0, where in all cases but one the value is reduced by stricter filters, partly due to the exclusion of those profiles that do not meet the conditions of MO theory, and partly due to the smaller number of profiles included.

The reduction in data by both filtering and averaging is illustrated by Fig. 4.3, which shows z_0 plot against time. There was no obvious systematic change in z_0 over time, despite the gradual change in surface cover at SK (upglacier from the wind tower) from snow to bare ice. The error bars on each z_0 value, which come from the standard deviation of z_0 in each group of ten un-averaged minute-interval profiles, are smaller for the tightly grouped lower values of z_0 than they are for the higher values, which are much more scattered. To discount other possible influences on the distribution of z_0, we tested the effects of wind direction and atmospheric stability, finding that the impact of both was small (see Sections A.2 and A.3, Fig. A.3 and A.4).

Table 4.3 Summary of effects of original and alternative filters on number of profiles and z_0 value. The original number of unfiltered profiles for each site was 10130 at SK and 5682 at Stor. Standard deviation of z_0 is given along with mean z_0 values for each level of filtering and each averaging period. No standard deviation is given for stability corrected z_0 on Stor as only one value for z_0 was produced.

	SK						**Stor**					
	Number of profiles		**% of original**		**z_0 (mm)**		**Number of profiles**		**% of original**		**z_0 (mm)**	
Averaging period	**10**	**15**	**10**	**15**	**10**	**15**	**10**	**15**	**10**	**15**	**10**	**15**
Relaxed filters	306	204	3%	2%	8.9 (±13.5)	9.4 (±14.3)	168	118	2.9%	2.1%	6.3 (±7.6)	6.3 (±6.7)
Standard filters	70	45	0.7%	0.44%	6.8 (±9.9)	5.5 (±9.3)	7	3	1.2%	0.05%	20.9 (±22)	6.7 (±3.3)
Stability corrected	6	4	0.06%	0.04%	2.0 (±0.63)	1.7 (±0.3)	1	1	0.02%	0.02%	2.4 (±0)	2.5 (±0)

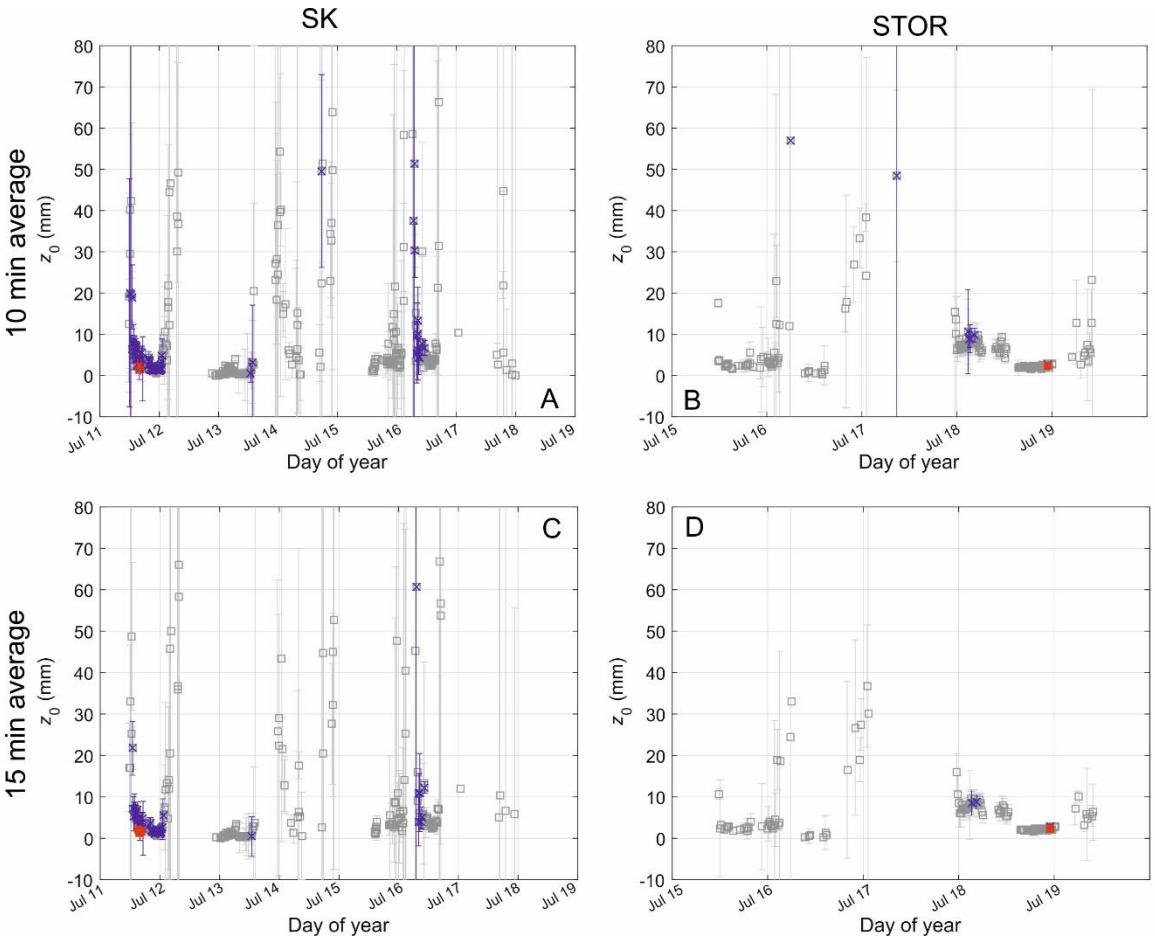

Fig. 4.3 Results of analysis of profile z_0 over time. Data from SK is shown in the left column, and Stor in the right. Results from input data which has been averaged over 10 minutes is shown in the top row, over 15 minutes in the bottom row. Data filtered using a relaxed filter are shown in grey, blue data points have been filtered with standard filters and red points show those to which the MO stability correction has been applied. Error bars are calculated from the standard deviation of z_0 from profiles of each minute that comprises each averaged block of data (i.e. ten profiles where data are averaged over ten minutes). Some error bars extend beyond the axis range used here.

To test the sensitivity of z_0 to filter thresholds, we first varied the r^2 filter between 0.9 and 1 (Fig. 4.4a and b), finding that relaxing the filter slightly (e.g. r^2 = 0.95) increased the number of profiles included by an order of magnitude at both glaciers and for both average time periods, also increasing z_0 (10 min: SK = 8.7 mm, Stor = 6.2 mm, 15 min: SK = 9.3 mm, Stor = 6.2 mm). Varying the maximum allowable change in temperature between 0 and 1°C min^{-1} made little difference to z_0, with changes of <5 mm at both sites (Fig. A.5a & A.5c), indicating that atmospheric conditions were largely stationary throughout the data collection period. Finally, allowing profiles with wind speeds slower than 1 m s^{-1} increased z_0 in both cases (Fig. A.5b & A.5d), but risked including data below the cup anemometer stall speed (0.7 m s^{-1}). Raising the minimum wind speed reduced the number of profiles and slightly reduced z_0 (by <5 mm).

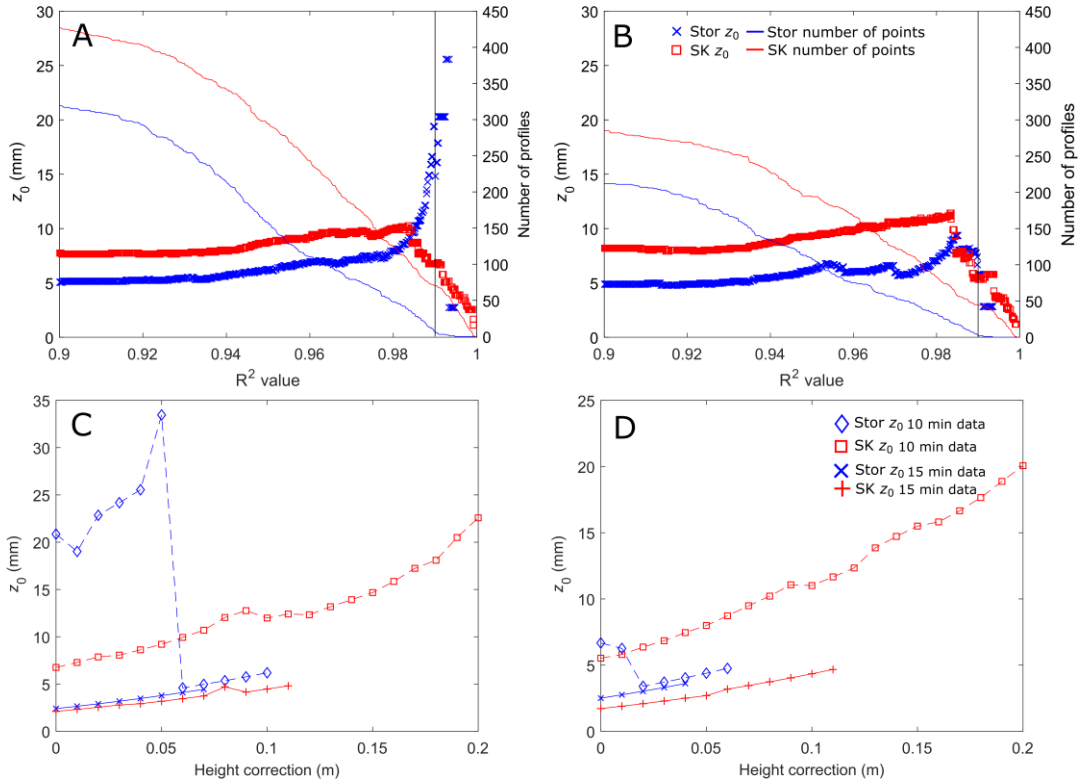

Fig. 4.4 Effect on z_0 of altering the r^2 filter for 10 minute (a) and 15 minute (b) averaging times. A vertical line illustrates the 0.99 threshold normally used. Effects of adding a height correction are shown for averaging periods of 10 minutes (C) and 15 minutes (D).

In keeping with the findings of others (c.f. Munro, 1989; Sicart *et al.*, 2014), adding any height correction increased z_0 at both sites (Fig. 4.4c). 10 minute averaged z_0 from SK more than tripled from 6.7 mm to 22.5 mm when a 0.2 m height correction was added. Stability corrected z_0 at both glaciers increased by <3 mm in all cases. While the order of magnitude increase observed by Munro (1989) when a 0.1 m correction is added was not seen here, the trend was largely for greater height corrections to increase z_0 until profiles were modified to the extent that they were rejected by filtering. The exception was the Stor data filtered by standard filters, which actually reduced when a height correction of >0.05 m was applied, as the two profiles which caused the higher mean value were filtered out. Almost the same patterns were given by the 15 minute averaged data, although z_0 was generally lower (Fig. 4d). The increase seen in SK z_0 with the standard filters was more pronounced, with a quadrupling of z_0 from 5.5 mm to 20.1 mm.

4.4.2 Microtopographic z_0

Direct comparison between methods showed that at both sites, microtopographic z_0 closely

matched profile values to within <3 mm (Fig. 4.5). Compared to values of 1.9 mm at Stor and 2 mm at SK derived from aerodynamic profiles, wind-perpendicular transects (see Fig. A.6 for examples) produced a median z_0 of 4.6 mm (Stor) and 2.4 mm (SK), and raster-based z_0 values were 4.1 mm (Stor) and 2.1 mm (SK). The median value was chosen for transect z_0 for its robustness to the outliers in the substantial spread of values obtained. Other directional values given by the raster method fell within 0.5 mm of each other, suggesting the surfaces were isotropic over the length scales relevant for z_0 here; only z_0 for the prevailing wind direction is shown.

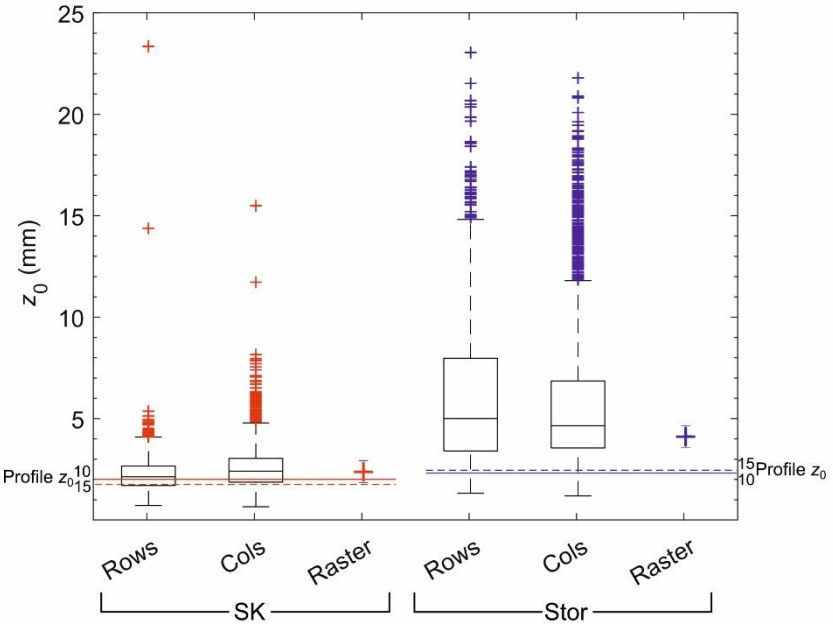

Fig. 4.5 Comparison of z_0 obtained from rasters, transects and stability corrected aerodynamic profiles. Due to the orientation of the glaciers, columns were wind-perpendicular on Stor, as were rows on SK. Colours of raster z_0 markers are coordinated with the profile z_0 reference lines (labelled). Profile z_0 given for 10 (solid lines) and 15 (dashed line) minute averaging periods, including stability are also shown, with error bars indicating the values given by precision analysis.

Roughness element height, or the height metric denoted by *h**, has previously been proposed as the greatest control on z_0 (Nield *et al.*, 2013). Our transect z_0 data bear this out (Table 4.4), although when each parameter of the raster method (for each raster used in subsequent scale tests–SK n = 29, Stor n = 39) was tested for a relationship with z_0, the maximum coefficient of determination (between *h** and z_0) was quite low at both sites (r^2 = 0.2). Nonetheless, similar *h** values for the raster and transect methods have given similar z_0 values despite the large differences in s and S_A.

The mean 3D precision of SfM-derived DEMs was 7 mm at SK and 5.7 mm on Stor. This

translated to a z_0 precision of ±0.052 mm (SK) and ±0.027 mm (Stor). SfM processing was therefore considered to be a negligible source of calculated z_0 variability (Fig. A.7).

Table 4.4 Summary of Lettau (1969) equation terms for raster and transect methods at both study sites. The values for the prevailing wind direction are given in each case, and transect values are the median of all rows/columns perpendicular to the prevailing wind. Note that s and S_A are included for information only, they represent very different areas for each method and are not comparable. Estimates of error for the raster method are taken from the standard deviation of values given by precision analysis (see A.4). Those for the transect method are the standard deviation of all values produced.

	SK				Stor			
	z_0 (mm)	h^* (m)	s (m^2)	S_A (m^2)	z_0 (mm)	h^* (m)	s (m^2)	S_A (m^2)
Raster	2.4 [0.05]	0.04	12.6	100.00	4.1 [0.03]	0.06	14.3	100.00
Transect	2.1[0.9]	0.05[0.01]	0.008[0.01]	0.1[0.2]	4.6[3.5]	0.1[0.02]	0.02[0.02]	0.16[0.6]

For gradually larger plots, raster z_0 on Stor varied from 1.04 to 3.44 mm, and transect z_0 from 1.70 to 9.17 mm (Fig. 4.6a and b). On SK, raster z_0 ranged between 1.5 and 7.1 mm, and transect z_0 between 1.1 and 5.6 mm. The relationship between z_0 and scale is as expected for SK (c.f. Miles *et al.*, 2017; Quincey *et al.*, 2017). Raster z_0 follows a clear trend with plot size, whereas transect z_0 shows some variation but increases overall – both demonstrate significant relationships (r^2>0.9, p<0.05). The relationship is less clear on Stor, with the raster z_0 increasing with plot size up to 13 m, then decreasing slightly but remaining at ~4.6 mm. Transect z_0 shows more variation, reaching a maximum of 8.4 mm at 18 m and staying around 6.6 mm at greater lengths, and indeed showing a large spread of values for any given plot size.

When DEM resolution was coarsened gradually from 0.005 to 0.5 m per pixel, the effect at both sites was for z_0 to decrease (Fig. 4.6c and d). At SK, raster z_0 decreased from 2.1 mm to 0.1 mm, and at Stor from 4.1 mm to 0.16 mm. Median transect z_0 decreased from 2.1 mm to 0.2 mm at SK and from 4.6 mm to 0.4 mm at Stor. A clear inflection is visible on both plots, potentially indicating a switch between form (>0.02 m pix^{-1}) and grain (<0.02 m pix^{-1}) roughness being represented in the topographic data. In this case the increased z_0 at finer resolution highlights the importance of finer scales of roughness elements.

z_0 was found to be influenced by the detrending method used (Table 4.5). The length over

which original DEMs were smoothed to obtain a coarse DEM was varied from 0.5 – 5 m. Longer smoothing lengths (e.g. 5 m) left a greater area above the detrended mean, thus greater h^*, and greater overall silhouette area (s). While S_A was also increased for transect data, the number of upcrossings (f) decreased substantially. Even with a DEM size of just 10 m^2 the method and degree of detrending bears significant weight on the resulting z_0 value.

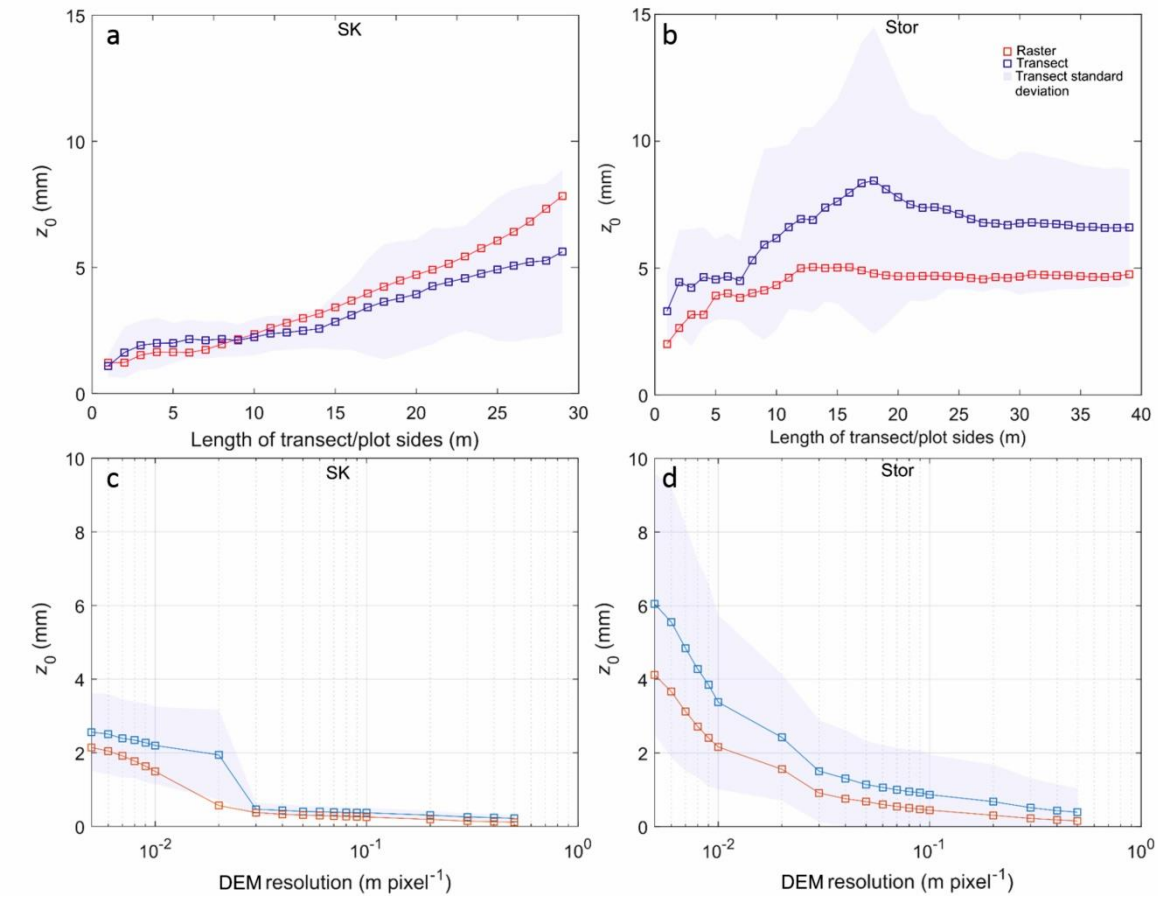

Fig. 4.6 Comparison of raster and transect z_0 with scale (a and b) and DEM resolution (c and d). The key in panel b is valid for all panels.

Table 4.5 Summary of detrending method effects on z_0 and terms of Lettau (1969) equation. Values along the top row in metres refer to the length of window used to smooth original data. *f* refers to the number of upcrossings used in the Munro (1989) equation.

		SK					Stor				
		Planar/linear	5 m	2 m	1 m	0.5 m	Planar/linear	5 m	2 m	1 m	0.5 m
DEM	z_0 (mm)	1.7	11	3.1	1.2	0.4	3.1	3.2	1.9	1.4	0.9
	h^* (m)	0.03	0.2	0.06	0.03	0.01	0.04	0.05	0.03	0.03	0.02
	s (m^2)	12.6	10.6	9.9	9.2	7.5	14.3	12.4	11.9	11.6	10.8
	S_A (m^2)	100	100	100	100	100	100	100	100	100	100
Transect	z_0 (mm)	2.1(±0.9)	1.5(±0.3)	1.6(±0.7)	1.2(±0.9)	0.7(±0.9)	4.6(±3.5)	5.2(±1.4)	3.1(±2.6)	2.5(±3.5)	1.6(±3.5)
	h^* (m)	0.05(±0.01)	0.05(±0.01)	0.04(±0.7)	0.02(±0.01)	0.01(±0.01)	0.1(±0.02)	0.1(±0.02)	0.06(±0.02)	0.04(±0.02)	0.03(±0.9)
	s (m^2)	0.01(±0.01)	0.01(±0.01)	0.004(±0.01)	0.001(±0.01)	0.0004(±0.01)	0.03(±0.02)	0.02(±0.03)	0.007(±0.03)	0.003(±0.02)	0.001(±0.02)
	S_A (m^2)	0.15(±0.2)	0.1(±0.9)	0.04(±0.4)	0.01(±0.2)	0.004(±0.2)	0.40(±0.6)	0.2(±1.6)	0.06(±0.8)	0.03(±0.6)	0.01(±0.6)
	f	31(±11)	26(±4)	51(±8)	90(±11)	168(±11)	25(±13)	23(±5)	42(±9)	63(±13)	101(±13)

4.5 Discussion

4.5.1 Profile z_0

We employed the aerodynamic profile method to calculate z_0 over two glaciers during the 2017 ablation season, using the same experimental set up and methods as Quincey *et al.* (2017). After intensive field data collection z_0 was derived from profiles of wind speed and air temperature using MO similarity theory. Following the application of the MO stability correction, the profile z_0 values found for SK (1.7 - 2.0 mm) and Stor (2.4 – 2.5 mm) fall within the range that has been found previously for clean ice (i.e. not debris-covered) glaciers (see summary tables in Brock *et al.*, 2006; Miles *et al.*, 2017). In particular, the values for Storglaciären were very close to those used in an earlier study that used profiles at the same site (Hock and Holmgren, 1996). Without the stability correction, values fall within the upper end of the same range and overlap with those commonly found over debris-covered glaciers (~10^1 mm) (Takeuchi *et al.*, 2000; Brock *et al.*, 2010; Quincey *et al.*, 2017). Applying the MO stability correction was found to reduce the scatter of z_0 values obtained, which is thought to be for a combination of two reasons: first, that only those profiles that most closely fit MO theory are retained, and second, that the number of profiles retained is greatly reduced.

Generally, site observations are reflected by the z_0 values obtained; Stor was visibly rougher than the site at SK, although a more pronounced progression of average daily z_0 values was expected at SK, where the fetch transitioned from snow, through slush, to bare ice during the data collection period. This is attributed to the study duration, where the site likely was not observed for long enough to allow detailed temporal analysis.

As with other similar studies, we found that using wind/temperature profiles to find z_0 is a very low-yield approach (c.f. Smeets *et al.*, 1998; Denby and Smeets, 2000; Brock *et al.*, 2006; Sicart *et al.*, 2014; Miles *et al.*, 2017; Quincey *et al.*, 2017). Moreover, sensors had to be monitored and repaired due to harsh weather conditions meaning that instruments cannot be set up and left unattended for long periods (the wind tower at Storglaciären collapsed overnight from 12th-13th July, hence the shortened dataset). Aggressive filtering of aerodynamic data left a small proportion of z_0 estimates remaining, 0.5% for SK and 0.6% for Stor (Fig. 4.3); this calls into question the ability of those few z_0 values to represent the roughness length adequately and echoes past criticisms of the suitability of MO stability theory for use over glaciers (Denby and Greuell, 2000; Denby and Smeets, 2000). By slightly relaxing the threshold used to filter out poor profile fits from r^2 = 0.99 to r^2 = 0.95, we were able to increase the number of profiles included by an order of magnitude while maintaining a similar z_0 and still only using statistically strong fits (Table 4.3), although z_0 was increased

above the majority of published values for similar surfaces.

Past workers have attempted to account for local topographic variability so that z_0 measurements are made from the mean surface elevation rather than one point (e.g. Munro, 1989; Sicart *et al.*, 2014). Our testing corroborated past observations that adding a height correction increased z_0, although as shown by data from Storglaciären, the effect was not consistent (particularly with a limited dataset).

The inclusion of a stability correction, whether based on the Obukhov length *L* or the bulk Richardson number (Mölg *et al.*, 2008; Anderson *et al.*, 2010; Brock *et al.*, 2010; Radić *et al.*, 2017), has been questioned for its effect on the validity of MO similarity theory over glaciers, as both corrections have led to overestimations of the sensible-heat fluxes (Fitzpatrick *et al.*, 2017; Radić *et al.*, 2017). Here, the effect of including the MO stability correction was to drastically reduce the number of z_0 values produced (Fig. 4.3a and b), at the same time reducing z_0 to values similar to those obtained microtopographically (Fig. 4.5) and in other studies.

4.5.2 Microtopographic z_0

Estimates of z_0 were made using microtopographic data derived from SfM surveys of the two sites. Monte Carlo-based precision analysis (Appendix A.4) showed that the impact of uncertainties within the bundle adjustment stage of the SfM workflow on microtopographic z_0 were minimal (two orders of magnitude smaller than z_0), offering confidence to this kind of data collection. A 'base case' was defined for microtopographic investigations at each site, where grid size was kept at 10 x 10 m and DEM resolution was 0.005 m pixel^{-1}. The transect and raster methods were then used to estimate z_0 for comparison with profile values, using the median of all rows and columns for transect z_0 and the prevailing wind direction for raster z_0. Estimates for both methods compared well with profile measurements, to within <3 mm (Fig. 4.5), despite the large spread of values given by the transect method. Values also compare with those obtained over similar surfaces in other studies, where z_0 has been microtopographically estimated at ≤5 mm (Brock *et al.*, 2006; Smith *et al.*, 2016b; Fitzpatrick *et al.*, 2019). While Nield *et al.* (2013) point out that the height metric exerts the greatest control over z_0 and offer some guidance for which metric might be more appropriate for different kinds of terrain, Smith *et al.* (2016b) point out that the rationale for twice the standard deviation of roughness elements is not explicit in Munro (1989). As the full range of elevations is sampled, not just the peak elevation of each obstacle (indeed the elevation

field cannot really be disaggregated into a set of 'obstacles'), we chose to maintain the $2\sigma_d$ definition of *h** to preserve the influence of the larger roughness elements.

As with other studies of glacial z_0 (Rees and Arnold, 2006; Miles *et al.*, 2017; Quincey *et al.*, 2017), we found significant scale dependence within both microtopographic methods tested, which undermines the fact that values compare well to profile z_0. Generally, z_0 increased as it was estimated from larger grids and longer transects, suggesting that validation with independent methods (i.e. aerodynamic profiles) is the best way to decide on the appropriate scale. Similarly, z_0 decreased when calculated from coarser resolution elevation data (Fig. 4.6c and d), demonstrating the fractal properties of the surface (Arnold and Rees, 2004) and owing to the removal of finer-scale variability and an effectively smoother surface (Quincey *et al.*, 2017). Interestingly, Fitzpatrick *et al.* (2019) obtained values of $z_0 \approx 3$ mm over bare ice in British Columbia, Canada, using their block method (which finds z_0 for 1 m^2 cells based on the surrounding 9 m^2 moving window). Their values are comparable to those found here despite the smaller plot size (expected smaller z_0) and coarser resolution of 1 m $pixel^{-1}$ (also expected smaller z_0). Despite the realistic values given by the microtopographic methods used here, their scale and resolution dependence are critical shortcomings that should be addressed as microtopographic methods develop. Fitzpatrick *et al.* (2019) also present a scale-independent transect method - this valuable progression has yet to be developed into a 3D method that can take full advantage of the scope of high-resolution survey techniques, and has yet to be tested glacier-wide.

Using a smaller plot size or coarser resolution elevation data has the benefit that detrending becomes a more straightforward task, as the influence of the overall slope becomes smaller (Smith, 2014). Table 4.5 demonstrates that the level of detrending can alter the character of the surface and thus z_0. Where smaller plots or shorter transects are used (e.g. <10 m) then linear/planar detrending is usually sufficient. Over scales >10 m the overall slope of the glacier surface can start to distort the detrended data, particularly on more convex surfaces like SK, necessitating other approaches. A possible solution to this is to calculate z_0 using a moving window (e.g. Fitzpatrick *et al.*, 2019), whereby z_0 is calculated for each cell based on adjacent cells within a specified radius (or window) - this way larger grids can still be used without the complication of deciding on the most appropriate detrending technique. This is more computationally demanding than performing the detrending step once per plot and assumes that the resolution/scale dependence problem has been considered beforehand.

4.5.3 Future work

In order to ensure future attempts at parameterising z_0 microtopographically are validated correctly, the data against which they are validated must be reliable. Our test of relaxing the r^2 filter for aerodynamic profile fits should be tested with other datasets, so the yield from the method can be maximized. In the absence of eddy covariance equipment and data, we found the z_0 values obtained from wind profiles to be realistic compared to those in other similar studies (e.g. Brock *et al.*, 2006; Quincey *et al.*, 2017), and would suggest that the method be used with care, giving consideration to the sensitivities and uncertainties discussed here.

The characterisation of surface geometry should also be interrogated further, to ensure that the basis of the microtopographic approach is sound. The raster method improves upon the transect method by accounting for some of the effects of shading/sheltering (Smith *et al.*, 2016b), yet the effects of wake interference between adjacent and successive roughness elements (Raupach, 1992) remains unaccounted for. The partition of drag between roughness elements and the underlying 'surface' (Raupach, 1992) will also depend on the upper and lower limits of topographic scale used to define a roughness element, considering the self-similar nature of glacier surfaces (Arnold and Rees, 2004).

Scale is another important area which should receive attention if 3D microtopographic methods are to be used to find glacier-wide distributed values of z_0. Here, a 10 x 10 m grid where each cell was 5 x 5 mm produced values very close to those obtained from aerodynamic profiles. In a scenario where glacier-wide microtopographic z_0 were being calculated using remotely sensed data, obtaining and processing data of the same resolution used here would be extremely computationally demanding. Moreover, as shown by this study, maintaining the same resolution and increasing scale would inflate z_0 estimates. Ideally, a scale independent 3D method would be used. Until this is developed, z_0 could potentially be reduced enough to balance the inflation by using a degraded resolution. If this can be calibrated correctly over a broad range of empirical data from different ice surfaces, then the feasibility of acquiring spatially and temporally distributed z_0 estimates from other readily available sources of remotely sensed data (i.e. satellites) could be explored.

4.6 Conclusions

We implemented the two most common methods for quantifying the aerodynamic roughness length (z_0) of glaciers, which are based on aerodynamic profiles or

microtopographic data. Each has uncertainties and sensitivities which can ultimately impact the calculation of the contribution of the turbulent fluxes to the surface energy balance. Here, we provided a synthesis of these uncertainties and sensitivities, and presented an analysis of those we found to have the greatest impact on z_0. We conclude that:

1. While the eddy covariance method remains the standard for measuring flux and z_0, where such data are unavailable the profile and microtopographic methods can provide realistic z_0 values from equipment that is cheaper and more practical. The typical threshold for what constitutes an acceptable log-linear profile of air temperature or wind velocity can potentially be relaxed slightly, e.g. from r^2 = 0.99 to r^2 = 0.95, increasing the number of included profiles, although this requires further investigation to ensure impact on z_0 is limited.

2. The transect and raster methods both produced estimates of z_0 comparable to values derived from aerodynamic profiles at the resolution and scale used in this study. The transect method produced a large spread of values, of which the average was close to profile z_0 yet some were an order of magnitude greater; the raster method, however, produced singular values which were extremely close to profile z_0. Both methods are susceptible to scale and resolution dependence, and the choice of detrending method. The choice of height metric (denoted by h^*) is also important – uniform roughness elements can be represented by their mean height, yet this does not adequately approximate the surface where heights are uneven. Incorporating drag and sheltering effects could align the microtopographic approach more closely to its intended aerodynamic representation.

3. Calibrating the balance between scale and resolution of microtopographic data will be an important step in future work attempting to upscale the microtopographic approach to obtain glacier-wide estimates of z_0. This will enable us to test the feasibility of using broader scale (i.e. satellite) remotely sensed data as a means for obtaining spatially and temporally distributed z_0.

Acknowledgments

JRC is supported by a NERC PhD studentship (NE/L002574/1). Fieldwork was funded by an INTERACT transnational access grant awarded to MWS under the European Union H2020 Grant Agreement No.730938. The authors declare that they have no conflicts of interest.

References

Anderson, B., Mackintosh, A., Stumm, D., George, L., Kerr, T., Winter-Billington, A. & Fitzimons, S. (2010) 'Climate sensitivity of a high-precipitation glacier in New-Zealand', *Journal of Glaciology*, 56(195), pp. 114-128(15). doi: 10.3189/002214310791190929.

Andreas, E. L., Persson, P. O. G., Grachev, A. A., Jordan, R. E., Horst, T. W., Guest, P. S. & Fairall, C. W. (2010) 'Parameterizing Turbulent Exchange over Sea Ice in Winter', *Journal of Hydrometeorology*, 11(1), pp. 87–104. doi: 10.1175/2009JHM1102.1.

Arnold, N. S. & Rees, W. G. (2004) 'Self-similarity in glacier surface characteristics', *Journal of Glaciology*, 49(167), pp. 547–554. doi: doi:10.3189/172756503781830368.

Arnold, N. S., Rees, W. G., Hodson, A. J. & Kohler, J. (2006) 'Topographic controls on the surface energy balance of a high Arctic valley glacier', *Journal of Geophysical Research: Earth Surface*, 111(2). doi: 10.1029/2005JF000426.

Baechlin, W., Theurer, W. & Plate, E. J. (1992) 'Dispersion of gases released near the ground in built up areas: Experimental results compared to simple numerical modelling', *Journal of Wind Engineering and Industrial Aerodynamics*, 44(1–3), pp. 2721–2732. doi: 10.1016/0167-6105(92)90066-J.

Bagnold, R. A. (1941) *The Physics of Blown Sand and Desert Dunes*. New York: Dover Publications Inc.

Bandyopadhyay, P. R. (1987) 'Rough-wall turbulent boundary layers in the transition regime', *Journal of Fluid Mechanics*, 180(1), p. 231. doi: 10.1017/S0022112087001794.

Banke, E. G. & Smith, S. D. (1973) 'Wind stress on Arctic sea ice', *Journal of Geophysical Research*, 78(33), pp. 7871–7883. doi: 10.1029/jc078i033p07871.

Bradley, E. F. (1968) 'A micrometeorological study of velocity profiles and surface drag in the region modified by a change in surface roughness', *Quarterly Journal of the Royal Meteorological Society*, 94(401), pp. 361–379. doi: 10.1002/qj.49709440111.

Braun, M. & Hock, R. (2004) 'Spatially distributed surface energy balance and ablation modelling on the ice cap of King George Island (Antarctica)', *Global and Planetary Change*, 42(1–4), pp. 45–58. doi: 10.1016/j.gloplacha.2003.11.010.

Bravo, C., Loriaux, T., Rivera, A. & Brock, B. W. (2017) 'Assessing glacier melt contribution to streamflow at Universidad Glacier, central Andes of Chile', *Hydrology and Earth System Sciences*, 21(7), pp. 3249–3266. doi: 10.5194/hess-21-3249-2017.

Brock, B. W., Mihalcea, C., Kirkbride, M. P., Diolaiuti, G., Cutler, M. E. J. & Smiraglia, C. (2010) 'Meteorology and surface energy fluxes in the 2005-2007 ablation seasons at the Miage debris-covered glacier, Mont Blanc Massif, Italian Alps', *Journal of Geophysical Research Atmospheres*, 115(9), pp. 1–16. doi: 10.1029/2009JD013224.

Brock, B. W., Willis, I. C. & Sharp, M. J. (2006) 'Measurement and parameterization of aerodynamic roughness length variations at Haut Glacier d'Arolla, Switzerland', *Journal of Glaciology*, 52(177), pp. 281–297. doi: 10.3189/172756506781828746.

Burba, G. (2013) *Eddy Covariance Method-for Scientific, Industrial, Agricultural, and Regulatory Applications*. Lincoln, Nebraska: LI-COR Biosciences. doi: 10.1007/s00704-004-0095-y.

Carrivick, J. L. & Hock, R. (1998) 'Measured and modelled melt and the surface energy balance on Storglaciären', in Klingbjer, P. (ed.) *Tarfala Research Station Annual Report, 1999*, pp. 28–33.

Carrivick, J. L., Smith, M. W. & Carrivick, D. M. (2015) 'Terrestrial laser scanning to deliver high-resolution topography of the upper Tarfala valley, arctic Sweden', *Gff*, 137(4), pp. 383–396. doi: 10.1080/11035897.2015.1037569.

Carrivick, J. L., Smith, M. W. & Quincey, D. J. (2016) *Structure from Motion in the Geosciences*. John Wiley & Sons.

Counihan, J. (1971) 'Wind Tunnel Determination of the Roughness Length As a Function of the Three-Dimensional Roughness Elements', *Atmospheric Environment*, 5(1967), pp. 637–642.

Denby, B. (1999) 'Second-Order Modelling of Turbulence in Katabatic Flows', *Boundary-Layer Meteorology*, 92(1), pp. 65–98. doi: 10.1023/A:1001796906927.

Denby, B. & Greuell, W. (2000) 'The Use of Bulk and Profile Methods for Determining Surface Heat Fluxes in the Presence of Glacier Winds', *Journal of Glaciology*, 46(154), pp. 445–452.

Denby, B. & Smeets, C. J. P. P. (2000) 'Derivation of Turbulent Flux Profiles and Roughness Lengths from Katabatic Flow Dynamics', *Journal of Applied Meteorology*, 39(9), pp. 1601–1612. doi: 10.1175/1520-0450(2000)039<1601:DOTFPA>2.0.CO;2.

Dyer, A. J. & Hicks, B. B. (1970) 'Flux-gradient relationships in the constant flux layer', *Quarterly Journal of the Royal Meteorological Society*, 96(410), pp. 715–721.

Elliott, W. P. (1958) 'The growth of the atmospheric internal boundary layer', *Eos, Transactions American Geophysical Union*, 39(6), pp. 1048–1054. doi: 10.1029/TR039i006p01048.

Fassnacht, S. R., Stednick, J. D., Deems, J. S. & Corrao, M. V. (2009) 'Metrics for assessing snow surface roughness from Digital imagery', *Water Resources Research*, 46(4). doi: 10.1029/2008WR006986.

Fausto, R. S., Van As, D., Box, J. E., Colgan, W., Langen, P. L. & Mottram, R. H. (2016) 'The implication of nonradiative energy fluxes dominating Greenland ice sheet exceptional ablation area surface melt in 2012', *Geophysical Research Letters*, 43(6), pp. 2649–2658. doi: 10.1002/2016GL067720.

Favier, V., Wagnon, P., Chazarin, J. P., Maisincho, L. & Coudrain, A. (2004) 'One-year measurements of surface heat budget on the ablation zone of Antizana Glacier 15, Ecuadorian Andes', *Journal of Geophysical Research Atmospheres*, 109(18), pp. 1–15. doi: 10.1029/2003JD004359.

Fey, C. & Wichmann, V. (2017) 'Long-range terrestrial laser scanning for geomorphological change detection in alpine terrain – handling uncertainties', *Earth Surface Processes and Landforms*, 42(5), pp. 789–802. doi: 10.1002/esp.4022.

Fitzpatrick, N., Radić, V. & Menounos, B. (2017) 'Surface Energy Balance Closure and Turbulent Flux Parameterization on a Mid-Latitude Mountain Glacier, Purcell Mountains, Canada', *Frontiers in Earth Science*, 5(September), pp. 1–20. doi: 10.3389/feart.2017.00067.

Fitzpatrick, N., Radić, V. & Menounos, B. (2019) 'A multi-season investigation of glacier

surface roughness lengths through in situ and remote observation', *The Cryosphere*, 13, pp. 1051–1071. doi: https://doi.org/10.5194/tc-13-1051-2019.

Foken, T. (2006) '50 years of the Monin-Obukhov similarity theory', *Boundary-Layer Meteorology*, 119(3), pp. 431–447. doi: 10.1007/s10546-006-9048-6.

Foken, T. (2008) *Micrometeorology*. Berlin: Springer.

Fryrear, D. W. (1965) 'Soil cover and wind erosion', *Transactions of the American Society of Agricultural and Biological Engineers*, 28(3), pp. 781–784.

Garratt, J. R. (1992) *The Atmospheric Boundary Layer*. Cambridge: Cambridge University Press.

Giesen, R. H., Andreassen, L. M., Oerlemans, J. & Van Den Broeke, M. R. (2014) 'Surface energy balance in the ablation zone of Langfjordjøkelen, an arctic, maritime glacier in northern Norway', *Journal of Glaciology*, 60(219), pp. 57–70. doi: 10.3189/2014JoG13J063.

Gorter, W., van Angelen, J. H., Lenaerts, J. T. M. & van den Broeke, M. R. (2014) 'Present and future near-surface wind climate of Greenland from high resolution regional climate modelling', *Climate Dynamics*, 42(5–6), pp. 1595–1611. doi: 10.1007/s00382-013-1861-2.

Greuell, W. & Genthon, C. (2004) 'Modelling land-ice surface mass balance', in *Mass Balance of the Cryosphere*, pp. 117–168. doi: 10.1017/CBO9780511535659.007.

Grohmann, C. H., Smith, M. J. & Riccomini, C. (2011) 'Multiscale analysis of topographic surface roughness in the Midland Valley, Scotland', *IEEE Transactions on Geoscience and Remote Sensing*. doi: 10.1109/TGRS.2010.2053546.

Hock, R. (2005) 'Glacier melt: a review of processes and their modelling', *Progress in Physical Geography*, 29(3), pp. 362–391. doi: 10.1191/0309133305pp453ra.

Hock, R., Carrivick, J. L. & Jonsell, U. (1999) 'Glacio-meteorological studies on Storglaciären in 1999', in *Tarfala Research Station Annual Report, 1999*, pp. 20–23.

Hock, R. & Holmgren, B. (1996) 'Some Aspects of Energy Balance and Ablation of Storglaciären , Northern Sweden', *Geografiska Annaler Series A-Physical Geography*, 78(2), pp. 121–131.

Inoue, J. & Yoshida, M. (1980) 'Ablation and Heat Exchange over the Khumbu Glacier', *Journal of the Japanese Society of Snow and Ice*, 41(Special), pp. 26–33. doi: 10.5331/seppyo.41.Special_26.

Irvine-Fynn, T. D. L., Sanz-Ablanedo, E., Rutter, N., Smith, M. W. & Chandler, J. H. (2014) 'Measuring glacier surface roughness using plot-scale, close-range digital photogrammetry', *Journal of Glaciology*, 60(223), pp. 957–969. doi: 10.3189/2014JoG14J032.

James, M. R., Chandler, J. H., Eltner, A., Fraser, C., Miller, P. E., Mills, J. P., Noble, T., Robson, S. & Lane, S. N. (2019) 'Guidelines on the use of Structure from Motion Photogrammetry in Geomorphic Research', *Earth Surface Processes and Landforms*. doi: 10.1002/esp.4637.

James, M. R. & Robson, S. (2012) 'Straightforward reconstruction of 3D surfaces and topography with a camera: Accuracy and geoscience application', *Journal of Geophysical Research: Earth Surface*, 117(F03017). doi: 10.1029/2011JF002289.

James, M. R., Robson, S., D'Oleire-Oltmanns, S. & Niethammer, U. (2017a) 'Optimising UAV topographic surveys processed with structure-from-motion: Ground control quality, quantity and bundle adjustment', *Geomorphology*, 280, pp. 51–66. doi:

10.1016/j.geomorph.2016.11.021.

James, M. R., Robson, S. & Smith, M. W. (2017b) '3-D uncertainty-based topographic change detection with structure-from-motion photogrammetry: Precision maps for ground control and directly georeferenced surveys', *Earth Surface Processes and Landforms*, 42, pp. 1769–1788. doi: 10.1002/esp.4125.

Lettau, H. (1969) 'Note on Aerodynamic Roughness-Parameter Estimation on the Basis of Roughness-Element Description', *Journal of Applied Meteorology*, 8(5), pp. 828–832. doi: http://dx.doi.org/10.1175/1520-0450(1969)008<0828:NOARPE>2.0.CO;2.

Litt, M., Sicart, J. E., Helgason, W. D. & Wagnon, P. (2014) 'Turbulence Characteristics in the Atmospheric Surface Layer for Different Wind Regimes over the Tropical Zongo Glacier (Bolivia, 16∘S)', *Boundary-Layer Meteorology*, 154(3), pp. 471–495. doi: 10.1007/s10546-014-9975-6.

Litt, M., Sicart, J. E., Six, D., Wagnon, P. & Helgason, W. D. (2017) 'Surface-layer turbulence, energy balance and links to atmospheric circulations over a mountain glacier in the French Alps', *Cryosphere*, 11(2), pp. 971–987. doi: 10.5194/tc-11-971-2017.

Macdonald, R. W., Griffiths, R. F. & Hall, D. J. (1998) 'An improved method for the estimation of surface roughness of obstacle arrays', *Atmospheric Environment*, 32(11), pp. 1857–1864. doi: 10.1016/S1352-2310(97)00403-2.

MacKinnon, D. J., Clow, G. D., Tigges, R. K., Reynolds, R. L. & Chavez, P. S. (2004) 'Comparison of aerodynamically and model-derived roughness lengths (zo) over diverse surfaces, central Mojave Desert, California, USA', *Geomorphology*, 63(1–2), pp. 103–113. doi: 10.1016/j.geomorph.2004.03.009.

Miles, E. S., Steiner, J. F. & Brun, F. (2017) 'Highly variable aerodynamic roughness length (z0) for a hummocky debris-covered glacier', *Journal of Geophysical Research: Atmospheres*, 122(16), pp. 8447–8466. doi: 10.1002/2017JD026510.

Mölg, T., Cullen, N. J., Hardy, D. R., Kaser, G. & Klok, L. (2008) 'Mass balance of a slope glacier on Kilimanjaro and its sensitivity to climate', *International Journal of Climatology*, 28, pp. 881–892. doi: 10.1002/joc.

Monin, A. S. & Obukhov, A. M. (1954) 'Basic Laws of Turbulent Mixing in the Ground Layer of the Atmosphere', *Trans. Geophys. Inst. Akad. Nauk. USSR*, 24(151), pp. 163–187.

Munro, D. S. (1989) 'Surface roughness and bulk heat transfer on a glacier: comparison with eddy correlation', *Journal of Glaciology*, 35(121), pp. 343–348.

Nield, J. M., King, J., Wiggs, G. F. S., Leyland, J., Bryant, R. G., Chiverrell, R. C., Darby, S. E., Eckardt, F. D., Thomas, D. S. G., Vircavs, L. H. & Washington, R. (2013) 'Estimating aerodynamic roughness over complex surface terrain', *Journal of Geophysical Research Atmospheres*, 118(23), pp. 12948–12961. doi: 10.1002/2013JD020632.

Pelletier, J. D. & Field, J. P. (2016) 'Predicting the roughness length of turbulent flows over landscapes with multi-scale microtopography', *Earth Surface Dynamics*, 4(2), pp. 391–405. doi: 10.5194/esurf-4-391-2016.

Quincey, D. J., Smith, M. W., Rounce, D. R., Ross, A. N., King, O. & Watson, C. S. (2017) 'Evaluating morphological estimates of the aerodynamic roughness of debris covered glacier ice', *Earth Surface Processes and Landforms*. doi: 10.1002/esp.4198.

Radić, V., Menounos, B., Shea, J., Fitzpatrick, N., Tessema, M. A. & Déry, S. J. (2017)

'Evaluation of different methods to model near-surface turbulent fluxes for a mountain glacier in the Cariboo Mountains, BC, Canada', *Cryosphere*, 11(6), pp. 2897–2918. doi: 10.5194/tc-11-2897-2017.

Raupach, M. R. (1992) 'Drag and drag partition on rough surfaces', *Boundary-Layer Meteorology*, 60(4), pp. 375–395. doi: 10.1007/BF00155203.

Rees, W. G. (1998) 'A rapid method of measuring snow-surface profiles', *Journal of Glaciology*, 44(c), pp. 674–675. Available at: http://adsabs.harvard.edu/abs/1998JGlac..44..674R.

Rees, W. G. & Arnold, N. S. (2006) 'Scale-dependent roughness of a glacier surface: Implications for radar backscatter and aerodynamic roughness modelling', *Journal of Glaciology*, 52(177), pp. 214–222. doi: 10.3189/172756506781828665.

Rounce, D. R., Quincey, D. J. & McKinney, D. C. (2015) 'Debris-covered glacier energy balance model for Imja-Lhotse Shar Glacier in the Everest region of Nepal', *Cryosphere*, 9(6), pp. 2295–2310. doi: 10.5194/tc-9-2295-2015.

Schlichting, H. (1937) 'Experimental investigation of the problem of surface roughness', *National Advisory Committee for Aeronautics: Technical Memorandum 823*. Available from https://ntrs.nasa.gov/citations/19930094593 [Accessed 18/11/2021]

Sellers, W. D. (1965) *Physical Climatology*. Chicago: University of Chicago Press.

Sicart, J. E., Litt, M., Helgason, W., Tahar, V. Ben & Chaperon, T. (2014) 'A study of the atmospheric surface layer and roughness lengths on the high-altitude tropical Zongo glacier, Bolivia', *Journal of Geophysical Research*, 119(7), pp. 3793–3808. doi: 10.1002/2013JD020615.

Sicart, J. E., Wagnon, P. & Ribstein, P. (2005) 'Atmospheric controls of the heat balance of Zongo Glacier (16°S, Bolivia)', *Journal of Geophysical Research D: Atmospheres*, 110(12), pp. 1–17. doi: 10.1029/2004JD005732.

Smeets, C. J. P. P., Duynkerke, P. G. & Vugts, H. F. (1998) 'Turbulence characteristics of the stable boundary layer over a mid-latitude glacier. Part I: a combination of katabatic and large-scale forcing', *Boundary-Layer Meteorology*, 87(1), pp. 117–145. doi: 10.1023/A:1000860406093.

Smeets, C. J. P. P., Duynkerke, P. G. & Vugts, H. F. (1999) 'Observed wind profiles and turbulent fluxes over an ice surface with changing surface roughness', *Boundary-Layer Meteorology*, 92(1994), pp. 101–123. doi: 10.1023/A:1001899015849.

Smith, M. W. (2014) 'Roughness in the Earth Sciences', *Earth-Science Reviews*, 136, pp. 202–225. doi: 10.1016/j.earscirev.2014.05.016.

Smith, M. W., Carrivick, J. L. & Quincey, D. J. (2016a) 'Structure from motion photogrammetry in physical geography', *Progress in Physical Geography*, 40(2), pp. 247–275. doi: 10.1177/0309133315615805.

Smith, M. W., Cox, N. J. & Bracken, L. J. (2011) 'Terrestrial laser scanning soil surfaces: A field methodology to examine soil surface roughness and overland flow hydraulics', *Hydrological Processes*, 25(6), pp. 842–860. doi: 10.1002/hyp.7871.

Smith, M. W., Quincey, D. J., Dixon, T., Bingham, R. G., Carrivick, J. L., Irvine-Fynn, T. D. L. & Rippin, D. M. (2016b) 'Aerodynamic roughness of glacial ice surfaces derived from high-resolution topographic data', *Journal of Geophysical Research F: Earth Surface*, 121(4), pp.

748–766. doi: 10.1002/2015JF003759.

Stiperski, I. & Rotach, M. W. (2016) ‘On the Measurement of Turbulence Over Complex Mountainous Terrain’, *Boundary-Layer Meteorology*, 159(1), pp. 97–121. doi: 10.1007/s10546-015-0103-z.

Stull, R. (1988) *An introduction to boundary layer meteorology*. London: Kluwer.

Takeuchi, Y., Kayastha, R. B. & Nakawo, M. (2000) ‘Characteristics of ablation and heat balance in debris-free and debris-covered areas on Khumbu Glacier, Nepal Himalayas, in the pre-monsoon season’, *IAHS Publication*, 264(2), pp. 53–61.

Vavrus, S. J. (2013) ‘Extreme Arctic cyclones in CMIP5 historical simulations’, *Geophysical Research Letters*, 40(23), pp. 6208–6212. doi: 10.1002/2013GL058161.

Wieringa, J. (1993) ‘Representative roughness parameters for homogeneous terrain’, *Boundary-Layer Meteorology*, 63(4), pp. 323–363. doi: 10.1007/BF00705357.

Wooding, R. A., Bradley, E. F. & Marshall, J. K. (1973) ‘Drag due to regular arrays of roughness elements of varying geometry’, *Boundary-Layer Meteorology*, 5(3), pp. 285–308. doi: 10.1007/BF00155238.

Chapter 5 : Correcting for systematic underestimation of topographic glacier aerodynamic roughness values from Hintereisferner, Austria

Correcting for systematic underestimation of topographic glacier aerodynamic roughness values from Hintereisferner, Austria

Joshua R. Chambers[1], Mark W. Smith[1], Thomas Smith[1], Rudolf Sailer[2], Duncan J. Quincey[1], Jonathan L. Carrivick[1], Lindsey Nicholson[3], Jordan Mertes[4], Ivana Stiperski[3] and Mike R. James[5].

[1]School of Geography and water@leeds, University of Leeds, Leeds, LS2 9JT, UK

[2]Department of Geography, Universität Innsbruck, Bruno Sander Haus, Innrain 52, Innsbruck, A-6020, Austria

[3]Department of Atmospheric and Cryospheric Sciences, Universität Innsbruck, Bruno Sander Haus, Innrain 52, Innsbruck, A-6020, Austria

[4]Centre for Environmental and Climate Science, Lund University, Ekologihuset, Sölvegatan 37, Lund, Sweden

[5]Lancaster Environment Centre, Lancaster University, Lancaster, UK

Citation

Chambers, J. R., Smith, M. W., Smith, T., Sailer, R., Quincey, D. J., Carrivick, J. L., Nicholson, L., Mertes, J., Stiperski, I. & James, M. R. (2021). Correcting for systematic underestimation of topographic glacier aerodynamic roughness values from Hintereisferner, Austria. *Frontiers in Earth Science*. DOI: 10.3389/feart.2021.691195

Abstract

Spatially-distributed values of glacier aerodynamic roughness (z_0) are vital for robust estimates of turbulent energy fluxes and ice and snow melt. Microtopographic data allow rapid estimates of z_0 over discrete plot-scale areas, but are sensitive to data scale and resolution. Here, we use an extensive multi-scale dataset from Hintereisferner, Austria, to develop a correction factor to derive z_0 values from coarse resolution (up to 30 m) topographic data that are more commonly available over larger areas. Resulting z_0 estimates are within an order of magnitude of previously validated, plot-scale estimates and aerodynamic values. The method is developed and tested using plot-scale microtopography data generated by structure from motion photogrammetry combined with glacier-scale data acquired by a permanent *in-situ* terrestrial laser scanner. Finally, we demonstrate the application of the method to a regional-scale digital elevation model acquired by airborne laser scanning. Our workflow opens up the possibility of including spatio-temporal variations of z_0 within glacier surface energy balance models without the need for extensive additional field data collection.

5.1 Introduction

The aerodynamic roughness length parameter (z_0) is recognized as one of the key uncertainties in glacier surface energy balance (SEB) modelling (Cullen *et al.*, 2007; Sicart *et al.*, 2014; Litt *et al.*, 2017; Fitzpatrick *et al.*, 2019). It is defined as the topographically-controlled height above the surface at which horizontal wind speed reaches zero (Stull, 1988; Garratt, 1992) and is typically derived from the direct observation of turbulent eddies through eddy covariance (Munro, 1989; Sicart *et al.*, 2014; Fitzpatrick *et al.*, 2019), or from extrapolation of log-linear fits of wind speed and air temperature profiles (Denby and Greuell, 2000; Brock *et al.*, 2006; Quincey *et al.*, 2017). Accurately quantifying z_0 is essential for calculating and predicting glacier ablation because z_0 is incorporated into calculations of the turbulent fluxes of sensible and latent heat between a surface and the adjacent atmosphere using the 'bulk aerodynamic approach' (Hock, 2005). Using this approach, the sensible (Q_S) and latent (Q_L) heat fluxes are defined as:

$$Q_S = \rho_a c_a C_H u(T_a - T_s) \tag{5.1}$$

$$Q_L = \rho_a L_{v/s} C_E u(q_a - q_s) \tag{5.2}$$

where ρ_a is the density of air (kg m^{-3}), c_a its specific heat capacity (J kg^{-1} K^{-1}) and $L_{v/s}$ the latent heat of vaporization or sublimation. In finding the bulk exchange parameters C_H and C_E using flux-gradient theory, an important step is finding the friction velocity (u_*) using

$$u(z) = \frac{1}{\kappa_0} u_* \ln\left(\frac{z}{z_0}\right) \tag{5.3}$$

as u is related to the logarithm of measurement height (z, m) in a profile (here assuming neutral stratification). κ_0 is the dimensionless von Karman's constant, 0.4, and z_0 is the surface roughness parameter. Substituting into (5.1), the bulk equation for the sensible heat flux becomes

$$Q_S = \rho_a c_a k_0 u_* \frac{T_a - T_s}{\ln(z/z_0)}. \tag{5.4}$$

The turbulent fluxes commonly comprise ~35% - 50% of a glacier SEB and have an increasingly important role in cloudy and windy conditions (Giesen *et al.*, 2014), when they can become the dominant source of energy over short timescales (daily and sub-daily), contributing >75% of melt energy (Fausto *et al.*, 2016). In maritime climates their dominance increases (Anderson *et al.*, 2010). Despite the importance of z_0, it is common for it to be generalised spatially across glacier surfaces and climatic zones, and through time (e.g. Lewis *et al.*, 1998; Giesen *et al.*, 2014; Bravo *et al.*, 2017), at least partly because it is difficult to measure. Obtaining eddy covariance data or aerodynamic profiles from field

measurements is challenging and provides only point-based z_0 values; consequently, research has been driven towards estimation of spatially distributed z_0 values from microtopography (Lettau, 1969; Munro, 1989), accelerated by the increasing availability of fine-resolution (sub-meter) and broad-scale topographic data.

Past work has identified that z_0 is spatially and temporally dynamic, with topographic z_0 values that have been validated against values from eddy covariance (EC) data or aerodynamic profiles (Brock *et al.*, 2006; Irvine-Fynn *et al.*, 2014; Miles *et al.*, 2017; Quincey *et al.*, 2017; Chambers *et al.*, 2019; Fitzpatrick *et al.*, 2019; Liu *et al.*, 2020). In particular, the rapid data collection enabled by structure from motion photogrammetry (SfM; Smith *et al.*, 2016a) and terrestrial laser scanning (TLS; Lemmens, 2011; Telling *et al.*, 2017) has led to work focusing on development and validation of topographic methods, mostly concentrated on plot-scale data (tens of meters). However, the acknowledged scale- and resolution-dependency of topographically-estimated z_0 (Rees and Arnold, 2006) complicates the application of these methods to glacier-scale distributed energy balance models, because coarser resolution data lead to substantial underestimates of z_0 and an order of magnitude change in z_0 can double the calculated turbulent fluxes (Munro, 1989).

Initial efforts to produce glacier-scale maps of z_0 have been promising (Smith *et al.*, 2016b; 2020; Fitzpatrick *et al.*, 2019), but here we seek to further these attempts by producing more robust topographic estimates of z_0 at the glacier scale. We employ a simple workflow to correct for systematic underestimation of z_0 when using coarser resolution data that can also be used to produce first-order estimates across the surrounding region and beyond. Specifically, we first present a multi-scale analysis of topographic z_0 from data collected during the 2018 ablation season on Hintereisferner, Austria, and identify power law relations between data resolution and derived topographic z_0. Second, through comparison with wind tower and EC data, we use these power laws to develop a correction factor for z_0 estimates derived from coarse scale, widely available glacier surface topographic data, to bring them within one order of magnitude of likely true values, thus limiting the knock-on effects of over- or underestimation on the turbulent fluxes (c.f. Munro, 1989). Finally, we demonstrate the broader utility of the method by applying it to other nearby glacier surfaces covered by a freely available regional topographic dataset for Austria.

5.2 Data and Methods

5.2.1 Location

Field data were collected at Hintereisferner (46° 48'N, 10° 47'E) in the Austrian Alps (Fig. 5.1), from 1-16 August 2018 during the Hintereisferner Experiment (HEFEX; Mott *et al.*, 2020).

Hintereisferner (HEF) is located high in the Rofenache catchment in the southern Otztal Alps, in the inner-alpine dry region (Strasser *et al.*, 2018). The Rofenache catchment ranges from 1891 to 3772 m a.s.l, with an annual mean temperature of 2.5°C at 1900 m a.s.l. (Strasser *et al.*, 2018). Snow cover commonly persists from October through until June at elevations above 3000 m a.s.l. Glaciers in the Otztal Alps, of which there are more than 50 (Abermann *et al.*, 2009; Rastner *et al.*, 2015), have been in retreat throughout the latter half of the 20th century and lost an average of 8.2% of their area between 1997 and 2006 (Abermann *et al.*, 2009).

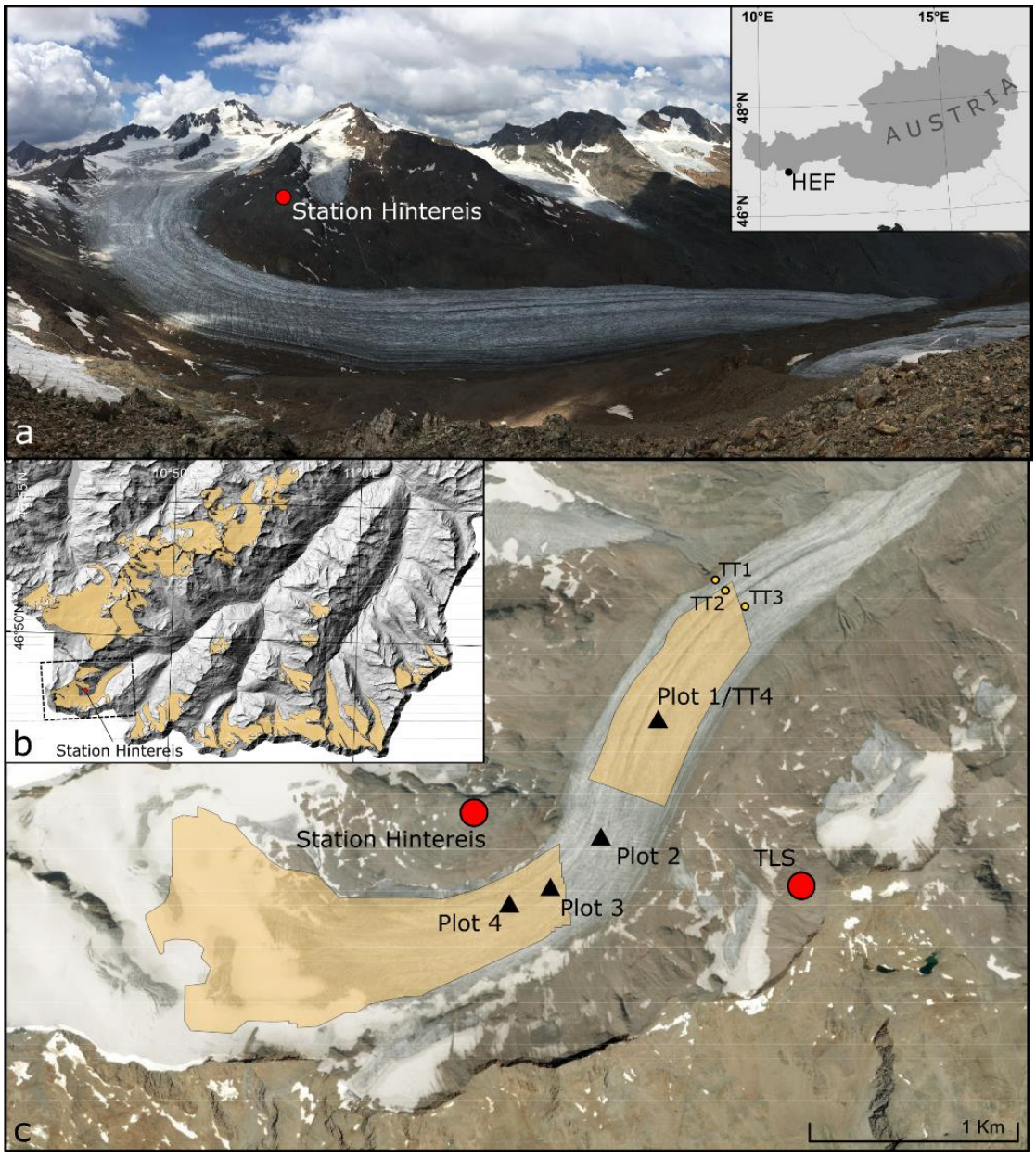

Fig. 5.1 Location of Hintereisferner (HEF). (a) A digital photograph taken from the TLS installation with the location of HEF within Austria (inset). (b) The Ötztal Alps region, Tyrol, using part of the ALS DEM used in this study (Open Data Austria, 2020), highlighted with polygons of glaciers > 0.5 km^2 (Buckel *et al.*, 2018). (c) Aerial imagery of HEF (ESRI; Orthophoto Tirol) with plot locations, upper/lower glacier TLS scan regions, Station Hintereis research base (2964 m a.s.l.) and TLS (3244 m a.s.l.).

HEF is ~6 km long and ranges in elevation from ~3740 m to the current (2018) terminus at 2498 m. It's present-day area is around 6.22 km2 but the glacier is receding rapidly, with an estimated reduction in area of 15% from 2001 to 2011, while the terminus retreated by around 390 m in the same decade (Klug et al., 2018). Mass balance records extend back to 1952/53 (Fischer, 2010) and HEF has been used as a type-site for gauging the overall health of Austrian glaciers and those of the wider European Alps, some of which, at current rates of retreat could be almost non-existent within a century (Vincent et al., 2017). Additional reconstructions suggest that HEF has been in near-constant retreat since the Little Ice Age, c.1855 (Greuell, 1992), with an increasing rate of mass loss as its tributary glaciers have become detached over the last two centuries (Fischer, 2010).

HEF has been the subject of a multitude of studies. Mass balance has been recorded using ablation stakes (Blümcke and Hess, 1899; Van De Wal et al., 1992; Kuhn et al., 1999) and numerical modelling (Escher-Vetter, 1985; Greuell, 1992; Schlosser, 1997; Fischer, 2010; Klug et al., 2018; Wijngaard et al., 2019). Remotely sensed data from airborne and satellite platforms have been used to study the glacier surface (Fritzmann et al., 2011), its reflectance properties (Koelemeijer et al., 1993) and allowed it to be included in valuable regional glacier inventories that document the decline of ice masses in the Alps (Patzelt, 1980; Lambrecht and Kuhn, 2007).

5.2.2 Data Collection

Data collection consisted of two main components: topographic surveys at multiple scales and meteorological data collection. Four plots were selected in the field (Fig. 5.2), chosen to be as distinct in surface appearance as possible bearing in mind the safety risk associated with installing instrumentation and manually surveying very steep or heavily crevassed plots. Plot 1 (Fig. 5.2a), the furthest down-glacier, was crosscut by supraglacial meltwater channels and was the most modified by melt processes having been exposed the longest after snowline retreat. Plot 2, shown in Fig. 5.2b, appeared smoother than Plot 1, with some low (<0.2 m) flow-parallel ridges, some perpendicular crevasse traces and small moulins. Plot 3 was centred on an area of streamlined, well defined longitudinal ridges with no discernible cross-glacier features (Fig. 5.2c). Plot 4 was the smoothest visually, with only minor surface variability and some small meltwater channels (Fig. 5.2d).

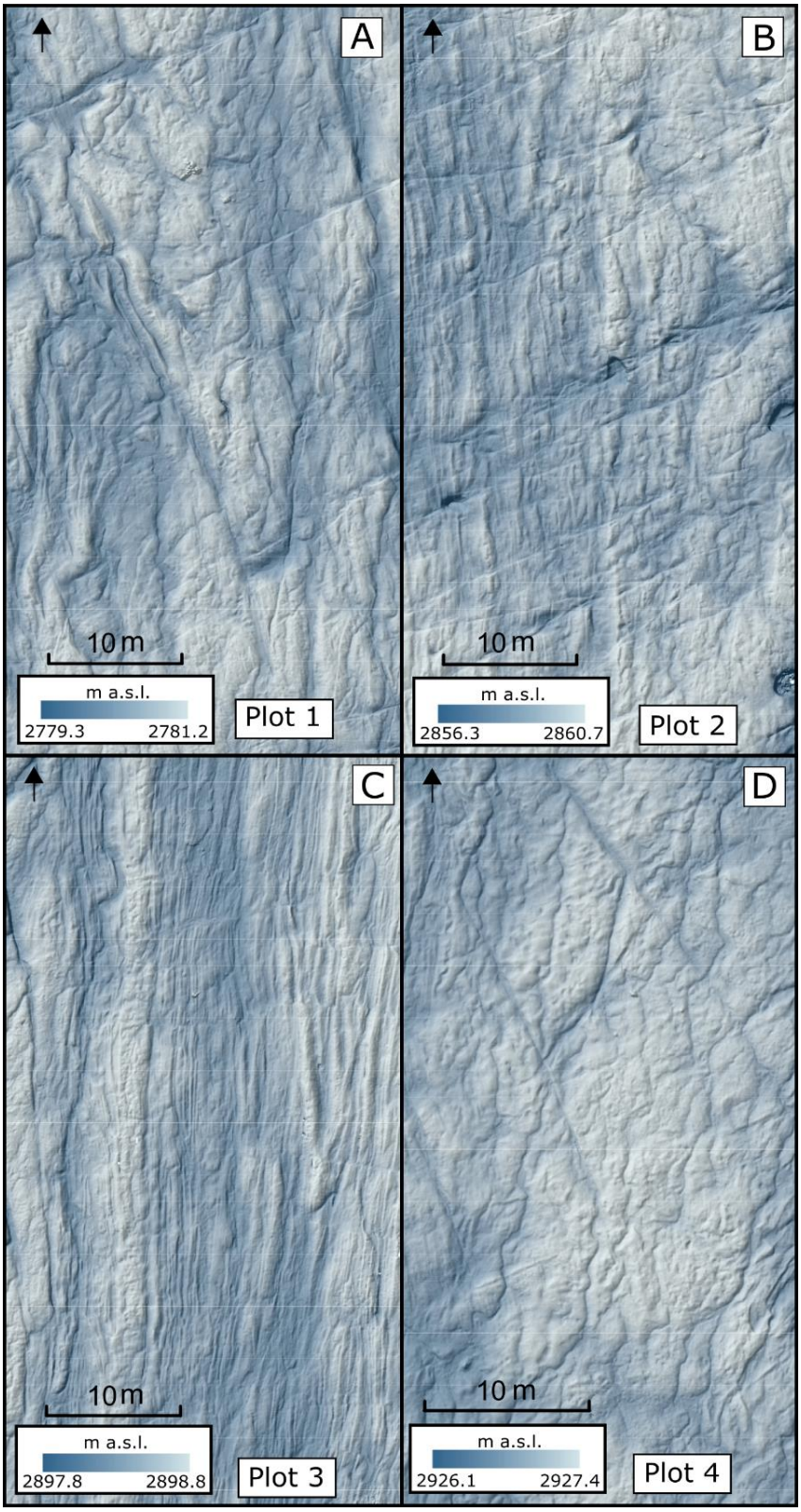

Fig. 5.2 Examples of hillshaded DEMs generated from UAV imagery of each Plot. Black arrows indicate glacier flow direction.

A wind tower was installed at each plot (see Section 5.2.7) during the period when topographic surveys were carried out. As fieldwork was completed near the peak of the

ablation season, air temperatures were positive for the study duration (Fig. 5.3a) with diurnal extremes of 3-4°C at night and 10-18°C during the day. The maximum temperature was 19.8°C recorded on 5th August and the minimum was 1.3°C on 8th August. Mean wind speed for the data collection period was 2.5 m s^{-1}, although occasionally fluctuated above 5 m s^{-1} (Fig. 5.3b). The maximum recorded was 7.7 m s^{-1} on 14th August, while the minimum was below the stall speed of the cup anemometers (<1 m s^{-1}) on multiple occasions. Wind direction was recorded relative to the down-glacier direction and was predominantly around 165°, indicating the presence of down-glacier flow characteristic of density driven katabatic winds (Fig. 5.3c), which were also observed by Mott *et al.* (2020). Convective storms accounted for the majority of precipitation, with notable events in the afternoons of the 1st, 6th, 10th and 13th August.

As part of HEFEX, four turbulence towers (TT1-4; Section 5.2.7) were present throughout the data collection period (Mott *et al.*, 2020). TT4 was located within Plot 1, while TT1-3 were installed further down-glacier. Independent estimates of z_0 from these towers was used for validation of topographic and wind tower z_0.

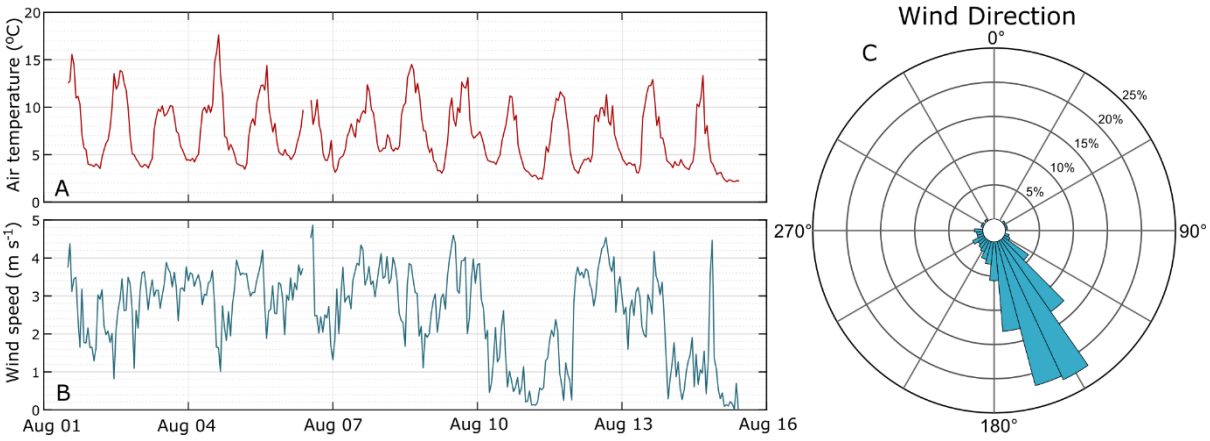

Fig. 5.3 Meteorological data collected during study period. Both air temperature (a) and wind speed (b) are shown as hourly averages at ~1 m above the glacier surface. A short gap in data on 6th August was caused by a hardware fault. Wind direction (c) is also hourly average with 0° set to the down glacier direction. All data are for Plot 1.

Topographic surveys

Topographic z_0 (z_{0DEM}) was estimated using topographic data obtained via five methods covering a range of scales:

Small plots (10 x 10 m): ground-based SfM using an Olympus OMD EM-10 camera mounted on a survey pole at ~6 m above ground level on 10, 11 and 13 August. z_0 from this method is

referred to as $z_{0Ground}$

Large plots (~30 x 70 m): ground-based SfM surveys encompassing [1], on 8, 10, 11, 12 and 13 August using the same camera as above but with the survey pole at ~9 m above the surface (z_{0Pole})

Airborne plot surveys: SfM surveys of the same plots/dates as [2] using a DJI Phantom 3 uncrewed aerial vehicle (UAV) with gimbal-stabilized digital camera at ~30 m above the surface (z_{0UAV})

Glacier-scale: the upper and lower glacier (see Fig. 5.1) was surveyed on 3, 7, 12 and 16 August using a RIEGL VZ-6000 TLS situated on the true right of the valley, near the summit of "im Hinteren Eis", a vantage point (Fig. 5.1a) from which most of the glacier surface can be seen (z_{0TLS})

Regional-scale: Airborne Laser Scan (ALS) data, obtained from flights in 2001-2009 (between August and October) using ALTM3000 ALS, data freely available (Open Data Austria, 2020) (z_{0ALS}).

5.2.3 Plot-scale SfM surveys ($z_{0Ground}$, z_{0Pole}, z_{0UAV})

SfM uses the principles of photogrammetry to digitally reconstruct surfaces or objects in 3D (Ullman, 1979; Brown and Lowe, 2005; Snavely *et al.*, 2008) and has been used to obtain estimates of z_0 on ice surfaces (Irvine-Fynn *et al.*, 2014; Smith *et al.*, 2016b; 2020; Chambers *et al.*, 2019). We followed the same principles for each SfM survey, based on workflows and recommendations in James *et al.* (2017) and O'Connor *et al.* (2017), completing surveys of Plot 1 on 10 and 13 August, Plot 2 on 8 August, Plot 3 on 11 August and Plot 4 on 12 August.

Camera specifications, camera calibration and survey area geometry (Table 5.1) were used to calculate the footprint of each image, which determined the distance between images required to achieve 60-80% overlap and the number of images needed for the survey area. Images were predominantly nadir and followed a regular grid pattern, with an additional ~10% of images taken obliquely (<20° off nadir). All survey plots were marked out using a regular grid of 9 ($z_{0Ground}$) or 21 (z_{0Pole} and z_{0UAV}) ground control points (GCPs), the locations of which were recorded using a Leica GS10 differential GPS, with a sub-centimetre mean accuracy for each plot. Typical 3D root mean square (RMS) control point error was ±0.03 m and RMS re-projection error was 1.66 pixels (2.6 μm). Uncertainty in z_0 estimates associated with the SfM process is assumed to be negligible, following previous analysis in

Chambers *et al.* (2019). Where z_{0DEM} values are given for any plot, the standard deviation of the relevant plot is also given as a proxy for any further uncertainties, and the same is included for z_{0TLS} values.

Table 5.1 Details of cameras used and survey design for SfM data collection

Specification	Ground	Pole	UAV
Camera make and model	Olympus OM-D E-M10/Canon Powershot SX600 HS	Olympus OM-D E-M10	Sony EXMOR 1/2.3”
Camera Lens model	M. Zuiko Digital 14–42 mm/Built-in	M. Zuiko Digital 14–42 mm	FOV 94° 20 mm (35 mm format equivalent) f/2.8
Sensor size (mm)	17.3 x 13.0/6.2 x 4.6	17.3 x 13.0	6.16 x 4.62
Image size (pixels)	4608 x 3456	4608 x 3456	4000 x 3000
Pixel pitch (µm)	3.74/1.34	3.74	1.54
Height above surface	6 m	~9 m	~30 m
Focal length (mm)	~28/~25	14	4
GSD (mm)	0.8/0.3	2.4	11.6
Max. (mean) images per plot	71 (64)	583 (465)	343 (274)
Camera locations	360° survey (inward facing)	Regular grid/~20% of image total 360° survey	Regular grid/~20% of image total 360° survey
Camera angle	~20° off nadir	Nadir/~20% of image total <20° off nadir	Nadir/~20% of image total <20° off nadir
Camera trigger	Manual	Remote (smartphone app)	Continuous with 2 s interval

Data were processed in Agisoft Photoscan Professional Edition Version 1.4.0 using the following settings: high accuracy, generic preselection enabled for all methods, reference preselection enabled for UAV surveys (as the position of the UAV is recorded for each image), camera calibration parameters F, Cx, Cy, K1-3 and P1 and P2 included, high reconstruction quality and aggressive depth filtering. Dense point clouds were imported into CloudCompare 2.10 (CloudCompare, 2020), where they were manually

inspected/cleaned. Digital elevation models (DEMs) were constructed using linear interpolation with nearest non-empty neighbours, ensuring a regular grid shape with the top of the grid aligned with the direction of flow (roughly South-North). DEMs were produced at each of the grid resolutions shown in Table 5.2, using all of the neighbourhood sizes also listed.

Table 5.2 List of grid resolutions and sliding neighbourhood sizes used in multi-scale analysis.

Source	Grid resolutions (m)	Sliding neighbourhood sizes (m x m)
$z_{0Ground}$	0.005	0.1, 0.5, 1, 5
	0.01	0.1, 0.5, 1, 5
	0.05	0.5, 1, 5
z_{0Pole}/z_{0UAV}	0.01	0.5, 1
	0.05	0.5, 1, 5, 10
	0.1	0.5, 1, 5, 10
	0.5	5, 10
	1	5, 10
z_{0TLS}	5	5, 10
	10	50, 100, 150
	20	100, 200
	30	150, 300

5.2.4 Glacier- and regional-scale surveys (z_{0TLS}, z_{0ALS})

A permanent *in-situ* Riegl VZ-6000 terrestrial laser scanner (TLS) was used to survey the majority of the glacier ablation zone using a near-infrared wavelength (1050 nm) suited to snow and ice surfaces (University of Innsbruck, 2020a). The TLS is housed in a climate-controlled container near the summit of "im Hinteren Eis" (46.79586° N, 10.78277° E, 3244 m a.s.l.). The point acquisition rate was approx. 23,000 points per second. Horizontal and vertical spatial resolution was ~0.17 m at 1000 m range, giving a theoretical density of 10 points per m^2 mid-glacier, and 2 points per m^2 at the head of the accumulation zone and near the terminus (University of Innsbruck, 2020b), due to the beam angle (Carrivick *et al.*, 2015). Validation of scans from this TLS suggests <0.15 m difference to ALS data and <0.1 m between TLS scans (University of Innsbruck, 2020b). Surveys were split into two sections, upper and lower glacier, and carried out on 3rd, 7th, 12th and 16th August 2018. TLS DEM creation was carried out using CloudCompare 2.10 (as described in Section 5.2.4).

Regional (gridded) elevation data were acquired for the entire Austrian Alps at 10 m

resolution (Open Data Austria, 2020). This regional product was created by interpolation of 2.5 m airborne laser scanning (ALS) data obtained during flights (details in Table B.1) over the Ötztal Alps, Tyrol, from 2006-2012 (Bollmann *et al.*, 2011; Fritzmann *et al.*, 2011; Sailer *et al.*, 2012; Fischer *et al.*, 2015). The reported vertical accuracy on relatively flat and smooth surfaces is ± 0.07 m (σ = 0.07 m), with an absolute standard error on slopes <37° of ± 0.04 m (Bollmann *et al.*, 2011; Sailer *et al.*, 2014). ALTM 3100 and Gemini ALS sensors were used in the Tyrol area, with an average density of 0.25 points m^{-1}. Glacier outlines were taken from the Austrian Glacier Inventory 4 (Buckel and Otto, 2018; Buckel *et al.*, 2018).

5.2.5 Topographic z_0 estimation and correction factor development

z_0 was estimated from topographic datasets using the DEM-based method of Smith *et al.* (2016) alongside a sliding neighbourhood operation, wherein an operation is applied to each cell of a grid with a specified number of surrounding cells forming the neighbourhood. The centre of the neighbourhood then slides to next cell until the operation has been applied to the entire grid. For this study, the sliding neighbourhood function within MATLAB© R2017a was used. This approach is similar to that used by Fitzpatrick *et al.* (2019) but differs in how each parameter is defined. Most DEM methods, including those of Smith *et al.* (2016), Fitzpatrick *et al.* (2019) and that used here, are based on the Lettau (1969) equation

$$z_0 = 0.5 h^* \frac{s}{S_A}, \tag{5.5}$$

where for each neighbourhood, 0.5 is the average drag coefficient of roughness elements, h^* is their average vertical extent (here we used twice the standard deviation of elevations over the detrended mean plane, mm, following Munro (1989)), s represents average silhouette area (mm^2) and S_A is the surface area of the neighbourhood in the horizontal plane (mm^2). s was calculated as the sum of the heights (mm) of all cells which visible above their respective preceding cell, as seen from the prevailing down-glacier wind direction, multiplied by cell width (mm). Detrending was performed on each neighbourhood by removing the best-fit plane. TLS- and ALS-derived DEMs were additionally detrended by subtracting the moving mean calculated at 5 x grid resolution, which removed coarse scale topography but preserved finer scale topographic variability, *i.e.* perturbations of <1 m (Glenn *et al.*, 2006; Smith, 2014). Resolution dependence was investigated by deriving z_{0DEM} from grids with incrementally increased resolutions as listed in Table 2, while scale dependence was investigated by incrementally increasing neighbourhood sizes.

Power law behaviour displayed at Plot 1 (surveys from Day 10) was used to develop

correction factors for each resolution. Correction factors were based on the quotient of modelled z_0 for different grid resolutions and wind tower-derived z_0 (z_{0WT}), which was available from more locations across the glacier than z_0 derived from turbulence towers (z_{0EC}). Correction factors (*CF*) were calculated using:

$$CF(Res) = \frac{z_{0WT}}{a+b(Res)}, \quad (5.6)$$

where *Res* is a given resolution, *a* is the intercept and *b* is the corresponding gradient of a power law model fitted to a plot of grid resolution and z_{0DEM}. The model fitted to the Plot 1 Day 10 data had a goodness of fit of r^2 = 0.4, RMSE of 3 mm and p <0.01, for 49 data points (47 degrees of freedom). The residuals of the model were normally distributed and displayed homoscedasticity when plotted against predicted values. While some scatter remained in corrected z_{0DEM} values, the predictive performance of the linear model was superior to non-linear models which were also tested, which under-predicted z_{0DEM} at coarser grid resolutions and over-corrected it as a consequence.

Correction factors were calibrated using the data from Plot 1, then validated with Plots 2, 3, 4 and data from Plot 1 on Day 13, then TLS DEMs of Hintereisferner. Finally, they were used to project z_{0DEM} values for the ALS DEMs of other local glaciers. An index of correction factor values for grids with resolutions of 0.005 m up to 30 m is included in Table 5.3.

5.2.6 Aerodynamic z_0 estimation (z_{0WT}, z_{0EC})

Two wind towers provided point-based profile z_0 measurements (z_{0WT}). Since the prevailing wind was down-glacier the wind towers were placed toward the down-glacier end of each of the 30 x 70 m plots, thereby capturing part of the tower footprint within the plots (Fitzpatrick *et al.*, 2019). One tower was placed at Plot 1 for the duration of the study and the second 'roving' tower, with the same set up as the first, was erected at Plot 2 from 5-8 August, Plot 3 from 8-12 August and Plot 4 from 12-15 August.

Each tower comprised five NRG 40 cup anemometers (uncertainty ±0.14 m s^{-1}; starting at 0.3, 0.65, 1.22, 1.79 and 2.32 m above the surface, re-measured at each visit), one NRG 200P (uncertainty ±1.6°) wind vane and five shielded and passively-ventilated Extech RHT10 temperature and humidity loggers (uncertainty ±1°C & ±3%), following previous installations and processing steps (Chambers *et al.*, 2019; Quincey *et al.*, 2017). Data were averaged over 15 minute intervals and processed using an r^2 filter of 0.99 for log-linear profile fits, a minimum wind speed threshold of 1 m s^{-1} and a stationarity filter of 0.25 °C m^{-1}. A stability correction based on Monin-Obukhov (MO) similarity theory was applied to all profiles, as is

common practice for glacier surfaces (Conway and Cullen, 2013; Stigter *et al.*, 2017; Steiner *et al.*, 2018).

Table 5.3 Index of correction factors for each grid resolution.

Grid resolution (m)	Neighbourhood size (m x m)	Correction Factor (log_{10})
0.005	0.1	0.22
0.005	0.5	0.22
0.005	1	0.22
0.005	5	0.22
0.01	0.1	0.32
0.01	0.5	0.32
0.01	1	0.32
0.01	5	0.32
0.05	0.5	0.56
0.05	1	0.56
0.05	5	0.56
0.05	10	0.56
0.1	0.5	0.66
0.1	1	0.66
0.1	5	0.66
0.1	10	0.66
0.5	5	0.9
0.5	10	0.9
1	5	1.01
1	10	1.01
5	25	1.25
5	50	1.25
5	100	1.25
10	50	1.35
10	100	1.35
10	150	1.35
20	100	1.45
20	200	1.45
30	150	1.51
30	300	1.51

Means and standard deviations for z_{0WT} are given in Table 5.4. The limited duration of data collection and other sources of uncertainty affect the results given by the wind tower method, which can end up yielding very few data points due to the prevalence of katabatic winds; in these conditions, where the wind speed maximum is close to the surface, profiles do not adhere to MO theory (Denby, 1999). The longest duration of wind tower data collection was available for Plot 1 (15 days), which was used to calibrate the parameters of the correction factor (equation 5.6). Despite the small number of profiles that fit MO theory

once corrected for atmospheric stability, the resulting dataset is more representative of typical atmospheric conditions than the shorter duration of other Plots. Values of z_{0WT} from Plots 2, 3 and 4 were used for comparison with other z_{0DEM} values, bearing in mind the inherent limitations of the method. Applying the MO stability correction ensured that, while the number of fitted profiles was smaller, profiles from katabatic conditions were not likely to be included erroneously.

Table 5.4 Summary of z_{0WT} (mm) from wind towers. Mean z_{0WT} for the entire measurement duration for each plot is shown, including mean z_{0WT} corrected for stability, with standard deviation (mm) in square brackets. *n* is the number of profiles that fit MO similarity theory.

Plot	z_0 (mm)	*n*	Corrected z_0 (mm)	*n*
1	18.77 [13.88]	30	3.05 [1.24]	2
2	26.37 [10.99]	142	17.68 [7.61]	22
3	5.18 [5.95]	151	6.67 [5.29]	3
4	22.59 [16.82]	101	19.19 [0.00]	1

The set-up of turbulence towers is described fully in Mott *et al.* (2020). On each tower, turbulence data were recorded by Campbell CSAT3 sonic anemometers at two levels, sampling at 20 Hz. Turbulent fluxes were calculated at 1 minute intervals and averaged to 30 minutes, and z_{0EC} (Table 5.5) was derived following Fitzpatrick *et al.* (2019), with assumed neutral stratification ($z/L > 0$ and $z/L < 0.2$) and additional quality control filters in place for atmospheric stability, wind direction (150 - 250°), minimum wind speed (2 m s^{-1}), friction velocity (> 0.1 m s^{-1}) and stationarity. TT4 was located next to the wind tower in Plot 1, with mean z_{0EC} for the entire study period providing an extra level of validation. Values of z_{0EC} from TT1-3 were used to provide independent validation, but did not overlap with any Plots or the TLS data.

Table 5.5 Summary of z_{0EC} (mm) from EC towers. Mean z_{0EC} for the entire measurement duration for both levels at each tower is shown with standard deviation (mm) in square brackets, including overall mean. *n* is the number of values that fit the quality control criteria.

	Level 1		Level 2		
EC tower	z_{0EC} (mm)	*n*	z_{0EC} (mm)	*n*	Mean z_{0EC} (mm)
TT1	7.68 [14.48]	31	13.7 [22.3]	27	10.7
TT2	6.5 [14.19]	51	10.29 [14.3]	34	8.39
TT3	7.62 [13.48]	24	8.46 [10.57]	22	8.04
TT4	2.29 [3.39]	76	1.84 [4.44]	71	2.07

5.3 Results

5.3.1 Scale and resolution relationships

Mean z_{0DEM} as an average of all topographic methods, was 1.6 mm (σ = 3.3 mm), compared to 3.05 mm (σ = 1.24 mm) for z_{0WT} and 2.07 mm (σ = 3.92 mm) for z_{0EC}. Fig. 5.4a shows that finer grid resolutions were associated with greater mean z_{0DEM} values for each resolution between 0.005 m (mean z_{0DEM} = 9.8 mm, σ = 7.5 mm) and 10 m (mean z_{0DEM} = 0.1 mm, σ = 0.05 mm). At coarser grid resolutions, i.e. 10, 20 and 30 m, mean z_{0DEM} increased by 0.1 mm to 0.3 mm; these resolutions had fewer associated data points and the <0.5 mm variation is considered inconsequential. Larger z_{0DEM} estimates were given at each resolution when larger neighbourhood sizes were used, which increased the scale over which z_{0DEM} was calculated. The average increase in z_{0DEM} when neighbourhood size was increased from the minimum was 0.7 mm (σ = 0.8 mm). Exceptions to this observation included resolutions of 0.005, 0.01, 5 and 20 m, where in each case there was one instance of decreased z_{0DEM} with an increase of neighbourhood size. Similar trends were observed for each of the other plots (Fig. 5.4c – f).

5.3.2 Correction factor calibration

Calibration of correction factors was performed on the data from Plot 1 Day 10 (Fig. 5.4a). Once grid resolution and z_{0DEM} were $\log_{10}$ transformed, the fitted linear model (with 95% confidence intervals) had an intercept of -0.52 ± 0.17 and slope of -0.34 ± 0.13 (RMSE = 3 mm; p <0.01, 47 degrees of freedom). Correction factors increased with resolution from 0.22 at 0.005 m to 1.51 at 30 m. Application of the correction factors, as shown in Fig. 5.4b, resulted in a shift in mean z_{0DEM} from 1.6 mm to 3.04 mm (σ = 3.1 mm). On average, z_{0DEM} was increased by 3.6 mm (σ = 3.1 mm). The mean difference between z_{0WT} and corrected z_{0DEM} was 2.2 mm (σ = 5.7 mm), and 3.15 mm (σ = 5.7 mm) between z_{0ECT} and corrected z_{0DEM}. Values of z_{0DEM} at the finest resolutions were slightly over-corrected, but the performance of the correction factors at the coarsest resolutions is the main focus, since it is desirable that similar corrections can be applied to coarse resolution data in other locations.

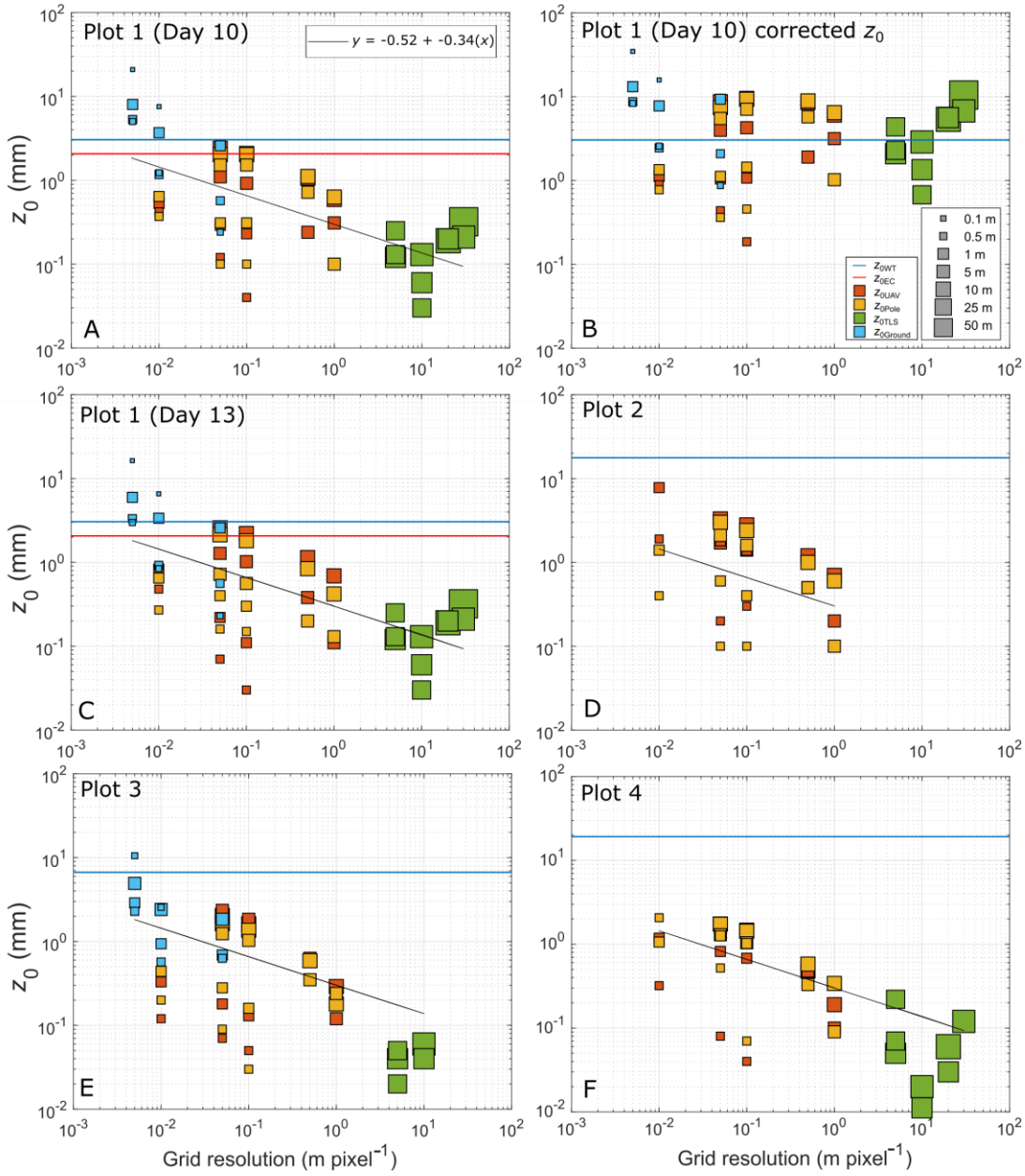

Fig. 5.4 DEM grid resolution against z_{0DEM} on log-log scale. Each data point represents z_{0DEM} calculated using a particular method, resolution and window size, extracted at the wind tower location within the Plot. (A) Plot 1 Day 10 uncorrected z_{0DEM}, along with power law model developed using Plot 1 Day 10 data. (B) Corrected z_{0DEM} for Plot 1 Day 10, where the correction factor for each DEM resolution is applied to raw input data. (C) Plot 1 Day 13 uncorrected z_{0DEM} with Plot 1 Day 10 model to demonstrate its applicability elsewhere. (D) Plot 2 uncorrected z_{0DEM}, again with model from Plot 1 Day 10 for illustration. (E) Plot 3 uncorrected z_{0DEM}. (F) Plot 4 uncorrected z_{0DEM}. The legends in (A) and (B) apply to all plots. The blue lines show z_{0WT} for each plot (see Table 4) and red line show z_{0EC} at Plot 1.

5.3.3 Correction factor validation

The model from Plot 1 Day 10 was applied to the data from the remaining Plots (Fig. 5.4c – f), where the fit and predictive capability was checked. The data from Plot 1 Day 13 (Fig. 5.4c) showed only minor differences to Plot 1 Day 10, including some small increases in z_{0DEM}, so

the performance of the model was similar (r^2 = 0.4). In Fig. 4d, the data from Plot 2 (limited to UAV and Pole surveys) show a similar spread to those at Plot 1 and the mean corrected z_{0DEM} was 3.8 mm (σ = 2.9 mm). The model appeared to describe the data less well (r^2 = 0.1) due to relatively high scatter compared to the more extensive datasets at other Plots. At Plot 3 (Fig. 5.4e) mean z_{0DEM} was corrected to 1.7 mm (σ = 3.6 mm), which may have been an under-correction compared to the other Plots arising from a smaller sample of z_{0TLS} data giving a weaker fit (r^2 = 0.3). Plot 4 (Fig. 5.4f) had the smallest z_{0TLS} values (minimum 0.01 mm) and the highest z_{0WT} values (19.2 mm). Here, mean z_{0DEM} was corrected to 2.1 mm (σ = 2.6 mm), with the model fitting the data as well as in Plot 1 (r^2 = 0.4).

5.3.4 Glacier-scale correction factor tests

Fig. 5.5 shows corrected z_{0TLS} calculated from glacier-scale TLS data, produced from 10 m resolution input data and 10 m x 10 m neighbourhoods. The lower glacier scan exhibited a smaller range of z_{0TLS} values (0.2 – 16.2 mm) than the upper (0.03 to 167.9 mm), with higher z_{0TLS} attributed to an area covered by a thin layer of supraglacial debris. The mean lower glacier z_{0TLS} was 1.7 mm (σ = 2.1 mm). The z_{0TLS} values for the upper glacier covered four orders of magnitude, which reflected the presence of both heavy crevassing and icefalls alongside areas of smooth ice and those that were still snow-covered or recently exposed. The mean z_{0TLS} for the upper glacier was 0.9 mm (σ = 4.3 mm), indicating that smoother surfaces were prevalent and that rougher surfaces caused extreme high z_{0TLS} in a minority of cases. Inset panels (Fig. 5.5i – 5.5v) show comparisons of the different z_{0DEM}, z_{0WT} and z_{0EC} values for each Plot.

Generally, corrected $z_{0Ground}$, z_{0UAV} and z_{0Pole} was smaller than z_{0WT}. Plot 1 Days 10 and 13 produced the most consistent z_{0DEM} values across all methods (Fig. 5.5i and 5.5ii), unsurprisingly given the model was calibrated to Plot 1. All z_{0DEM} was lower than z_{0WT} at Plots 2, 3 and 4; however, the observed z_{0WT} values at Plots 2 and 4 were unexpectedly high (see Section 5.4.1). Mean correction error for available data at Plots 1 and 3 was 1.9 mm (σ = 5.2 mm), 12 mm at Plot 2 and 16.1 mm at Plot 4. Plot 2 was not covered by TLS data so could not be compared fully. Plot 3 overlapped with the lower edge of the upper glacier scan, meaning z_{0TLS} was not available at resolutions of 20 and 30 m.

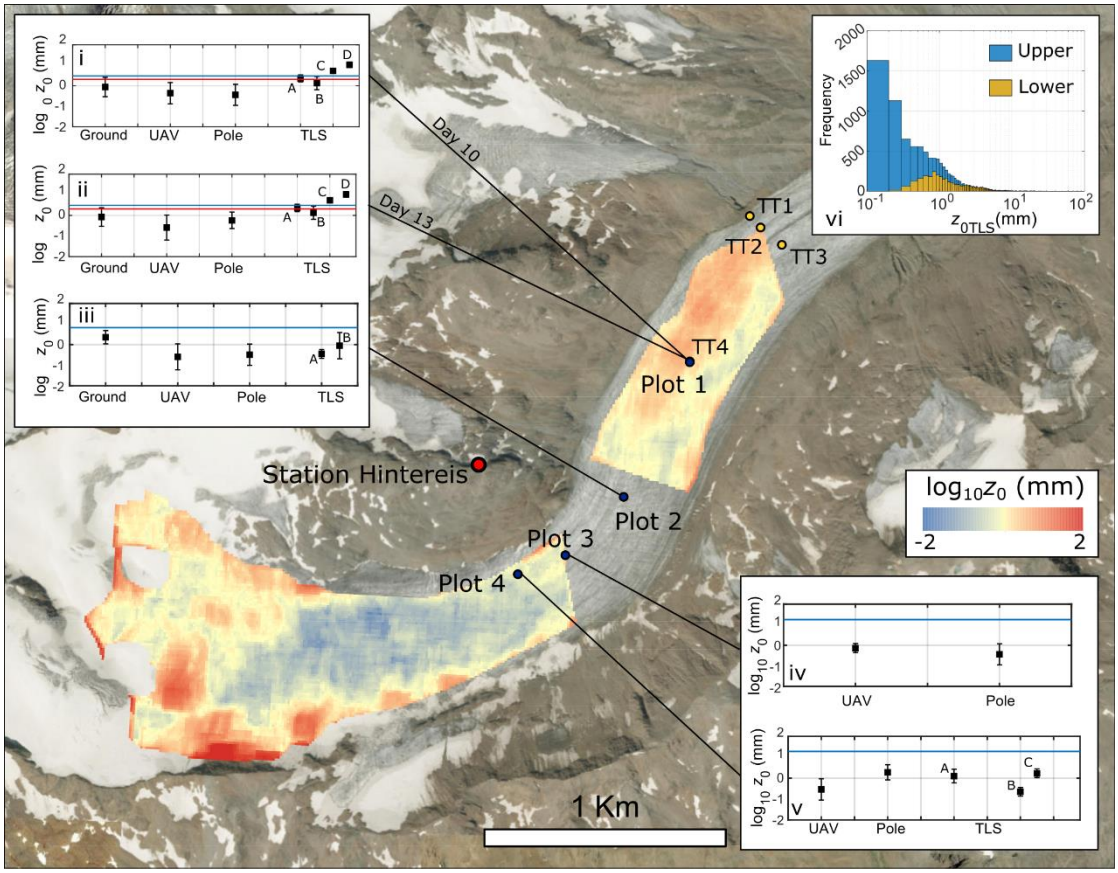

Fig. 5.5 Upscaled and corrected z_{0TLS}. Data shown is $\log_{10}$ transformed z_{0TLS} at 10 m resolution obtained using 10 x 10 m neighbourhoods. Inset graphs (i – v) show comparisons of z_{0DEM} from different sources with z_{0WT} (blue lines) and z_{0EC} (red lines) where data overlapped. Ground, UAV and Pole data used 0.05 m resolution/0.5 m neighbourhoods. TLS(A) used 5 m/50 m; TLS(B) 10 m/100 m; TLS(C) 20 m/200 m; TLS(D) 30 m/300 m. Error bars show the standard deviation of z_{0DEM} at all tested grid resolutions for each method. Inset (vi) shows the distribution of z_{0TLS} for the upper and lower glacier. The blue lines show z_{0WT} for each plot (see Table 4) and red lines show z_{0EC} at Plot 1.

5.3.5 Application to regional ALS data

In order to demonstrate the potential for use of this upscaling approach at other locations without wind tower validation, z_{0DEM} was calculated and corrected for glaciers surrounding Hintereisferner that are >0.5 km^2 in area. Comparing corrected z_{0ALS} and z_{0TLS} values over Hintereisferner (Fig. 5.6a and 5.6b), r^2 for the upper and lower glacier was 0.6 and 0.5 respectively (both p <0.01) suggesting that the distribution and values matched well (Fig. B.1). Due to the temporal misalignment between the datasets, z_{0ALS} was not expected to replicate z_{0TLS} exactly, yet the spatial patterns and the distributions of both upper and lower glacier are similar, and are included here for demonstration in Fig. 5.6a and 5.6b (insets). The sliding neighbourhood operation allowed z_0 to be estimated quickly for all glaciers at once from a single DEM of the region (Fig. 5.7a). A correction factor of 1.35 was selected from the index (Table 5.3) according to resolution and neighbourhood size (10 m pixel^{-1} resolution,

100 x 100 m neighbourhood size), and then applied to the uncorrected grid of $\log_{10} z_{0ALS}$.

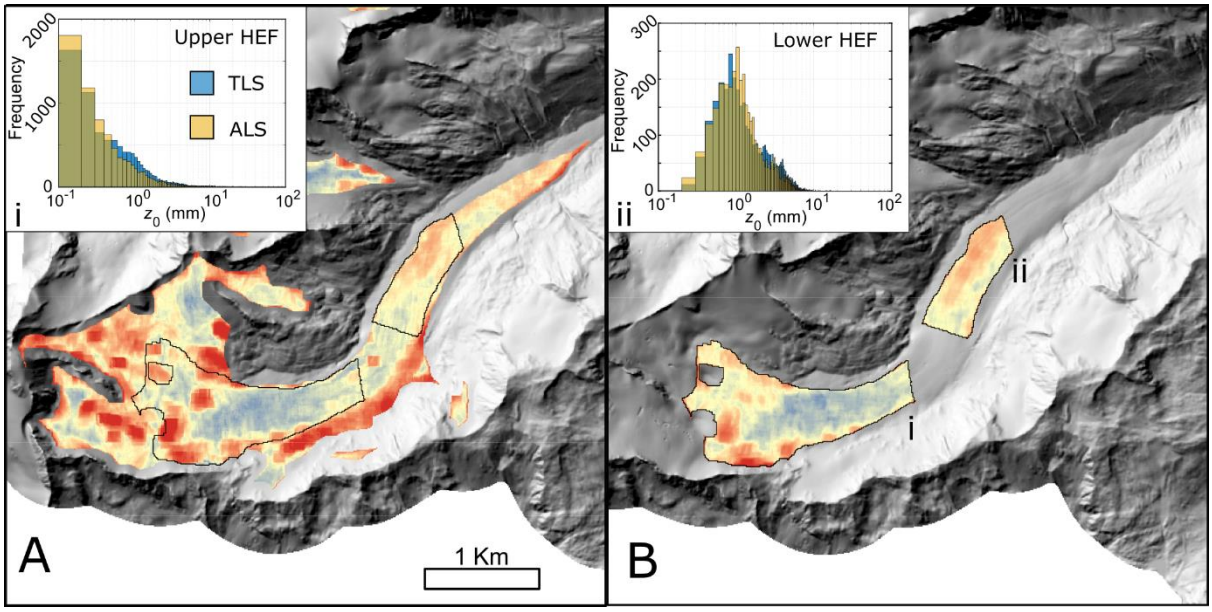

Fig. 5.6 Testing and implementation of correction factor. Corrected z_{0ALS} for HEF (A) with TLS area overlain. Corrected z_{0TLS} shown in (B). Comparison of distributions for upper (i) and lower (ii) glacier shown in insets – ALS data in front of TLS data.

Regionally, corrected z_{0ALS} was generally 0.1 – 10 mm (Fig. 5.7a). Zones of z_0 <0.1 mm coincided with the highest elevation areas where persistent snow cover is likely, while zones of 10 – 100 mm covered areas of supraglacial debris, medial moraine (Fig. 5.7c), light crevassing and rough ice. The roughest areas (>100 mm) matched heavily crevassed areas such as icefalls (Fig. 5.7b), ice margins and where the glacier polygon overlapped with bedrock. Extreme values of z_{0ALS} (>> 100 mm) were coincident with areas of very high relief, such as icefalls, heavy crevassing and ice-marginal where uncertainty in elevation data is greatest. Visual comparison of z_{0ALS} with inset images (Fig. 5.7b, c and d) confirmed that expected spatial distributions of z_0 can be derived from our workflow at the regional scale, as well as the glacier scale.

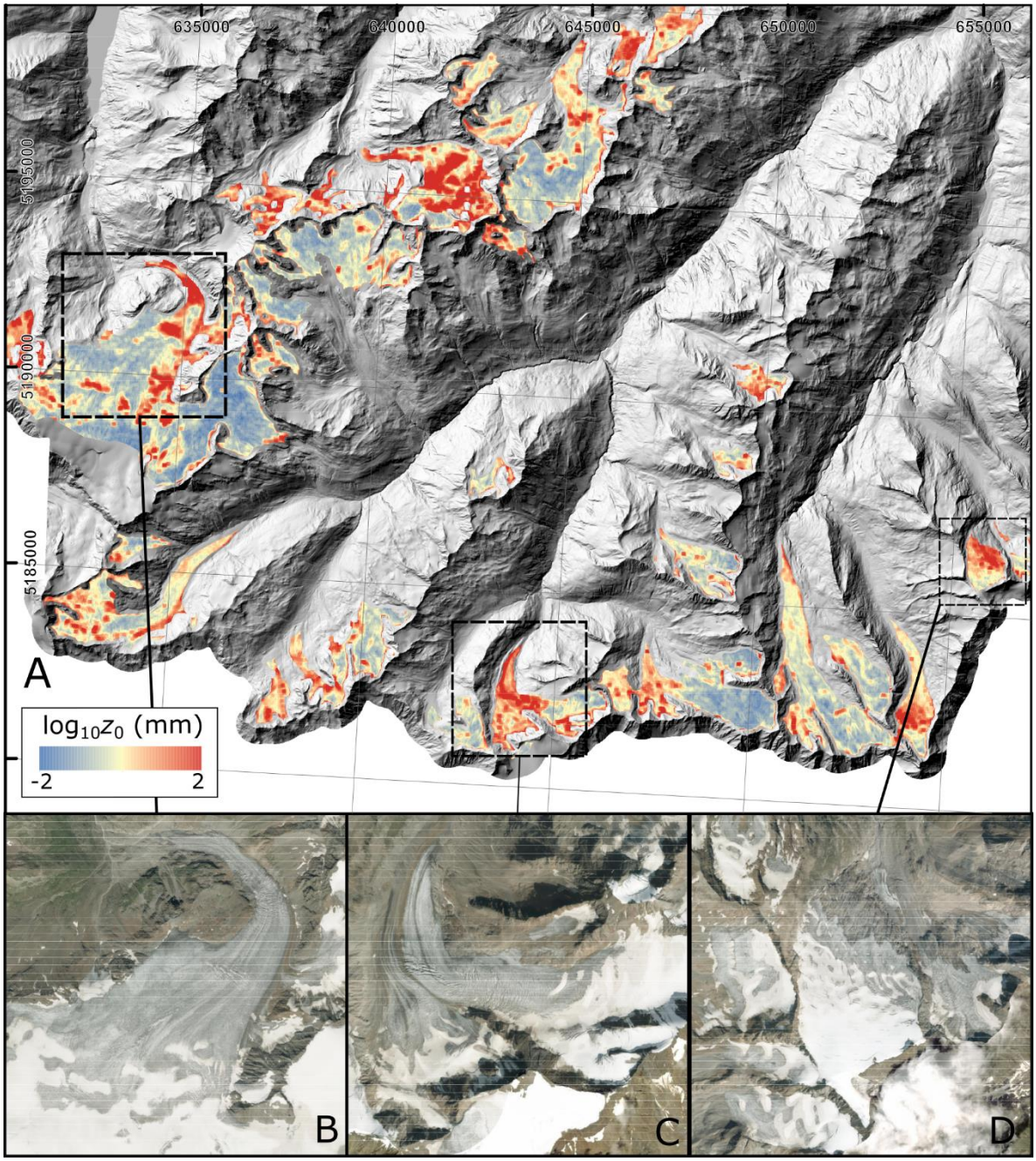

Fig. 5.7 Corrected z_{0ALS} for glaciers in the region around HEF (A). Lower images show enlarged imagery of select glaciers, including (B) Gepatsch Ferner, (C) Marzellferner and (D) Rotmoosferner (Source: ArcGIS World Imagery Basemap). Elevation data from Open Data Österreich (Digitales 10m - Geländemodell aus Airborne Laserscan Daten). Glacier outlines from Austrian Glacier Inventory 4 (Buckel & Otto, 2018). Glaciers restricted to those with area > 0.5 km^2. z_{0ALS} calculated using 100 m neighbourhoods. All z_0 is log10 transformed.

5.4 Discussion

5.4.1 Robustness of z_0 estimates

Several studies have demonstrated similarity between topographic and aerodynamic z_0 over glaciers at the plot-scale (see Brock *et al.*, 2006 & Miles *et al.*, 2017 for extensive compilations), lending confidence to our topographic estimates at finer resolutions. The

values we obtained for 10 x 10 m and 30 x 70 m plots using ground-based, UAV and pole-based surveys fall well within expected bounds (same order of magnitude) of z_0 for an ablating Alpine glacier (~0.1 – 10 mm; c.f. Munro, 1989; Brock *et al.*, 2006), with the exception of the finest resolutions of 0.005 m. Power law behaviour was observed in the distribution of 3D z_{0DEM} against DEM grid resolution (Fig. 5.4), as also shown by Rees and Arnold (2006) for 2D transect z_0 estimates. Where Rees and Arnold (2006) noted a difficulty in obtaining a dataset that spanned a continuous range of scales and resolutions, modern survey techniques have afforded us the opportunity to collect and analyse data at resolutions across five orders of magnitude and at scales across four orders.

The z_{0DEM} estimates within this study are also comparable to those given for different surfaces on Hintereisferner obtained using a slightly different topographic approach (Smith *et al.*, 2020). A temporal model developed in Smith *et al.* (2020) noted that z_0 was generally associated with the length of time that ice surface areas had been exposed by snow melt, as well as by physical factors such as surface gradient, which accounts for some of the highest z_0 values. The z_{0TLS} values for rougher surfaces like crevasses and a rock pedestal were more extreme in this study compared to the plots used by Smith *et al.* (2020), which were up to ~20 mm, compared to 10^2 mm in this study. It is likely that our data incorporated some ice-marginal areas given the mismatch in resolutions between the TLS data and the glacier outline polygons derived from coarser resolution imagery. Other characteristic ice surfaces, such as the smooth/dirty ice, supraglacial channel and pressure ridge plots surveyed at the plot-scale in detail by Smith *et al.* (2020) compare well with the estimates of z_{0DEM} here (within <5 mm generally).

The sliding neighbourhood algorithm used to obtain z_{0DEM} estimates in this study is similar to that described and used by Fitzpatrick *et al.* (2019), who used sliding neighbourhoods to calculate a "drag parameter" (F_{D_local}). Fitzpatrick *et al.* then attempted to account for fetch when calculating z_0 for a point (z_{0_bloc}) by equally weighting all cells within an area then finding their sum. Despite some minor differences in the initial calculation of each parameter, the range of values found for F_{D_local} by Fitzpatrick *et al.* (2019) is the same as the range of corrected z_{0DEM} values found in this study (~10^{-5} to ~10^0 m). For further comparison, we also calculated z_{0_bloc} for the z_{0UAV} grids of each Plot, by equally weighting z_0 within all cells and finding their sum. We found that the given z_{0_bloc} values from our Plots were at least an order of magnitude smaller than corrected z_{0UAV} values. It is worth noting that the area used for calculating z_{0_bloc} here was only ~70 x 30 m, compared to the ~2000 x 2000 m used by Fitzpatrick *et al.* (2019), so the smaller order of magnitude is likely to be a function of the

smaller number of values within a plot. Additionally, we consider the sliding neighbourhood method used here to be more practical when trying to model glacier-wide z_0 for use in a distributed SEB model because it does not require topographic data from beyond the margins of the glacier; although fetch is not explicitly accounted for, doing so would require the incorporation of turbulence characteristics across different surfaces and especially near the margins of the glacier (Nicholson and Stiperski, 2020), which would detract from the intended simplicity of our approach.

A key area of uncertainty exists in the z_{0WT} values derived from Plots 2 (17.86 mm) and 4 (19.18 mm), which were both greater than expected considering field observations of the surface characteristics, z_{0WT} and z_{0EC} values at other plots and those from similar glaciers (e.g. Brock *et al.*, 2006). Confidence in the value at Plot 4 is low because only one z_0 value was obtained after stability correction; conversely, confidence is higher for Plot 2, where the 22 values given (Table 5.4) suggest either (i) potential underestimation by topographic methods or (ii) a stronger wind speed gradient likely due to a near-surface wind speed maximum under katabatic conditions (c.f. Mott *et al.*, 2020). While z_{0WT} values were included for comparison, we acknowledge that the short duration of data collection at Plots 2, 3 and 4 (<4 days for each) reduces confidence in their results. It is typical to collect much longer time-series in order to ensure that the average aerodynamic properties of the surface are captured even after aggressive data filtering (Stull, 1988; Radić *et al.*, 2017; Fitzpatrick *et al.*, 2019). These uncertainties further highlight the merits of a topographic approach, which does not rely on a lengthy field campaign.

We are confident that the longer data collection period at Plot 1 (2 weeks) was sufficient for it to be used to calibrate the parameters of the correction factor and that, at worst, it indicated the likely order of magnitude of z_0. This is supported by topographic estimates of z_0, which were similar for Days 10 and 13, and by the mean z_{0EC} values for the same Plot which was less than 1 mm smaller and had a standard deviation that would still put z_0 within the same order of magnitude. Other theoretical and methodological flaws in the retrieval of z_0 from wind profiles and EC data using MO similarity theory, such as the likely presence of katabatic winds (Mott *et al.*, 2020) and collecting data over an ablating surface (Denby, 1999; Denby and Greuell, 2000; Litt *et al.*, 2014; Radić *et al.*, 2017), deterred us from seeking a perfect match between corrected z_{0DEM} and z_{0WT}.

5.4.2 Correction factor performance

The correction factor was developed by calibrating topographic z_0 from Plot 1 with z_{0WT} for the same plot, assuming z_{0DEM} to be representative of a portion of the footprint of the wind tower (c.f. Fitzpatrick *et al.*, 2019). Our goal was to match the wind-tower-derived z_0 values to within an order of magnitude. Small differences in z_0 will alter resultant turbulent flux values, but it is unreasonable to simply accept any one value as being absolute because z_0 changes rapidly in both time and space over several orders of magnitude (Smith *et al.*, 2016b; 2020). Furthermore, it is difficult to measure a 'true' value of z_0, as even EC data (often seen as the benchmark) relies to an extent on modelling and associated embedded assumptions (Cullen *et al.*, 2007; Radić *et al.*, 2017). Therefore, z_{0WT} values were used as a calibration point to ensure z_{0DEM} was calibrated to within an order of magnitude of the true z_0. Of course, further aerodynamic data from this and other regions would strengthen the upscaling workflow developed here. However, this upscaling method provides a more reasonable estimate of distributed z_0 than is achievable using aerodynamic methods by themselves or through the use of past topographic z_0 techniques.

From visual inspection, and bearing in mind the absence of validation data beyond Hintereisferner itself, the correction factor appears to produce a realistic representation of spatial z_0 variability at multiple scales (Fig. 5.6) when resulting values are compared to past studies. Spatial patterns in the derived values are maintained and correspond to areas that appear smoother/rougher based on surface features identified in satellite imagery. Areas of dubiously high values ($> 10^2$ mm) are coincident with areas where the DEM is least reliable, including heavily crevassed regions, icefalls and other areas of high relief (Sailer *et al.*, 2014). While the distribution of z_0 matches expectations from the perspective of surface roughness, it is worth noting that the footprint, or fetch, of each particular DEM cell is not considered. The fetch includes all aerodynamically important areas upwind of a point (Kljun *et al.*, 2015) which, over glaciers, has been observed to extend from ~100 m to 200 m, depending on the wind speed (Fitzpatrick *et al.*, 2019). This leads to the question of how the sharp transitions between areas of contrasting roughness that can be seen in Figs 5.5 and 5.6 can be accounted for in a straightforward model such as that used in this study, or indeed if they can be at all, as the nature of turbulent air flow over glaciers is extremely complex when considering the influence of the valley sides, different surfaces and tributary valleys (Stiperski and Rotach, 2016; Mott *et al.*, 2020; Nicholson and Stiperski, 2020). It may be possible to account for fetch in topographic models in the future, considering advances in the availability of fine-resolution fields of meteorological variables such as wind speed (Sauter and Galos, 2016) and

capabilities for modelling their interactions with terrain at small (100 m) scales (Fiddes and Gruber, 2014; Peleg *et al.*, 2017). That being said, the topographic z_0 methods employed here were developed only to use the properties of a surface to produce a value similar to an aerodynamically-derived value for the same point (Lettau, 1969; Munro, 1989); our workflow is intended to retain this rationale whilst indicating broader patterns. Additional complexities could be factored in with further work, depending on the application.

5.4.3 Implications

Use of the correction factor presented here allowed a realistic z_0 value to be derived from a relatively coarse resolution DEM of Hintereisferner, Austria, of the type typically available for whole glacierized regions of the cryosphere. Additional testing and ground-truthing, ideally with sonic anemometers, would allow further calibration of the power laws and correction factors, especially in areas with varying debris sizes and coverage (e.g. Miles *et al.*, 2017; Nicholson and Stiperski, 2020) and in areas covered by snow, that were not sampled in our study. Our workflow is an advance in the use of topographic methods for estimating z_0 that can be applied (with caution until further validated) to other glaciers without the need for additional field data collection. It provides a more robust estimate of z_0 than is achievable by collecting 2D transects, or by implementing z_0 values borrowed from the literature and we foresee that the prevailing practice of using a constant or assumed z_0 value in both distributed and single-point SEB models could potentially be eliminated.

A worthwhile additional step will be to develop the workflow for spatially distributed z_0 grids established here into a model that includes a temporal dimension. Fully distributed z_0 could then be incorporated in a distributed surface energy balance (SEB) model, to analyse the effects that this new quantification of z_0 has on the turbulent fluxes and resultant meltwater production. This development would be especially useful when combined with the more widespread availability of national ALS campaign datasets (such as that used herein for Austria), or regional DEM datasets such as the ArcticDEM, the Reference Elevation Model for Antarctica and the High Mountain Asia DEM (Shean, 2017; Porter *et al.*, 2018; Howat *et al.*, 2019) and increasing availability of multi-temporal DEMs from platforms such as WorldView 2, Pléiades and Geo-Eye-1 (Belart *et al.*, 2017, Shean *et al.*, 2020). A work-flow diagram is provided in the Supplementary Information (Fig. B.2) to facilitate replication of the method, with the caution that full testing across different sites exhibiting a variety of surface characteristics, and using topographic data from a range of different sources, is still required.

5.5 Conclusions

We carried out a multi-scale investigation of topographic z_0 over Hintereisferner, Austria. Data from SfM, TLS and ALS were employed to rapidly capture z_0 at resolutions from sub-cm to 30 m. z_0 values exhibited a power law behaviour with data resolution. From this relationship we devised correction factors that adjusted topographic z_0 so that it was within an order of magnitude of previously validated, more robust values from both finer resolutions and z_0 calculated from wind profiles. While sensitivities and uncertainties in z_0 estimates persist due to scale/resolution dependence and the simplification of aerodynamic processes, the method presented here has allowed z_0 to be rapidly estimated at the glacier scale, capturing more detail and variability than is possible with point-scale or 2D techniques. We used the same upscaling method to demonstrate how topographic z_0 can be estimated at the glacier scale across an entire region. Further analysis for sites within different climatic zones is required to calibrate the correction factors, but the workflow provides a robust foundation for obtaining spatially distributed z_0 without the need for lengthy field campaigns with delicate meteorological equipment, by being compatible with regional elevation datasets that are increasingly becoming publicly available.

Acknowledgments

We gratefully acknowledge the use of the TLS facility and data, financed by the University of Innsbruck and jointly operated by the Department of Geography and the Department of Atmospheric and Cryospheric Research. We thank the reviewers for their helpful and constructive feedback that greatly improved this manuscript. We also thank an anonymous reviewer for their comments on an earlier draft of the manuscript.

References

Abermann, J., Lambrecht, A., Fischer, A. & Kuhn, M. (2009) 'The Cryosphere Quantifying changes and trends in glacier area and volume in the Austrian Otztal Alps (1969-1997-2006)', *The Cryosphere*, 3, pp. 205–215. Available at: www.the-cryosphere.net/3/205/2009/.

Anderson, B., Mackintosh, A., Stumm, D., George, L., Kerr, T., Winter-Billington, A. & Fitzimons, S. (2010) 'Climate sensitivity of a high-precipitation glacier in New-Zealand', *Journal of Glaciology*, 56(195), pp. 114-128(15). doi: 10.3189/002214310791190929.

Blümcke, A. & Hess, H. (1899) 'Untersuchungen am Hintereisferner', der Deutsche und Österreichische Alpenverein.

Bollmann, E., Sailer, R., Briese, C., Stotter, J. & Fritzmann, P. (2011) 'Potential of airborne laser scanning for geomorphologie feature and process detection and quantifications in high alpine mountains', *Zeitschrift fur Geomorphologie*, 55(SUPPL. 2), pp. 83–104. doi: 10.1127/0372-8854/2011/0055S2-0047.

Bravo, C., Loriaux, T., Rivera, A. & Brock, B. W. (2017) 'Assessing glacier melt contribution to streamflow at Universidad Glacier, central Andes of Chile', *Hydrology and Earth System Sciences*, 21(7), pp. 3249–3266. doi: 10.5194/hess-21-3249-2017.

Brock, B. W., Willis, I. C. & Sharp, M. J. (2006) 'Measurement and parameterization of aerodynamic roughness length variations at Haut Glacier d'Arolla, Switzerland', *Journal of Glaciology*, 52(177), pp. 281–297. doi: 10.3189/172756506781828746.

Brown, M. & Lowe, D. G. (2005) 'Unsupervised 3D Object Recognition and Reconstruction in Unordered Datasets', *Proceedings of the Fifth International Conference on 3-D Digital Imaging and Modeling*. doi: 10.1109/3DIM.2005.81.

Buckel, J. & Otto, J. C. (2018) 'The Austrian Glacier Inventory GI 4 (2015) in ArcGis (shapefile) format.', *Pangaea*. doi: https://doi.org/10.1594/PANGAEA.887415.

Buckel, J., Otto, J. C., Prasicek, G. & Keuschnig, M. (2018) 'Glacial lakes in Austria - Distribution and formation since the Little Ice Age', *Global and Planetary Change*, 164, pp. 39–51. doi: 10.1016/j.gloplacha.2018.03.003.

Carrivick, J. L., Smith, M. W. & Carrivick, D. M. (2015) 'Terrestrial laser scanning to deliver high-resolution topography of the upper Tarfala valley, arctic Sweden', *Gff*, 137(4), pp. 383–396. doi: 10.1080/11035897.2015.1037569.

Chambers, J. R., Smith, M. W., Quincey, D. J., Carrivick, J. L., Ross, A. N. & James, M. R. (2019) 'Glacial Aerodynamic Roughness Estimates: Uncertainty, Sensitivity, and Precision in Field Measurements', *Journal of Geophysical Research: Earth Surface*, 125(2). doi: 10.1029/2019JF005167.

CloudCompare (2020) *CloudCompare*. Available at: http://cloudcompare.org/ (Accessed: 20 August 2020).

Conway, J. P. & Cullen, N. J. (2013) 'Constraining turbulent heat flux parameterization over a temperate maritime glacier in New Zealand', *Annals of Glaciology*, 54(63), pp. 41–51. doi: 10.3189/2013AoG63A604.

Cullen, N. J., Mölg, T., Kaser, G., Steffen, K. & Hardy, D. R. (2007) 'Energy-balance model validation on the top of Kilimanjaro, Tanzania, using eddy covariance data', *Annals of*

Glaciology, 46, pp. 227–233. doi: 10.3189/172756407782871224.

Denby, B. (1999) 'Second-order modelling of turbulence in katabatic flows', *Boundary-Layer Meteorology*, 92(1), pp. 65–98.

Denby, B. & Greuell, W. (2000) 'The Use of Bulk and Profile Methods for Determining Surface Heat Fluxes in the Presence of Glacier Winds', *Journal of Glaciology*, 46(154), pp. 445–452.

Escher-Vetter, H. (1985) 'Energy Balance Calculations for the Ablation Period 1982 at Vernagtferner, Oetztal Alps.', *Annals of Glaciology*, 6, pp. 158–60. doi: doi:10.3189/1985AoG6-1-158-160.

Fausto, R. S., Van As, D., Box, J. E., Colgan, W., Langen, P. L. & Mottram, R. H. (2016) 'The implication of nonradiative energy fluxes dominating Greenland ice sheet exceptional ablation area surface melt in 2012', *Geophysical Research Letters*, 43(6), pp. 2649–2658. doi: 10.1002/2016GL067720.

Fiddes, J. & Gruber, S. (2014) 'TopoSCALE v.1.0: Downscaling gridded climate data in complex terrain', *Geoscientific Model Development*, 7(1), pp. 387–405. doi: 10.5194/gmd-7-387-2014.

Fischer, A. (2010) 'Glaciers and climate change: Interpretation of 50 years of direct mass balance of Hintereisferner', *Global and Planetary Change*, 71(1–2), pp. 13–26. doi: 10.1016/j.gloplacha.2009.11.014.

Fischer, A., Seiser, B., Stocker Waldhuber, M., Mitterer, C. & Abermann, J. (2015) 'Tracing glacier changes in Austria from the Little Ice Age to the present using a lidar-based high-resolution glacier inventory in Austria', *Cryosphere*, 9(2), pp. 753–766. doi: 10.5194/tc-9-753-2015.

Fitzpatrick, N., Radić, V. & Menounos, B. (2019) 'A multi-season investigation of glacier surface roughness lengths through in situ and remote observation', *The Cryosphere*, 13, pp. 1051–1071. doi: https://doi.org/10.5194/tc-13-1051-2019.

Fritzmann, P., Hone, B., Vetter, M., Sailer, R., Stotter, J. & Bollmann, E. (2011) 'Surface classification based on multi-temporal airborne lidar intensity data in high mountain environments a case study from hintereisferner, Austria', *Zeitschrift fur Geomorphologie*, 55(SUPPL. 2), pp. 105–126. doi: 10.1127/0372-8854/2011/0055S2-0048.

Garratt, J. R. (1992) *The Atmospheric Boundary Layer*. Cambridge: Cambridge University Press.

Giesen, R. H., Andreassen, L. M., Oerlemans, J. & Van Den Broeke, M. R. (2014) 'Surface energy balance in the ablation zone of Langfjordjøkelen, an arctic, maritime glacier in northern Norway', *Journal of Glaciology*, 60(219), pp. 57–70. doi: 10.3189/2014JoG13J063.

Glenn, N. F., Streutker, D. R., Chadwick, D. J., Thackray, G. D. & Dorsch, S. J. (2006) 'Analysis of LiDAR-derived topographic information for characterizing and differentiating landslide morphology and activity', *Geomorphology*, 73(1–2), pp. 131–148. doi: 10.1016/j.geomorph.2005.07.006.

Greuell, W. (1992) 'Hintereisferner, Austria: ntass-balance reconstruction and nunterical ntodelling of the historical length variations', *Journal of Glaciology*, 38(129), pp. 233–244. doi: https://doi.org/10.3189/S0022143000003646.

Hock, R. (2005) 'Glacier melt: a review of processes and their modelling', *Progress in*

Physical Geography, 29(3), pp. 362–391. doi: 10.1191/0309133305pp453ra.

Howat, I. M., Porter, C., Smith, B. E., Noh, M. J. & Morin, P. (2019) 'The reference elevation model of antarctica', *Cryosphere*, 13(2), pp. 665–674. doi: 10.5194/tc-13-665-2019.

Irvine-Fynn, T. D. L., Sanz-Ablanedo, E., Rutter, N., Smith, M. W. & Chandler, J. H. (2014) 'Measuring glacier surface roughness using plot-scale, close-range digital photogrammetry', *Journal of Glaciology*, 60(223), pp. 957–969. doi: 10.3189/2014JoG14J032.

James, M. R., Robson, S., D'Oleire-Oltmanns, S. & Niethammer, U. (2017) 'Optimising UAV topographic surveys processed with structure-from-motion: Ground control quality, quantity and bundle adjustment', *Geomorphology*, 280, pp. 51–66. doi: 10.1016/j.geomorph.2016.11.021.

Klug, C., Bollmann, E., Galos, S. P., Nicholson, L., Prinz, R., Rieg, L., Sailer, R., Stötter, J. & Kaser, G. (2018) 'Geodetic reanalysis of annual glaciological mass balances (2001-2011) of Hintereisferner, Austria', *Cryosphere*, 12(3), pp. 833–849. doi: 10.5194/tc-12-833-2018.

Koelemeijer, R. T., Ohannes, J. & Tjemkes, S. (1993) 'Surface reflectance of Hintereisferner, Austria, frotn Landsat 5 TM itnagery', *Annals of Glaciology*, 17, pp. 17–22. doi: https://doi.org/10.3189/S0260305500012556.

Kuhn, M., Dreiseitl, E., Hofinger, S., Markl, G., Span, N. & Kaser, G. (1999) 'Measurements and Models of the Mass Balance of Hintereisferner', *Geografiska Annaler, Series A: Physical Geography*, 81(4), pp. 659–670. doi: 10.1111/1468-0459.00094.

Lambrecht, A. & Kuhn, M. (2007) 'Glacier changes in the Austrian Alps during the last three decades, derived from the new Austrian glacier inventory', *Annals of Glaciology*, 46, pp. 177–184. doi: https://doi.org/10.3189/172756407782871341.

Lemmens, M. (2011) 'Terrestrial Laser Scanning', in *Geo-information*, pp. 101–121. doi: 10.1007/978-94-007-1667-4.

Lettau, H. (1969) 'Note on Aerodynamic Roughness-Parameter Estimation on the Basis of Roughness-Element Description', *Journal of Applied Meteorology*, 8(5), pp. 828–832. doi: http://dx.doi.org/10.1175/1520-0450(1969)008<0828:NOARPE>2.0.CO;2.

Lewis, K. J., Fountain, A. G. & Dana, G. L. (1998) 'Surface energy balance and meltwater production for a Dry Valley glacier, Taylor Valley, Antarctica', *Annals of Glaciology*, 27, pp. 603–609. doi: 10.3189/1998AoG27-1-603-609.

Litt, M., Sicart, J. E., Helgason, W. D. & Wagnon, P. (2014) 'Turbulence Characteristics in the Atmospheric Surface Layer for Different Wind Regimes over the Tropical Zongo Glacier (Bolivia, 16∘S)', *Boundary-Layer Meteorology*, 154(3), pp. 471–495. doi: 10.1007/s10546-014-9975-6.

Litt, M., Sicart, J. E., Six, D., Wagnon, P. & Helgason, W. D. (2017) 'Surface-layer turbulence, energy balance and links to atmospheric circulations over a mountain glacier in the French Alps', *Cryosphere*, 11(2), pp. 971–987. doi: 10.5194/tc-11-971-2017.

Liu, J., Chen, R. & Han, C. (2020) 'Spatial and temporal variations in glacier aerodynamic surface roughness during the melting season, as estimated at the August-one ice cap, Qilian mountains, China', *Cryosphere*, 14(3), pp. 967–984. doi: 10.5194/tc-14-967-2020.

Miles, E. S., Steiner, J. F. & Brun, F. (2017) 'Highly variable aerodynamic roughness length (z0) for a hummocky debris-covered glacier', *Journal of Geophysical Research: Atmospheres*, 122(16), pp. 8447–8466. doi: 10.1002/2017JD026510.

Mott, R., Stiperski, I. & Nicholson, L. (2020) 'Spatio-temporal flow variations driving heat exchange processes at a mountain glacier', *Cryosphere*, 14(12), pp. 4699–4718. doi: 10.5194/tc-14-4699-2020.

Munro, D. S. (1989) 'Surface roughness and bulk heat transfer on a glacier: comparison with eddy correlation', *Journal of Glaciology*, 35(121), pp. 343–348.

Nicholson, L. & Stiperski, I. (2020) 'Comparison of turbulent structures and energy fluxes over exposed and debris-covered glacier ice', *Journal of Glaciology*, 66(258). doi: https://doi.org/10.1017/jog.2020.23.

O'Connor, J., Smith, M. J. & James, M. R. (2017) 'Cameras and settings for aerial surveys in the geosciences: Optimising image data', *Progress in Physical Geography*, 41(3), pp. 325–344. doi: 10.1177/0309133317703092.

Open Data Austria (2020) *Austria Digital Elevation Model*. Available at: https://www.data.gv.at/katalog/dataset/land-ktn_digitales-gelandemodell-dgm-osterreich (Accessed: 20 August 2020).

Patzelt, G. (1980) 'The Austrian glacier inventory: status and first results', *Proceedings of the Riederalp Workshop, September 1978*.

Peleg, N., Fatichi, S., Paschalis, A., Molnar, P. & Burlando, P. (2017) 'An advanced stochastic weather generator for simulating 2-D high-resolution climate variables', *Journal of Advances in Modeling Earth Systems*, 9(3), pp. 1595–1627. doi: 10.1002/2016MS000854.

Porter, C. *et al.* (2018) *ArcticDEM*. doi: https://doi.org/10.7910/DVN/OHHUKH.

Quincey, D. J., Smith, M. W., Rounce, D. R., Ross, A. N., King, O. & Watson, C. S. (2017) 'Evaluating morphological estimates of the aerodynamic roughness of debris covered glacier ice', *Earth Surface Processes and Landforms*. doi: 10.1002/esp.4198.

Radić, V., Menounos, B., Shea, J., Fitzpatrick, N., Tessema, M. A. & Déry, S. J. (2017) 'Evaluation of different methods to model near-surface turbulent fluxes for a mountain glacier in the Cariboo Mountains, BC, Canada', *Cryosphere*, 11(6), pp. 2897–2918. doi: 10.5194/tc-11-2897-2017.

Rastner, P., Nicholson, L., Sailer, R., Notarnicola, C. & Prinz, R. (2015) 'Mapping the snow line altitude for large glacier samples from multitemporal Landsat imagery', in *2015 8th International Workshop on the Analysis of Multitemporal Remote Sensing Images, Multi-Temp 2015*. Institute of Electrical and Electronics Engineers Inc. doi: 10.1109/Multi-Temp.2015.7245788.

Rees, W. G. & Arnold, N. S. (2006) 'Scale-dependent roughness of a glacier surface: Implications for radar backscatter and aerodynamic roughness modelling', *Journal of Glaciology*, 52(177), pp. 214–222. doi: 10.3189/172756506781828665.

Sailer, R., Bollmann, E., Hoinkes, S., Rieg, L., Sproß, M. & Stötter, J. (2012) 'Quantification of geomorphodynamics in glaciated and recently deglaciated terrain based on airborne laser scanning data', *Geografiska Annaler, Series A: Physical Geography*, 94(1), pp. 17–32. doi: 10.1111/j.1468-0459.2012.00456.x.

Sailer, R., Rutzinger, M., Rieg, L. & Wichmann, V. (2014) 'Digital elevation models derived from airborne laser scanning point clouds: Appropriate spatial resolutions for multi-temporal characterization and quantification of geomorphological processes', *Earth Surface Processes and Landforms*, 39(2), pp. 272–284. doi: 10.1002/esp.3490.

Sauter, T. & Galos, S. (2016) 'Effects of local advection on the spatial sensible heat flux variation on a mountain glacier', *Cryosphere*, 10(6), pp. 2887–2905. doi: 10.5194/tc-10-2887-2016.

Schlosser, E. (1997) 'Numerical simulation of fluctuations of Hintereisferner, Otztal Alps, since AD 1850', *Annals of Glaciology*, 24, pp. 199–202. Available at: https://www.cambridge.org/core.

Shean, D. (2017) *High Mountain Asia 8-meter DEM Mosaics Derived from Optical Imagery, Version 1*, *NASA National Snow and Ice Data Center Distributed Active Archive Center*. doi: https://doi.org/10.5067/KXOVQ9L172S2.

Sicart, J. E., Litt, M., Helgason, W., Tahar, V. Ben & Chaperon, T. (2014) 'A study of the atmospheric surface layer and roughness lengths on the high-altitude tropical Zongo glacier, Bolivia', *Journal of Geophysical Research*, 119(7), pp. 3793–3808. doi: 10.1002/2013JD020615.

Smith, M. W. (2014) 'Roughness in the Earth Sciences', *Earth-Science Reviews*, 136, pp. 202–225. doi: 10.1016/j.earscirev.2014.05.016.

Smith, M. W., Carrivick, J. L. & Quincey, D. J. (2016a) 'Structure from motion photogrammetry in physical geography', *Progress in Physical Geography*, 40(2), pp. 247–275. doi: 10.1177/0309133315615805.

Smith, M. W., Quincey, D. J., Dixon, T., Bingham, R. G., Carrivick, J. L., Irvine-Fynn, T. D. L. & Rippin, D. M. (2016b) 'Aerodynamic roughness of glacial ice surfaces derived from high-resolution topographic data', *Journal of Geophysical Research F: Earth Surface*, 121(4), pp. 748–766. doi: 10.1002/2015JF003759.

Smith, T. I., Smith, M. W., Chambers, J. R., Sailer, R., Nicholson, L., Mertes, J., Quincey, D. J., Carrivick, J. L. & Stiperski, I. (2020) 'A scale-dependent model to represent changing aerodynamic roughness of ablating glacier ice based on repeat topographic surveys', *Journal of Glaciology*, pp. 1–15. doi: 10.1017/jog.2020.56.

Snavely, N., Seitz, S. M. & Szeliski, R. (2008) 'Modeling the world from Internet photo collections', *International Journal of Computer Vision*, 80(2), pp. 189–210. doi: 10.1007/s11263-007-0107-3.

Steiner, J. F., Litt, M., Stigter, E., Shea, J., Bierkens, M. F. P. & Immerzeel, W. W. (2018) 'The importance of turbulent fluxes in the surface energy balance of a debris covered glacier in the Himalayas', *Frontiers in Earth Science*, 6(October), pp. 1–25. doi: 10.3389/FEART.2018.00144.

Stigter, E. M., Wanders, N., Saloranta, T. M., Shea, J. M., Bierkens, M. F. P. & Immerzeel, W. W. (2017) 'Assimilation of snow cover and snow depth into a snow model to estimate snow water equivalent and snowmelt runoff in a Himalayan catchment', *Cryosphere*, 11(4), pp. 1647–1664. doi: 10.5194/tc-11-1647-2017.

Stiperski, I. & Rotach, M. W. (2016) 'On the Measurement of Turbulence Over Complex Mountainous Terrain', *Boundary-Layer Meteorology*, 159(1), pp. 97–121. doi: 10.1007/s10546-015-0103-z.

Strasser, U., Marke, T., Braun, L., Escher-Vetter, H., Juen, I., Kuhn, M., Maussion, F., Mayer, C., Nicholson, L., Niedertscheider, K., Sailer, R., Stötter, J., Weber, M. & Kaser, G. (2018) 'The Rofental: A high Alpine research basin (1890-3770ma.s.l.) in the Ötztal Alps (Austria) with over 150 years of hydrometeorological and glaciological observations', *Earth System*

Science Data, 10(1), pp. 151–171. doi: 10.5194/essd-10-151-2018.

Stull, R. (1988) *An introduction to boundary layer meteorology*. London: Kluwer.

Telling, J., Lyda, A., Hartzell, P. & Glennie, C. (2017) 'Review of Earth science research using terrestrial laser scanning', *Earth-Science Reviews*, 169(April), pp. 35–68. doi: 10.1016/j.earscirev.2017.04.007.

Ullman, S. (1979) 'The interpretation of structure from motion.', *Proceedings of the Royal Society of London. Series B, Containing papers of a Biological character. Royal Society (Great Britain)*, 203(1153), pp. 405–426. doi: 10.1098/rspb.1979.0006.

University of Innsbruck (2020a) *Permanent Terrestrial Laserscanner 'Im hinteren Eis'*. Available at: https://www.uibk.ac.at/geographie/projects/i_he/ (Accessed: 20 August 2020).

University of Innsbruck (2020b) *Remotely sensed data*. Available at: https://www.uibk.ac.at/projects/station-hintereis-opal-data/remotely-sensed-data/ (Accessed: 20 August 2020).

Vincent, C., Fischer, A., Mayer, C., Bauder, A., Galos, S. P., Funk, M., Thibert, E., Six, D., Braun, L. & Huss, M. (2017) 'Common climatic signal from glaciers in the European Alps over the last 50 years', *Geophysical Research Letters*, 44(3), pp. 1376–1383. doi: 10.1002/2016GL072094.

Van De Wal, R. S. W., Oerlemans, J. & Van Der Rage, J. C. (1992) 'A study of ablation variations on the tongue of Hintereisferner , Austrian Alps', *Journal of Glaciology*, 38(130), pp. 319–324. doi: https://doi.org/10.3189/S0022143000002203.

Wijngaard, R. R., Steiner, J. F., Kraaijenbrink, P. D. A., Klug, C., Adhikari, S., Banerjee, A., Pellicciotti, F., van Beek, L. P. H., Bierkens, M. F. P., Lutz, A. F. & Immerzeel, W. W. (2019) 'Modeling the response of the langtang glacier and the hintereisferner to a changing climate since the little ice age', *Frontiers in Earth Science*, 7. doi: 10.3389/feart.2019.00143.

Chapter 6 : Evaluating the impact of distributing aerodynamic roughness on the modelled surface energy balance of an alpine glacier

Evaluating the impact of distributing aerodynamic roughness on the modelled surface energy balance of an alpine glacier

Joshua R. Chambers[1], Claudio Bravo[1], Mark W. Smith[1], Duncan J. Quincey[1], Lindsey Nicholson[2], Ivana Stiperski[2], Rainer Prinz[2], Rudolf Sailer[3] and Jordan Mertes[4].

[1]School of Geography and water@leeds, University of Leeds, Leeds, LS2 9JT, UK

[2]Department of Atmospheric and Cryospheric Sciences, Universität Innsbruck, Bruno Sander Haus, Innrain 52, Innsbruck, A-6020, Austria

[3]Department of Geography, Universität Innsbruck, Bruno Sander Haus, Innrain 52, Innsbruck, A-6020, Austria

[4]Centre for Environmental and Climate Science, Lund University, Ekologihuset, Sölvegatan 37, Lund, Sweden

Citation

Chambers, J. R., Smith, M. W., Bravo, C. & Quincey, D. J., Nicholson, L., Stiperski, I., Prinz, R., Sailer, R. and Mertes, J. [In Prep]. Evaluating the impact of distributing aerodynamic roughness on the modelled surface energy balance of an alpine glacier

Submitted to: Journal of Glaciology (10th August 2021)

Abstract

In a glacier surface energy balance, the sensible and latent heat fluxes (turbulent fluxes) are an important source of melt energy and are often calculated from meteorological data using the bulk aerodynamic approach. The surface roughness of a glacier strongly influences the magnitude of the turbulent fluxes and is represented by the aerodynamic roughness length parameter, z_0. Distributed glacier surface energy balance models account for the spatial variability of energy fluxes and ablation at the surface of a glacier through time, yet fully distributed values of z_0 have yet to be incorporated. In this study we use fully distributed z_0 to model the surface energy balance for the first time. We build on previous efforts to obtain spatially distributed estimates of z_0 and develop a model to add a temporal dimension based on albedo-z_0 equivalence and space-for-time substitution. Through comparison with model runs that use a fixed, static value of z_0, we show that using fully distributed z_0 can resolve spatial and temporal patterns in the turbulent fluxes that are potentially important for robust melt modelling. Annually, the turbulent fluxes contribute more to the surface energy balance when modelled with a fixed z_0 of 1 mm (as is common in glacier energy balance studies) than when z_0 is fully distributed. However, when restricted to the ablation season, the turbulent fluxes modelled with distributed z_0 are ~30% greater than those modelled using fixed z_0, due to the expanded range of z_0 values. This work shows that it is possible to include fully distributed z_0 values in a distributed glacier surface energy balance model, and the magnitude of the influence that distributed z_0 has on the model outputs shows that it is likely to be increasingly important to do so.

6.1 Introduction

The widespread retreat of glaciers and ice sheets is known to be caused by and indicative of a warming climate (Roe *et al.*, 2021); the impacts of extensive glacier ice melt are broad, ranging from rising sea levels to jeopardised water security and changing local hazards (Hock *et al.*, 2019). In order to constrain potential impacts, quantitative estimates of melt volumes can be calculated from a glacier surface energy balance (SEB) model, which summarises the energy inputs and outputs at the glacier surface atmosphere boundary (Brock and Arnold, 2000; Hock, 2005; Arnold *et al.*, 2006). The SEB is commonly expressed as

$$M = Q_R + Q_S + Q_L + G + R \quad (6.1)$$

where *M* is the energy available for melt, Q_R is the net radiative heat flux, comprising both incoming and outgoing short and longwave radiation, Q_S and Q_L respectively are the sensible and latent heat fluxes (or turbulent fluxes), *G* is the subsurface heat flux and *R* is the sensible heat flux supplied by precipitation, all expressed in W m^{-2}. For the SEB of a temperate glacier, the radiative heat fluxes are the dominant source of energy for melt and the turbulent fluxes are usually secondary, with periods of short-term dominance relating to periods of cloudy, warm or windy conditions (Brock *et al.*, 2000; Hock, 2005; Anderson *et al.*, 2010; Fausto *et al.*, 2016b). However, the sources of uncertainty in turbulent flux calculations often seem proportionally greater than their contribution to the SEB (Brock *et al.*, 2000; Fitzpatrick *et al.*, 2017).

The radiative heat fluxes can be quantified from measurements taken by an automatic weather station (AWS) and then applied in a glacier SEB model, which is used to quantify ice and snow melt and contribution to stream flow at a given time for the observed conditions. Measurements of the radiative heat fluxes at a glacier surface are often produced from a single AWS and are confined to the point scale, requiring the substantial assumption that the observed point is representative of other locations (Oerlemans and Klok, 2002; Giesen *et al.*, 2014; Fausto *et al.*, 2016b; Fitzpatrick *et al.*, 2017).

The turbulent fluxes are commonly estimated from meteorological data using the bulk aerodynamic approach, in which surface roughness is one of the three main influences on the turbulent fluxes, alongside wind speed and atmospheric stability (Cuffey and Paterson, 2010). The aerodynamic roughness length (z_0) is defined as the topographically controlled height above a surface at which horizontal wind speed reaches zero (Stull, 1988; Garratt, 1994) and characterises the effects of surface roughness in the bulk approach. The value assigned to z_0 is often acknowledged as a key source of uncertainty in the SEB (Conway and

Cullen, 2013; Fausto *et al.*, 2016b; Fitzpatrick *et al.*, 2017), so improvements to its parameterisation are a priority for reducing uncertainty in SEB and subsequent melt calculations.

When the required data are available, z_0 can be modelled from direct observation of turbulent eddies using eddy covariance (EC; Burba, 2013; Fitzpatrick *et al.*, 2019; Munro, 1989; Sicart *et al.*, 2014), or extrapolated from log-linear fits of wind speed and air temperature profiles (Kutzbach, 1961; Denby and Greuell, 2000; Brock *et al.*, 2006; Chambers *et al.*, 2019). These methods employ data that are often the result of intensive field campaigns with delicate instruments and yield point-based values of z_0 that do not represent the variability in z_0 of several orders of magnitude that has been observed over a single glacier surface (e.g. Brock *et al.*, 2006).

A distributed SEB model can make use of observations at more than one location so that the fluxes and melt can be simulated across an entire glacier (Arnold *et al.*, 2006; Ayala *et al.*, 2017; Braun & Hock, 2004; Hock & Holmgren, 2005 & Bravo *et al.*, 2021). Approaches to distribution of the principal SEB components have been studied widely (Hock, 2005; MacDougall and Flowers, 2011; Petersen and Pellicciotti, 2011; Shaw *et al.*, 2020). For instance, incoming shortwave radiation is split into direct and diffuse components in order to account for the effects of topography (Hock and Holmgren, 2005), then modelled using digital elevation data (Fu and Rich, 2002), using the relationship between observed and potential shortwave radiation (Sicart *et al.*, 2010). Albedo is another component that has been examined in detail; its importance to the energy balance is recognised and various parameterisations have been proposed (Oerlemans and Knap, 1998; Brock *et al.*, 2000; Hock and Holmgren, 2005). The importance of z_0 has long been acknowledged, with an often-stated effect being a doubling of the turbulent fluxes for an order of magnitude increase in z_0 (Munro, 1989; Hock and Holmgren, 1996; Brock *et al.*, 2000). There is extensive evidence of the variability of z_0 in both summer and winter, and the importance of its representation in turbulent flux calculations, with many studies incorporating an analysis of the sensitivity of the energy balance to z_0, or reporting values that differ to those found elsewhere in the literature (Morris, 1982; Harding *et al.*, 1989; Munro, 1989; Hock and Holmgren, 1996; Braun and Hock, 2004; Brock *et al.*, 2006; Sicart *et al.*, 2014; Fitzpatrick *et al.*, 2017). Yet, z_0 is often assigned a fixed uniform value of 1 mm in both distributed and point-scale SEB models (e.g. Braun and Hock, 2004; Hock and Holmgren, 2005; Arnold *et al.*, 2006; Gusain *et al.*, 2009; Ayala *et al.*, 2017; Bravo *et al.*, 2017).

Recent research has shown that robust 3D estimates of z_0 can be derived from topographic

data, allowing rapid acquisition of spatially and temporally distributed values that compare well to EC and profile-derived z_0 (Irvine-Fynn *et al.*, 2014; Miles *et al.*, 2017; Chambers *et al.*, 2019; 2021; Fitzpatrick *et al.*, 2019; Liu *et al.*, 2020). Topographic data derived from structure from motion photogrammetry (SfM; Smith *et al.*, 2016a) or terrestrial laser scanning (TLS; Lemmens, 2011; Telling *et al.*, 2017) have been used to produce estimates of z_0 at the plot-scale (tens of metres, centimetre resolution), but with limited scope for upscaling to the glacier-scale due to inherent scale- and resolution-dependence (Rees and Arnold, 2006; Quincey *et al.*, 2017; Chambers *et al.*, 2021). Broader scale TLS surveys have been used to generate glacier-scale grids of z_0 based on its relationship with other surface roughness metrics, with the use of numerous plot-scale validation points (Smith *et al.*, 2016b; 2020), while airborne laser scanning (ALS) survey data have been used to create z_0 grids using sliding neighbourhood algorithms (Fitzpatrick *et al.*, 2019; Chambers *et al.*, 2021). With the sliding neighbourhood approach, a value of z_0 is assigned to each grid cell based on the geometric properties of neighbouring cells. While this workflow has successfully produced spatially distributed glacier-scale maps of z_0, the use of coarse resolution (tens of metres per pixel) data systematically under-estimates z_0. To address this bias, Chambers *et al.* (2021) developed a correction factor that can bring under-estimated z_0 to within an order of magnitude of pre-validated values.

Despite substantial progress being made towards successful representation of spatial patterns of z_0, at the time of writing, attempts to incorporate spatially distributed z_0 into a SEB model have been limited. Sicart *et al.* (2011) used an elevational gradient to assign z_0 values, applying a value of 10 mm at the site of an AWS and decreasing the value by 15% every 100 m at higher elevations. Over a debris-covered glacier, Fyffe *et al.* (2014) used a fixed z_0 value for ice and another for snow, implementing the ice value when snow-cover was <50%. In a recent example, Bravo *et al.* (2021) assigned surface classifications to modelled albedo values, with each surface prescribed a z_0 value from previously published studies. While certainly an improvement on employing a fixed value, or on using one value for ice and another for snow, the diversity of surface geometries present within each classification still remains underrepresented.

Part of the reason that spatially and temporally distributed values of z_0 have not been more easily incorporated into SEB models stems from the complex evolution of glacier surfaces over time. It is often acknowledged that snow surfaces have smaller z_0 than ice surfaces and, for simplicity, each is prescribed a single value (~0.1 mm for snow and ~1 mm for ice; e.g., Greuell and Oerlemans, 1989; Giesen *et al.*, 2014; Bravo *et al.*, 2017). Snow surfaces can be

geometrically diverse, with observed values ranging from 0.2 to 30 mm (Jackson and Carroll, 1978; Wagnon *et al.*, 1999; Brock *et al.*, 2006; Gromke *et al.*, 2011), and the same can be said for ice, for which values from 0.1 to >>100 mm have been observed (Grainger and Lister, 1966; Brock *et al.*, 2006; Nicholson *et al.*, 2016; Miles *et al.*, 2017). The progression from snow to ice through the ablation season introduces further complexity, as surfaces become more or less rough depending on the underlying glaciological characteristics. Various trajectories of surface evolution have been observed: Guo *et al.* (2011) noted that the snow surface became rougher as it melted and z_0 increased, before the smooth ice surface underneath was exposed and z_0 decreased again; Smith *et al.* (2020) observed scale-dependent increasing roughness of ice surfaces through the ablation season, while Smeets and van den Broeke (2008) observed a rapid increase in z_0 as a rough, hummocky ice surface was exposed.

The aim of this study is to unify these different potential trajectories and incorporate fully distributed z_0 values in a distributed SEB model, so that the order of the impact on modelled turbulent fluxes, SEB and ablation can be investigated. Using Hintereisferner, Austria, as a case study, we used the workflow developed in Chambers *et al.* (2021) to generate a bias-corrected glacier scale map of z_0 from topographic data, and incorporated it with the albedo-reclassification approach of Bravo *et al.* (2021) and observations of z_0 trajectories made by Smith *et al.* (2020). We implemented the resulting z_0 values in a distributed SEB model at a daily time-step for the year from 30th September 2016 until 30th September 2017. We demonstrate the effects of including spatially and temporally distributed z_0 compared to static z_0 on the turbulent fluxes, overall energy balance and estimated ablation for the SEB year, and analyse the ablation season in isolation. We then investigate the potential impacts of distributed vs. static z_0 on the turbulent fluxes, energy balance and ablation under different simulated climate scenarios.

6.2 Location and data collection

6.2.1 Location

The distributed SEB model was implemented using data from Hintereisferner (46^o 48'N, 10^o 47'E), a temperate mountain glacier in the Rofenache catchment of the southern Otztal Alps (Fig. 6.1) in the inner-alpine dry region of the Austrian Alps (Strasser *et al.*, 2018). Hintereisferner has been widely studied and is a WGMS reference glacier thanks to its mass balance records that extend back to 1952/53 (Fischer, 2010). This glacier was selected due to the availability of meteorological and topographic data, which were used in a previous

study to develop a workflow for obtaining up-scaled, distributed topographic estimates of z_0 (Chambers *et al.*, 2021). More site details are given in Smith *et al.* (2020), Mott *et al.* (2020) and Chambers *et al.* (2021).

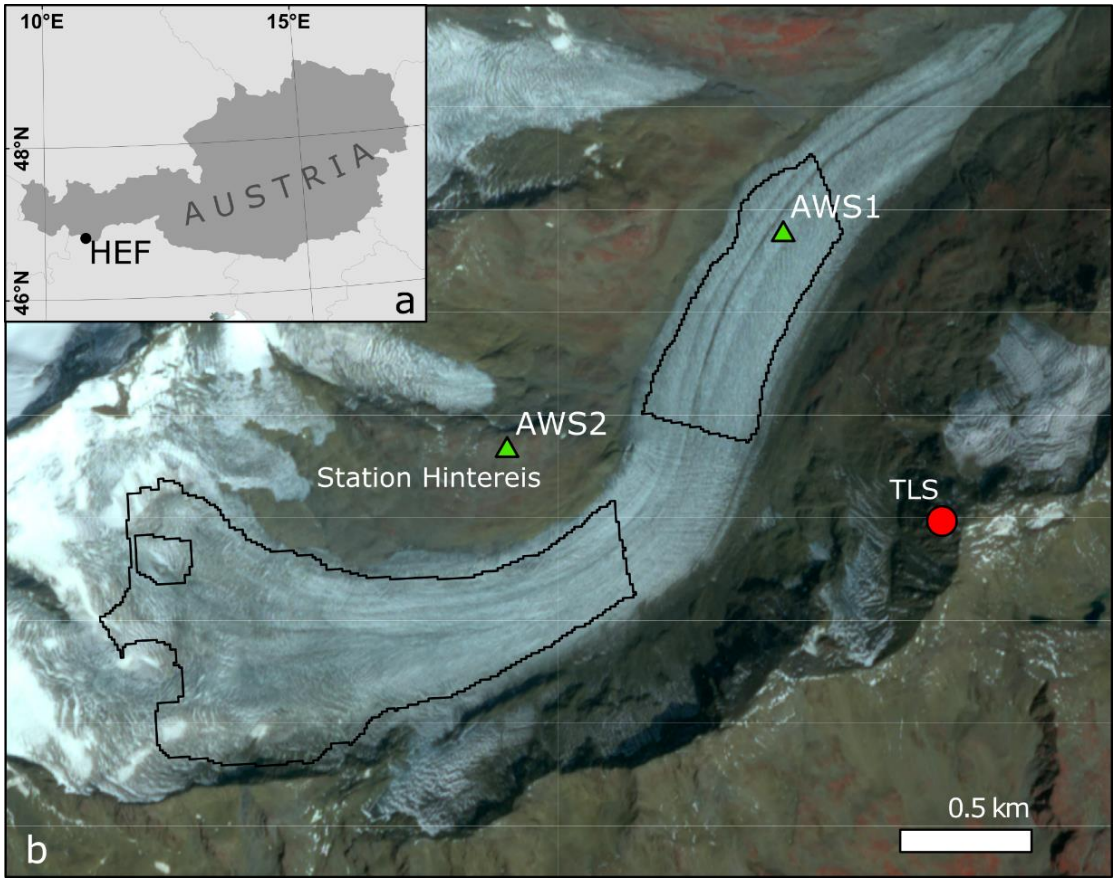

Fig. 6.1 Location of Hintereisferner (HEF) within Austria (a). Locations of AWS are shown in (b) by green triangles, along with the location of the TLS (red circle) and Station Hintereis. The extent of TLS scans, which forms the modelling domain, is shown by the black outline. Background false colour image courtesy of Planet Labs© dated 28th August 2018.

6.2.2 Data

Data used in the development of the z_0 upscaling workflow were collected in August 2018 and processed as described in Chambers *et al.* (2021). Briefly, this consisted of aerial, pole and ground-based SfM surveys with concomitant meteorological data collection from wind towers and turbulence towers. Wind towers were fitted with five NRG 40 cup anemometers, one NRG 200P wind vane and five shielded and passively-ventilated Extech RHT10 temperature and humidity loggers. Turbulence towers were fitted with sonic anemometers, set up as described in Mott *et al.* (2020). TLS surveys of the glacier were carried out on 3rd, 7th, 12th and 16th August 2018 using a permanent *in-situ* Riegl VZ-6000 housed in a climate-controlled container near the summit of “im Hinteren Eis” (46.79586° N, 10.78277° E, 3244

m a.s.l.) and operated by the University of Innsbruck (University of Innsbruck, 2020). Based on observed similarities in z_0 over glacier surfaces from year to year (Fitzpatrick *et al.*, 2019), it was assumed for the purpose of this study that the TLS data collected during HEFEX in August 2018 were representative of the glacier surface at the same time in 2017, which is the energy balance year covered by this study. Representation of the glacier surface throughout the rest of the year is addressed in Section 6.3.4.

Energy balance data came from two permanent automatic weather stations (AWS) installed by the University of Innsbruck in 2010 (near Station Hintereis, 46.79861° N, 10.76041° E, 3026 m a.s.l.) and 2014 (on the glacier surface, 46.80577° N, 10.77442° E, 2718 m a.s.l.). Both AWS log continuously, but data gaps exist due to technical faults and the time taken to rectify them. The data used here span the most complete 12 month dataset available for both AWS, with gaps where data were unavailable for one or both (Fig. 6.2). Consequently, the energy balance year, with gaps, runs from 30th September 2016 until 22nd March 2017, then 29th May 2017 until 29th August 2017. Each AWS recorded the meteorological variables summarised in Table 6.1. Data were recorded as 10 minute averages, which were then aggregated to daily means. The SEB ran at a daily time-step because the focus of this study is the magnitude of the influence of spatio-temporally distributed z_0 on SEB outputs, rather than specific values of the SEB for the study period.

6.3 Methods

6.3.1 Modelling approach

Initial runs of the model used static z_0 values of 1 mm and 10 mm so that: (i) the sensitivity of the turbulent fluxes, SEB and ablation estimates to z_0 magnitude could be demonstrated and the frequently-stated assertion that doubling of turbulent fluxes for an order of magnitude increase in z_0 (Munro, 1989; Hock and Holmgren, 1996; Brock *et al.*, 2000) could be tested. Subsequent model runs used a static z_0 of 1 mm and fully distributed z_0 so that: (ii) the spatial distribution of model outputs could be compared and (iii) daily and monthly temporal trends could be investigated. Final model runs used artificially increased air temperatures and wind speed data along with static and distributed z_0, to assess the potential impact of implementing distributed z_0 in SEB models in different and possible future climates. Model runs were executed for the entire SEB year, with specific attention paid to the ablation season.

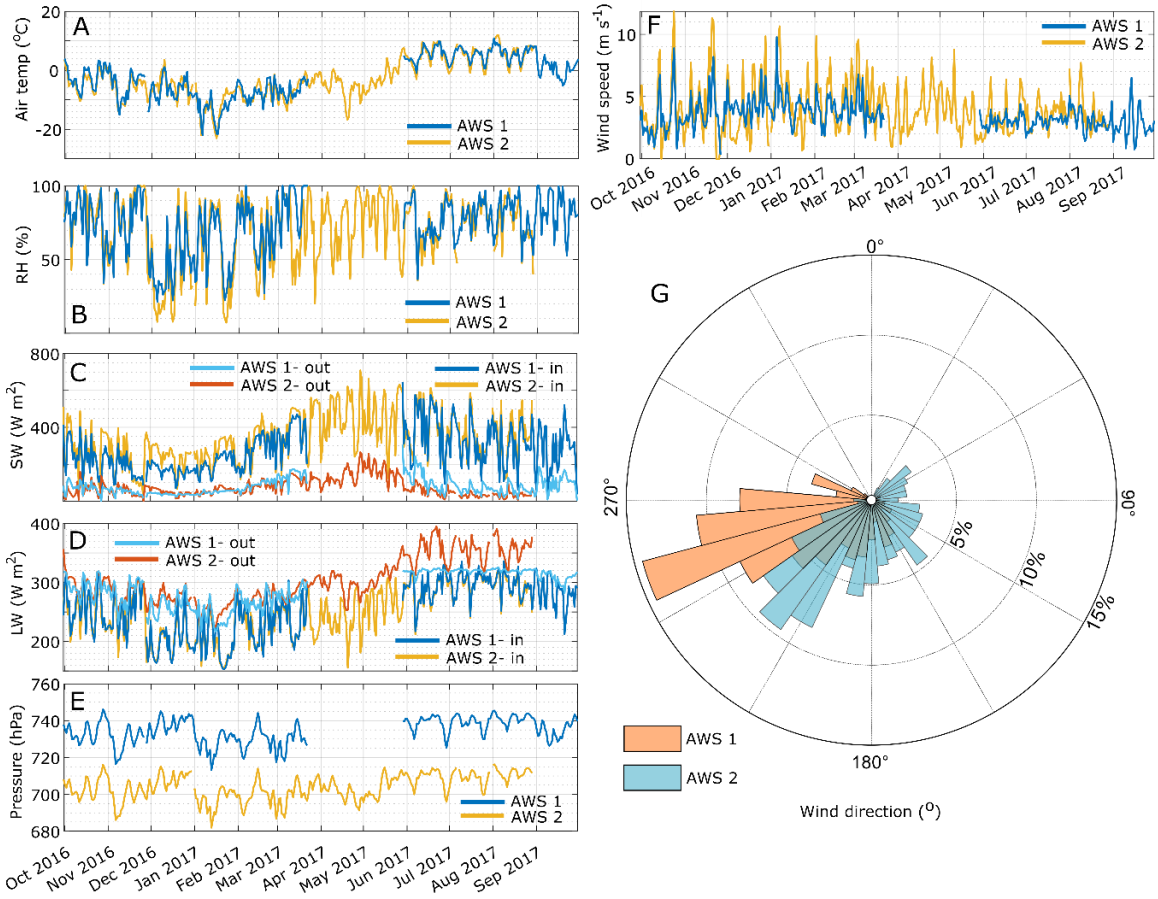

Fig. 6.2 Summary of meteorological data from AWS spanning SEB year from 30th September 2016 to 30th September 2017. AWS1 was located on the glacier, AWS2 was off-glacier (see Fig. 6.1). Gap in AWS1 data extends from 22nd March to 29th May 2017, gap in AWS2 data from 29th August to 30th September 2017.

Table 6.1 Details of AWS sensors and instruments. Applies to both AWS. Accuracy figures as stated by manufacturers.

Variable	Sensor	Units	Accuracy
Air temperature	Vaisala HMP45c	°C	±0.3°C at 0°C
Relative humidity	Vaisala HMP45c	%	±1% at 20°C
Wind speed	Young 05103	m s^{-1}	±0.3 m s^{-1}
Wind direction	Young 05103	Degrees (°)	±3°
Distance to surface	SR50A sonic ranger	M	±0.01m
Shortwave radiation in/out	Kipp & Zonen CNR4	W m^{-2}	<5% uncertainty
Longwave radiation in/out	Kipp & Zonen CNR4	W m^{-2}	<5% uncertainty
Air pressure	Vaisala PTB110	hPa	±1 hPa at -20 - 45°C

6.3.2 Energy balance model

The total energy available for melt (*M*) was determined by forcing meteorological variables in the following formula (all in W m^{-2}):

$$M = (1 - \alpha)SW_{in} + LW_{in} + LW_{out} + Q_S + Q_L \quad (6.2)$$

Where α is the albedo, SW_{in} is incoming shortwave radiation and LW_{in} and LW_{out} are incoming and outgoing longwave radiation respectively. Collectively, these are also known as the radiative fluxes (Q_R). In this case, the sensible heat from rain (*R*) was not calculated as it was considered negligible (Sicart *et al.*, 2005; Gillett and Cullen, 2011). Evidence suggests that the assumption of negligible subsurface heat flux (*G*) is incorrect due to temperatures <<0°C in the winter snow pack (Sauter *et al.*, 2020). However, because the focus of this study is the magnitude of the effect of using distributed z_0 on the energy balance rather than the specific values themselves, and due to the lack of validation of subsurface temperatures, it was decided that *G* should be discounted.

As is the convention in glaciological applications, energy fluxes towards the surface were denoted as positive (thus providing energy for melt) and fluxes away from the surface were negative. Each variable and the overall energy balance was calculated and distributed following Bravo *et al.* (2021) with the exceptions of α and z_0. Ablation was assumed to occur when M was positive and the glacier surface was at 0°C, from

$$Ablation = \frac{M}{L_m \rho_w} \quad (6.3)$$

where L_m is the latent heat of fusion (kJ kg^{-1}) and ρ_w is the density of water (1000 kg m^{-3}). Sublimation (*S*, W m^{-2}) was also calculated from

$$S = \frac{Q_L}{L_s \rho_w} \quad (6.4)$$

where L_s is the latent heat of sublimation (kJ kg^{-1}), but it was zero throughout. Meteorological variables were spatially distributed on to a 10 m resolution digital elevation model (DEM) interpolated from a TLS scan of the upper and lower glacier on 12th August 2018 (Fig. 6.1). Details of spatial distribution methods are given in Table 6.2.

Table 6.2 Details of spatial distribution of meteorological variables over Hintereisferner. From Bravo *et al.* (2021)

Variable	Symbol	Units	Method/Assumption	Reference
Air temperature	T_α	°C	Observed lapse rate	Bravo *et al.* (2019)
Surface temperature	T_s	°C	Dew point air temperature used as snow surface temperature proxy. T_s set to zero when T_α>0	Raleigh *et al.* (2013)
Atmospheric pressure	P	Pa	Hydrostatic equation	Wallace and Hobbs (2006)
Air vapour pressure	e_a	Pa	Observed gradient	Shea and Moore (2010)
Saturation vapour pressure	e_{sat}	Pa	Function of air temperature	Bolton (1980)
Surface vapour pressure	e_s	Pa	Ice and snow surfaces are saturated. Equal to e_{sat} or set to 6.11 hPa when T_s=0	Collier *et al.* (2014)
Wind speed	u	m s^{-1}	Observed lapse rate	Fyffe *et al.* (2014)

6.3.3 Albedo

Albedo was retrieved from surface reflectance data of Landsat 8 scenes that covered the study site acquired on 5th October 2016 and 14th March, 17th May, 18th June, 4th July and 22nd September 2017. An additional scene from Landsat 7 on the 29th August 2017 was used to provide coverage of the ablation season because no cloud-free Landsat 8 scenes from that month existed. Otherwise, where more than one cloud-free scene per month existed, the scene with the clearest view over the glacierised area was selected; where there were no cloud-free scenes available from either Landsat 7 or 8 the month was excluded. We followed USGS guidance on converting Landsat Digital Numbers to top-of-atmosphere reflectance using rescaling coefficients provided in the scene metadata (USGS, 2021), then followed the workflow of Naegeli *et al.* (2019) to retrieve albedo over glaciers in the Alps. This approach applies a narrow-to-broadband conversion (Liang, 2000) to surface reflectance data to produce shortwave broadband albedo (α_{short}) as follows:

$$\alpha_{short} = 0.356b_{1/2} + 0.130b_{3/4} + 0.373b_{4/5} + 0.085b_{5/6} + 0.072b_7 + 0.0018 \quad (6.5)$$

where $b_{n/m}$ is the narrowband reflectance number from Landsat 7 ETM+ (*n*) or Landsat 8 OLI (*m*). Unrealistic values greater than 1 or less than 0.05 were set to no data and the albedo product was resampled using bilinear interpolation from 30 m to 10 m resolution to match the TLS DEM. Changes in albedo through time were modelled using linear interpolation between the dates of Landsat scenes to extend coverage to the full SEB year.

6.3.4 Distributed z_0 model

We calculated and corrected spatially distributed z_0 from the 10 m TLS DEM using the workflow and correction factors detailed in Chambers *et al.* (2021), assuming that the DEM represented the glacier surface at the peak of the ablation season in 2017. To model temporal trajectories of z_0, we developed a basic representation of seasonal variations as shown in Fig. 6.3. First, each of the Landsat albedo grids was reclassified into surface types in order to assign z_0 values to different surfaces throughout the year (Fig. 6.4a). This approach was also used by Bravo *et al.* (2021), with the exception here that any grid cell with albedo <0.45 was classed as bare ice.

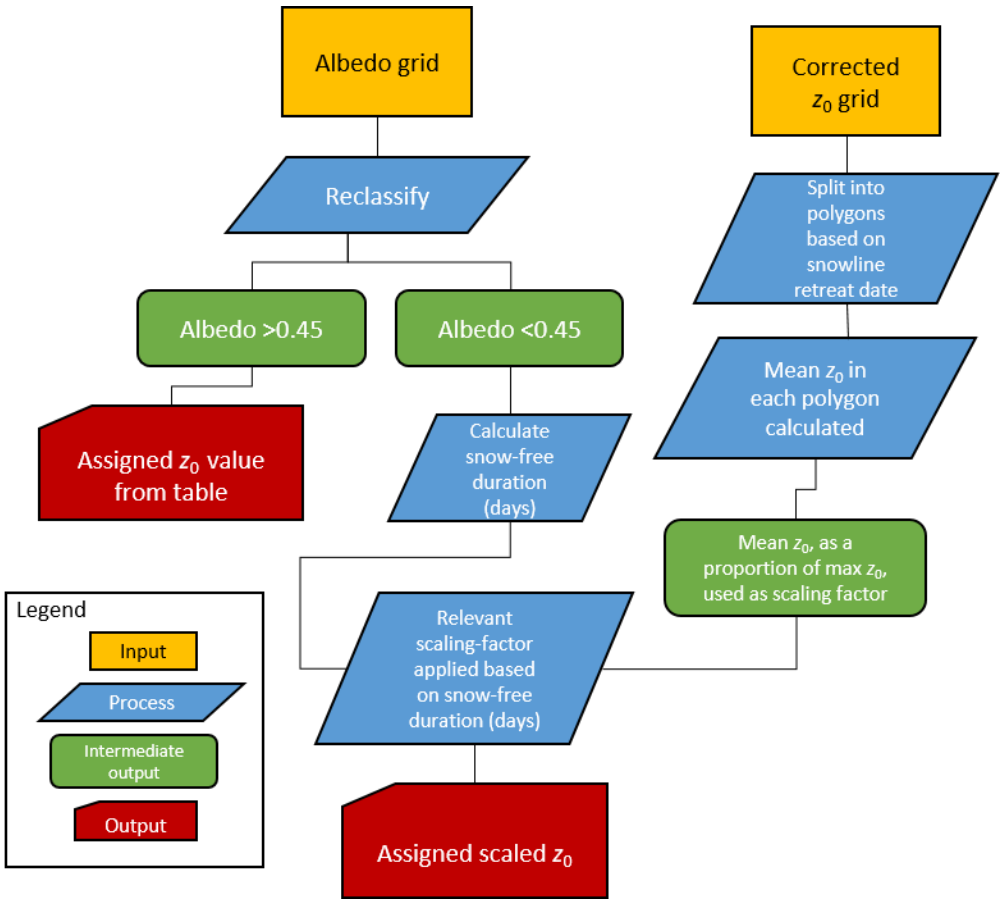

Fig. 6.3 Flow diagram of steps taken to model temporal development of z_0. See main text and Fig. 6.4 for additional detail, albedo classification-based z_0 values and scaling factors.

Then, areas of the glacier classified as bare ice were assigned a scaled z_0 value based on the length of time that the surface had been snow-free (Fig. 6.4b). Scaling factors were defined using the space-for-time substitution carried out by Smith *et al.* (2020), who used snow-line retreat dates to show that bare ice surfaces that had been snow-free the longest had higher z_0 than those that had been exposed for less time. With the longest exposed area (44+ days) set as the maximum roughness, the mean z_0 within each of the other space-for-time areas shown in Fig. 6.4b was then converted to a proportion of the maximum (Table 6.3). This proportion was used as the scaling factor.

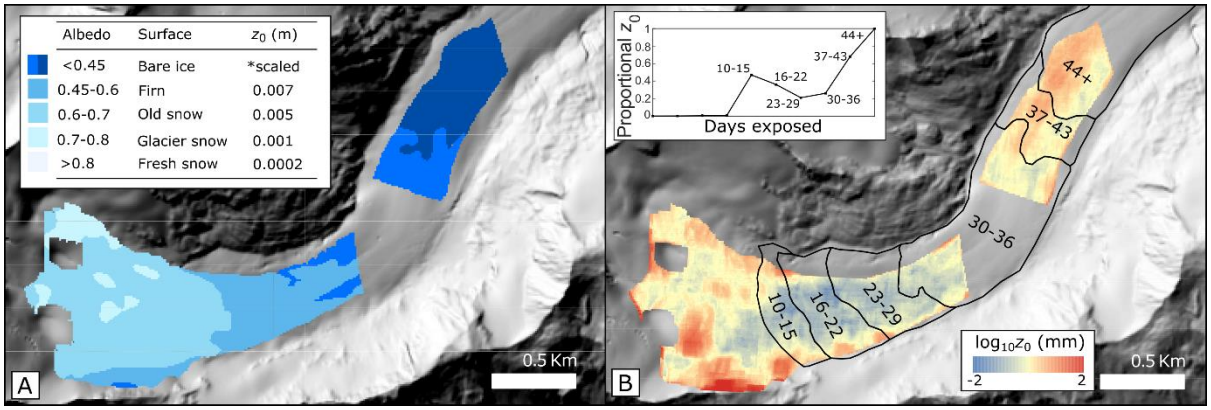

Fig. 6.4 Development of temporal model used to distribute z_0. (A) shows an example of a reclassified albedo grid with z_0 values assigned from the inset table. The two shades assigned to the Bare Ice classification represent bare ice that has been exposed for different lengths of time (darker blue is older). (B) shows the space-for-time substitution polygons used to calculated scaling factors, drawn over z_{0TLS} from Chambers *et al.* (2021) – the numbers in each polygon are the number of days the surface has been exposed. The mean z_0 value within each polygon is plotted on the inset graph as a proportion of the maximum z_0 (assumed to be coincident with the longest exposure duration).

Table 6.3 z_0 scaling factors for each space-for-time area

Exposure length (days)	Mean z_0 (mm)	Scaling factor
10-15	0.9	0.47
16-22	0.7	0.36
23-29	0.4	0.21
30-36	0.5	0.26
37-43	1.3	0.68
44+	1.9	1

To estimate how long ice surfaces had been exposed, we identified the date of the first Landsat scene in which a surface was classified as bare ice (albedo <0.45) and assumed that any snow cover had melted within the last 15 days (scaling factor of $0.47z_0$). Then, using the length of time in days between Landsat scenes, the cumulative total number of days since each surface had been exposed was calculated for subsequent Landsat scenes until the scene with the minimum snow cover (29th August). At this point, the majority of the glacier had been classified as bare ice for long enough to reach the maximum z_0 value (scaling factor of 1). This process gave a z_0 grid for each of the dates of the Landsat scenes; z_0 trajectories between these dates were estimated using linear interpolation, the same as for albedo. (See GIF[1] for demonstration of temporal model results).

[1] Distributed z_0 model GIF – available on eThesis only

6.4 Simulating the SEB under adjusted climate scenarios

To assess the importance of modelling a glacier SEB with fully distributed z_0, we ran a sensitivity test by forcing additional model runs with artificially adjusted data. These tests were used to simulate hypothetical scenarios in which the climate is more favourable for enhanced turbulent fluxes, representing scenarios that may or may not align with projected climate changes and other contemporary climates. First, average daily air temperature was increased by 1.5°C and 2°C, then 2.5°C. All other meteorological variables remained unchanged during the tests. While these single parameter sensitivity tests are useful for indicating the order of the influence of distributed vs. static z_0, it is understood that the differences in output values are likely to include the effects of other inherent changes as a result of increased temperatures (including changes in humidity, cloudiness and pressure values).

Next, simulations were run with daily mean wind speed artificially increased by 0.5, 1 and 1.5 m s^{-1}, again keeping all other variables unchanged. The mean wind speed from AWS1 for the study period was 3.5 m s^{-1} so the scenarios represent annual mean wind speeds of 4, 4.5 and 5 m s^{-1} which are common over glaciers. Furthermore, the turbulent fluxes over alpine glaciers are most sensitive to fluctuations in wind speeds between 3-5 m s^{-1} (Dadic *et al.*, 2013). Increased wind speeds are not necessarily projected for the European Alps (Vautard *et al.*, 2010; Moemken *et al.*, 2018; Graf *et al.*, 2019), but are included in the tests here in an attempt to characterise their role for other climatic settings in which temperate glaciers are found, where the turbulent fluxes have high relative importance to the SEB (Klok *et al.*, 2005; Anderson *et al.*, 2010; Gillett and Cullen, 2011).

6.5 Results

6.5.1 SEB results

Initial runs of the SEB model were carried out to investigate the sensitivity of the turbulent fluxes, M and modelled ablation to different static z_0 values. Mean annual values of Q_S, Q_L, M and ablation, averaged across the glacier, are shown Fig. 6.5. An order of magnitude increase in z_0 (from 1 mm to 10 mm) more than doubled mean annual Q_S, from 40 to 84 W m^{-2} and mean annual Q_L from 1.3 to 2.8 W m^{-2}. The effect on the overall energy balance was greater, with mean annual M nearly tripling from 24 to 69 W m^{-2}. Mean annual ablation estimates also increased, from 1.3 to 2.2 m w.e. (water equivalent), showing that variation in z_0 has a substantial effect on both M and ablation.

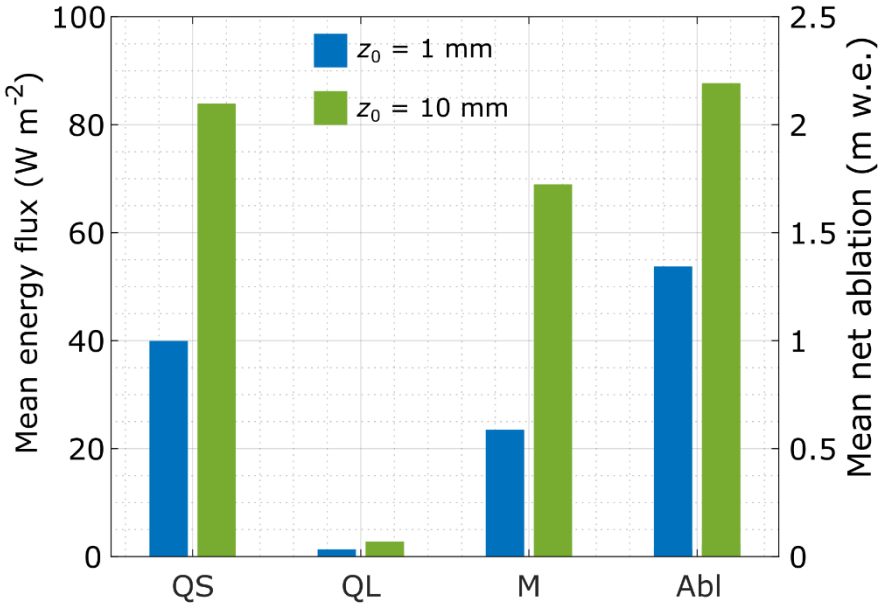

Fig. 6.5 Comparison of annual averages across the glacier of (left-hand axis) turbulent fluxes ($\boldsymbol{Q_S}$ and $\boldsymbol{Q_L}$), energy available for melt (M) and (right-hand axis) ablation (Abl) when modelled with static z_0 values of 1 mm (blue) and 10 mm (green).

Subsequent model runs were used to compare the effects of using fully distributed z_0 (z_{0DIST}) and a static z_0 value of 1 mm ($z_{0STATIC}$). In both cases, mean annual SW_{in} was 93 W m^{-2}; however, a high mean annual albedo of 0.7 contributed to a mean SW flux of 30.2 W m^{-2}. Due to negative mean surface temperatures, mean LW_{in} (227 W m^{-2}) was offset by mean outgoing LW_{out} (276 W m^{-2}) and the LW flux was an energy sink.

Spatial differences in annual mean values of M and the turbulent fluxes are shown in Fig. 6.6. Daily means are shown in animated GIFs[2]. Grids in the left-hand column of Fig. 6.6 show mean annual values for z_{0DIST}. The sensible heat flux (Q_S) had an annual mean of 38.1 W m^{-2} (z_{0DIST}) and 39.6 W m^{-2} ($z_{0STATIC}$). The mean latent heat flux (Q_L) was 1.8 W m^{-2} (z_{0DIST}) and 1.3 W m^{-2} ($z_{0STATIC}$). The overall mean energy available for melt (M) was 22.2 W m^{-2} (z_{0DIST}) and 23.6 W m^{-2} ($z_{0STATIC}$). In terms of spatial distribution, generally greater values of M, Q_S and Q_L were modelled in the upper glacier than the lower glacier. For each flux the highest values were modelled in a specific region on the true-right of the glacier. Other areas with higher values coincided with an area of ice-fall in the upper glacier and a thin covering of supraglacial debris on parts of the lower glacier. The low albedo of the debris cover meant it was assigned to the bare ice surface classification (the greater z_0 values estimated for this

[2] SEB GIFs: distributed z_0 and fixed z_0 (eThesis only)

region are visible in Fig. 6.4b). The influence of the temporal z_0 model is especially visible in the upper glacier, where some uniformity of z_0 occurs in polygons consistent between all three variables.

The right-hand column of Fig. 6.6 shows grids of difference between variables when modelled with z_{0DIST} and $z_{0STATIC}$. Since the grids show $z_{0DIST} - z_{0STATIC}$, positive values occur where z_{0DIST} is greater than $z_{0STATIC}$ and negative values occur where $z_{0STATIC}$ is greater than z_{0DIST}. Zero indicates the same outcome from both z_0 values. Grids of difference for M and Q_S show very similar distributions and suggest that, as an average of the SEB year, Q_S and M are greater when z_0 is fixed to 1 mm. This is strongly the case in areas of the upper true-left of the glacier and the lower glacier. In other areas of the upper glacier z_{0DIST} had larger values, especially around the ice-fall and the area on the true-right of the glacier that shows the greatest values overall. The difference in grids for Q_L was much less pronounced, with z_{0DIST} producing slightly greater values across most of the glacier surface.

Analysis of temporal trends of the SEB components in Fig. 6.7 shows that the greater average Q_S and M modelled with $z_{0STATIC}$ (Fig. 6.6.) is concentrated in the winter months and is more than outweighed by the increases in Q_S and M during the ablation season when modelled with z_{0DIST} (Fig. 6.7c). Both Fig. 6.7a and 6.7b show that Q_S was the most consistent source of energy, although surface temperatures <0°C through the winter prevented any ablation. SW flux was the dominant source of ablation energy during the summer months, whereas the LW flux was a consistent energy sink throughout the year. Q_L fluctuated between energy source and sink but was, overall, an energy source for ablation, contributing an annual total of 474.5 W m^{-2} (z_{0DIST}) and 346.9 W m^{-2} ($z_{0STATIC}$) when averaged across the glacier.

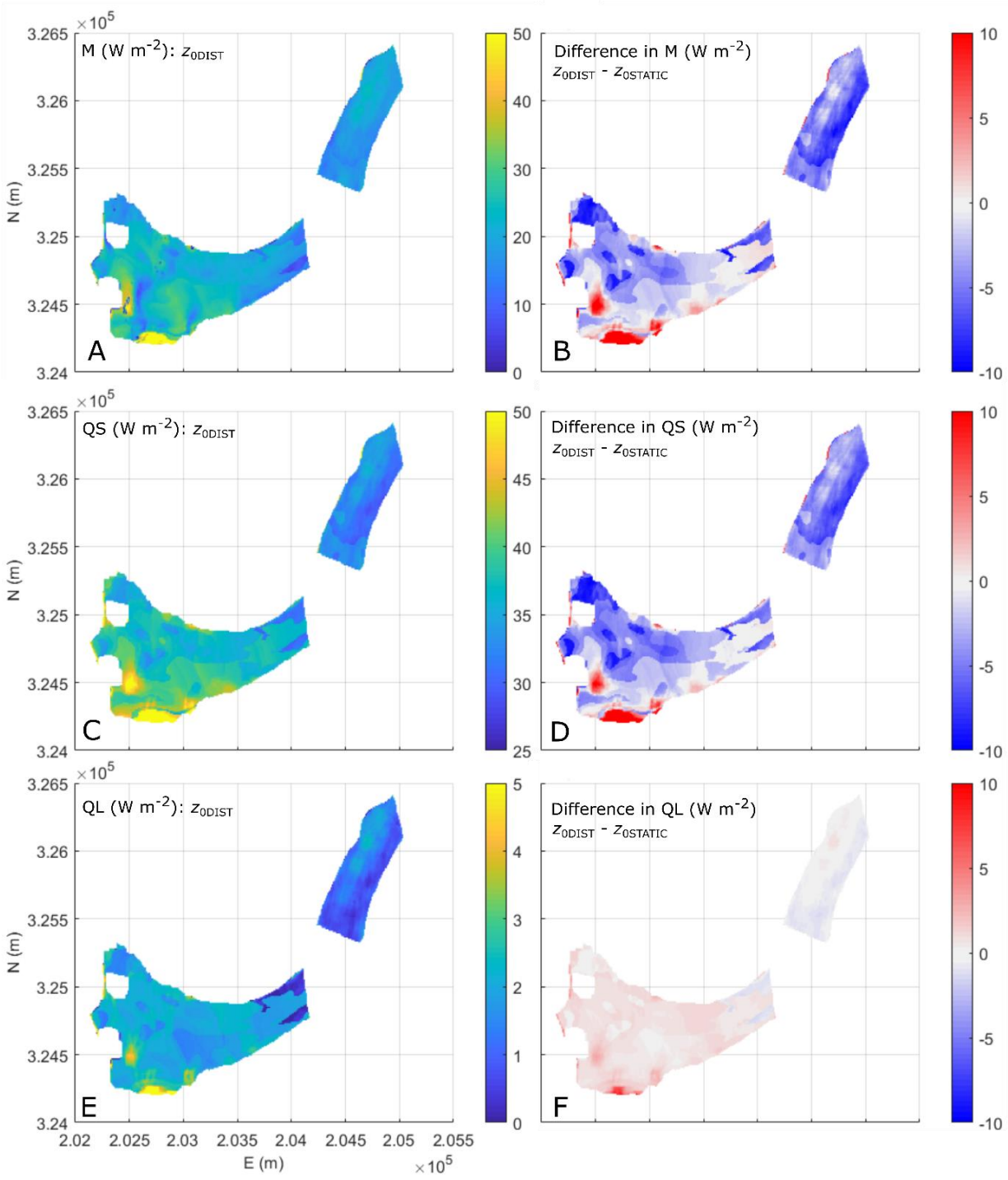

Fig. 6.6 Spatial distribution of mean energy available for melt (A) and turbulent fluxes (C & E) for the SEB year 31st September 2016 to 31st September 2017 modelled with z_{0DIST}. Difference between M, $\boldsymbol{Q_S}$ and $\boldsymbol{Q_L}$ modelled with z_{0DIST} and $z_{0STATIC}$ shown in B, D and F.

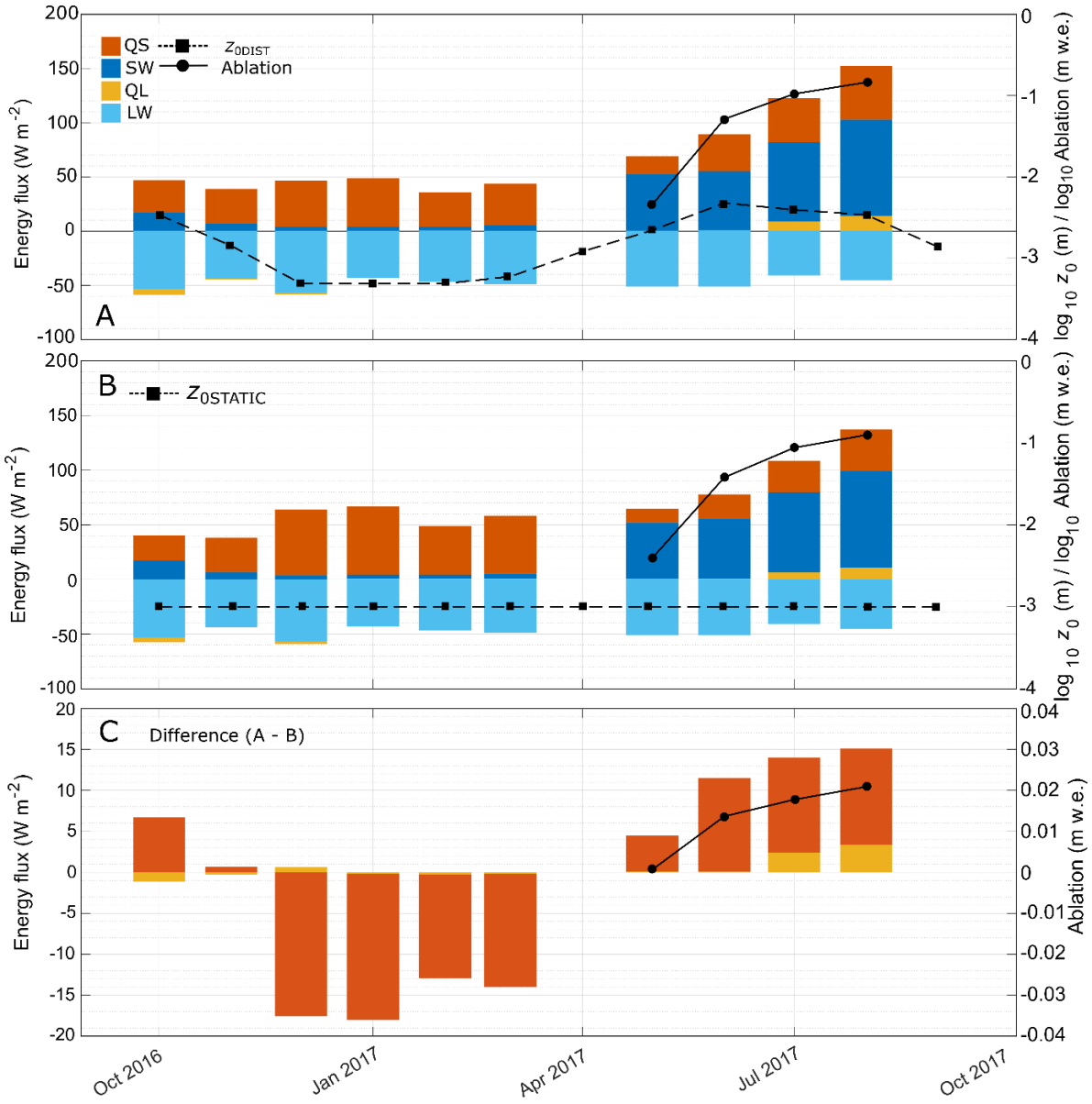

Fig. 6.7 Monthly mean of energy fluxes averaged across the whole of Hintereisferner modelled with z_{0DIST} (A) and $z_{0STATIC}$ (B). For both plot, mean z_0 and mean monthly ablation are shown on the right-hand axis $\log_{10}$ transformed. Difference in mean monthly fluxes and ablation shown in (C). Legend in (A) applies to all plots.

Seasonal variability during the winter months was also masked when fluxes were modelled with a constant, uniform z_0. Prevalent snow cover, particularly in December and January, was assigned a z_0 value of 0.2 mm in the distributed model so the turbulent fluxes and M were smaller than when modelled with $z_{0STATIC}$. An average of 38.2% more energy from QS was modelled with z_{0DIST} during summer months between May and August (when ablation was also modelled) than when z_0 was fixed to 1 mm (Fig. 6.7c). When compared only on days when melt was modelled (Table 6.4), the turbulent fluxes provided a mean of 10.9 W m^{-2} (30%) more energy to the SEB when modelled with z_{0DIST} than with $z_{0STATIC}$.

Table 6.4 Summary of ablation and fluxes through ablation season for z_{0DIST} and $z_{0STATIC}$. Standard deviations of values included in square brackets. SWF is the shortwave flux ($(\mathbf{1}-\boldsymbol{\alpha})\boldsymbol{SW_{in}}$) as defined in equation (6.2). LWF is the longwave flux ($\boldsymbol{LW_{in}}+\boldsymbol{LW_{out}}$) from the same equation.

	z_{0DIST}		$z_{0STATIC}$	
	Mean on days with modelled melt (n = 89)	Mean contribution to SEB (%)	Mean on days with modelled melt (n = 88)	Mean contribution to SEB (%)
Ablation (m w.e.)	0.016 [0.016]	-	0.015 [0.013]	-
M (W m^{-2})	65.22 [68.99]	-	55.04 [55.60]	-
SWF (W m^{-2})	64.39 [37.93]	98.73	64.39 [37.93]	119.82
LWF (W m^{-2})	-46.58 [18.02]	-71.42	-46.58 [18.02]	-84.25
Q_S (W m^{-2})	39.34 [32.19]	60.32	29.99 [23.13]	54.49
Q_L (W m^{-2})	7.29 [22.69]	11.12	5.69 [16.39]	10.34

Within the temporal model, mean monthly z_{0DIST} reached a peak in May (Fig. 6.7a). Inspection of the distribution of z_{0DIST} on individual days shows that the glacier surface is predominantly classified as firn, which was assigned a z_0 value of 7 mm, but was likely to be end of season snow. Values of z_0 greater than 7 mm were present later in the ablation season, but the glacier-wide mean z_0 was lower because of the presence of patches of snow cover that persisted until July and because some bare-ice surface had a modelled z_0 lower than that of firn.

6.5.2 Ablation

Fig. 6.8a and 6.8b show the spatial distribution of net annual ablation modelled with z_{0DIST} and $z_{0STATIC}$. Areas of high modelled ablation appeared across the glacier surfaces when z_{0DIST} was used (Fig. 6.8a); the highest ablation estimates coincided with the ice-fall, the patch on the glacier right-hand margin, areas where firn was a dominant surface type and the area of small supraglacial debris on the lower glacier. A more continuous distribution was modelled with $z_{0STATIC}$, where the smallest estimates of ablation were located farther up-glacier and most ablation was modelled towards the glacier terminus. The distribution of net annual modelled ablation for both approaches is shown in Fig. 6.8c, where z_{0DIST} displays a greater frequency of higher ablation than $z_{0STATIC}$. In Fig. 6.8d, the mean monthly ablation modelled using z_{0DIST} is consistently greater than that modelled with $z_{0STATIC}$, resulting in a 23% larger mean annual ablation of 1.6 ±0.3 m w.e. (z_{0DIST}) compared to 1.3 ±0.2 m w.e ($z_{0STATIC}$).

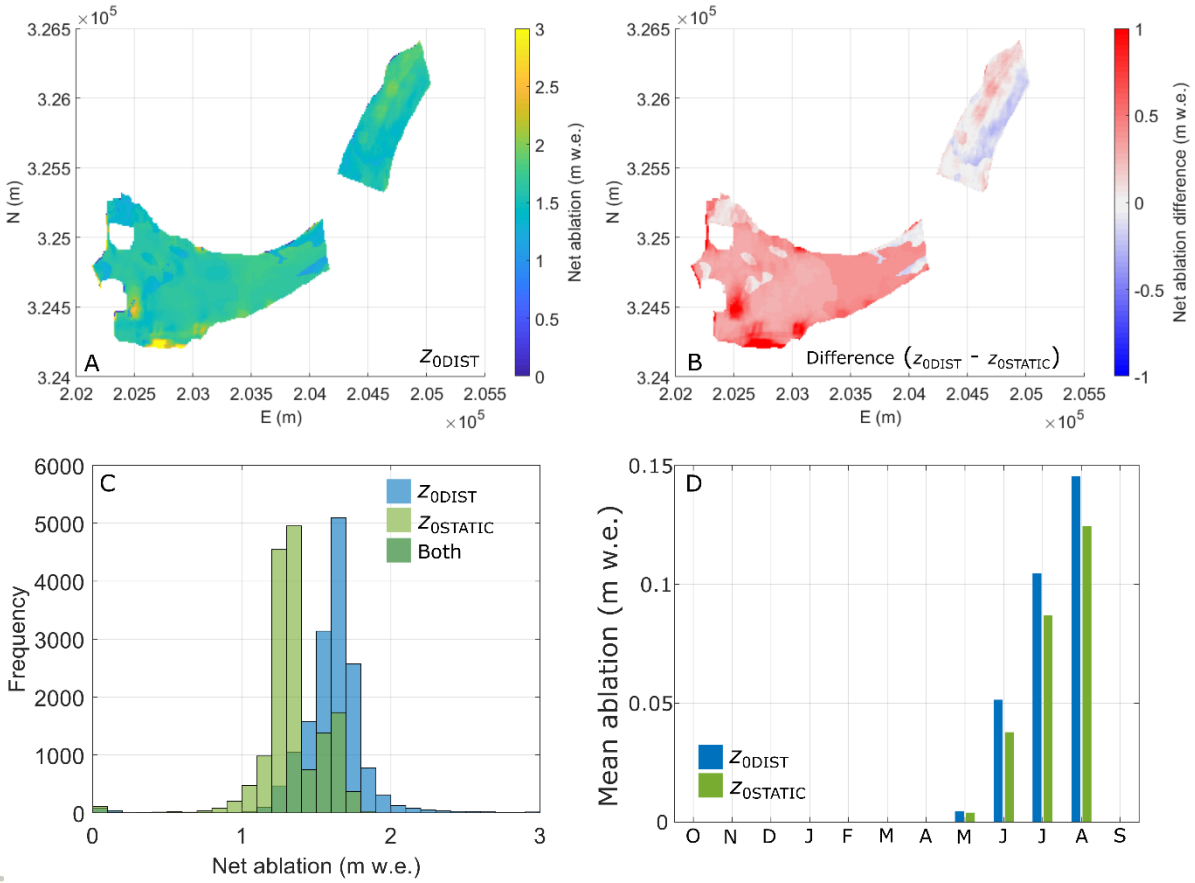

Fig. 6.8 Summary of ablation modelled with z_{0DIST} and $z_{0STATIC}$. Spatial distribution of net ablation for the SEB year is shown for z_{0DIST} (A), while the difference in ablation between z_{0DIST} and $z_{0STATIC}$ is shown in (B). (C) shows distribution of net ablation values for the year and (D) shows monthly mean ablation for the whole glacier.

Inspection of the ablation season shows similar day-to-day patterns in energy fluxes and ablation modelled by z_{0DIST} and $z_{0STATIC}$, with higher levels of both modelled by z_{0DIST} as expected (Fig. 6.9a and 6.9b). In both cases, the days with the greatest modelled ablation were associated with greater amounts of energy provided by the turbulent fluxes, primarily Q_S. As demonstrated by the examples in Table 6.5, increases and decreases in Q_S were associated with larger impacts on modelled ablation than changes in the SW flux. This is verified by Fig. 6.10, which shows that temporal changes in mean ablation more closely follow the changes in Q_S (r^2 = 0.7, p<0.01) than the SW flux (r^2 = 0.2, p<0.01).

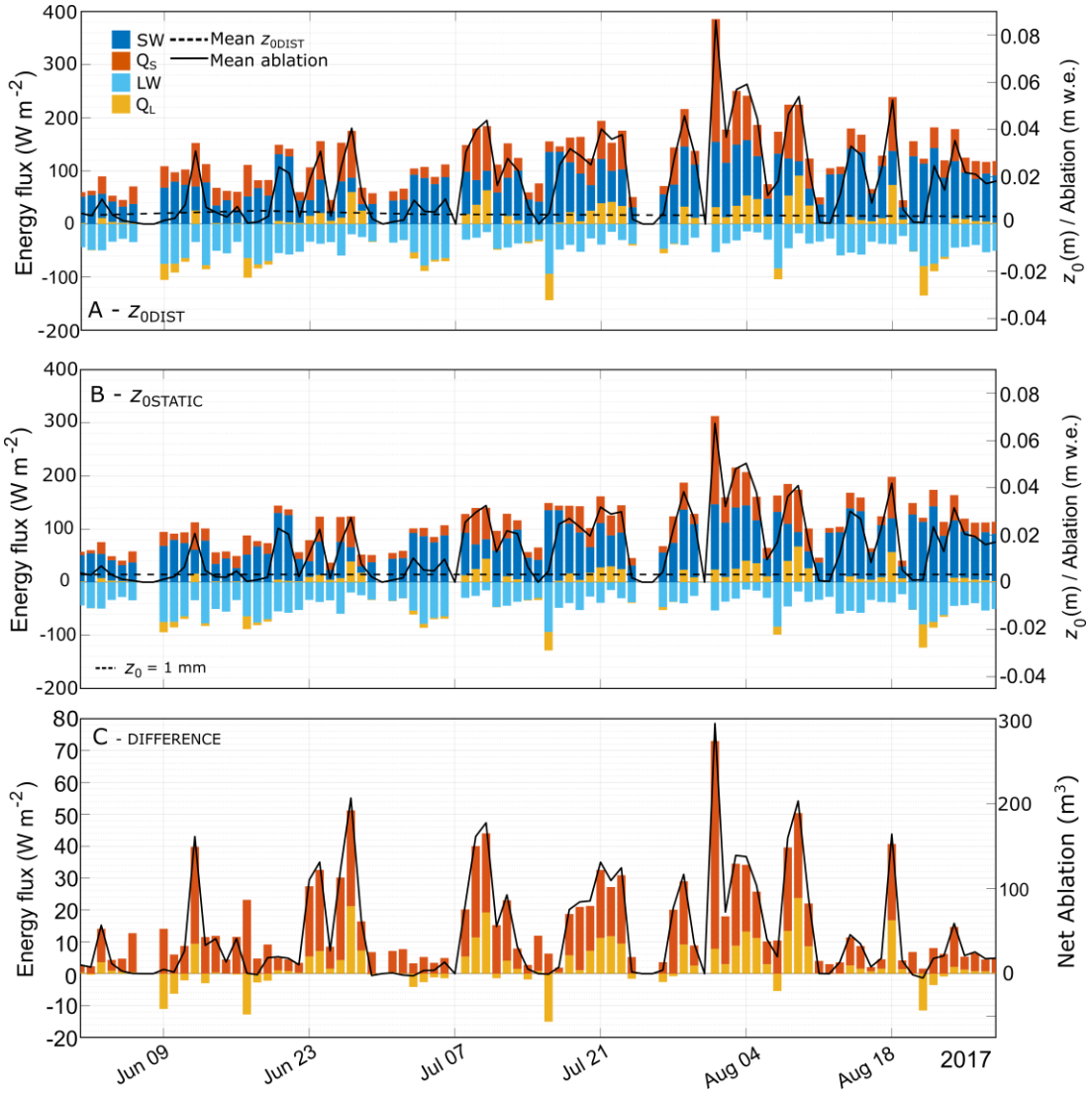

Fig. 6.9 Daily surface energy balance and ablation through the ablation season. Daily mean fluxes, ablation and z_0, averaged across the entire glacier are shown for z_{0DIST} (A) and $z_{0STATIC}$ (B). The difference in mean energy fluxes, as well as the difference in net daily ablation totals for the glacier, are also shown (C).

Table 6.5 Ablation and fluxes for selected days to illustrate impact of $\boldsymbol{Q_S}$ on ablation modelled with z_{0DIST}. 1st August had the highest modelled $\boldsymbol{Q_S}$, 15th August had a lower $\boldsymbol{Q_S}$ but SW flux similar to that on 1st August. 29th August had the highest modelled SW flux. Standard deviations shown in square brackets.

	1 August (highest Q_S)	15 August (similar SW flux)	22 August (highest SW flux)
Mean ablation (m w.e.)	0.086 [0.03]	0.029 [0.005]	0.025 [0.004]
SW flux (W m^{-2})	122.9 [13.6]	127.6 [11.6]	142.9 [15.2]
LW flux (W m^{-2})	-53.2 [7.9]	-57.7 [8.4]	-74.9 [7.5]
Q_S (W m^{-2})	231.3 [118.7]	32.8 [13.5]	38.9 [23.5]
Q_L (W m^{-2})	31.6 [10.3]	7.6 [3.0]	-14.3 [14.5]

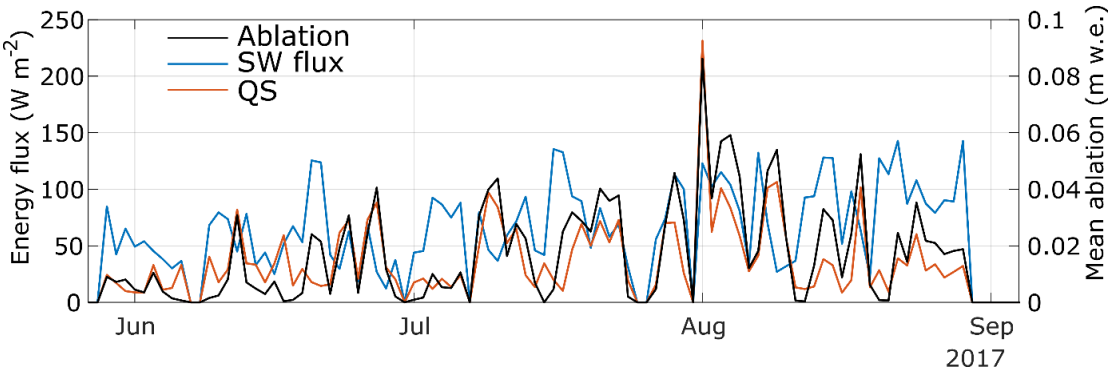

Fig. 6.10 Time series of daily mean sensible heat flux (Q_S), shortwave radiation flux (SW flux) and ablation for the ablation season (days on which ablation was modelled) from z_{0DIST} model.

6.5.3 Impact of z_{0DIST}/$z_{0STATIC}$ under adjusted climate scenarios

The overall effect of forcing the model with increased average daily air temperatures, with both z_{0DIST} and $z_{0STATIC}$, was to increase the contribution of energy from the turbulent fluxes to the SEB on days when melt was modelled (Fig. 6.11a and 6.11b). When modelled with no increase in air temperature, the turbulent fluxes accounted for 9% more of the annual SEB with z_{0DIST} (66%) than with $z_{0STATIC}$ (57%). When forced with warmer air temperatures, annual mean turbulent flux contribution for z_{0DIST} increased to 74% with 1.5°C warming, 77% with 2°C warming and 79% with 2.5°C warming, compared to 67%, 70% and 72% with $z_{0STATIC}$ for each scenario respectively. The total number of days with modelled melt also increased, from 89 to 99 with z_{0DIST} and from 88 to 96 with $z_{0STATIC}$. The simulated change in mean daily ablation was greater when modelled using z_{0DIST}, rising from 0.019 m w.e. to 0.026 m w.e. across the four scenarios (Fig. 6.11b), representing up to a 37% increase when daily mean air temperatures were 2.5°C warmer. When modelled with $z_{0STATIC}$, there was a 31% increase in mean daily net ablation for 2.5°C warming. This suggests that even though increases in turbulent flux contribution to the SEB were smaller when modelled with z_{0DIST}, they led to greater overall increases in ablation than those projected using $z_{0STATIC}$.

Similar increases were observed when mean daily wind speeds were increased (Fig. 6.11c and 6.11d). Overall, the increase in turbulent flux contribution to the SEB with mean wind speed increased by 1.5 m s^{-1} was greatest when modelled with $z_{0STATIC}$ (58% to 71%), compared with z_{0DIST} (66% to 77%). Conversely, the resulting increase in modelled ablation was larger for z_{0DIST} (0.019 m w.e. to 0.029 m w.e.) than it was for $z_{0STATIC}$ (0.016 m w.e. to 0.023 m w.e.). Again, while the larger increase in turbulent flux contribution to the SEB was seen for $z_{0STATIC}$, the greater impact in terms of ablation was observed for z_{0DIST}.

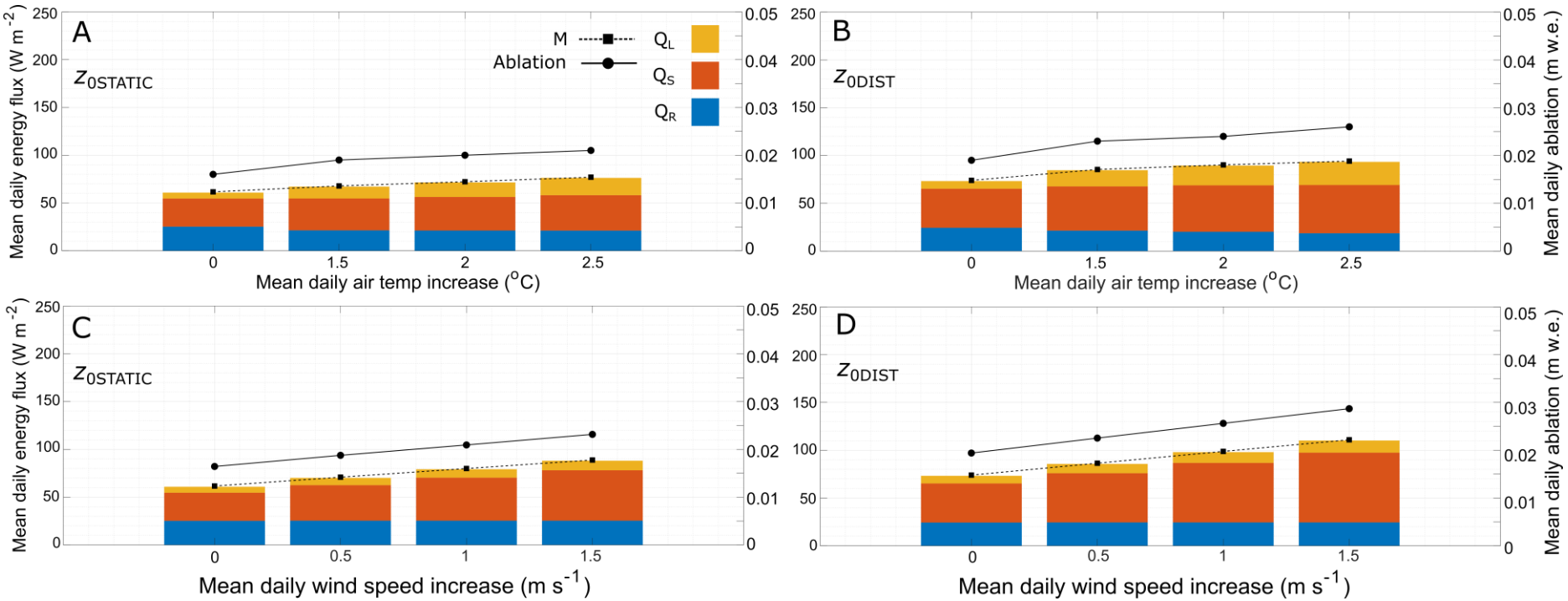

Fig. 6.11 Results of simulated climate scenario experiments. Increases in air temperature are shown for $z_{0STATIC}$ (A) and z_{0DIST} (B), and increased wind speeds for $z_{0STATIC}$ (C) and z_{0DIST} (D). Legend applies to all panels. In all cases, increase of zero reflects the SEB and ablation modelled for the SEB year September 2016 to September 2017. Mean values calculated from days with modelled ablation.

6.6 Discussion

6.6.1 Significance and implications of using fully distributed z_0

The sensitivity of turbulent fluxes to z_0 has been reported previously; the effect that an order of magnitude increase in z_0 doubles the turbulent fluxes is commonly acknowledged (Hock and Holmgren, 1996; Brock and Arnold, 2000; Hock, 2005; Fitzpatrick *et al.*, 2019). This doubling effect was replicated here when runs of z_0 of 1 mm were compared to runs with a z_0 of 10 mm. There was a 110% increase in Q_S, 109% increase in Q_L and a 193% increase in the overall energy available for melt. Runs with 10 mm z_0 modelled 66.6% more ablation than when z_0 was 1 mm (Fig. 6.4).

In this study, we also compared model runs using a fixed value of z_0 and fully distributed z_0. Overall, the energy contributed by the turbulent fluxes to the energy balance and the total energy available for melt were greater when modelled using a fixed z_0 value ($z_{0STATIC}$), and this was most pronounced during periods when air temperatures were <0°C. These were periods when the glacier was generally snow-covered, and so the distributed z_0 model (z_{0DIST}) was assigned a z_0 of 0.2 mm, compared to the 1 mm used as the fixed value. Since it was assumed that there was no surface melt when air temperatures were <0°C, the influence of z_0 during these times was not considered to be as important as during the ablation season, when melt was modelled.

When the ablation season is compared between model runs, the contribution of the turbulent fluxes to the energy balance and the overall amount of energy available for melt were greater using z_{0DIST}. This can be directly attributed to the fact that z_{0DIST} (mean 3.8 mm) was greater than $z_{0STATIC}$ (1 mm) throughout most of the ablation season. As a consequence, 21% more ablation was modelled using z_{0DIST} than was modelled using $z_{0STATIC}$. It is worth noting that the energy provided by the turbulent fluxes, the energy available for melt and the volume of ablation are all dependent on the exact value of z_0 chosen, but 1 mm is common (Van As, 2011; Fausto *et al.*, 2016b). Accurate and spatially variable representation of z_0 is therefore critical if turbulent fluxes and consequent melt volumes are to be modelled robustly. The incorporation of fully distributed z_0 into a SEB model has shown a potential method to achieve this representation.

The importance of using fully representative z_0 values was further demonstrated by model runs with artificially adjusted meteorological inputs (Fig. 6.11). We acknowledge here that the experiments cannot account for the multiple feedbacks with the climate system that increased mean daily air temperatures would cause, or the possibly enhanced effects owing to the high relief of mountain areas (Hock *et al.*, 2019). Equally, predictions of future wind

speeds in the European Alps are uncertain (Vautard *et al.*, 2010; Moemken *et al.*, 2018; Graf *et al.*, 2019). As noted previously, additional effects of increasing single parameters such as air temperature are likely to include altered relative humidity and cloudiness, as well as calculated variables such as saturation vapour pressure and surface temperatures. However, the changes were applied to each variable prior to calculation of the turbulent fluxes, so there is no anticipated impact on the findings of the study.

Fig. 6.11 shows the sensitivity of the turbulent fluxes and volume of ablation to air temperature and wind speed through the model outputs for increasingly warm/windy scenarios – here, outputs showed a particular sensitivity to increases in both variables. Slightly larger increases in the turbulent fluxes, energy for melt and ablation were observed with increased mean wind speeds, reflecting the sensitivity of the fluxes to wind speeds between 3-5 m s^{-1} (Dadic *et al.*, 2013). The differences in model outcomes between runs with fixed and distributed z_0 further highlight the added potential for under or overestimation of model outputs if z_0 is not adequately represented. This is especially relevant for modelling contemporary and future melt in regions where the turbulent fluxes play an important role. For example, current regional climate models underrepresent the role of the turbulent fluxes over glaciers on the periphery of the Greenland Ice Sheet (Fausto *et al.*, 2016b; van den Broeke *et al.*, 2017), where climatic phenomena such as the conditions that cause widespread melt events (Fausto *et al.*, 2016a; Cullather *et al.*, 2020), and blocking anticyclones (Ward *et al.*, 2020) exhibit conditions favourable for increased contribution of turbulent fluxes to the SEB. Thus, adequate representation of z_0 is going to become increasingly important as the likelihood of the occurrence of these conditions increases (Fausto *et al.*, 2016b).

6.6.2 Distribution of z_0

Performance of the z_0 correction workflow was assessed in Chambers *et al.* (2021). Overall, corrected z_0 estimated from TLS data demonstrated strong similarity to z_0 derived from UAV-based structure-from-motion surveys, aerodynamic profiles from wind towers and sonic anemometers, falling within one order of magnitude of each. Variation in daily topographic z_0 over Hintereisferner spanned between three and nine orders of magnitude, similar to the substantial spatial variability recorded over other glaciers (Brock *et al.*, 2000; Sicart *et al.*, 2014; Fitzpatrick *et al.*, 2019). Our results highlight the importance of spatial variation in z_0 and sub-annual temporal variation; however, variation between years is likely to be less important. Observations elsewhere of roughness characteristics persisting from one year to

the next (Sicart *et al.*, 2014; Fitzpatrick *et al.*, 2019) suggest that our approach is valid even if the available topographic data do not coincide with the exact period over which the SEB is modelled. Nevertheless, additional topographic data from different times in the year would certainly be beneficial because, as with albedo, linearly interpolating between separate dates risks oversimplifying roughness trajectories. Our model has the capacity to accommodate different roughness trajectories like those observed by Guo *et al.* (2014) and Smeets and van den Broeke (2008) as the bare ice z_0 values are independent of those used for snow surfaces.

The use of fixed z_0 values for different categories of snow surface (Fig. 6.3a) is likely to have led to some over- or underestimation of ablation during the early part of the ablation season when snow cover, or firn cover, was still widespread. The differences in surface are accounted for in part by the albedo-roughness substitution, but the values for each used here, following Bravo *et al.* (2021), do not fully represent the diversity of z_0 found over the surfaces (Gromke *et al.*, 2011). The effects of this oversimplification have a notable influence on the resulting SEB model outputs, as can be seen in Figs. 6.5 and 6.6. Both the correction workflow and temporal model are, as yet, untested on topographic z_0 derived from snow, firn and intermediate surfaces which can have variable z_0 trajectories as smooth snow is degraded by melt processes (Clifton *et al.*, 2008; Gromke *et al.*, 2011; Guo *et al.*, 2011). Another limitation of both the albedo and z_0 distribution models can be seen in an artefact in the SEB model results on the true-right near the head of the glacier (Figs. 6.5 & 6.7). As discussed in Chambers *et al.* (2021), TLS data in this area are likely to incorporate some ice-marginal features and create erroneously high z_0 values. This area is also coincident with an area of shadow on Landsat scenes that persists throughout the year, giving unrealistically low albedo values.

6.6.3 Distribution of other variables

The use of elevation for distributing meteorological variables is common practice, and has been shown to provide insight into energy exchanges at varying spatial and temporal scales (Braun and Hock, 2004; Fyffe *et al.*, 2014; Molg *et al.*, 2020; Bravo *et al.*, 2021). Nevertheless, one of the main limiting factors of the SEB model stems from the point-specific nature of AWS locations, especially where off- and on-glacier sites are mixed, and in cases where only one AWS exists. This can lead to bias in distributions of air temperature data (Bravo *et al.*, 2019) and wind speed data, both of which influence the resulting estimates of the sensible

heat flux (Sauter and Galos, 2016). On Hintereisferner specifically, the distribution of wind speed using elevation gradients masks complex air flow patterns caused by the steep valley sides, which affect the preservation of katabatic winds and distribution of turbulent heat exchange over the glacier surface (Mott *et al.*, 2020). It is unclear at this stage whether such generalisations lead to under or overestimation of the sensible heat flux; however, inclusion of additional AWS locations would allow for more robust distribution.

The impact of not including values for the subsurface heat flux (*G*) should also be noted. Modelling by Sauter *et al.* (2020) projected that subsurface temperatures on Hintereisferner could be <<0°C through the winter. While these temperatures have not yet been validated, the implication is that a substantial amount of energy would be used at the start of the melt season to increase them. This would mean that the duration of the ablation season and the overall volume of melt modelled in this study are overestimates, specifically the amount of snowmelt at the onset of the melt season (Wheler and Flowers, 2011). This is an important consideration for glacier SEB modelling in general, but not expected to have a great effect on the findings of this study because *G* was discounted in both the z_{0DIST} and $z_{0STATIC}$ cases. If anything, it is likely that greater fluxes toward the surface modelled using z_{0DIST} would accelerate the warming of subsurface temperatures and initiate melt earlier than $z_{0STATIC}$.

The approach used to retrieve albedo from Landsat products has been used over mountain glaciers with a high degree of accuracy (<0.01) compared to other methods (Naegeli *et al.*, 2017; 2019). To model temporal change in albedo, other studies using distributed SEB modelling have employed approaches based on snowfall events, in which albedo is a function of air temperatures and time since the most recent snowfall (Ayala *et al.*, 2017; Bravo *et al.*, 2021; Brock *et al.*, 2000; Klok & Oerlemans, 2004; Oerlemans & Klok, 2002; Oerlemans & Knap, 1998). Precipitation data were not available for Hintereisferner for the study period, so here we used a simple linear interpolation between dated Landsat albedo grids. While the detail of albedo changes over short timescales is masked (Fig. 6.12), modelled albedo compared well to albedo calculated from the on-glacier AWS (r^2 = 0.7, ρ <0.01) and the overall annual trend was replicated with a divergence in mean daily albedo of 0.02 (σ = 0.14).

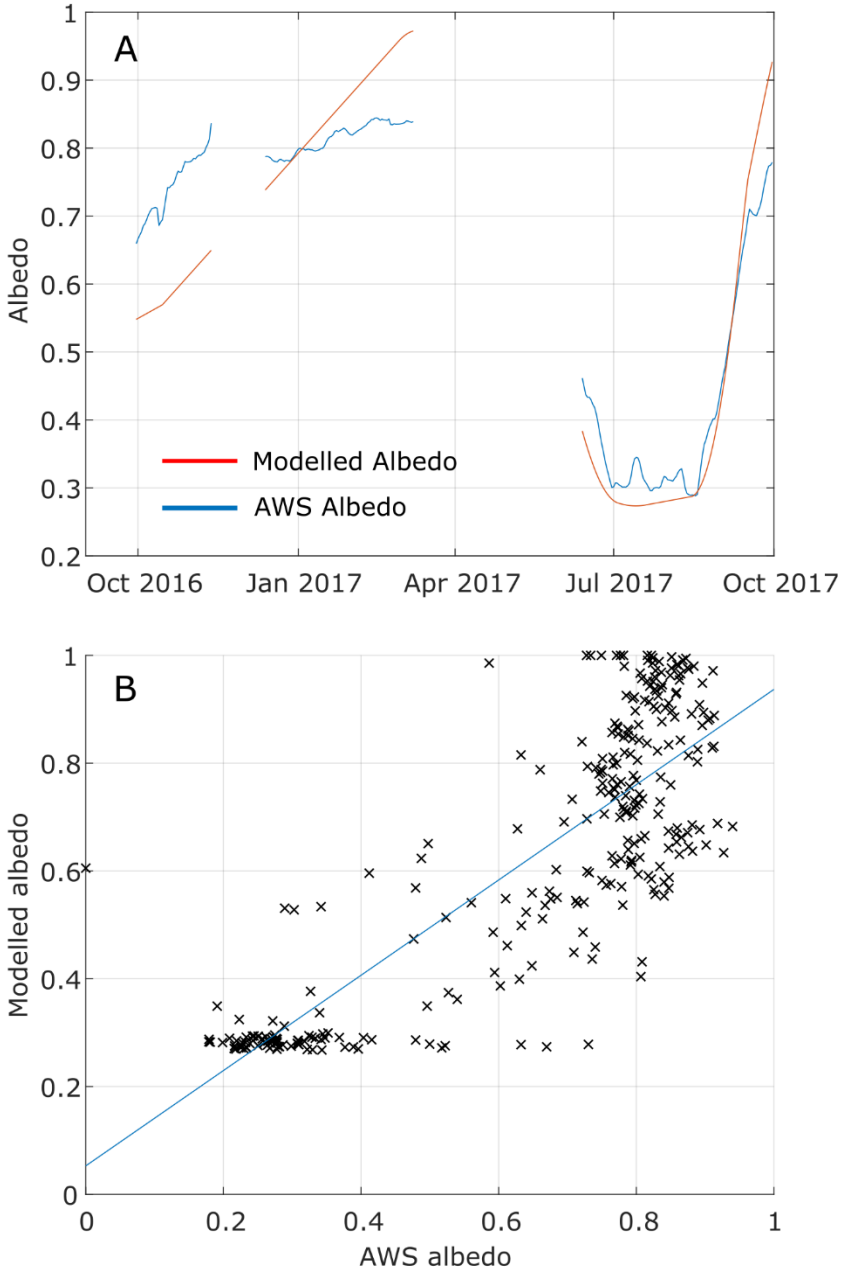

Fig. 6.12 Albedo timseries showing modelled and AWS-derived albedo (30 day moving mean) for the SEB year (A).. Comparison of modelled and AWS-derived albedo with a fitted linear model (B).

6.6.4 Model performance

While the focus of this paper is the inclusion of a distributed z_0 parameter rather than an absolute quantification of the energy balance for Hintereisferner *per se*, a limited number of data do exist to compare our simulations with. A 1D point-scale SEB model (Greuell and Oerlemans, 1989) shows some divergence with our results; in particular it estimates Q_S to be approximately half of what we found in our study, but Q_R was almost five times higher. It should be noted though that Greuell and Oerlemans (1989) used data collected from an AWS

located at a point 2500 m a.s.l. in 1986, which is suspected to now be beyond the current glacier terminus position, as well as limiting their analysis to a ten day period at the peak of the ablation season. More comparable data exist from the World Glacier Monitoring Service, who host mass balance information from calculations undertaken for Hintereisferner by the University of Innsbruck. Here, our modelled net annual mass loss across the glacier surface (1.6 ±0.3 m w.e.) is similar to the annual value (1.9 m w.e.) given by the WGMS for the 2017 hydrological year (WGMS, 2020, updated, and earlier reports). It is perfectly feasible that the 0.3 m w.e. shortfall between these two measurements could be accounted for by ablation during the months of April, May and September, data for which were missing in the current study.

6.7 Conclusions

In this study we presented the first known use of fully spatially and temporally distributed glacier aerodynamic roughness, z_0, in a distributed SEB model. Full distribution of z_0 was achieved using coarse resolution (10 m) topographic data without the need for additional *in situ* data collection, showing that inclusion of distributed, representative z_0 estimates need no longer be considered a substantial barrier to SEB modelling. Spatial distribution was achieved using a correction factor that accounts for systematic under-correction of z_0 estimates derived from coarse-scale topographic data, of the kind that is widely available for glacerised regions (Chambers *et al.*, 2021). Temporal distribution was based on reclassified albedo grids retrieved from Landsat scenes from various dates alongside a space-for-time substitution that adjusted z_0 based on how long the bare ice surface has been exposed (Smith *et al.*, 2020).

SEB model outputs from runs using different fixed values of z_0 demonstrated the sensitivity of the turbulent fluxes and overall energy balance to z_0, with an order of magnitude increase in z_0 leading to a doubling of the turbulent fluxes and almost a tripling of the energy available for melt.

Model runs incorporating static and distributed z_0 elucidated the differences in spatial and temporal patterns in turbulent flux contributions to the SEB that are masked by the use of a fixed z_0 value. Using a fixed value for z_0 can model greater turbulent fluxes over a year, but up to 38% greater sensible heat flux was modelled during the ablation season using distributed z_0 than for the same period using fixed z_0. This increase translated to a 30% greater contribution by the turbulent fluxes to the SEB and 21% more ablation, confirming

that the turbulent fluxes and ablation volumes can be substantially under- or overestimated through the use of a fixed z_0 value. We show that distributed, representative z_0 can be, and we argue should be, incorporated into a distributed SEB model.

In sensitivity tests, when air temperature was artificially increased in order to simulate different climatic regimes, the sensitivity of modelled melt to z_0 increased when distributed z_0 was incorporated, leading to an increase in daily ablation of up to 37%, compared to 31% when z_0 was fixed to 1 mm. Similarly, when wind speeds were increased instead the sensitivity of modelled melt to z_0 was greater when distributed z_0 was used than when z_0 was fixed; 52% more ablation was modelled for a 1.5 m s^{-1} increase in wind speeds with distributed z_0, compared to 43% for static z_0.

The work presented here highlights the importance of correct representation of z_0 in conditions that favour the turbulent fluxes over a temperate mountain glacier, providing a solid foundation from which further work can seek to make distributed estimates of z_0 more robust, particularly over snow surfaces, by ensuring that z_0 is adequately represented in glacier SEB models.

References

Anderson, B., Mackintosh, A., Stumm, D., George, L., Kerr, T., Winter-Billington, A. & Fitzimons, S. (2010) 'Climate sensitivity of a high-precipitation glacier in New-Zealand', *Journal of Glaciology*, 56(195), pp. 114-128(15). doi: 10.3189/002214310791190929.

Arnold, N. S., Rees, W. G., Hodson, A. J. & Kohler, J. (2006) 'Topographic controls on the surface energy balance of a high Arctic valley glacier', *Journal of Geophysical Research: Earth Surface*, 111(2). doi: 10.1029/2005JF000426.

Van As, D. (2011) 'Warming, glacier melt and surface energy budget from weather station observations in the Melville Bay region of northwest Greenland', *Journal of Glaciology*, 57(202), pp. 208–220. doi: 10.3189/002214311796405898.

Ayala, A., Pellicciotti, F., Peleg, N. & Burlando, P. (2017) 'Melt and surface sublimation across a glacier in a dry environment: Distributed energy-balance modelling of Juncal Norte Glacier, Chile', *Journal of Glaciology*, 63(241), pp. 803–822. doi: 10.1017/jog.2017.46.

Braun, M. & Hock, R. (2004) 'Spatially distributed surface energy balance and ablation modelling on the ice cap of King George Island (Antarctica)', *Global and Planetary Change*, 42(1–4), pp. 45–58. doi: 10.1016/j.gloplacha.2003.11.010.

Bravo, C., Loriaux, T., Rivera, A. & Brock, B. W. (2017) 'Assessing glacier melt contribution to streamflow at Universidad Glacier, central Andes of Chile', *Hydrology and Earth System Sciences*, 21(7), pp. 3249–3266. doi: 10.5194/hess-21-3249-2017.

Bravo, C., Quincey, D. J., Ross, A. N., Rivera, A., Brock, B., Miles, E. & Silva, A. (2019) 'Air Temperature Characteristics, Distribution, and Impact on Modeled Ablation for the South Patagonia Icefield', *Journal of Geophysical Research: Atmospheres*, 124(2), pp. 907–925. doi: 10.1029/2018JD028857.

Brock, B. W. & Arnold, N. S. (2000) 'A spreadsheet-based (Microsoft Excel) point surface energy balance model for glacier and snowmelt studies.', *Earth Surface Processes and Landforms*, 25(October 2015), pp. 649–658. doi: 10.1002/1096-9837(200006)25.

Brock, B. W., Willis, I. C. & Sharp, M. J. (2006) 'Measurement and parameterization of aerodynamic roughness length variations at Haut Glacier d'Arolla, Switzerland', *Journal of Glaciology*, 52(177), pp. 281–297. doi: 10.3189/172756506781828746.

Brock, B. W., Willis, I. C., Sharp, M. J. & Arnold, N. S. (2000) 'Modelling seasonal and spatial variations in the surface energy balance of Haut Glacier d'Arolla, Switzerland', *Annals of Glaciology*, 31(January 2016), pp. 53–62. doi: 10.3189/172756400781820183.

van den Broeke, M., Box, J., Fettweis, X., Hanna, E., Noël, B., Tedesco, M., van As, D., van de Berg, W. J. & van Kampenhout, L. (2017) 'Greenland Ice Sheet Surface Mass Loss: Recent Developments in Observation and Modeling', *Current Climate Change Reports*. Springer, pp. 345–356. doi: 10.1007/s40641-017-0084-8.

Burba, G. (2013) *Eddy Covariance Method-for Scientific, Industrial, Agricultural, and Regulatory Applications*. Lincoln, Nebraska: LI-COR Biosciences. doi: 10.1007/s00704-004-0095-y.

Chambers, J. R., Smith, M. W., Quincey, D. J., Carrivick, J. L., Ross, A. N. & James, M. R. (2019) 'Glacial Aerodynamic Roughness Estimates: Uncertainty, Sensitivity, and Precision in Field Measurements', *Journal of Geophysical Research: Earth Surface*, 125(2). doi:

10.1029/2019JF005167.

Chambers, J. R., Smith, M. W., Smith, T., Sailer, R., Quincey, D. J., Carrivick, J. L., Nicholson, L., Mertes, J., Stiperski, I. & James, M. R. (2021) 'Correcting for Systematic Underestimation of Topographic Glacier Aerodynamic Roughness Values From Hintereisferner, Austria', *Frontiers in Earth Science*, 9, pp. 1–16. doi: 10.3389/feart.2021.691195.

Clifton, A., Manes, C., Rüedi, J. D., Guala, M. & Lehning, M. (2008) 'On shear-driven ventilation of snow', *Boundary-Layer Meteorology*, 126(2), pp. 249–261. doi: 10.1007/s10546-007-9235-0.

Conway, J. P. & Cullen, N. J. (2013) 'Constraining turbulent heat flux parameterization over a temperate maritime glacier in New Zealand', *Annals of Glaciology*, 54(63), pp. 41–51. doi: 10.3189/2013AoG63A604.

Cuffey, K. M. & Paterson, W. S. B. (2010) *The Physics of Glaciers*. Fourth. Oxford: Elsevier. doi: 10.1063/1.2915138.

Cullather, R. I., Andrews, L. C., Croteau, M. J., Digirolamo, N. E., Hall, D. K., Lim, Y. K., Loomis, B. D., Shuman, C. A. & Nowicki, S. M. J. (2020) 'Anomalous Circulation in July 2019 Resulting in Mass Loss on the Greenland Ice Sheet', *Geophysical Research Letters*, 47(17). doi: 10.1029/2020GL087263.

Dadic, R., Mott, R., Lehning, M., Carenzo, M., Anderson, B. & Mackintosh, A. (2013) 'Sensitivity of turbulent fluxes to wind speed over snow surfaces in different climatic settings', *Advances in Water Resources*, 55, pp. 178–189. doi: 10.1016/j.advwatres.2012.06.010.

Denby, B. & Greuell, W. (2000) 'The Use of Bulk and Profile Methods for Determining Surface Heat Fluxes in the Presence of Glacier Winds', *Journal of Glaciology*, 46(154), pp. 445–452.

Fausto, R. S., Van As, D., Box, J. E., Colgan, W. & Langen, P. L. (2016a) 'Quantifying the surface energy fluxes in South Greenland during the 2012 high melt episodes using in-situ observations', *Frontiers in Earth Science*, 4. doi: 10.3389/feart.2016.00082.

Fausto, R. S., Van As, D., Box, J. E., Colgan, W., Langen, P. L. & Mottram, R. H. (2016b) 'The implication of nonradiative energy fluxes dominating Greenland ice sheet exceptional ablation area surface melt in 2012', *Geophysical Research Letters*, 43(6), pp. 2649–2658. doi: 10.1002/2016GL067720.

Fischer, A. (2010) 'Glaciers and climate change: Interpretation of 50 years of direct mass balance of Hintereisferner', *Global and Planetary Change*, 71(1–2), pp. 13–26. doi: 10.1016/j.gloplacha.2009.11.014.

Fitzpatrick, N., Radić, V. & Menounos, B. (2017) 'Surface Energy Balance Closure and Turbulent Flux Parameterization on a Mid-Latitude Mountain Glacier, Purcell Mountains, Canada', *Frontiers in Earth Science*, 5(September), pp. 1–20. doi: 10.3389/feart.2017.00067.

Fitzpatrick, N., Radić, V. & Menounos, B. (2019) 'A multi-season investigation of glacier surface roughness lengths through in situ and remote observation', *The Cryosphere*, 13, pp. 1051–1071. doi: https://doi.org/10.5194/tc-13-1051-2019.

Fu, P. & Rich, P. M. (2002) *A geometric solar radiation model with applications in agriculture and forestry*, *Computers and Electronics in Agriculture*. Available at: www.elsevier.com/locate/compag.

Fyffe, C. L., Reid, T. D., Brock, B. W., Kirkbride, M. P., Diolaiuti, G., Smiraglia, C. & Diotri, F. (2014) 'A distributed energy-balance melt model of an alpine debris-covered glacier', *Journal of Glaciology*, 60(221), pp. 587–602. doi: 10.3189/2014JoG13J148.

Garratt, J. R. (1994) 'The atmospheric boundary layer - review', *Earth - Science Reviews*, 37(1–2), pp. 89–134. doi: 10.1016/0012-8252(94)90026-4.

Giesen, R. H., Andreassen, L. M., Oerlemans, J. & Van Den Broeke, M. R. (2014) 'Surface energy balance in the ablation zone of Langfjordjøkelen, an arctic, maritime glacier in northern Norway', *Journal of Glaciology*, 60(219), pp. 57–70. doi: 10.3189/2014JoG13J063.

Gillett, S. & Cullen, N. J. (2011) 'Atmospheric controls on summer ablation over Brewster Glacier, New Zealand', *International Journal of Climatology*, 31(13), pp. 2033–2048. doi: 10.1002/joc.2216.

Graf, M., Scherrer, S. C., Schwierz, C., Begert, M., Martius, O., Raible, C. C. & Brönnimann, S. (2019) 'Near-surface mean wind in Switzerland: Climatology, climate model evaluation and future scenarios', *International Journal of Climatology*, 39(12), pp. 4798–4810. doi: 10.1002/joc.6108.

Grainger, M. E. & Lister, H. (1966) 'Wind speed, stability and eddy viscosity over melting ice surfaces', *Journal of Glaciology*, 6(43), pp. 101–127.

Greuell, W. & Oerlemans, J. (1989) 'Energy balance calculations on and near Hintereisferner (Austria) and an estimate of the effect of greenhouse warming on ablation.', in Oerlemans, J. (ed.) *Glacier Fluctuations and Climatic Change: Proceedings of the Symposium on Glacier Fluctuations and Climatic Change*. Dordrecht (Netherlands): Kluwer, pp. 305–323.

Gromke, C., Manes, C., Walter, B., Lehning, M. & Guala, M. (2011) 'Aerodynamic Roughness Length of Fresh Snow', *Boundary-Layer Meteorology*, 141(1), pp. 21–34. doi: 10.1007/s10546-011-9623-3.

Guo, X., Yang, K., Zhao, L., Yang, W., Li, S., Zhu, M., Yao, T. & Chen, Y. (2011) 'Critical Evaluation of Scalar Roughness Length Parametrizations Over a Melting Valley Glacier', *Boundary-Layer Meteorology*, 139(2), pp. 307–332. doi: 10.1007/s10546-010-9586-9.

Gusain, H. S., Singh, K. K., Mishra, V. D., Srivastava, P. K. & Ganju, A. (2009) 'Study of surface energy and mass balance at the edge of the antarctic ice sheet during summer in dronning maud land, east antarctica', *Antarctic Science*, 21(4), pp. 401–409. doi: 10.1017/S0954102009001989.

Harding, R. J., Entrasser, N., Escher-Vetter, H., Jenkins, A., Kaser, G., Kuhn, M., Morris, E. M. & Tanzer, G. (1989) 'Energy and Mass Balance Studies in the Firn Area of the Hintereisferner', in Oerlemans, J. (ed.) *Glacier Fluctuations and Climatic Chang*. doi: 10.1007/978-94-015-7823-3_21.

Hock, R. (2005) 'Glacier melt: a review of processes and their modelling', *Progress in Physical Geography*, 29(3), pp. 362–391. doi: 10.1191/0309133305pp453ra.

Hock, R. & Holmgren, B. (1996) 'Some Aspects of Energy Balance and Ablation of Storglaciären , Northern Sweden', *Geografiska Annaler Series A-Physical Geography*, 78(2), pp. 121–131.

Hock, R. & Holmgren, B. (2005) 'A distributed surface energy-balance model for complex topography and its application to Storglaciären, Sweden', *Journal of Glaciology*, 51(172), pp. 25–36. doi: https://doi.org/10.3189/172756505781829566.

Hock, R., Rasul, G., Adler, C., Cáceres, B., Gruber, S., Hirabayashi, Y., Jackson, M., Kääb, A., Kang, S. & Kutuzov, S. (2019) 'High Mountain Areas', in *IPCC Special Report on the Ocean and Cryosphere in a Changing Climate*. Geneva, Switzerland, pp. 131–202.

Irvine-Fynn, T. D. L., Sanz-Ablanedo, E., Rutter, N., Smith, M. W. & Chandler, J. H. (2014) 'Measuring glacier surface roughness using plot-scale, close-range digital photogrammetry', *Journal of Glaciology*, 60(223), pp. 957–969. doi: 10.3189/2014JoG14J032.

Jackson, B. S. & Carroll, J. J. (1978) 'Aerodynamic roughness as a function of wind direction over asymmetric surface elements', *Boundary-Layer Meteorology,* 14(1969), pp. 323–330.

Klok, E. J., Nolan, M. & Van Den Broeke, M. R. (2005) 'Analysis of meteorological data and the surface energy balance of McCall Glacier, Alaska, USA', *Journal of Glaciology*, 51(174), pp. 451–461. doi: 10.3189/172756505781829241.

Klok, E. J. & Oerlemans, J. (2004) 'Modelled climate sensitivity of the mass balance of Morteratschgletscher and its dependence on Albedo parameterization', *International Journal of Climatology*, 24(2), pp. 231–245. doi: 10.1002/joc.994.

Kutzbach, J. (1961) 'Investigations of the modification of wind profiles by artificially controlled surface roughness', in Lettau, H. (ed.) *Studies of the Three-Dimensional Structure of the Planetary Boundary Layer*. University of Wisconsin--Madison, pp. 71–115.

Lemmens, M. (2011) 'Terrestrial Laser Scanning', in *Geo-information*, pp. 101–121. doi: 10.1007/978-94-007-1667-4.

Liang, S. (2000) 'Narrowband to broadband conversions of land surface albedo I Algorithms', *Remote Sensing of Environment*, 76(2), pp. 213–238. doi: https://doi.org/10.1016/S0034-4257(00)00205-4.

Liu, J., Chen, R. & Han, C. (2020) 'Spatial and temporal variations in glacier aerodynamic surface roughness during the melting season, as estimated at the August-one ice cap, Qilian mountains, China', *Cryosphere*, 14(3), pp. 967–984. doi: 10.5194/tc-14-967-2020.

MacDougall, A. H. & Flowers, G. E. (2011) 'Spatial and temporal transferability of a distributed energy-balance glacier melt model', *Journal of Climate*, 24(5), pp. 1480–1498. doi: 10.1175/2010JCLI3821.1.

Miles, E. S., Steiner, J. F. & Brun, F. (2017) 'Highly variable aerodynamic roughness length (z0) for a hummocky debris-covered glacier', *Journal of Geophysical Research: Atmospheres*, 122(16), pp. 8447–8466. doi: 10.1002/2017JD026510.

Moemken, J., Reyers, M., Feldmann, H. & Pinto, J. G. (2018) 'Future Changes of Wind Speed and Wind Energy Potentials in EURO-CORDEX Ensemble Simulations', *Journal of Geophysical Research: Atmospheres*, 123(12), pp. 6373–6389. doi: 10.1029/2018JD028473.

Molg, T., R. Hardy, D., Collier, E., Kropač, E., Schmid, C., J. Cullen, N., Kaser, G., Prinz, R. & Winkler, M. (2020) 'Mesoscale atmospheric circulation controls of local meteorological elevation gradients on Kersten Glacier near Kilimanjaro summit', *Earth System Dynamics*, 11(3), pp. 653–672. doi: 10.5194/esd-11-653-2020.

Morris, E. M. (1982) 'Sensitivity of the European Hydrological System snow models', in *Hydrological Aspects of Alpine and High Mountain Areas, Proc. Symposium International Association of Hydrological Sciences*. Exeter, pp. 221–231.

Mott, R., Stiperski, I. & Nicholson, L. (2020) 'Spatio-temporal flow variations driving heat exchange processes at a mountain glacier', *Cryosphere*, 14(12), pp. 4699–4718. doi:

10.5194/tc-14-4699-2020.

Munro, D. S. (1989) 'Surface roughness and bulk heat transfer on a glacier: comparison with eddy correlation', *Journal of Glaciology*, 35(121), pp. 343–348.

Naegeli, K., Damm, A., Huss, M., Wulf, H., Schaepman, M. & Hoelzle, M. (2017) 'Cross-Comparison of Albedo Products for Glacier Surfaces Derived from Airborne and Satellite (Sentinel-2 and Landsat 8) Optical Data', *Remote Sensing*, 9(2), p. 110. doi: 10.3390/rs9020110.

Naegeli, K., Huss, M. & Hoelzle, M. (2019) 'Change detection of bare-ice albedo in the Swiss Alps', *Cryosphere*, 13(1), pp. 397–412. doi: 10.5194/tc-13-397-2019.

Nicholson, L. I., Pętlicki, M., Partan, B. & MacDonell, S. (2016) '3-D surface properties of glacier penitentes over an ablation season, measured using a Microsoft Xbox Kinect', *Cryosphere*, 10(5), pp. 1897–1913. doi: 10.5194/tc-10-1897-2016.

Oerlemans, J. & Klok, E. J. (2002) 'Energy Balance of a Glacier Surface: Analysis of Automatic Weather Station Data from the Morteratschgletscher, Switzerland', *Arctic, Antarctic, and Alpine Research*, 34(4), pp. 477–485. doi: 10.1080/15230430.2002.12003519.

Oerlemans, J. & Knap, W. (1998) 'A 1 year record of global radiation and albedo in the ablation zone of Morteratschgletscher, Switzerland', *Journal of Glaciology*, 44(147), pp. 231–238. doi: https://doi.org/10.3189/S0022143000002574.

Petersen, L. & Pellicciotti, F. (2011) 'Spatial and temporal variability of air temperature on a melting glacier: Atmospheric controls, extrapolation methods and their effect on melt modeling, Juncal Norte Glacier, Chile', *Journal of Geophysical Research Atmospheres*, 116(23). doi: 10.1029/2011JD015842.

Quincey, D. J., Smith, M. W., Rounce, D. R., Ross, A. N., King, O. & Watson, C. S. (2017) 'Evaluating morphological estimates of the aerodynamic roughness of debris covered glacier ice', *Earth Surface Processes and Landforms*. doi: 10.1002/esp.4198.

Rees, W. G. & Arnold, N. S. (2006) 'Scale-dependent roughness of a glacier surface: Implications for radar backscatter and aerodynamic roughness modelling', *Journal of Glaciology*, 52(177), pp. 214–222. doi: 10.3189/172756506781828665.

Roe, G. H., Christian, J. E. & Marzeion, B. (2021) 'On the attribution of industrial-era glacier mass loss to anthropogenic climate change', *The Cryosphere*, 15(4), pp. 1889–1905. doi: 10.5194/tc-15-1889-2021.

Sauter, T., Arndt, A. & Schneider, C. (2020) 'COSIPY v1.3 – an open-source coupled snowpack and ice surface energy and mass balance model', *Geoscientific Model Development*, 13(11), pp. 5645–5662. doi: 10.5194/gmd-13-5645-2020.

Sauter, T. & Galos, S. (2016) 'Effects of local advection on the spatial sensible heat flux variation on a mountain glacier', *Cryosphere*, 10(6), pp. 2887–2905. doi: 10.5194/tc-10-2887-2016.

Shaw, T. E., Brock, B. W., Fyffe, C. L., Pellicciotti, F., Rutter, N. & Diotri, F. (2020) 'Air temperature distribution and energy-balance modelling of a debris-covered glacier'. Available at: http://creativecommons.

Sicart, J. E., Hock, R., Ribstein, P. & Chazarin, J. P. (2010) 'Sky longwave radiation on tropical Andean glaciers: parameterization and sensitivity to atmospheric variables', *Journal of Glaciology*, 56(199), pp. 854–860. doi: https://doi.org/10.3189/002214310794457182.

Sicart, J. E., Hock, R., Ribstein, P., Litt, M. & Ramirez, E. (2011) 'Analysis of seasonal variations in mass balance and meltwater discharge of the tropical Zongo Glacier by application of a distributed energy balance model', *Journal of Geophysical Research Atmospheres*, 116(13). doi: 10.1029/2010JD015105.

Sicart, J. E., Litt, M., Helgason, W., Tahar, V. Ben & Chaperon, T. (2014) 'A study of the atmospheric surface layer and roughness lengths on the high-altitude tropical Zongo glacier, Bolivia', *Journal of Geophysical Research*, 119(7), pp. 3793–3808. doi: 10.1002/2013JD020615.

Sicart, J. E., Wagnon, P. & Ribstein, P. (2005) 'Atmospheric controls of the heat balance of Zongo Glacier (16°S, Bolivia)', *Journal of Geophysical Research D: Atmospheres*, 110(12), pp. 1–17. doi: 10.1029/2004JD005732.

Smeets, C. J. P. P. & van den Broeke, M. R. (2008) 'Temporal and spatial variations of the aerodynamic roughness length in the ablation zone of the greenland ice sheet', *Boundary-Layer Meteorology*, 128(3), pp. 315–338. doi: 10.1007/s10546-008-9291-0.

Smith, M. W., Carrivick, J. L. & Quincey, D. J. (2016a) 'Structure from motion photogrammetry in physical geography', *Progress in Physical Geography*, 40(2), pp. 247–275. doi: 10.1177/0309133315615805.

Smith, M. W., Quincey, D. J., Dixon, T., Bingham, R. G., Carrivick, J. L., Irvine-Fynn, T. D. L. & Rippin, D. M. (2016b) 'Aerodynamic roughness of glacial ice surfaces derived from high-resolution topographic data', *Journal of Geophysical Research F: Earth Surface*, 121(4), pp. 748–766. doi: 10.1002/2015JF003759.

Smith, T. I., Smith, M. W., Chambers, J. R., Sailer, R., Nicholson, L., Mertes, J., Quincey, D. J., Carrivick, J. L. & Stiperski, I. (2020) 'A scale-dependent model to represent changing aerodynamic roughness of ablating glacier ice based on repeat topographic surveys', *Journal of Glaciology*, pp. 1–15. doi: 10.1017/jog.2020.56.

Strasser, U., Marke, T., Braun, L., Escher-Vetter, H., Juen, I., Kuhn, M., Maussion, F., Mayer, C., Nicholson, L., Niedertscheider, K., Sailer, R., Stötter, J., Weber, M. & Kaser, G. (2018) 'The Rofental: A high Alpine research basin (1890-3770ma.s.l.) in the Ötztal Alps (Austria) with over 150 years of hydrometeorological and glaciological observations', *Earth System Science Data*, 10(1), pp. 151–171. doi: 10.5194/essd-10-151-2018.

Stull, R. (1988) *An introduction to boundary layer meteorology*. London: Kluwer.

Telling, J., Lyda, A., Hartzell, P. & Glennie, C. (2017) 'Review of Earth science research using terrestrial laser scanning', *Earth-Science Reviews*, 169(April), pp. 35–68. doi: 10.1016/j.earscirev.2017.04.007.

University of Innsbruck (2020) *Permanent Terrestrial Laserscanner 'Im hinteren Eis'*. Available at: https://www.uibk.ac.at/geographie/projects/i_he/ (Accessed: 20 August 2020).

USGS (2021) *Using the USGS Landsat Level-1 Data Product*. Available at: https://www.usgs.gov/core-science-systems/nli/landsat/using-usgs-landsat-level-1-data-product (Accessed: 2 April 2021).

Vautard, R., Cattiaux, J., Yiou, P., Thépaut, J. N. & Ciais, P. (2010) 'Northern Hemisphere atmospheric stilling partly attributed to an increase in surface roughness', *Nature Geoscience*, 3(11), pp. 756–761. doi: 10.1038/ngeo979.

Wagnon, P., Ribstein, P., Francou, B. & Pouyaud, B. (1999) 'Annual cycle of energy balance

of Zongo glacier, Cordillera Real, Bolivia', *Journal of Geophysical Research Atmospheres*, 104, pp. 3907–3923.

Ward, J. L., Flanner, M. G. & Dunn-Sigouin, E. (2020) 'Impacts of Greenland Block Location on Clouds and Surface Energy Fluxes Over the Greenland Ice Sheet', *Journal of Geophysical Research: Atmospheres*, 125(22). doi: 10.1029/2020JD033172.

WGMS (2020) *World Glacier Monitoring Service: Hintereisferner, Alps*. Available at: http://wgms.ch/products_ref_glaciers/hintereisferner-alps/ (Accessed: 8 June 2021).

Wheler, B. A. & Flowers, G. E. (2011) 'Glacier subsurface heat-flux characterizations for energy-balance modelling in the Donjek Range, southwest Yukon, Canada', *Journal of Glaciology*, 57(201), pp. 121–133. doi: 10.3189/002214311795306709.

Part III: Discussion and Conclusions

Chapter 7 : Discussion and Conclusions

7.1 Introduction

In this chapter, the findings of this thesis are discussed in the context of the wider literature and their implications for the field of glacier surface energy balance modelling. First, the key points of Chapters 4, 5 and 6 are summarised to show how they fulfil the original thesis objectives (Section 7.2). Next, the contributions that this work makes to the field of glacier SEB modelling are discussed in Section 7.3 along with improvements that could be made (Section 7.4), followed by a discussion of other issues encountered during this research in Section 7.5. Ideas for future research are presented in Section 7.6, and finally the overall conclusions of the thesis are given in Section 7.7.

7.2 Overview of thesis and fulfilment of objectives

In Chapter 4, the sensitivities, precision and uncertainties of commonly used methods of estimating z_0 were investigated to address Objective 1. The aerodynamic profile method proved to be very low-yield in terms of the data collected compared with the resulting number of z_0 values, as found by others who employed it (e.g. Smeets *et al.*, 1998; Denby and Smeets, 2000; Miles *et al.*, 2017). Aggressive filtering discarded >99% of the data in some cases (Chapter 4, Section 4.4.1) and the filter thresholds also impacted the resulting z_0 values, in particular, the filters for profile fits (r^2 filter), stationarity and minimum wind speed (Fig. 4.4). The 2D and 3D microtopographic methods have their own host of sensitivities (Chapter 4, Section 4.4.2). Both are sensitive to scale and resolution (Fig. 4.6), which has been reported previously for plot-scale studies (Miles *et al.*, 2017; Quincey *et al.*, 2017) and is of particular relevance to any attempt to produce a glacier-scale z_0 map (Fitzpatrick *et al.*, 2019). The dependence on resolution caused the greatest changes in z_0 in terms of order of magnitude; yet, the dependence on scale exacerbated a further sensitivity to detrending method. As broader scale data are required for distributed maps of z_0, the level of detrending can alter the character of the surface and the value of z_0 (Table 4.5; Miles *et al.*, 2017; Quincey *et al.*, 2017).

Chapter 5 details the work carried out in fulfilment of Objective 2. Comparison of microtopographic z_0 from 3D plots with the grid resolution of the underlying topographic data revealed power law behaviour (Fig. 5.4), similar to that noted by Rees and Arnold (2006) for 2D transects. Consistency in this behaviour between independent plots allowed systematic underestimation of z_0 at coarser resolutions to be corrected using a factor derived from the quotient of modelled microtopographic z_0 and wind tower z_0. A suite of correction

factors was developed for different grid resolutions which, when applied to z_0 estimates from data of a corresponding resolution, adjusted the value of z_0 so that it was in line with aerodynamic profile and eddy covariance derived values, to within one order of magnitude (Section 5.3.4). This approach to glacier-scale z_0 mapping was used to produce z_0 maps of Hintereisferner, Austria, from glacier-scale TLS scans (Fig. 5.5), and to project the spatial distribution of z_0 for neighbouring glaciers using a regional ALS DEM (Fig. 5.7).

Development of a model that fully distributes z_0, incorporating the corrected glacier-scale maps of z_0, enabled Objective 3 to be completed in Chapter 6. Overall, the annual mean energy available for melt (M) and turbulent fluxes were greater when modelled using a fixed value of z_0 (Fig. 6.6); importantly, inspection of temporal trends revealed that this was caused by flux values when air temperatures were <0°C and no ablation was modelled (Fig. 6.7). Comparison of model runs with fixed (1 mm) and distributed z_0 values showed that, during the ablation season, the turbulent fluxes were up to 38% greater when modelled with distributed z_0 than during the same period modelled with fixed z_0, translating to 30% more energy available for melt and a 21% increase in modelled ablation. When using static z_0 values, it is likely that the turbulent fluxes and their contribution will be underestimated in other current and future climates that are more favourable for turbulent energy transfer. Experiments carried out with increased wind speeds and air temperatures showed that using distributed z_0 produces greater estimates of both the number of days with modelled ablation and the overall amount of ablation, than is modelled using a static z_0. This depends on the chosen static z_0 value, which in itself goes to show that it is important to include robust, distributed values of z_0 rather than a single unrepresentative value.

7.3 Contextualising thesis findings

This thesis has shown that it is possible to incorporate fully distributed, robust topographic estimates of z_0 into a distributed SEB model, and that it is important to do so. The workflow to generate spatially and temporally distributed z_0 estimates could, in theory, be applied to any glacier or ice mass for which gridded topographic data are available at resolutions of ~30 m per pixel or finer. Through implementation of the workflows developed in this thesis, it is perfectly feasible to suggest that the practice of assuming a fixed, static z_0 or adopting a z_0 value from another study, as has been commonplace in glaciology for decades, could be eliminated.

While adopting a z_0 value from a similar surface remains quite common (e.g. Bravo *et al.*, 2017; Sauter *et al.*, 2020), eddy covariance data, using observations from sonic

anemometers, are likely to continue to provide the most accurate reflection of the turbulent fluxes (Burba, 2013; Radić *et al.*, 2017). Unlike eddy covariance data, which are limited to the point scale, a key advantage of using the bulk method is that it can be spatially distributed; however, it has been argued that it is unsuitable for calculating the turbulent fluxes over a glacier surface (e.g. Denby and Greuell, 2000; Grisogono and Oerlemans, 2001; Radić *et al.*, 2017), as discussed in Chapter 4, Section 4.2.1. Despite this, the bulk method remains a viable option in the absence of advances in more suitable theories (Denby and Greuell, 2000; Denby and Smeets, 2000; Radić *et al.*, 2017), and with the increasing availability of topographic datasets with regional coverage at relatively fine scales (<c.30 m; Taylor *et al.*, 2021), it seems likely that the popularity of using the bulk method in distributed glacier SEB modelling will continue (Bravo *et al.*, 2021; Fyffe *et al.*, 2014; Molg *et al.*, 2020). Therefore, the work presented here is timely because with more widespread use of distributed SEB models, the parameterisation of distributed z_0 is a priority and the outcomes of this thesis are likely to be useful for others using the same method.

As discussed several times throughout this work, the spatial distribution of z_0 has recently received growing attention (Smith *et al.*, 2016; Miles *et al.*, 2017; Fitzpatrick *et al.*, 2019; van Tiggelen *et al.*, 2021). The approach to calculating spatially distributed z_0 taken here builds on the method first developed by Smith *et al.* (2016b), and the method used by Fitzpatrick *et al.* (2019). Where Smith *et al.*'s (2016b) method requires *in situ* data collection for validation, the method used here only requires topographic input data and a correction factor. Fitzpatrick *et al.*'s (2019) method also made use of a sliding neighbourhood algorithm, producing spatially distributed values which they term as a 'drag parameter'. Their method was only tested on input data of a single resolution (1 m) and provides z_0 estimates for a point, rather than a fully distributed grid of z_0 estimates as is produced using the method in this thesis (see Chapter 5, Section 5.4.1 for additional discussion of the differences). The use of a sliding neighbourhood for terrain or roughness analysis could be applied to other areas of geomorphological research, particularly those based on elevation summary statistics (Smith, 2014), with an example being the median absolute difference in elevations, which uses the geostatistical variogram (Trevisani and Rocca, 2015).

Temporal change in z_0 has received less attention than spatial variability, but was considered in Chapter 6 (Section 6.3.4) in the development of the temporal model, which builds on observations of temporal dynamics in z_0 over annual and sub-annual timescales. The author of this thesis contributed to the work of Smith *et al.* (2020a) which was undertaken at Hintereisferner at the same time as the HEFEX campaign, and which underpins the temporal

model developed in this work (see full paper in Appendix C). Repeat patch-scale surveys of different glacier surfaces identifying z_0 trajectories over the study period (two weeks) were carried out, along with a glacier-scale study of snow line retreat through the ablation season. Differences in temporal changes in z_0 were observed for the different spatial scales; patch-scale plots did not follow any consistent trajectory, becoming neither uniformly rougher nor smoother, while at the glacier scale, z_0 increased with the length of time since the surface had been exposed by the retreating snow line. This different behaviour was used to propose a scale-dependent model for z_0 evolution. The roughness trajectory through the ablation season, adapted from Guo *et al.* (2011) and shown by the green line in Appendix C, Fig. 9, was reflected by the space-for-time substitution carried out for the temporal z_0 model in Chapter 6 (Section 6.3.4). The difference in trajectory between Chapter 6 and the one shown by Smith *et al.* (2020a) is likely due to the difference in method used to calculate z_0 – Smith *et al.* (2020a) followed the approach of Smith *et al.* (2016b), who used a linear relationship between z_0 and the standard deviation of elevations, whereas in this thesis a sliding neighbourhood operation was employed.

A virtue of the temporal model developed in Chapter 6 is that the z_0 trajectory of the glacier surface is independent of the z_0 trajectory of the snow surface, meaning that other surface trajectories can be accounted for. As an example, Guo *et al.* (2011) observed a relatively smooth ice surface after the snow line retreated, which would be represented by a more pronounced dip in z_0 after the first section of time in Appendix C, Fig. 9. Conversely, Smeets and van den Broeke (2008) described an increase in z_0, when a hummocky ice surface was revealed by the retreating snow line. The model is complemented by the findings of Fitzpatrick *et al.* (2019), who observed that z_0 values were similar year-on-year, meaning that z_0 values observed at one time in a year are not likely to change substantially if measured again at the same time in a different year.

The ability to represent different z_0 trajectories and be applicable year after year makes the temporal model a useful starting point for characterising the different topographies of glaciers. The influence of topographic roughness on energy transfer over sea ice is another area of active research where the relationship between physical and aerodynamic roughness is being investigated (Andreas and Claffey, 1995; Andreas, 2011; Landy *et al.*, 2020). Recent topographic investigations of sea ice roughness make use of radar, and the properties of radar data products (e.g. Nolin and Mar, 2019) because the transient and changeable nature of sea ice means that DEM generation is not practical; therefore, there is currently limited potential for the findings of this thesis to advance such investigations. Future developments

in multi-temporal DEM generation (Taylor *et al.*, 2021) may mean that it becomes possible to model temporal change in sea ice roughness from 3D topographic datasets.

7.4 Areas for improvement

While the work presented in this thesis introduces numerous advances in representing z_0 in a SEB model, there remain a number of aspects of the proposed workflow that require further development. The first area for improvement concerns the lack of robust z_0 estimates over snow surfaces. Up to three orders of magnitude variability in z_0 have been observed over snow surfaces (Jackson and Carroll, 1978; Wagnon *et al.*, 1999; Brock *et al.*, 2006; Gromke *et al.*, 2011), meaning that snow melt during the early ablation season could be improperly calculated by the temporal model. While some difference in snow surface roughness is accounted for by the reclassified albedo grids, the albedo-roughness equivalence assumes a linear relationship between albedo and z_0, ignoring variability within categories and overlapping reflectance characteristics of different surfaces (Gardner and Sharp, 2010; Lhermitte *et al.*, 2014; Ryan *et al.*, 2017).

The second point for improvement is that testing and validation of the models is required at other sites. While the availability and quality of regional topographic datasets is improving (e.g. ArcticDEM; Porter *et al.*, 2018), z_0 values derived from wind towers or sonic anemometers that could be used for validation are relatively rare. However, a good number of past studies successfully estimate z_0 from microtopographic data with validation from wind towers or sonic anemometers (Munro, 1989; Brock *et al.*, 2006; Smith *et al.*, 2016; Fitzpatrick *et al.*, 2017; Miles *et al.*, 2017; Quincey *et al.*, 2017; Smith *et al.*, 2020a), implying that the upscaling model (Chapter 5, Section 5.2.6) could be developed in a new location from just microtopographic data and without need for further aerodynamic data. Nonetheless, *in situ* data collection is likely to be required in order to ensure an adequate range of resolutions and scales are sampled.

Data collection from more locations would also help to rectify bias in microtopographic z_0 estimates. Due to the nature of data collection on glaciers (mainly concerning safety), studies have preferentially been directed towards more accessible glaciers, and areas of them that are relatively smooth and have shallow gradients. Arguably, many glaciers have smooth surfaces and shallow gradients, but as often acknowledged, an order of magnitude increase in z_0 can double the turbulent fluxes (Munro, 1989), so inclusion of rougher surfaces is important to the SEB (Van Tiggelen *et al.*, 2021). Use of ALS to survey less accessible areas is

possible, although usually at a coarser resolution than is available with UAV-derived SfM data (Chapter 5, Section 5.2.5). Recent studies of z_0 over rougher glacier surfaces, including flights over the terminus area of marine-terminating glaciers in Svalbard, still experience accessibility issues regarding the placement of ground control points for georeferencing (Dachauer *et al.*, 2021). Work to enable fully georeferenced UAV surveys without the need for ground control has been promising, with the use of GNSS-supported aerial triangulation successfully allowing the velocity of the heavily crevassed calving face of Store Glacier, Greenland, to be calculated using repeat UAV surveys (Chudley *et al.*, 2019). Carrying out further investigations in more diverse locations with robust, georeferenced surveys would ensure that glacier z_0 estimates are not biased towards more accessible sites.

The third avenue for improvement of the fully distributed z_0 approach is the use of linear interpolation between dated Landsat scenes used for both albedo and z_0 modelling. Representing one of the key oversimplifications of the model, the use of linear interpolation masks the changes in albedo and z_0 that occur over timescales shorter than the intervals between Landsat scenes. The generalisation of changes in albedo caused by the approach used in this thesis could be reduced if additional Landsat scenes had been available, or if precipitation (snowfall) data were available. A model for characterising temporal changes in albedo from precipitation data was proposed by Oerlemans and Knap (1998), and has been implemented successfully by others (e.g. Sauter *et al.*, 2020; Bravo *et al.*, 2021). The precipitation model automatically adjusts the albedo of a surface to reflect recent snowfall. Such snowfall events would be worth resolving in a temporal z_0 model, as they have been shown to substantially reduce z_0 (Smeets and van den Broeke, 2008; Quincey *et al.*, 2017).

Finally, while the magnitude of the influence of including distributed z_0 in a SEB model is shown in Chapter 6, it was not possible to fully validate the output values from the SEB model to ensure that the model itself is accurate. Results from the model broadly aligned with WGMS values for the annual mass balance of Hintereisferner for the year of 2017 (Chapter 6, Section 6.6.4), but it was not possible to compare individual components of the energy balance. Most studies that use a distributed SEB model use ablation data as validation, whether from publicly available datasets or from contemporaneous ablation stake measurements (e.g. Arnold *et al.*, 1996; 2006; Braun and Hock, 2004; Hock and Holmgren, 2005; MacDougall and Flowers, 2011; Ayala *et al.*, 2017; Liang *et al.*, 2018). Some of these studies validate the radiative components of the SEB model with measured radiation from AWS at different sites across the glacier (Braun and Hock, 2004; Hock and Holmgren, 2005; Arnold *et al.*, 2006) and other studies use runoff data in order to validate ablation volumes

(Hock and Holmgren, 2005; Fyffe *et al.*, 2014; Bravo *et al.*, 2017) but none are able to verify turbulent flux values.

Verification of the turbulent fluxes requires a more specialised instrumental setup, usually employed only at the point scale. Several studies have calculated the SEB for a point using AWS data, validating the turbulent fluxes with eddy covariance data from sonic anemometers (Fitzpatrick *et al.*, 2017; Radić *et al.*, 2017; Cullen *et al.*, 2020). In each study, reasonable agreement is found between turbulent fluxes calculated using the bulk approach and using eddy covariance, although overestimation of the fluxes by the bulk approach is common when katabatic conditions prevail (Fitzpatrick *et al.*, 2017; Radić *et al.*, 2017). Comparison of eddy covariance-derived z_0 with z_0 from other sources (wind profiles and values from other studies) are usually favourable (Chapter 5, Section 5.3.1; Fitzpatrick *et al.*, 2019; Munro, 1989; Sicart *et al.*, 2014; Smeets and van den Broeke, 2008); however, there has yet to be a study that validates turbulent fluxes from a distributed SEB model against outputs from a distributed network of sonic anemometers. Moreover, the same has yet to be done comparing z_0 from a distributed network of sonic anemometers to the corresponding points of a glacier-scale z_0 grid.

Thus, the final point for improvement would be to perform a fully validated energy balance study. In ideal circumstances, data would be available from a network of AWS and sonic anemometers distributed across the glacier surface, along with topographic data from various points throughout the year and precipitation data so that interpolation of z_0 between topographic survey dates is robust. The SEB model could be validated against runoff data collected downstream of the glacier, while the turbulent fluxes and z_0 were validated using the sonic anemometers.

7.5 Wider problems encountered in the study

While the work carried out for this thesis represents a step in progress towards more robust calculations of glacier melt, several issues remain with the methods used to estimate microtopographic z_0 and with aerodynamic methods used to validate them. Even if improvements are made as discussed in the previous section, the points mentioned in this section would still need addressing.

The most commonly acknowledged issue when calculating the turbulent fluxes over a glacier using the bulk approach is that most of the assumptions of MO similarity theory are violated (Denby and Greuell, 2000). MO similarity theory was developed over flat, homogeneous

terrain, often farmland or forestry, and is not suited to the sloping, inhomogeneous surfaces of glaciers (Denby and Greuell, 2000; Foken, 2006). Katabatic winds frequently invalidate the requirements for MO similarity theory by creating strongly stable conditions (see Fig. 2.6) where the wind speed maximum is close to the surface and the wind speed profile is not log-linear (Munro and Davies, 1978; Oerlemans *et al.*, 1999; Denby and Smeets, 2000). In these conditions it is not possible to calculate z_0, and the fluxes as calculated at a measurement height z, are not representative of their true surface values. The result is that conditions satisfying the requirements for MO similarity theory are rarely met, and lots of data are discarded (e.g. Table 4.3; Miles *et al.*, 2017; Radić *et al.*, 2017). Alternative methods specifically designed to be used in katabatic conditions have been developed and have compared favourably to validation data (Denby and Smeets, 2000; Oerlemans and Grisogono, 2002; Radić *et al.*, 2017), but the traditional bulk method remains the most widely used. Work was carried out for this thesis with the acknowledgement of the limitations of the bulk method and profile-derived z_0 values. Results of the topographic methods used here have not been compared to the katabatic methods, so it is not clear if the findings would be different.

The use of microtopography to parameterise z_0 mandated a decision about the appropriate scale and resolution at which to calculate z_0, as is common with other roughness metrics (Smith, 2014). The dependence of calculations on measurement scale and data resolution is not unique to investigations of roughness, with most studies employing DEMs facing some sort of compromise between the two (Deng *et al.*, 2007; Grohmann *et al.*, 2011). For z_0, the matter of scale and resolution has taken two paths: the first includes investigations into the scale of terrain feature that influences z_0 and the turbulent exchange of energy and the resolution required to adequately sample those features; the second views scale and resolution as practical considerations that should be considered in order to ensure microtopographic estimates of z_0 match validation data.

The first point was of greater relevance when topographic estimates of z_0 were derived from manually surveyed 2D transects and the limits of sampling interval were dictated by increments on a tape measure (e.g. Munro, 1989; Brock *et al.*, 2006; Rees and Arnold, 2006). Rees and Arnold (2006) demonstrated the influence of scale and resolution dependence over different orders of each using 2D transects, and similar effects were shown here in Chapters 4 and 5. In Chapter 5 (Section 5.3.1) in particular, it was shown that while increasingly fine data resolutions are achievable, they risk overestimating z_0, as has been observed with other roughness metrics (e.g. Darby *et al.*, 2010). The second point has come into focus as ultra-

fine (sub-cm) resolutions have been achievable over increasing scales, from metres to tens of metres (e.g. Miles *et al.*, 2017; Quincey *et al.*, 2017; Fitzpatrick *et al.*, 2019). These enhanced capabilities have changed the question from whether or not aerodynamically important features are resolvable by the data, to what combination of resolution and scale can provide a z_0 value most similar to validation data whilst covering the broadest area in greatest detail (Chapter 5; Fitzpatrick *et al.*, 2019; Quincey *et al.*, 2017). In this thesis, some combinations provided better matches than others (e.g. ~0.1 m resolution, 1-10 m scale) but the correction factor meant that any combination of scale and resolution (within the tested limits) could be used to provide a robust estimate of z_0 within an acceptable degree of accuracy (< order of magnitude difference with validation data).

The final choice to consider about microtopographic approaches is that of: a) giving the method the strongest possible grounding in theory (e.g. Raupach, 1992; Chappell and Heritage, 2007), or b) providing the closest match to validation data with an empirical relationship. The approach taken in this thesis tends towards the latter through the use of the correction factor, although it is acknowledged that it is grounded in the original method by Lettau (1969) and subsequent adjustments for 3D data by Smith *et al.* (2016). Other workers have investigated methods of incorporating greater theoretical detail, in attempts to account for the aerodynamically important upwind area (fetch) of a point. Fitzpatrick *et al.* (2019) devised two methods for this: the first used essentially the same sliding neighbourhood routine as used in this thesis, with the additional step of giving each grid cell a weighting according to its importance within the flux footprint (where available), and the second used wind-parallel 2D transects covering the area upwind of the point of interest. Van Tiggelen *et al.* (2021) used a similar approach to estimate z_0 from ICESat-2 transects, with validation from SfM-derived z_0 and EC z_0. These approaches make good progress in accounting for topographic variation within the fetch of a point, but are less immediately practical for incorporation in a distributed SEB model than the method developed in this thesis. A sliding neighbourhood routine that calculates z_0 for a cell based on its fetch can be imagined, although current modelling capabilities lack the sophistication required to correctly represent the complex behaviour of turbulence at the ice margins (c.f. Mott *et al.*, 2020) so extracting such a fully realised glacier map of z_0 is likely to be some way off.

7.6 Insights and future work

The workflow to generate spatially and temporally distributed z_0 estimates could, in theory, be applied to any glacier or ice mass for which gridded topographic data are available at

resolutions of ~30 m per pixel or finer. Indeed, with the additional validation outlined previously, a global index of z_0 could be compiled in order to provide a reference dataset accessible by other researchers, eliminating the need for z_0 to be borrowed from similar studies or for z_0 to be assumed spatially and/or temporally constant. Publicly available regional datasets like the ArcticDEM, the Reference Elevation Model for Antarctica and the High Mountain Asia DEM (Shean, 2017; Porter *et al.*, 2018; Howat *et al.*, 2019) could be used to form a z_0 inventory, with additional locations added by researchers as data become available. Increasing availability of multi-temporal elevation datasets from platforms such as WorldView 2, Pléiades and Geo-Eye-1 (Belart *et al.*, 2017, Shean *et al.*, 2020) could mean that z_0 maps are as up-to-date as possible and that multi-temporal z_0 maps would be available for selected glaciers. Where such resources are not available, an albedo- z_0 equivalence could still be used (provided that the z_0 values assigned to different snow surfaces had been calibrated), with albedo retrieved from Landsat data.

Another possibility is for the creation of glacier surface energy balance monitoring sites that are updated in real-time. With a network of AWS installed across a glacier surface at key, representative sites, meteorological data could be harvested using telemetry. A similar operation is mentioned in a recent study by Sauter *et al.* (2020), who presented a model (COSIPY) that can use input data transmitted from AWS on Hintereisferner to forecast glacier mass and energy balance for the next 24 hours at a resolution of 30 m. (The authors state that the system will be publicly available online, but it was not at the time of writing). Sauter *et al.* (2020) use a fixed value for z_0, but go on to suggest that their modelled forecasts will be improved by topographic data from the permanent *in situ* TLS. In such a case, it would be possible to easily incorporate the z_0 distribution workflow presented in this thesis and run the model with up-to-date, robust z_0 values. In other (more likely) situations where there is not a TLS *in situ*, the albedo- z_0 equivalence could be implemented. Advances in accessible machine learning infrastructure such as Google Earth Engine (e.g. Smith *et al.*, 2020b) means that the most recent imagery (that meets pre-set quality criteria) for a given location could be automatically downloaded and used to derive estimates of z_0, incorporating any estimates from topographic data as validation.

Going further, it is possible to imagine an integrated system that makes use of regional topographic datasets along with modelled meteorological data. Increasingly accurate stochastic weather generators could provide datasets where AWS data are not available, or where AWS data records are incomplete (Dabhi *et al.*, 2020). Alternatively, fine-resolution fields of variables such as wind speed and air temperature are becoming more widely

available from reanalysis data (Sauter and Galos, 2016), so the possibility of combining these data with a global z_0 database could be explored. Ultimately, the greatest potential for the approach developed in this thesis, given adequate validation and calibration, is in providing more robust estimates of z_0 that can then be used to provide robust calculations of the glacier surface energy balance and subsequent ablation. This in turn will contribute to evaluations of sea level rise, geomorphic change and water security.

7.7 Conclusions

In this thesis, the most frequently employed methods of estimating z_0 from aerodynamic profiles and microtopography were compared, showing that the same scale- and resolution-dependence found in z_0 derived from 2D topographic data are present in z_0 from 3D data. It was shown that these dependencies can be exploited and a resolution-dependent correction factor applied to compensate for systematic underestimation of z_0 from coarser resolution topographic data. This allows robust, distributed estimates of z_0 at the glacier scale based on a well-validated empirical relationship. Other methods that estimate z_0 from microtopographic data exist and attempt to account for the aerodynamic properties of the fetch of a point in more detail, but currently lack the same capacity of the approach presented here to be spatially distributed.

Temporal changes in z_0, modelled over a year using an albedo- z_0 equivalence, can be combined with glacier-scale maps of z_0 to form a fully spatio-temporally distributed model, as done for the first time here. Compared to SEB model outputs obtained using a fixed, static z_0 value, the fully distributed z_0 model resolves in greater detail the seasonal changes in energy fluxes and ablation. Using a fixed value of z_0 misrepresents the seasonal importance of z_0 by overestimating energy fluxes and ablation in the winter and underestimating them during the ablation season.

Overall, this work has shown that it is not only possible to fully distribute z_0 and incorporate it into a distributed SEB model, but also that it is potentially important to do so. By showing the sensitivity of the turbulent fluxes, energy available for melt and modelled ablation to the chosen z_0 value, the necessity for adequate spatial and temporal characterisation of z_0 has also been demonstrated. The work in this thesis represents a significant step forward in the way glacier melt can be calculated; with some additional calibration and testing, the method presented here shows the potential to be expanded further through the development of a global z_0 database or through incorporation into automatic energy balance forecasting

models, helping to provide more robust SEB calculations which will be vital for understanding how our melting glaciers may change in the near future.

References

Andreas, E. L. (2011) ‘A relationship between the aerodynamic and physical roughness of winter sea ice’, *Quarterly Journal of the Royal Meteorological Society*, 137(659), pp. 1581–1588. doi: 10.1002/qj.842.

Andreas, E. L. & Claffey, K. J. (1995) ‘Air-ice drag coefficients in the western Weddell Sea 1. Values deduced from profile measurements’, *Journal of Geophysical Research*, 100(C3), pp. 4821–4831. doi: 10.1029/94JC02015.

Arnold, N. S., Rees, W. G., Hodson, A. J. & Kohler, J. (2006) ‘Topographic controls on the surface energy balance of a high Arctic valley glacier’, *Journal of Geophysical Research: Earth Surface*, 111(2). doi: 10.1029/2005JF000426.

Arnold, N. S., Willis, I. C., Sharp, M. J., Richards, K. S. & Lawson, W. J. (1996) ‘A distributed surface energy-balance tnodel for a small valley glacier. I. Developtnent and testing for Haut Glacier d’ Arolla, Valais, Switzerland’, *Journal of Glaciology*, 42(140), pp. 77–89. doi: doi:10.3189/S0022143000030549.

Ayala, A., Pellicciotti, F., Peleg, N. & Burlando, P. (2017) ‘Melt and surface sublimation across a glacier in a dry environment: Distributed energy-balance modelling of Juncal Norte Glacier, Chile’, *Journal of Glaciology*, 63(241), pp. 803–822. doi: 10.1017/jog.2017.46.

Braun, M. & Hock, R. (2004) ‘Spatially distributed surface energy balance and ablation modelling on the ice cap of King George Island (Antarctica)’, *Global and Planetary Change*, 42(1–4), pp. 45–58. doi: 10.1016/j.gloplacha.2003.11.010.

Bravo, C., Loriaux, T., Rivera, A. & Brock, B. W. (2017) ‘Assessing glacier melt contribution to streamflow at Universidad Glacier, central Andes of Chile’, *Hydrology and Earth System Sciences*, 21(7), pp. 3249–3266. doi: 10.5194/hess-21-3249-2017.

Brock, B. W., Willis, I. C. & Sharp, M. J. (2006) ‘Measurement and parameterization of aerodynamic roughness length variations at Haut Glacier d’Arolla, Switzerland’, *Journal of Glaciology*, 52(177), pp. 281–297. doi: 10.3189/172756506781828746.

Burba, G. (2013) *Eddy Covariance Method-for Scientific, Industrial, Agricultural, and Regulatory Applications*. Lincoln, Nebraska: LI-COR Biosciences. doi: 10.1007/s00704-004-0095-y.

Chappell, A. & Heritage, G. L. (2007) ‘Using illumination and shadow to model aerodynamic resistance and flow separation: An isotropic study’, *Atmospheric Environment*, 41(28), pp. 5817–5830. doi: 10.1016/j.atmosenv.2007.03.037.

Chudley, T. R., Christoffersen, P., Doyle, S. H., Abellan, A. & Snooke, N. (2019) ‘High-accuracy UAV photogrammetry of ice sheet dynamics with no ground control’, *Cryosphere*, 13(3), pp. 955–968. doi: 10.5194/tc-13-955-2019.

Cullen, N. J., Mo¨lg, T., Mo¨lg, M., Kaser, G., Steffen, K. & Hardy, D. R. (2020) *Energy-balance model validation on the top of Kilimanjaro, Tanzania, using eddy covariance data*. Available at: https://www.cambridge.org/core.

Dabhi, H., Rotach, M. W., Dubrovský, M. & Oberguggenberger, M. (2020) ‘Evaluation of a stochastic weather generator in simulating univariate and multivariate climate extremes in different climate zones across Europe’, *Meteorologische Zeitschrift*, 30(2), pp. 127–151. doi: 10.1127/metz/2020/1021.

Dachauer, A., Hann, R. & Hodson, A. J. (2021) 'Aerodynamic roughness length of crevassed tidewater glaciers from UAV mapping', *The Cryosphere Discussions*, pp. 1–23. doi: 10.5194/tc-2021-113.

Darby, S. E., Trieu, H. Q., Carling, P. A., Sarkkula, J., Koponen, J., Kummu, M., Conlan, I. & Leyland, J. (2010) 'A physically based model to predict hydraulic erosion of fine-grained riverbanks: The role of form roughness in limiting erosion', *Journal of Geophysical Research: Earth Surface*, 115(4). doi: 10.1029/2010JF001708.

Denby, B. & Greuell, W. (2000) 'The Use of Bulk and Profile Methods for Determining Surface Heat Fluxes in the Presence of Glacier Winds', *Journal of Glaciology*, 46(154), pp. 445–452.

Denby, B. & Smeets, C. J. P. P. (2000) 'Derivation of Turbulent Flux Profiles and Roughness Lengths from Katabatic Flow Dynamics', *Journal of Applied Meteorology*, 39(9), pp. 1601–1612. doi: 10.1175/1520-0450(2000)039<1601:DOTFPA>2.0.CO;2.

Deng, Y., Wilson, J. P. & Bauer, B. O. (2007) 'DEM resolution dependencies of terrain attributes across a landscape', *International Journal of Geographical Information Science*, 21(2), pp. 187–213. doi: 10.1080/13658810600894364.

Fitzpatrick, N., Radić, V. & Menounos, B. (2017) 'Surface Energy Balance Closure and Turbulent Flux Parameterization on a Mid-Latitude Mountain Glacier, Purcell Mountains, Canada', *Frontiers in Earth Science*, 5(September), pp. 1–20. doi: 10.3389/feart.2017.00067.

Fitzpatrick, N., Radić, V. & Menounos, B. (2019) 'A multi-season investigation of glacier surface roughness lengths through in situ and remote observation', *The Cryosphere*, 13, pp. 1051–1071. doi: https://doi.org/10.5194/tc-13-1051-2019.

Foken, T. (2006) '50 years of the Monin-Obukhov similarity theory', *Boundary-Layer Meteorology*, 119(3), pp. 431–447. doi: 10.1007/s10546-006-9048-6.

Fyffe, C. L., Reid, T. D., Brock, B. W., Kirkbride, M. P., Diolaiuti, G., Smiraglia, C. & Diotri, F. (2014) 'A distributed energy-balance melt model of an alpine debris-covered glacier', *Journal of Glaciology*, 60(221), pp. 587–602. doi: 10.3189/2014JoG13J148.

Gardner, A. S. & Sharp, M. J. (2010) 'A review of snow and ice albedo and the development of a new physically based broadband albedo parameterization', *Journal of Geophysical Research: Earth Surface*, 115(1). doi: 10.1029/2009JF001444.

Grisogono, B. & Oerlemans, J. (2001) 'Katabatic Flow: Analytic Solution for Gradually Varying Eddy Diffusivities', *Journal of the atmospheric sciences*, 58(21), pp. 3349–3354. doi: https://doi.org/10.1175/1520-0469(2001)058<3349:KFASFG>2.0.CO;2.

Grohmann, C. H., Smith, M. J. & Riccomini, C. (2011) 'Multiscale analysis of topographic surface roughness in the Midland Valley, Scotland', *IEEE Transactions on Geoscience and Remote Sensing*. doi: 10.1109/TGRS.2010.2053546.

Gromke, C., Manes, C., Walter, B., Lehning, M. & Guala, M. (2011) 'Aerodynamic Roughness Length of Fresh Snow', *Boundary-Layer Meteorology*, 141(1), pp. 21–34. doi: 10.1007/s10546-011-9623-3.

Guo, X., Yang, K., Zhao, L., Yang, W., Li, S., Zhu, M., Yao, T. & Chen, Y. (2011) 'Critical Evaluation of Scalar Roughness Length Parametrizations Over a Melting Valley Glacier', *Boundary-Layer Meteorology*, 139(2), pp. 307–332. doi: 10.1007/s10546-010-9586-9.

Hock, R. & Holmgren, B. (2005) 'A distributed surface energy-balance model for complex topography and its application to Storglaciären, Sweden', *Journal of Glaciology*, 51(172), pp. 25–36. doi: https://doi.org/10.3189/172756505781829566.

Howat, I. M., Porter, C., Smith, B. E., Noh, M. J. & Morin, P. (2019) 'The reference elevation model of antarctica', *Cryosphere*, 13(2), pp. 665–674. doi: 10.5194/tc-13-665-2019.

Jackson, B. S. & Carroll, J. J. (1978) 'Aerodynamic roughness as a function of wind direction over asymmetric surface elements', 14(1969), pp. 323–330.

Landy, J. C., Petty, A. A., Tsamados, M. & Stroeve, J. C. (2020) 'Sea Ice Roughness Overlooked as a Key Source of Uncertainty in CryoSat-2 Ice Freeboard Retrievals', *Journal of Geophysical Research: Oceans*, 125(5). doi: 10.1029/2019JC015820.

Lettau, H. (1969) 'Note on Aerodynamic Roughness-Parameter Estimation on the Basis of Roughness-Element Description', *Journal of Applied Meteorology*, 8(5), pp. 828–832. doi: http://dx.doi.org/10.1175/1520-0450(1969)008<0828:NOARPE>2.0.CO;2.

Lhermitte, S., Abermann, J. & Kinnard, C. (2014) 'Albedo over rough snow and ice surfaces', *Cryosphere*, 8(3), pp. 1069–1086. doi: 10.5194/tc-8-1069-2014.

Liang, L., Cuo, L. & Liu, Q. (2018) 'The energy and mass balance of a continental glacier: Dongkemadi Glacier in central Tibetan Plateau', *Scientific Reports*, 8(1). doi: 10.1038/s41598-018-31228-5.

MacDougall, A. H. & Flowers, G. E. (2011) 'Spatial and temporal transferability of a distributed energy-balance glacier melt model', *Journal of Climate*, 24(5), pp. 1480–1498. doi: 10.1175/2010JCLI3821.1.

Miles, E. S., Steiner, J. F. & Brun, F. (2017) 'Highly variable aerodynamic roughness length (z0) for a hummocky debris-covered glacier', *Journal of Geophysical Research: Atmospheres*, 122(16), pp. 8447–8466. doi: 10.1002/2017JD026510.

Molg, T., R. Hardy, D., Collier, E., Kropač, E., Schmid, C., J. Cullen, N., Kaser, G., Prinz, R. & Winkler, M. (2020) 'Mesoscale atmospheric circulation controls of local meteorological elevation gradients on Kersten Glacier near Kilimanjaro summit', *Earth System Dynamics*, 11(3), pp. 653–672. doi: 10.5194/esd-11-653-2020.

Mott, R., Stiperski, I. & Nicholson, L. (2020) 'Spatio-temporal flow variations driving heat exchange processes at a mountain glacier', *Cryosphere*, 14(12), pp. 4699–4718. doi: 10.5194/tc-14-4699-2020.

Munro, D. S. (1989) 'Surface roughness and bulk heat transfer on a glacier: comparison with eddy correlation', *Journal of Glaciology*, 35(121), pp. 343–348.

Munro, D. S. & Davies, J. A. (1978) 'On fitting the log-linear model to wind speed and temperature profiles over a melting glacier', *Boundary-Layer Meteorology*, 15(4), pp. 423–437. doi: 10.1007/BF00120604.

Nolin, A. W. & Mar, E. (2019) 'Arctic sea ice surface roughness estimated from multi-angular reflectance satellite imagery', *Remote Sensing*, 11(1). doi: 10.3390/rs11010050.

Oerlemans, J., Björnsson, H., Kuhn, M., Obleitner, F., Palsson, F., Smeets, C. J. P. P., Vugts, H. F. & De Wolde, J. (1999) 'Glacio-meteorological investigations on Vatnajokull, Iceland, Summer 1996: An overview', *Boundary-Layer Meteorology*, 92(1), pp. 3–26. doi: 10.1023/A:1001856114941.

Oerlemans, J. & Grisogono, B. (2002) 'Glacier winds and parameterisation of the related

surface heat fluxes', *Tellus A: Dynamic Meteorology and Oceanography*, 54(5), pp. 440–452. doi: 10.3402/tellusa.v54i5.12164.

Oerlemans, J. & Knap, W. (1998) 'A 1 year record of global radiation and albedo in the ablation zone of Morteratschgletscher, Switzerland', *Journal of Glaciology*, 44(147), pp. 231–238. doi: https://doi.org/10.3189/S0022143000002574.

Porter, C. *et al.* (2018) *ArcticDEM*. doi: https://doi.org/10.7910/DVN/OHHUKH.

Quincey, D. J., Smith, M. W., Rounce, D. R., Ross, A. N., King, O. & Watson, C. S. (2017) 'Evaluating morphological estimates of the aerodynamic roughness of debris covered glacier ice', *Earth Surface Processes and Landforms*. doi: 10.1002/esp.4198.

Radić, V., Menounos, B., Shea, J., Fitzpatrick, N., Tessema, M. A. & Déry, S. J. (2017) 'Evaluation of different methods to model near-surface turbulent fluxes for a mountain glacier in the Cariboo Mountains, BC, Canada', *Cryosphere*, 11(6), pp. 2897–2918. doi: 10.5194/tc-11-2897-2017.

Raupach, M. R. (1992) 'Drag and drag partition on rough surfaces', *Boundary-Layer Meteorology*, 60(4), pp. 375–395. doi: 10.1007/BF00155203.

Rees, W. G. & Arnold, N. S. (2006) 'Scale-dependent roughness of a glacier surface: Implications for radar backscatter and aerodynamic roughness modelling', *Journal of Glaciology*, 52(177), pp. 214–222. doi: 10.3189/172756506781828665.

Ryan, J. C., Hubbard, A., Box, J. E., Brough, S., Cameron, K., Cook, J. M., Cooper, M., Doyle, S. H., Edwards, A., Holt, T., Irvine-Fynn, T., Jones, C., Pitcher, L. H., Rennermalm, A. K., Smith, L. C., Stibal, M. & Snooke, N. (2017) 'Derivation of High Spatial Resolution Albedo from UAV Digital Imagery: Application over the Greenland Ice Sheet', *Frontiers in Earth Science*, 5. doi: 10.3389/feart.2017.00040.

Sauter, T., Arndt, A. & Schneider, C. (2020) 'COSIPY v1.3 – an open-source coupled snowpack and ice surface energy and mass balance model', *Geoscientific Model Development*, 13(11), pp. 5645–5662. doi: 10.5194/gmd-13-5645-2020.

Sauter, T. & Galos, S. (2016) 'Effects of local advection on the spatial sensible heat flux variation on a mountain glacier', *Cryosphere*, 10(6), pp. 2887–2905. doi: 10.5194/tc-10-2887-2016.

Shean, D. (2017) *High Mountain Asia 8-meter DEM Mosaics Derived from Optical Imagery, Version 1*, *NASA National Snow and Ice Data Center Distributed Active Archive Center*. doi: https://doi.org/10.5067/KXOVQ9L172S2.

Sicart, J. E., Litt, M., Helgason, W., Tahar, V. Ben & Chaperon, T. (2014) 'A study of the atmospheric surface layer and roughness lengths on the high-altitude tropical Zongo glacier, Bolivia', *Journal of Geophysical Research*, 119(7), pp. 3793–3808. doi: 10.1002/2013JD020615.

Smeets, C. J. P. P. & van den Broeke, M. R. (2008) 'Temporal and spatial variations of the aerodynamic roughness length in the ablation zone of the greenland ice sheet', *Boundary-Layer Meteorology*, 128(3), pp. 315–338. doi: 10.1007/s10546-008-9291-0.

Smeets, C. J. P. P., Duynkerke, P. G. & Vugts, H. F. (1998) 'Turbulence characteristics of the stable boundary layer over a mid-latitude glacier. Part I: a combination of katabatic and large-scale forcing', *Boundary-Layer Meteorology*, 87(1), pp. 117–145. doi: 10.1023/A:1000860406093.

Smith, M. W. (2014) ‘Roughness in the Earth Sciences’, *Earth-Science Reviews*, 136, pp. 202–225. doi: 10.1016/j.earscirev.2014.05.016.

Smith, M. W., Quincey, D. J., Dixon, T., Bingham, R. G., Carrivick, J. L., Irvine-Fynn, T. D. L. & Rippin, D. M. (2016) ‘Aerodynamic roughness of glacial ice surfaces derived from high-resolution topographic data’, *Journal of Geophysical Research F: Earth Surface*, 121(4), pp. 748–766. doi: 10.1002/2015JF003759.

Smith, T. I., Smith, M. W., Chambers, J. R., Sailer, R., Nicholson, L., Mertes, J., Quincey, D. J., Carrivick, J. L. & Stiperski, I. (2020a) ‘A scale-dependent model to represent changing aerodynamic roughness of ablating glacier ice based on repeat topographic surveys’, *Journal of Glaciology*, pp. 1–15. doi: 10.1017/jog.2020.56.

Smith, W. D., Dunning, S. A., Brough, S., Ross, N. & Telling, J. (2020b) ‘GERALDINE (Google Earth Engine supRaglAciaL Debris INput dEtector): A new tool for identifying and monitoring supraglacial landslide inputs’, *Earth Surface Dynamics*, 8(4), pp. 1053–1065. doi: 10.5194/esurf-8-1053-2020.

Taylor, L. S., Quincey, D. J., Smith, M. W., Baumhoer, C. A., McMillan, M. & Mansell, D. T. (2021) ‘Remote sensing of the mountain cryosphere: Current capabilities and future opportunities for research’, *Progress in Physical Geography: Earth and Environment*, p. 030913332110236. doi: 10.1177/03091333211023690.

Van Tiggelen, M., Smeets, P. C. J. P., Reijmer, C. H., Wouters, B., Steiner, J. F., Nieuwstraten, E. J., Immerzeel, W. W. & Van Den Broeke, M. R. (2021) ‘Mapping the aerodynamic roughness of the Greenland Ice Sheet surface using ICESat-2: Evaluation over the K-transect’, *Cryosphere*, 15(6), pp. 2601–2621. doi: 10.5194/tc-15-2601-2021.

van Tiggelen, M., Smeets, P., Reijmer, C., Wouters, B., Steiner, J., Nieuwstraten, E., Immerzeel, W. & van den Broeke, M. (2021) ‘Mapping the aerodynamic roughness of the Greenland ice sheet surface using ICESat-2: Evaluation over the K-transect’, *The Cryosphere Discussions*, pp. 1–28. doi: 10.5194/tc-2020-378.

Trevisani, S. & Rocca, M. (2015) ‘MAD: Robust image texture analysis for applications in high resolution geomorphometry’, *Computers and Geosciences*, 81, pp. 78–92. doi: 10.1016/j.cageo.2015.04.003.

Wagnon, P., Ribstein, P., Francou, B. & Pouyaud, B. (1999) ‘Annual cycle of energy balance of Zongo glacier, Cordillera Real, Bolivia’, *Journal of Geophysical Research Atmospheres*, 104, pp. 3907–3923.

Part IV: Appendices

Appendix A

Supporting information for Chapter 4: “Glacial Aerodynamic Roughness Estimates: Uncertainty, Sensitivity, and Precision in Field Measurements”

Contents of this section:

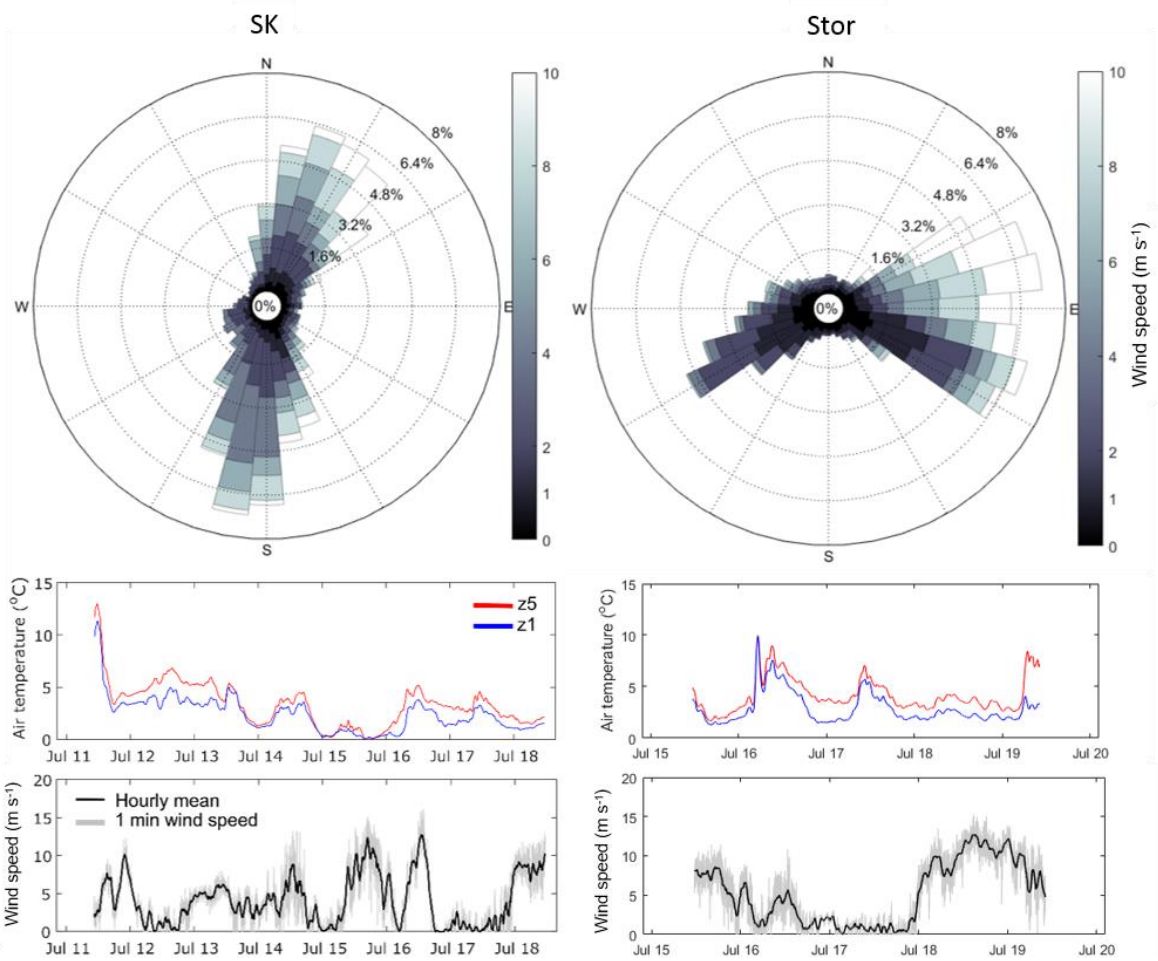

Figure A.1. Full set of meteorological data recorded from wind towers at SK and Stor. Wind roses show proportional wind speed and direction. Temperature time-series display hourly mean temperatures from the upper- and lowermost sensors. Wind speed plots show both the hourly mean and full variability.

Table A.1. Specifications of cameras used in data collection

Camera	Sensor size (mm)	Focal length (mm)	Image size (pix)	Camera height (m)	GSD (mm pix^{-1})
Panasonic DMC-TZ60	6.16 x 4.62	4.3	4896 x 3672	9.66	2.61
Phantom 3 UAV - Sony EXMOR 1/2.3"	6.16 x 4.62	3.61	4000 x 3000	29.2	12.46

Table A.2 Specifications of photogrammetric analysis

	Dense matching		Camera calibration
Site	Quality	Depth filtering	Parameters included
Stor	High	Aggressive	F, Cx, Cy, K1, K2, P1, P2
SK	High	Aggressive	F, Cx, Cy, B1, B2, K1, K2, K3, P1, P2

Table A.3 Source and number of images used in SfM processing.

	Images collected		Images used			
Site	Pole	UAV	Pole	UAV	Total	Aligned
SK	185	448	132	222	354	354
Stor	409	831	357	0	357	357

Table A.4 Summary of digital elevation models, and root mean square errors for ground control points used as control in SfM datasets.

Site	Size of DEM (m)	GCPs	X (m)	Y (m)	Z (m)	Total (m)
SK	40.7 x 36.6	4	0.015	0.011	0.009	0.021
Stor	137.1 x 55.8	10	0.002	0.007	0.007	0.010

A.1 SfM precision analysis

As stated in the main text, to test the effects of SfM precision on z_0, we followed the workflow of James *et al.* (2017) with some slight adjustments. After the initial image alignment, cleaning, georeferencing and camera model optimisation steps in Agisoft PhotoScan Vversion 1.4.0, we ran the bundle adjustment Python script, generating *n* synthetic point clouds which have pseudo-random offsets applied to image observations. The effect of this process is that X, Y and Z coordinates differ between each point cloud and the standard deviation of their variability is used as an estimate of precision. We interpolated a DEM from each point cloud and used the raster method (Smith *et al.*, 2016) to calculate z0 for the prevailing wind direction using the standard deviation of z0 across all surfaces as an estimate of z0 precision. Point cloud and z0 precision was sub-cm for both plots (Table S3). Overall, the difference in precision in the three dimensions was negligible, meaning that the SfM projects had reasonably strong network geometry. DEMs were interpolated from each point cloud using the inbuilt feature in PhotoScan, (which uses IDW for interpolation). The effects of different interpolation methods are not considered here, although they are presumed to introduce some minor variability in the resulting surface.

These initial investigations of the effect of SfM precision on z0 were carried out using sparse point clouds; at this stage the variability of z0 was the key factor and not the value of z0 itself. Further analysis (in main text) of microtopographic z0 was performed using dense clouds and DEMs interpolated from the dense clouds.

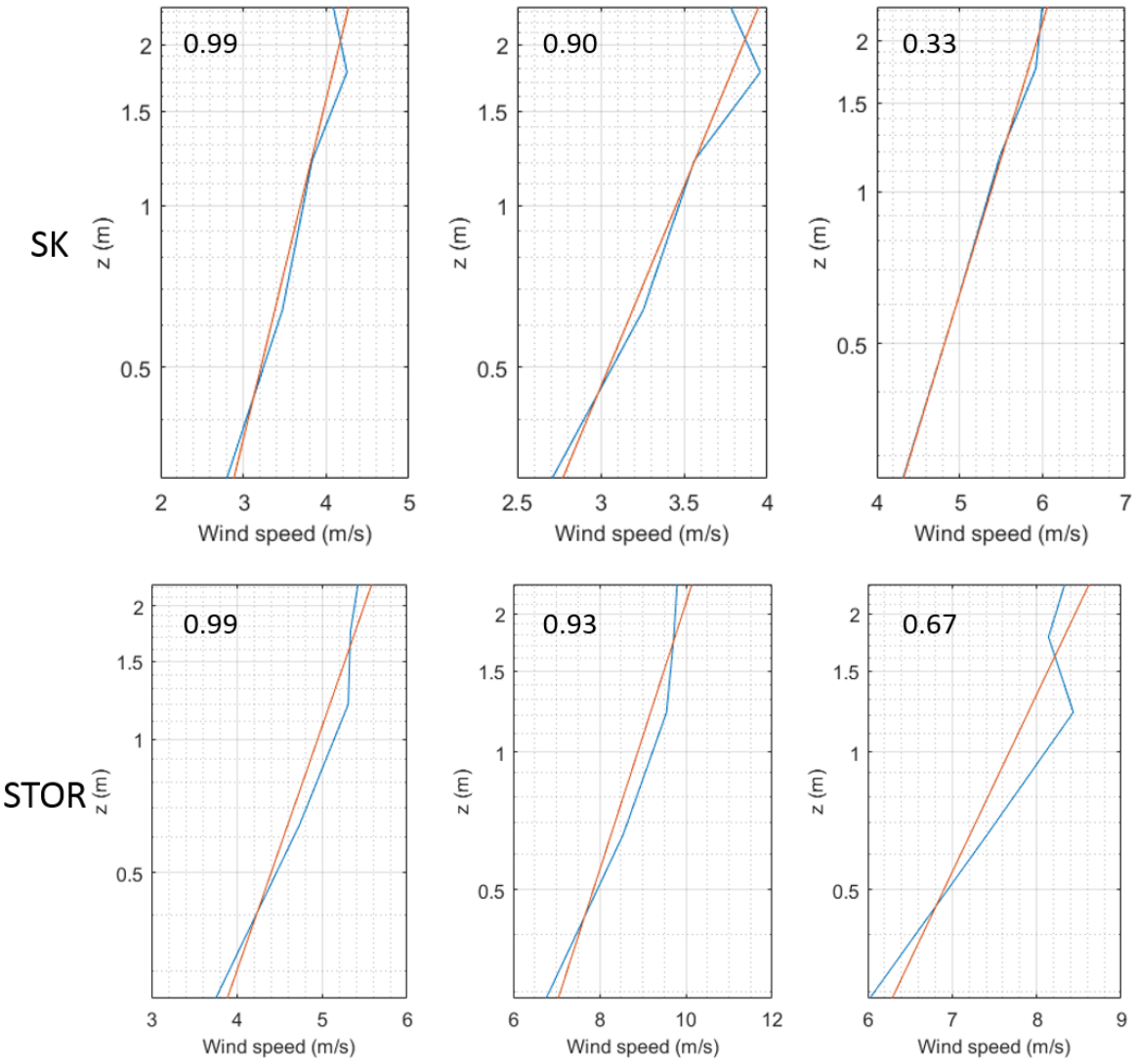

Figure A.2 Example profiles of log(z) against wind speed, with r^2 given in the top corner for each. The profiles with 0.99 r^2 were retained by the filters, the others were discarded.

A.2 Wind direction results

On SK there was no strong evidence for surface anisotropy, as wind direction did not have much impact on z_0 (Fig. S3). The surface may be anisotropic nonetheless, and z_0 may be higher in a cross-glacier direction; however, the wind was predominantly up- or down-glacier (Fig. S1), so barely any z_0 values calculated for cross-glacier wind directions (~90° or 270°). Some effect of wind direction on z_0 was evident on Stor, where z_0 was higher at ~110° than at ~50°, though a directly up-glacier wind would travel at 90° so this is not the same display of anisotropy as has been observed in other studies (e.g. Brock *et al.*, 2006; Quincey *et al.*, 2017).

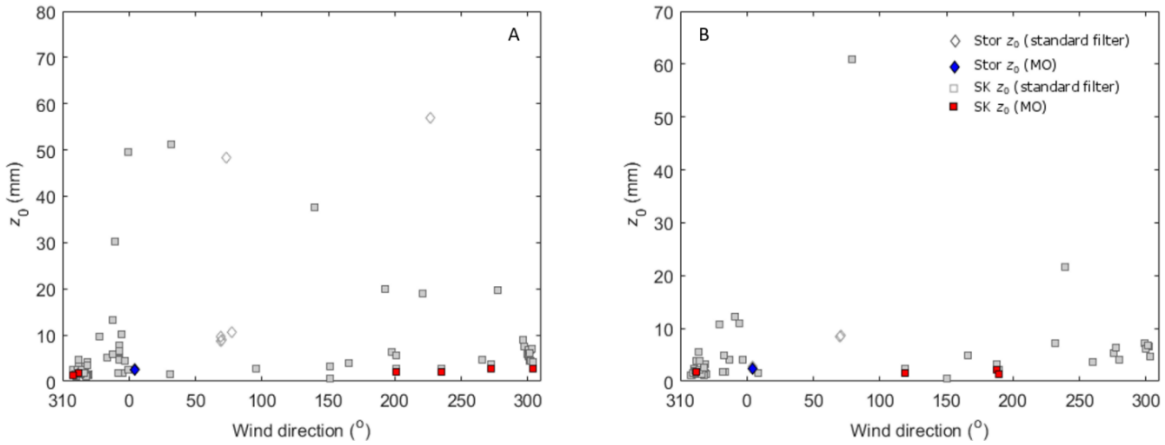

Figure A.3. z_0 plot by wind direction. 10 minute averaged data (A) and 15 minute averaged data (B). Note circular scale on x-axis to allow easier interpretation of values around 0°

A.3 Atmospheric stability results

To adhere to the assumptions of MO theory, data can be filtered for atmospheric stability. Where z/L<0, conditions are said to be unstable. Stable conditions occur where 0<z/L <~1. A stability threshold (e.g. -0.1 <z/L <0.2, Fitzpatrick *et al.*, 2017) is intended filter out conditions that are too strongly stable or unstable. This was not necessary here, as conditions at both sites during the study were weakly stable - z/L was mostly less than ~0.25 (Fig. S4), so a filter would have had little effect on the amount of data. Moreover, there is little evidence to suggest that atmospheric stability had any effect on z0.

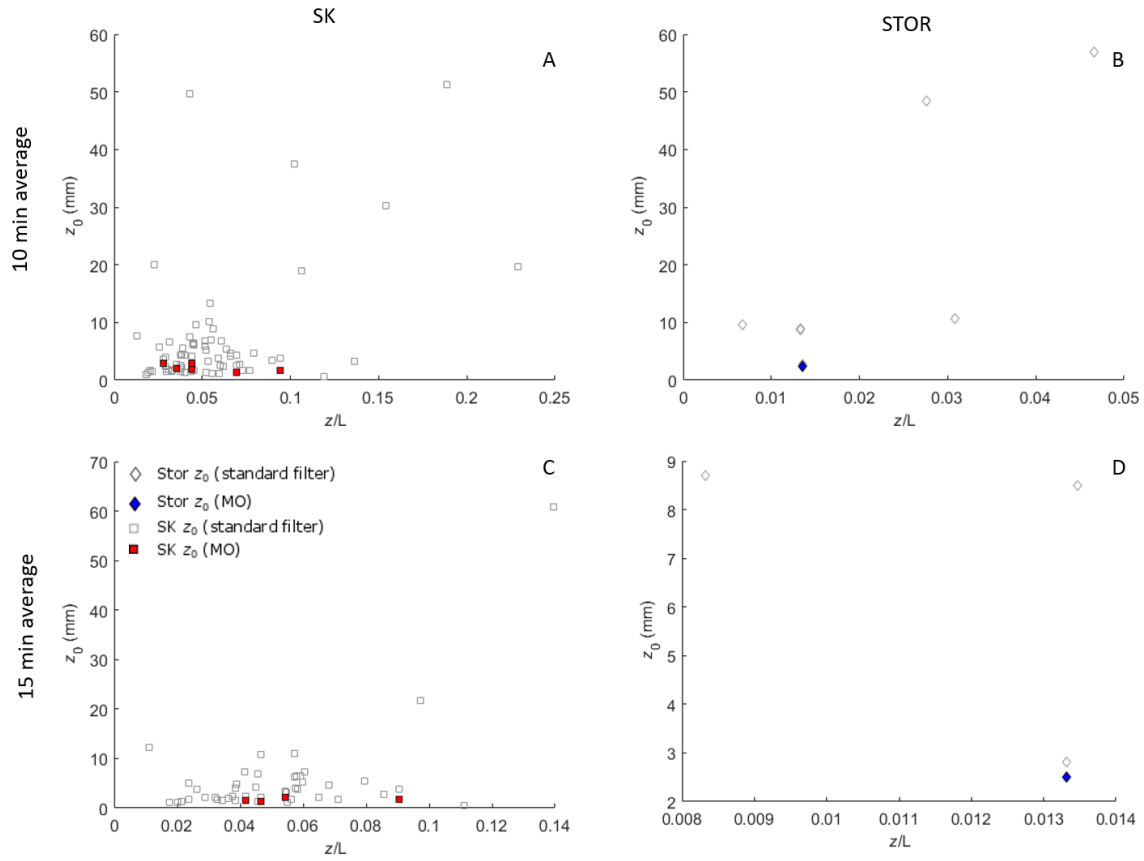

Figure A.4. Effect of atmospheric stability on z_0. (A) and (B) show results for data averaged over 10 minutes, (C) and (D) show results for 15 minute averaged data.

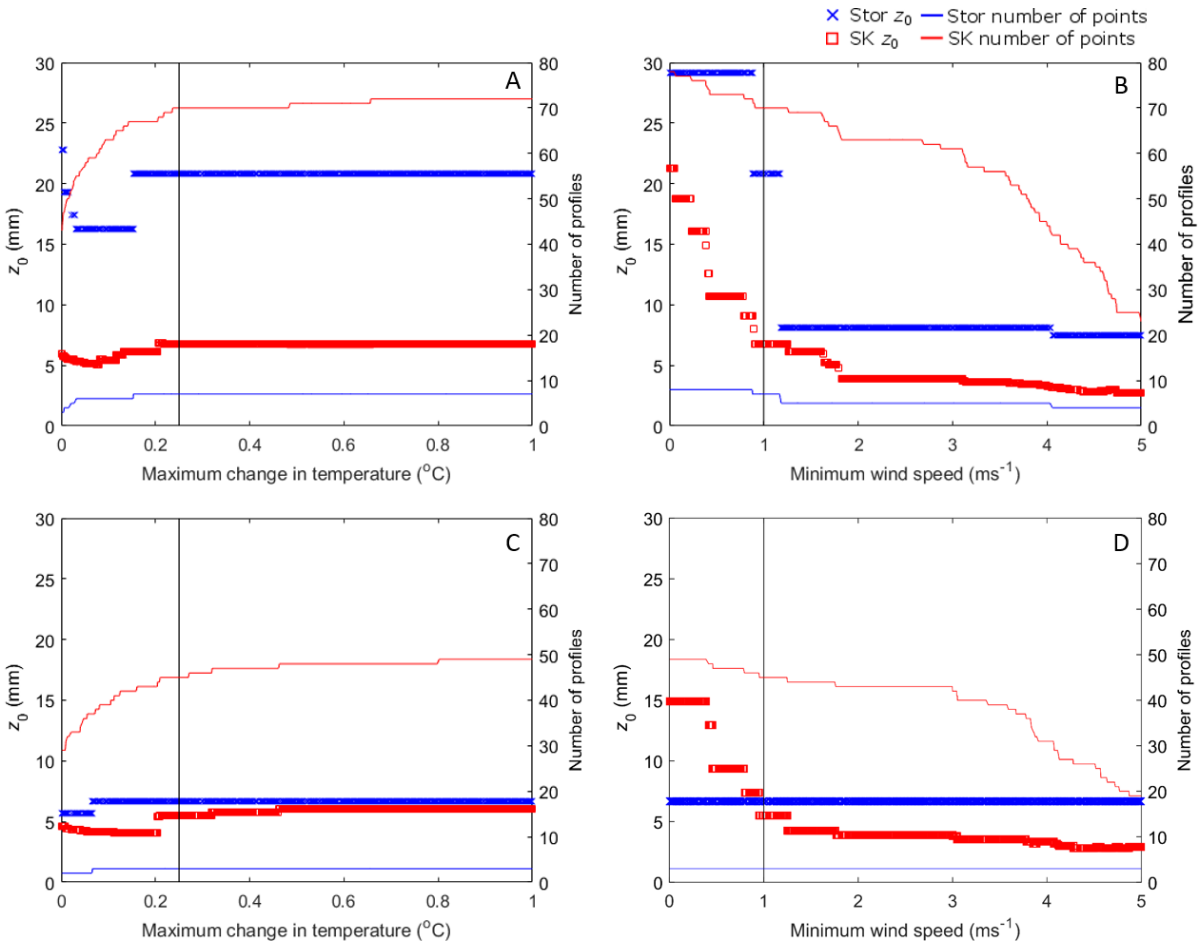

Figure A.5. Effect of different stationarity (A, C) and wind speed (B, D) filter thresholds on z_0. (A) and (B) show results for data averaged over 10 minutes, (C) and (D) show results for 15 minute averaged data.

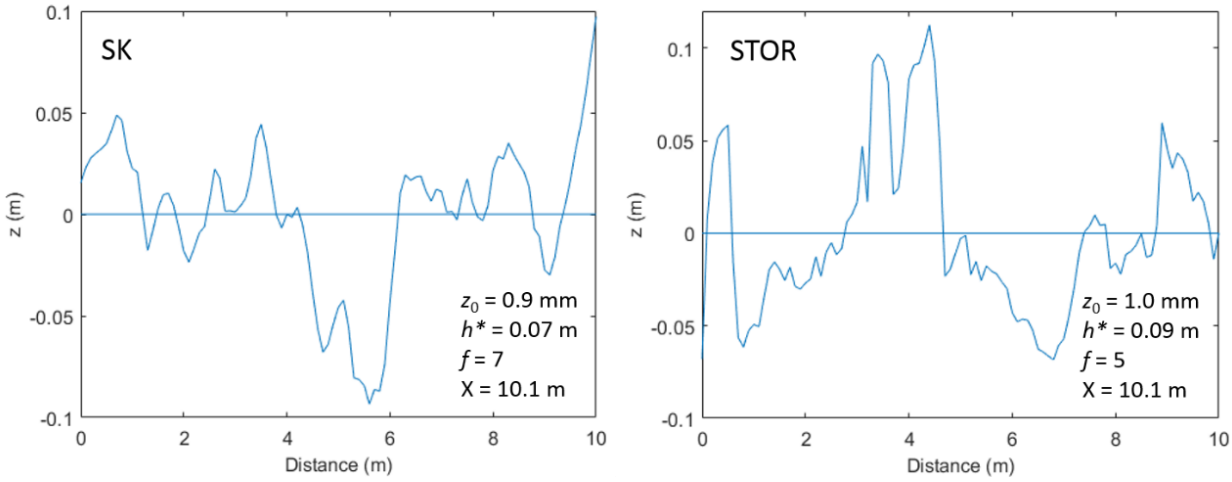

Figure A.6. Examples of detrended microtopographic transects from SK (left) and Stor (right). Values for the parameters of the Munro version of the Lettau equation are included.

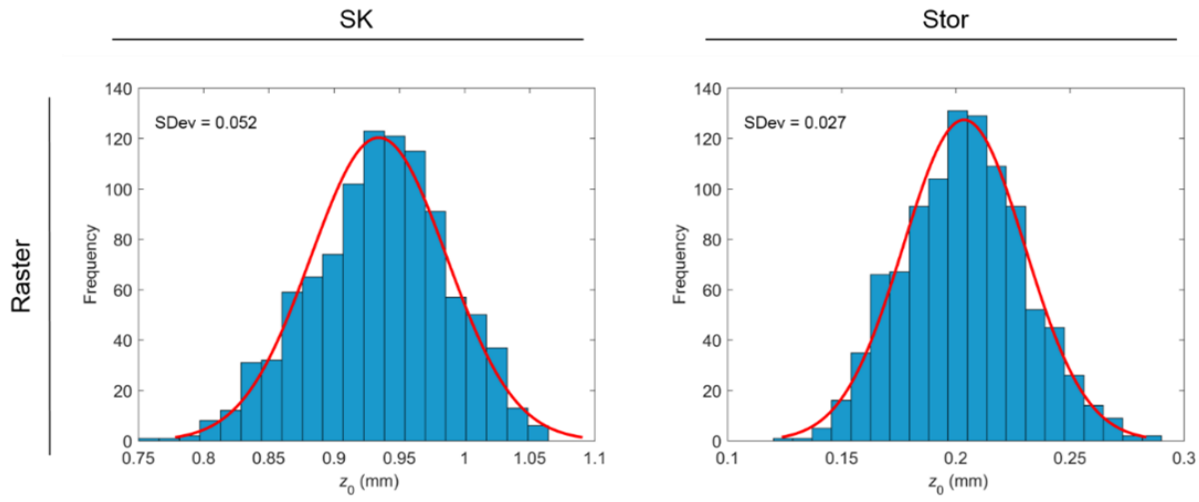

Figure A.7. Distribution of z_0 values calculated from MC surfaces, using raster method. Normal distribution is shown by the red line on each histogram.

Table A.5. Summary of SfM point precision and z_0 estimated from MC analysis using raster method.

	Point Precision (mm)				**Raster z_0 (mm)**		
Site	X	Y	Z	Mean	Mean	Range	Standard Deviation
SK	7.15	7	7.06	7.07	0.934	0.306	0.052
Stor	6.09	5.46	5.64	5.73	0.204	0.163	0.027

Appendix B

Supporting information for Chapter 4: “Correcting for systematic underestimation of topographic glacier aerodynamic roughness values from Hintereisferner, Austria”

Contents of this section:

Table B.1. Details of ALS data acquisition (from Sailer et al., 2012)

Flight Date	Sensor (Optech)	Mean height above surface (m)	Pulse frequency (Hz)	Mean point density (points m^{-2})
11/10/2001	ALTM 1225	900	25000	1.1
18/09/2002	ALTM 3033	900	33000	1.0
12/08/2003	ALTM 2050	1150	50000	0.8
26/09/2003	ALTM 1225	900	25000	1.0
05/10/2004	ALTM 2050	1000	50000	2.0
12/10/2005	ALTM 3100	1000	70000	3.4
08/10/2006	ALTM 3100	800	70000	2.0
11/10/2007	ALTM 3100	1000	70000	3.4
07/08/2008	ALTM 3100	1000	70000	2.4
09/09/2008	ALTM 3100	1000	50000	2.2
30/09/2009	ALTM 3100	1100	70000	2.7

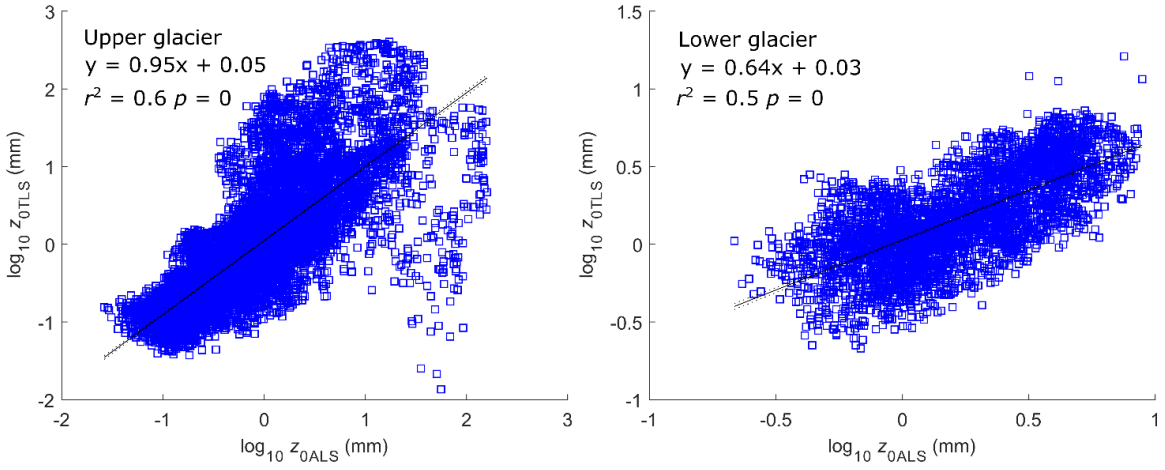

Fig. B.1. z_{0TLS} compared to z_{0ALS} for upper and lower glacier

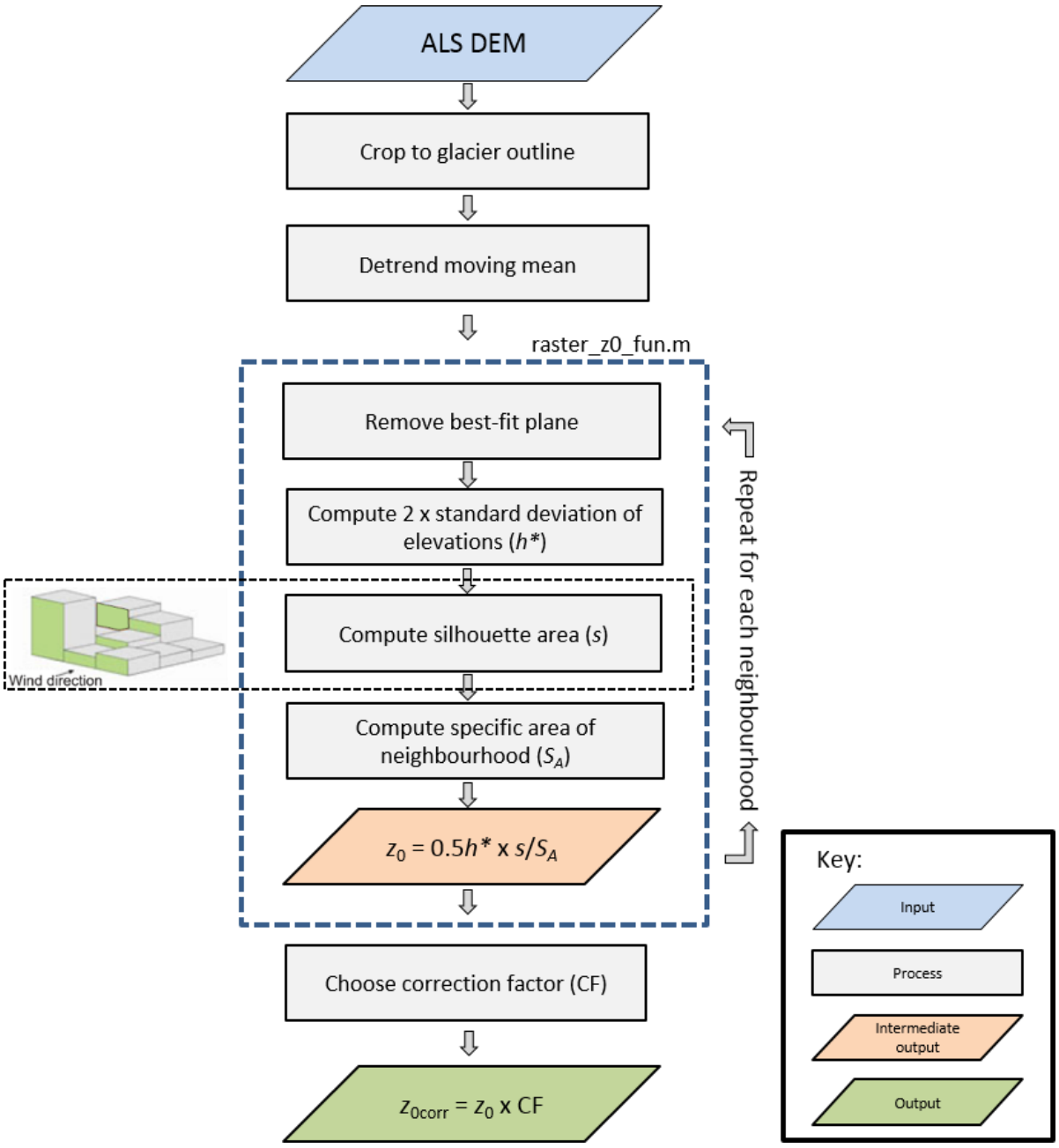

Fig. B2. Flow chart of processing steps

Appendix C

Copy of: “A scale-dependent model to represent changing aerodynamic roughness of ablating glacier ice based on repeat topographic surveys” by Smith *et al.* (2020)

Journal of Glaciology

Article

Cite this article: Smith T, Smith MW, Chambers JR, Sailer R, Nicholson L, Mertes J, Quincey DJ, Carrivick JL, Stiperski I (2020). A scale-dependent model to represent changing aerodynamic roughness of ablating glacier ice based on repeat topographic surveys. *Journal of Glaciology* **66**(260), 950–964. https://doi.org/10.1017/jog.2020.56

Received: 15 May 2020
Revised: 30 June 2020
Accepted: 1 July 2020
First published online: 4 August 2020

Key words:
Energy balance modelling; glacier melt; ice roughness; structure from motion photogrammetry

Author for correspondence:
Mark W. Smith,
E-mail: m.w.smith@leeds.ac.uk

cambridge.org/jog

A scale-dependent model to represent changing aerodynamic roughness of ablating glacier ice based on repeat topographic surveys

Thomas Smith[1], Mark W. Smith[1], Joshua R. Chambers[1], Rudolf Sailer[2], Lindsey Nicholson[3], Jordan Mertes[4], Duncan J. Quincey[1], Jonathan L. Carrivick[1] and Ivana Stiperski[3]

[1]School of Geography and water@leeds, University of Leeds, Leeds, LS2 9JT, UK; [2]Department of Geography, Universität Innsbruck, Bruno Sander Haus, Innrain 52, Innsbruck, A-6020, Austria; [3]Department of Atmospheric and Cryospheric Sciences, Universität Innsbruck, Bruno Sander Haus, Innrain 52, Innsbruck, A-6020, Austria and [4]Centre for Environmental and Climate Research, Lund University, Ekologihuset, Sölvegatan 37, Lund, Sweden

Abstract

Turbulent fluxes make a substantial and growing contribution to the energy balance of ice surfaces globally, but are poorly constrained owing to challenges in estimating the aerodynamic roughness length (z_0). Here, we used structure from motion (SfM) photogrammetry and terrestrial laser scanning (TLS) surveys to make plot-scale 2-D and 3-D microtopographic estimations of z_0 and upscale these to map z_0 across an ablating mountain glacier. At plot scales, we found spatial variability in z_0 estimates of over two orders of magnitude with unpredictable z_0 trajectories, even when classified into ice surface types. TLS-derived surface roughness exhibited strong relationships with plot-scale SfM z_0 estimates. At the glacier scale, a consistent increase in z_0 of ~0.1 mm d^{-1} was observed. Space-for-time substitution based on time since surface ice was exposed by snow melt confirmed this gradual increase in z_0 over 60 d. These measurements permit us to propose a scale-dependent temporal z_0 evolution model where unpredictable variability at the plot scale gives way to more predictable changes of z_0 at the glacier scale. This model provides a critical step towards deriving spatially and temporally distributed representations of z_0 that are currently lacking in the parameterisation of distributed glacier surface energy balance models.

1. Introduction

The physical roughness of a surface exerts drag on the air moving over it, leading to instabilities that drive turbulence within a wind profile and vertical mixing of air through turbulent eddies (Cuffey and Paterson, 2010). Over ice surfaces, such turbulence can deliver energy to the glacier surface in two ways:

(1) if the air in the boundary layer directly above the ice surface is warmer than the surface itself, then sensible heat is transferred to the ice surface (Morris, 1989);
(2) if the overlying air is more humid than the ice surface, eddies drive the transfer of latent heat to the surface through condensation or deposition (Cuffey and Paterson, 2010).

Accordingly, sensible and latent heat transfer are referred to as turbulent fluxes; both can be net sinks or sources of heat energy to ice surfaces under differing climatic conditions (Lewis and others, 1998; Greuell and others, 2001; Sicart and others, 2005). Figure 1 compares the balance of the turbulent and radiative components of the surface energy balance (SEB) for a global compilation of 47 glaciers during their ablation seasons. Typically, the literature gives more attention to the calculation of radiative fluxes, which have a much greater role in supplying melt energy to ice surfaces globally than turbulent fluxes. While not the dominant source of melt energy, turbulent fluxes can have a substantial contribution to a glacier SEB, particularly: (i) at high latitudes in the northern hemisphere where ice surfaces at lower altitudes are exposed to high summer air temperatures; and (ii) in maritime conditions where windy and cloudy conditions reduce the role of short-wave and long-wave radiation, e.g. Scandinavia and the West coast of New Zealand (Ishikawa and others, 1992; Giesen and others, 2014; Conway and Cullen, 2016). Conversely, in areas where both summer and winter temperatures remain extremely low, turbulent fluxes tend to be either very small or act as a net sink of melt energy (Sicart and others, 2005, Bravo and others, 2017).

Figure 1 demonstrates that turbulent fluxes can contribute >20% of total energy available for melt over an ablation season. However, for shorter timescales they can contribute as much as 76% to the SEB of an ice surface (e.g. Fausto and others, 2016*a*). Moreover, there is growing recognition that the role of turbulent fluxes in driving glacier ice melt is increasing as global climate moves towards wetter, windier and warmer conditions (van den Broeke and others, 2008; van den Broeke and others, 2011; Franco and others, 2013). This is particularly the case in polar regions where climate warming is amplified (IPCC, 2013).

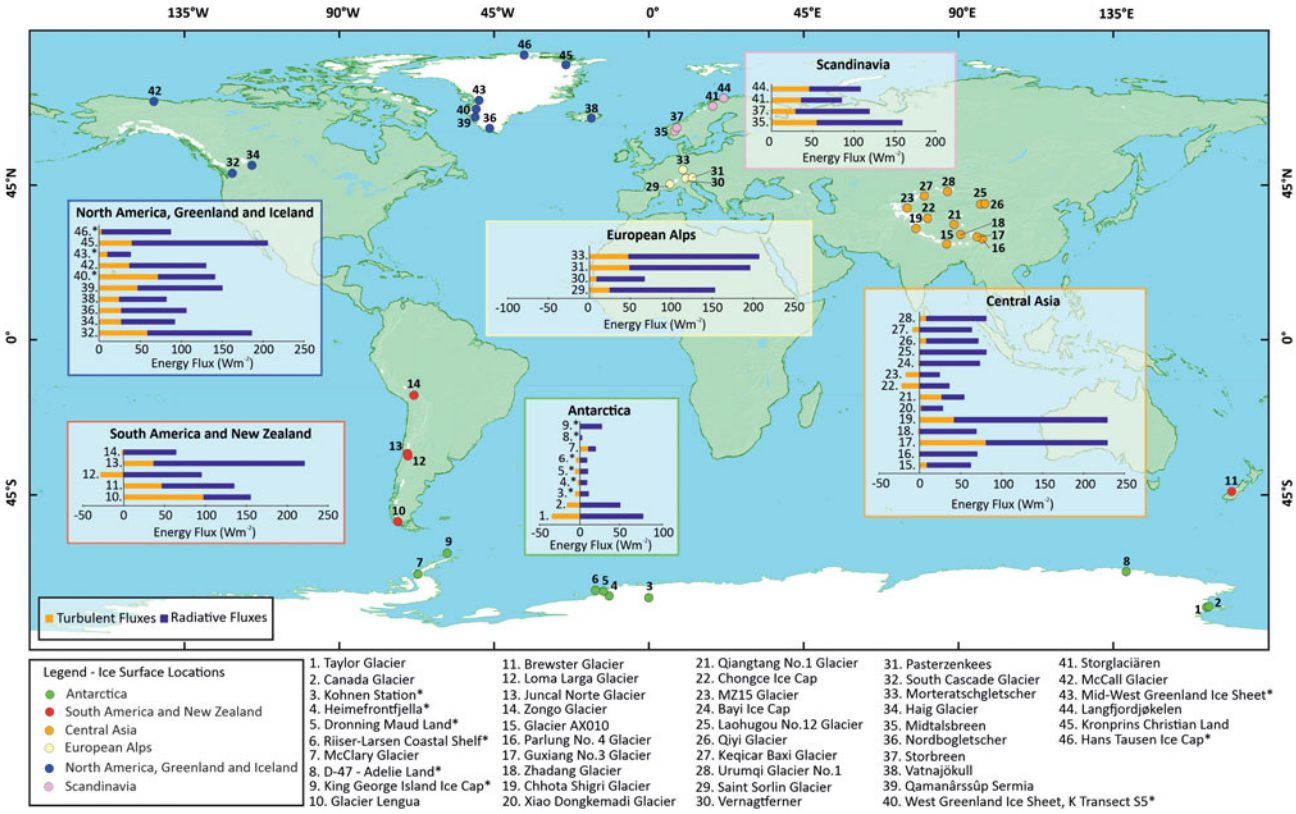

Fig. 1. The role of radiative and turbulent fluxes globally for studies on permanent snow or ice surfaces during the ablation season and of duration longer than 2 weeks. References for each of these data points are provided in online Supplementary Table S1. Values over ice sheets are indicated with an asterisk

A potential major source of error within turbulent flux calculations is the estimation of the aerodynamic roughness length (z_0), defined as the height above an ice surface at which the wind velocity drops to zero (Smith, 2014). Estimation of z_0 is challenging and often requires extensive and intensive field datasets. Three methods are commonly applied in order to assess the value for z_0 of a surface: (i) direct observations of turbulence using sonic anemometers (e.g. Greuell and Genthon, 2004; Fitzpatrick and others, 2019); (ii) extrapolation from log-linear profiles of horizontal wind speed and air temperature (e.g. Ishikawa and others, 1992; Bintanja and van den Broeke, 1995; Hock and Holmgren, 2005); and (iii) estimation using surface microtopographic data, usually following approaches based on Lettau (1969).

Both sonic anemometers and wind profiles only provide point values, and require expensive equipment deployed over long periods during which continuous maintenance is needed (Munro, 1989; Gromke and others, 2011; Nicholson and others, 2016; Radić and others, 2017). Moreover, substantial assumptions, sensitivities and uncertainties remain inherent to both techniques (cf. Chambers and others, 2019). Yet, z_0 has been observed to vary over several orders of magnitude through both space and time (e.g. Bintanja and van den Broeke, 1995; Smeets and others, 1999; Guo and others, 2011; Sicart and others, 2014; Nicholson and others, 2016; Quincey and others, 2017; Fitzpatrick and others, 2019). This variability is problematic because turbulent flux calculations are sensitive to z_0; an order of magnitude change in z_0 has been reported to lead to a doubling in the calculated value for turbulent fluxes (Munro, 1989; Brock and others, 2000). Despite this sensitivity, it is typically assumed that z_0 is spatially uniform (e.g. Azam and others, 2014; Giesen and others, 2014; Sun and others, 2018), temporally uniform (e.g. Greuell and Smeets, 2001; Ebrahimi and Marshall, 2016; Schmidt and others, 2017), or that z_0 can be treated as a model tuning parameter, used to calibrate models (e.g. Anslow and others, 2008; Hoffman and others, 2008; Favier and others, 2011). Each of these assumptions introduces considerable uncertainty into turbulent flux estimations and could conceal model deficiencies.

While temporal variability in z_0 is well documented both over an entire ablation season and over shorter timescales, there is disagreement on the extent to which this variation is progressive. Evidence exists for several possibilities: (i) multiple contrasting temporal trends over a single glacier (Brock and others, 2006; Smith and others, 2016); (ii) no discernible trends in z_0 (Sicart and others, 2014; Fitzpatrick and others, 2019); (iii) progressive increase of z_0 (Smeets and van den Broeke, 2008; Nicholson and others, 2016) and (iv) a clear evolution of z_0 during the melt season, with initially low z_0 increasing as snow cover melts to expose underlying ice, followed by a decrease in z_0 as bare ice is exposed and a second period of increasing z_0 as melt causes the development and growth of meltwater channels and ice hummocks leading to $z_0 > 10$ mm (Guo and others, 2011).

Given the pronounced spatial and temporal variability in z_0, its impact on turbulent flux estimates and the potential increase in importance of turbulent fluxes for melt with changing climate, there is a clear need to better understand the spatial and temporal variability of z_0. Such work is timely as distributed melt models are increasingly able to implement distributed and potentially dynamic estimates of z_0. While z_0 calculation from sonic anemometers or wind profiles is too data intensive to adequately sample this variability, the recent proliferation in the availability of high-resolution topographic data using structure for motion (SfM) photogrammetry (e.g. Irvine-Fynn and others, 2014; Smith and others, 2016; Miles and others, 2017; Quincey and others, 2017) and via both terrestrial and aerial light detection and ranging (LiDAR) techniques (e.g. Smith and others, 2016; Fitzpatrick and others, 2019) makes the microtopographic approach the best means of accounting for the spatial and temporal variability of z_0. Recently, 3-D methods of estimating z_0 from topographic data (e.g. Smith and others, 2016) have

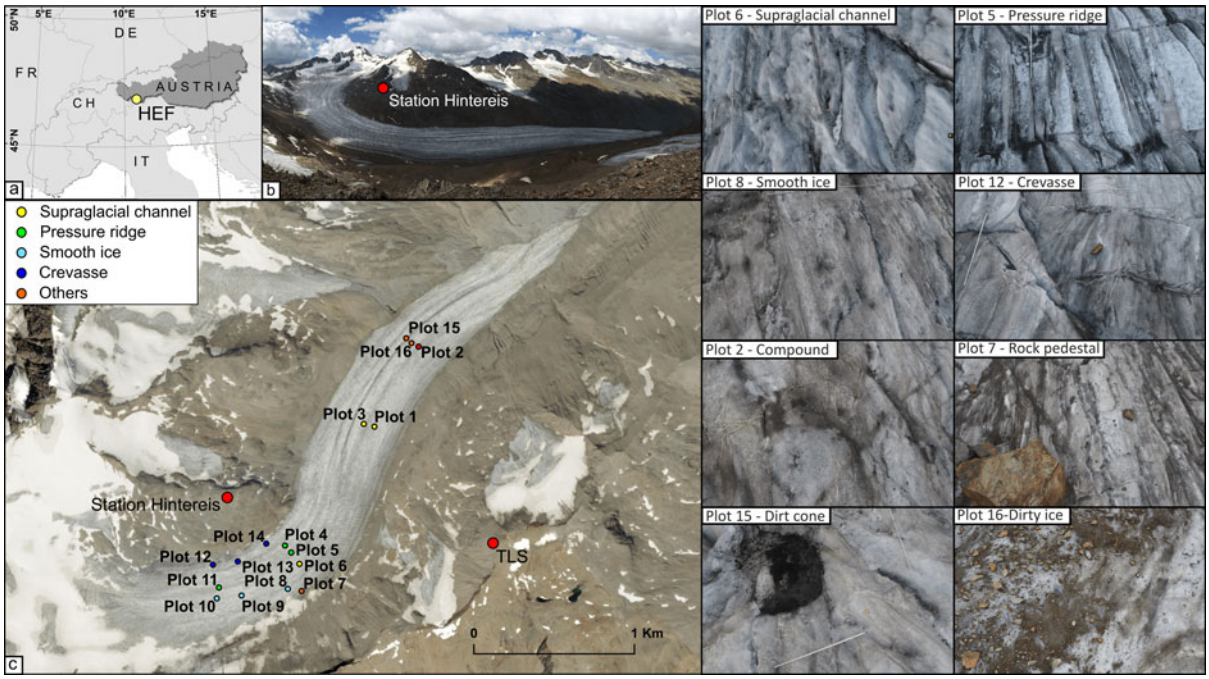

Fig. 2. (a) Location of Hintereisferner (HEF) within Austria; (b) Hintereisferner viewed from the southeast, close to the Terrestrial Laser Sanner location (3 August 2018). (c) Plot locations and contemporary glacier extent (3 August 2015); photos – example imagery for each ice facies of dimensions ~6 m × 5 m. Source for imagery in (c): Esri, Orthofoto Tirol.

sought to improve upon the more conventional 2-D profile-based methods and make use of the available topographic data. Initial attempts to upscale plot-based microtopographic estimates of z_0 to the glacier scale are promising (e.g. Smith and others, 2016), and the use of topographic data acquired from terrestrial and aerial LiDAR and potentially also from satellite imagery could allow spatially distributed representations of z_0 to become incorporated into distributed snow and ice melt models. Certainly, high-resolution stereo imagery from satellites such as WorldView and Pléiades has recently shown great promise in mapping snow depth (e.g. Marti and others, 2016; Deschamps-Berger and others, 2020; Shaw and others, 2020) and estimating glacier mass balance (e.g. Belart and others, 2017; Shean and others, 2020) and, although challenging, may also be suitable to observe z_0 variability.

Therefore, the aims of this study were: (i) to quantify at different scales the spatial and temporal variability of z_0 over glacier ice during peak melt season and (ii) to develop a theoretical representation of z_0 evolution that can be used as a foundation for more robust inclusion of z_0 dynamics in distributed SEB models.

2. Methods and study site

2.1 Study site

Hintereisferner (46°48′N, 10°47′E) is a ~6 km long valley glacier (Fig. 2), located in the catchment of Rofenache in the southern Ötztal Alps, Austria (Strasser and others, 2018). The glacier ranges from 3739 m a.s.l. at its highest point (Weißkugel) to 2498 m a.s.l. at the glacier terminus. The glacier has been studied extensively through ablation stake measurements (e.g. Blümcke and Hess, 1899; Ambach, 1961; van de Wal and others, 1992; Kuhn and others, 1999), observation of accumulation in snow pits (e.g. Patzelt, 1970; Kuhn and others, 1999) dye tracing of the internal drainage system (e.g. Behrens and others, 1975), SEB observations (e.g. van de Wal and others, 1992), numerical modelling of flow and mass balance (e.g. Greuell and others, 1992; Escher-Vetter and others, 2009; Fischer, 2010), digital elevation model (DEM) analysis (e.g. Geist and Stotter, 2007), LANDSAT imagery reflectance analysis (e.g. Koelemeijer and others, 1993) and airborne photogrammetry (e.g. Patzelt, 1980; Lambrecht and Kuhn, 2007). Supplementing much of this research is one of the longest continuous records of mass balance in the world (1952/53–present; Fischer, 2010), and extensive observations of glacier length which have been made since 1847 (Greuell, 1992).

As of 2018, the glacial extent of Hintereisferner was 6.22 km^2; this value represents a large reduction from the extent during the Little Ice Age (LIA) in 1855. The glacier has been in almost constant retreat since the LIA (Greuell, 1992); the rate of decline is currently rapid – from 2001 to 2011 alone the glacier terminus retreated 390 m (Klug and others, 2018). The ice is also thinning; between 1953 and 2006, surface lowering of over 100 m was observed in the vicinity of the glacier terminus, while up-glacier the surface elevation decreases were <40 m (Fischer, 2010). Such geometry changes and rapid mass loss is characteristic of glaciers throughout Austria (Fischer and others, 2015; Carrivick and others, 2015*a*) and across the entire European Alps with many glaciers now shrinking at a rate of 1% of their area per annum (Vincent and others, 2017).

Our field campaign lasted 15 d between 1 and 15 August 2018 and primarily involved the repeat survey of 16 plots of 10 m × 10 m. A wind tower comprising five NRG 40 cup anemometers, one NRG 200P wind vane and five shielded and passively-ventilated Extech RHT10 temperature and humidity loggers was installed at Plot 2 for the duration of the study. Temperature (5 min average) and wind speed and direction (30 min average) data are displayed in Figure 3. Day time temperatures (Fig. 3a) over the glacier reached peaks of >10°C for all study days, the highest temperature recorded was 19.8°C occurring in the afternoon of the 5th day of study. Minimum diurnal temperatures were always <5°C but did not drop below 2°C. Mean wind speed (Fig. 3b) was 2.5 m s^{-1} with peak values exceeding 5 m s^{-1}. Mean wind direction was 165° relative to the down-glacier direction, demonstrating that katabatic winds dominate over Hintereisferner during the ablation season in accordance with previous studies (Obleitner, 1994). Precipitation throughout the field campaign was mainly constrained to convective thunderstorms occurring in the afternoon; particularly heavy events were noted on 1st, 6th, 10th and 13th days of study.

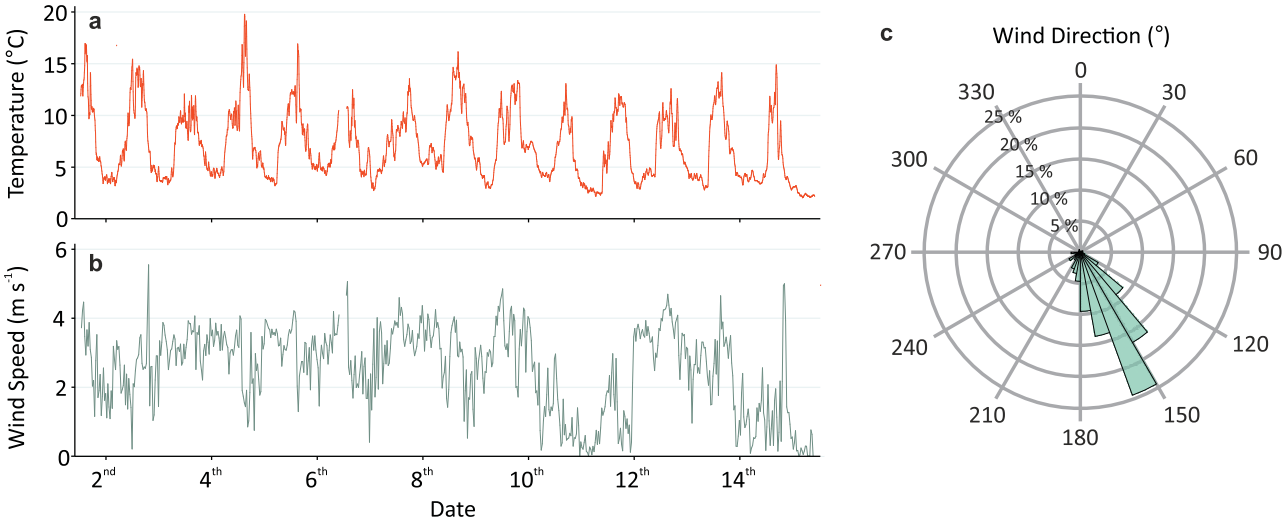

Fig. 3. (a) Temperature (°C) and (b) wind speed at ~1 m (m s^{-1}) throughout the study period (1–15 August 2018). A small gap within the data exists due to a fault with the data logger during the 6th day of study. (c) Wind direction (% of time) with down-glacier direction set to 0°.

2.2 Plot surveys

Sixteen plots containing eight distinct ice facies distributed around the ablation area of the glacier were identified (Fig. 2). Plots of 10 m × 10 m with a spatial resolution of <10 mm are adequate for characterisation of aerodynamic roughness (Rees and Arnold, 2006). Following an initial glacier survey, the most common ice facies were identified as: Supraglacial Channels, Pressure Ridges, Smooth Ice and Crevasses. Three replicate plots were demarcated for each of these surface roughness types to test for consistency in response. In addition, one plot was sampled for each of the less prominent ice facies identified: Rock Pedestal, Dirt Cone, Dirty Ice and Compound (i.e. multiple co-located features). Over 15 d, starting on 1 August 2018, each plot was surveyed with an average interval of 4 d; however, owing to inclement weather and logistical difficulties, this interval varied between plots (3–5 d).

High-resolution topographic data for the 16 plots were obtained via standard SfM photogrammetry workflows (James and others, 2017; O'Connor and others, 2017). A survey pole extended to a vertical height of ~6 m allowed for a large image footprint, a high degree of image overlap and good coverage of the plot area with a relatively low number of images. Approximately five rows of 12 off-nadir photographs with intervals of ~1.5 m between successive rows were taken during each survey to achieve a target of 80% sidelap and 60% frontlap between images. On each row, images were taken from different directions with additional images taken from the plot edges. Details of the camera parameters are displayed in Table 1.

Each plot was marked out using five ground control points (GCPs) placed on areas of flat ice in the corners and centre, secured into the ice with a metal peg and surveyed using a Leica GS10 differential GPS system in real-time kinematic (RTK) mode. Mean GCP accuracy was sub-centimetre for each plot. Owing to down-glacier movement of the ice patch and the dynamic nature of the glacier surface, GCP locations were resurveyed at each visit. The same ice surface was resurveyed each time, thus the absolute coordinates of the plots translated down-glacier through the survey period. SfM photogrammetry was performed using Agisoft Photoscan Professional Edition Version 1.4.0 following the workflow of James and others (2017). Typically, total 3-D root mean square (RMS) GCP error was ~0.02 m and RMS re-projection error generally <2 pixels. Dense point clouds were cropped to 10 m × 10 m centred on the middle GCP and octree subsampled to a point density ~4×10^4 points m^{-2} (~4×10^6 points per plot). The subsampled point clouds were then rasterised to create a DEM of resolution 5×10^{-3} m for all 59 surveys, using the mean elevation within each cell.

Table 1. Key features of SfM photogrammetry surveys and camera parameters

Specifications	Primary camera	Secondary camera
Make and model	Olympus EM 10	Canon PowerShot SX600 HS
Lens model	M. Zuiko Digital 14–42 mm	Built in
Weight (g)	396	188
Resolution (MP)	16.1	16.0
Sensor size (mm)	17.3 × 13.0	6.2 × 4.6
Image size (pixels)	4608 × 3456	4608 × 3456
Pixel pitch (μm)	3.74	1.34
GSD (mm)[a]	0.80	0.32
Focal length	~28 mm	~25 mm
Maximum (mean) images per plot	71 (64)	
Survey platform	Survey Pole at ~6 m above the ice surface	
Camera locations	360° survey	
Angle of imagery	~20° off vertical	
Camera trigger	Remote (via Smartphone)	

[a]Calculated ground surface distance (GSD) is based on the assumption that photographs were taken nadir to the surface. The secondary camera was used for six surveys due to technical issues with the primary camera.

2.3 Topographic z_0 estimation

From empirical work, Kutzbach (1961) and Lettau (1969) proposed a relationship to relate the surface form and density of roughness elements to z_0:

$$z_0 = 0.5h^* \frac{s}{S_A} \quad (1)$$

where 0.5 is the average drag coefficient of one roughness element, h^* is the average peak vertical extent of roughness elements (mm), s is the silhouette area of the average obstacle (mm^2) and S_A is the specific horizontal area of the plot (mm^2), given by

$$S_A = \frac{A}{n} \quad (2)$$

where n is the number of obstacles and A is the total area of site (mm^2).

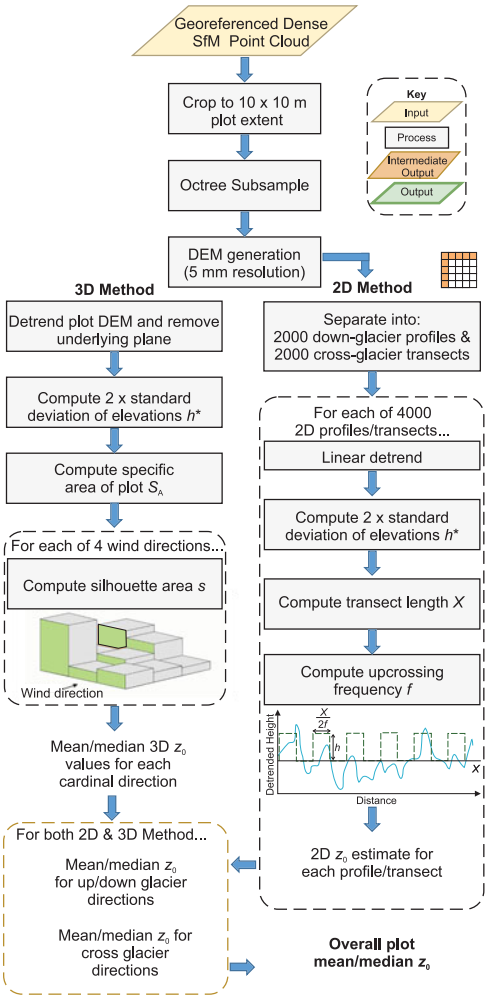

Fig. 4. Methodological steps for z_0 calculation.

In this study, we derived two alternative z_0 estimates from SfM-derived topographic data: first, the 2-D transect method of Munro (1989), and secondly, a more recently developed 3-D method that estimates z_0 from DEMs. While the 3-D method makes better use of the available topographic data and permits several assumptions to be relaxed, we also present results using the more conventional 2-D method to facilitate comparison between this and previous studies. The steps required to calculate z_0 using both methods are summarised in Figure 4.

Munro (1989) adapted Eqn (1) to allow for estimates of z_0 from transects. The method of Munro (1989) assumes that irregularly distributed roughness elements deviating around a mean elevation can be simplified to regularly distributed rectangles of height equal to h^* thereby removing the need to make an assessment of surface form in the calculation of silhouette area (s). Silhouette area is simply given by:

$$s = \frac{2\sigma_d X}{2f} \tag{3}$$

where h^* is approximated to be twice the SDs of detrended elevations ($2\sigma_d$) (mm) and equal to the representative obstacle height, X is the length of the transect measured (mm) and f is the number of extensions of the transect above zero on the mean detrended plane. The specific area (S_A) can be given by:

$$S_A = \left(\frac{X}{f}\right)^2 \tag{4}$$

so that,

$$z_0 = \frac{f}{X}(\sigma_d)^2. \tag{5}$$

To allow for 2-D estimations of z_0, as per Irvine-Fynn and others (2014) and Miles and others (2017), the DEMs were divided into transects at 0.005 m intervals giving 4000 transects for each survey, with 2000 aligned across- and 2000 down-glacier. Each transect was then detrended and an estimation of z_0 was made. Transect z_0 estimates were aggregated to mean and median flow-parallel and flow-perpendicular values and directionally averaged mean and median values were also calculated.

3-D estimations of z_0 were based on the method of Smith and others (2016), which aims to relax a number of the assumptions of Munro (1989) by using detrended DEMs derived from point clouds. Silhouette area was obtained directly for each cardinal direction by summing the exposed surface areas of each cell within a raster, and the specific area was taken to be equal to the area of the plot surveyed. Following Chambers and others (2019), the height scale h^* was set to equal twice the detrended standard deviation of elevations. Directional and plot averages can then be extracted for z_0 estimation.

Herein, the direction of transect z_0 estimates within each plot refers to the wind direction rather than the transect orientation, i.e. transects aligned across the glacier are referred to as 'parallel' (as roughness elements are exposed to a glacier flow-parallel wind) and transects aligned down-glacier are referred to as 'perpendicular' (as roughness elements are exposed to a glacier flow-perpendicular wind). For 3-D estimates up/down averaged values are exposed to a katabatic or anabatic flow and across values are exposed to an across glacier wind.

2.4 Glacier-scale surveys

Separate surveys of the upper and lower glacier were taken using a RIEGL VZ-6000 Terrestrial Laser Scanner on 3, 7, 12 and 16 August 2018. Combined, these surveys cover a glacier area of ~2 km^2. The TLS was located close to the summit of Im Hinteren Eis allowing almost the entire ablation zone to be encompassed within its field of view (Fig. 2). The near infrared laser wavelength of the RIEGL VZ-6000 is well suited to measurements of snow and ice surfaces and can achieve data acquisition rates of up to 220 000 measurements per second over a range of >6000 m within a 60° and 360° field of view vertically and horizontally, respectively (RIEGL, 2019). Due to high surface reflectivity and periods of low visibility, the laser pulse repetition rate was set to 30 kHz, extending the range of measurements, but reducing data acquisition rate to ~23 000 measurements per second. An angular increment of 0.01° allowed for horizontal and vertical spatial resolution of ~0.17 m at a range of 1000 m giving theoretical point densities of 10 points m^{-2} for the centre of the glacier and 2 points m^2 on the accumulation zone. Manufacturer stated accuracy and precision are 0.015 and 0.010 m, respectively (RIEGL, 2019) and initial analysis suggests only a 0.15 m deviation in elevations between TLS and airborne laser scanning of Hintereisferner and deviations <0.10 m between TLS scans. The largest source of associated error is likely to be caused by beam divergence (Carrivick and others, 2015*b*), which is stated as 0.12 m at a range of 1000 m.

TLS data were processed using the open-source topographic point cloud analysis toolkit (Brasington and others, 2012). Data were segregated into a regular grid of cell size 10 m × 10 m. A triangular tessellation between adjoining cells was then used to reconstruct the local surface and detrend the points relative to these planes. Elevation statistics were then calculated on a

cell-by-cell basis. Following Smith and others (2016), the standard deviation of the detrended elevations was used to represent TLS roughness (TLS σ_d).

To test for an underlying progressive evolution of z_0, a space-for-time substitution was used to artificially extend the observation period to 65 d. Two Canon EOS1200D single-lens reflex time-lapse cameras (https://www.foto-webcam.eu/webcam/hintereisferner1/2018/08/01/1200) mounted on the TLS cabin enabled the snow line to be tracked from the start of the 2018 ablation season until the study period. The snowline was digitised on each available image and converted into polygons classifying glacier ice areas into zones of exposure length. The glacier was classified into sections which have been exposed to melt for a given period of time. z_0 was estimated within each section and the effect of exposure time on z_0 observed.

2.5 Upscaling

To upscale plot-based SfM derived z_0 estimates to the glacier scale, a relationship between TLS σ_d and z_0 was established. TLS data were cropped to the extent of each SfM plot survey that took place within ± 1 d of a TLS scan ($n = 49$). One plot from each of the major ice facies was withheld for validation prior to regression analysis. Owing to concerns over the reproducibility of Crevasse and Rock Pedestal plots, these were excluded from the regression analysis. Linear regression relationships were formed between the remaining 24 TLS σ_d values and SfM z_0 estimates. These regression relationships were then applied to the glacier-scale TLS surveys for distributed z_0 estimates.

2-D and 3-D SfM z_0 estimates were made for each plot in multiple directions. To inform the linear regression relationships, the value most representative of z_0 during prevailing wind conditions was chosen. For the 2-D linear regression relationship plot average values of z_0 were used, which broadly give correct estimates of z_0 (e.g. Irvine-Fynn and others, 2014; Smith and others, 2016). The 3-D linear regression relationship was derived from down-glacier z_0 estimates that encompass the sheltering effects and topographic variability relevant to the estimation of z_0 for the prevailing wind direction. Wind direction has been identified as a likely source of error in turbulent flux calculation (Brock and others, 2006). The use of 3-D estimates which are representative of z_0 for the prevailing wind direction should reduce this error considerably.

3. Results

3.1 Spatial variability in plot-scale z_0

A statistically significant relationship between 2-D and 3-D z_0 estimates averaged for all directions was present for all surveys combined (Spearman's rank $\rho = 0.838$, $p < 0.01$, $n = 59$). The 2-D and 3-D z_0 values agree well for all surfaces where $z_0 < 5$ mm, but as z_0 increases beyond this value there is considerable deviation from a 1 : 1 fit (online Supplementary Fig. S1).

The variability of z_0 between plot types is presented in Table 2 and Figures 5 and 6. Estimates of z_0 ranged over two orders of magnitude between the eight surface types for both methods. Crevasse plots exhibited z_0 values an order of magnitude larger than other plot types for both estimation methods and wind directions, followed by Rock Pedestals and Dirt Cones. Conversely, Dirty Ice, Smooth Ice and Compound plots consistently presented the smallest z_0 values. Supraglacial Channels and Pressure Ridges both presented intermediate values of z_0 which exhibited pronounced anisotropy. However, the two calculation methods showed conflicting results on the impact of wind direction; the 2-D method showed higher z_0 values for down-glacier winds, whereas the 3-D method showed higher z_0 values for cross-glacier winds. This directional difference was apparent for all surface types.

ANOVA and Kruskal–Wallis tests were used to assess whether differences between the average values over ice facies are statistically significant. The z_0 values exhibited by Crevasse plots are distinct from the other ice facies (Fisher test $p < 0.001$). While Smooth Ice plots are characterised by lower values of z_0, this difference was only statistically significant when using the 3-D cross-wind estimates (Fisher test $p < 0.05$). z_0 estimates for Supraglacial Channel plots and Pressure Ridge plots were not distinct (Fig. 5).

3.2 Temporal variability in plot-scale z_0

The z_0 values for the repeat surveys of each plot are displayed in Figure 6. Typically, the evolution of 2-D and 3-D z_0 estimates followed the same trajectory. The z_0 values for all surface types at Hintereisferner were highly dynamic; yet, no clear trend was present over the observation period. Furthermore, no consistent response by surface type was observed.

The Supraglacial Channel plots (1, 3 and 6) displayed two distinctive trajectories: plot 1 exhibited a pronounced increase in z_0 which became more rapid between days 10 and 13, whereas plot 3 and plot 6 z_0 steadily decreased over the same period. Likewise, no consistent trajectory of z_0 was observed for the Pressure Ridge plots (4, 5 and 11): plot 4 demonstrated the highest temporal variability, with an initially rapid increase between days 2 and 4 followed by a sharp decline until day 11, and plots 5 and 11 showed only modest changes throughout the study period. Considering the Smooth Ice plots (8, 9 and 10), plot 8 displayed a gentle decline in z_0 across the observation period, whereas at plot 9 z_0 initially increased then decreased to a value similar to the starting value, and finally plot 10 provided a different evolution again, with z_0 increasing very gradually over the survey period, though changes at this plot were very small.

Table 2. Mean z_0 estimates by plot type, wind direction and estimation method

	2-D z_0 (mm)			3-D z_0 (mm)		
	Plot average	Down-glacier wind direction	Cross-glacier wind direction	Plot average	Down-glacier wind direction	Cross-glacier wind direction
Crevasse	37.05 [10.6]	35.28 [8.63]	38.83 [22.90]	24.25 [9.25]	22.85 [8.94]	25.64 [8.86]
Rock Pedestal	4.28 [0.97]	5.66 [1.14]	2.89 [0.85]	11.87 [3.01]	10.51 [3.18]	13.23 [2.85]
Supraglacial channel	5.63 [0.96]	8.10 [1.22]	3.16 [0.81]	6.27 [1.53]	5.41 [0.69]	7.13 [0.94]
Dirt Cone	5.43 [0.89]	6.38 [0.87]	4.48 [1.04]	8.48 [1.98]	7.44 [2.13]	9.52 [1.83]
Pressure Ridge	4.68 [0.87]	7.22 [1.41]	2.15 [0.34]	5.95 [1.31]	4.50 [1.55]	7.40 [1.53]
Dirty Ice	3.04 [0.66]	4.21 [0.85]	1.87 [0.46]	5.22 [1.45]	4.98 [1.39]	5.46 [1.51]
Smooth Ice	3.35 [0.66]	4.50 [0.93]	2.20 [0.71]	3.23 [0.74]	2.74 [0.69]	3.72 [0.94]
Compound	1.90	2.77	1.04	2.16	1.78	2.54

Individual plot measurements are displayed in Figure 6. The standard deviation of values is provided in square brackets.

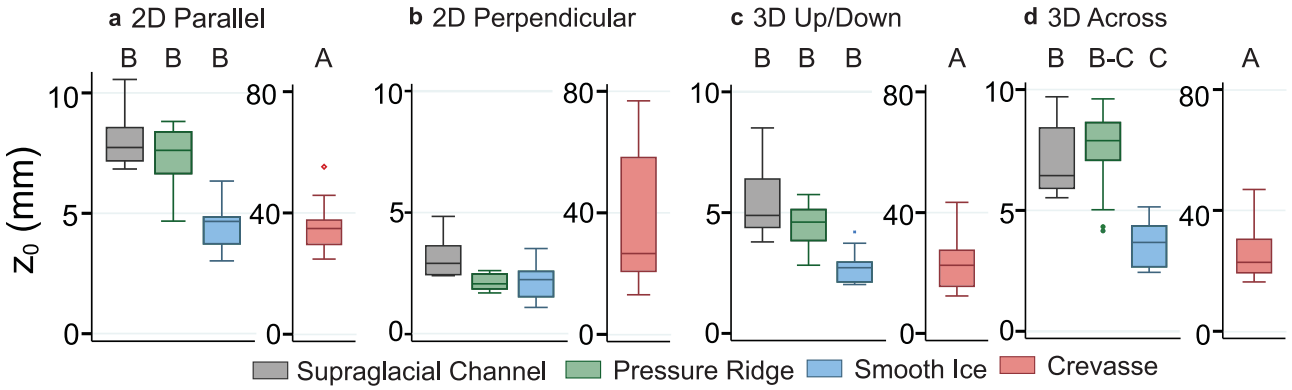

Fig. 5. A summary of the distribution of each z_0 metric for each surface type. Groupings from Fisher pairwise comparisons are displayed above the boxes. Ranges of values are indicated by the whiskers, interquartile range is indicated by the box, with the horizontal line within the box displaying the median. Points beyond 1.5 times the interquartile range from the upper/lower quartile are plotted separately.

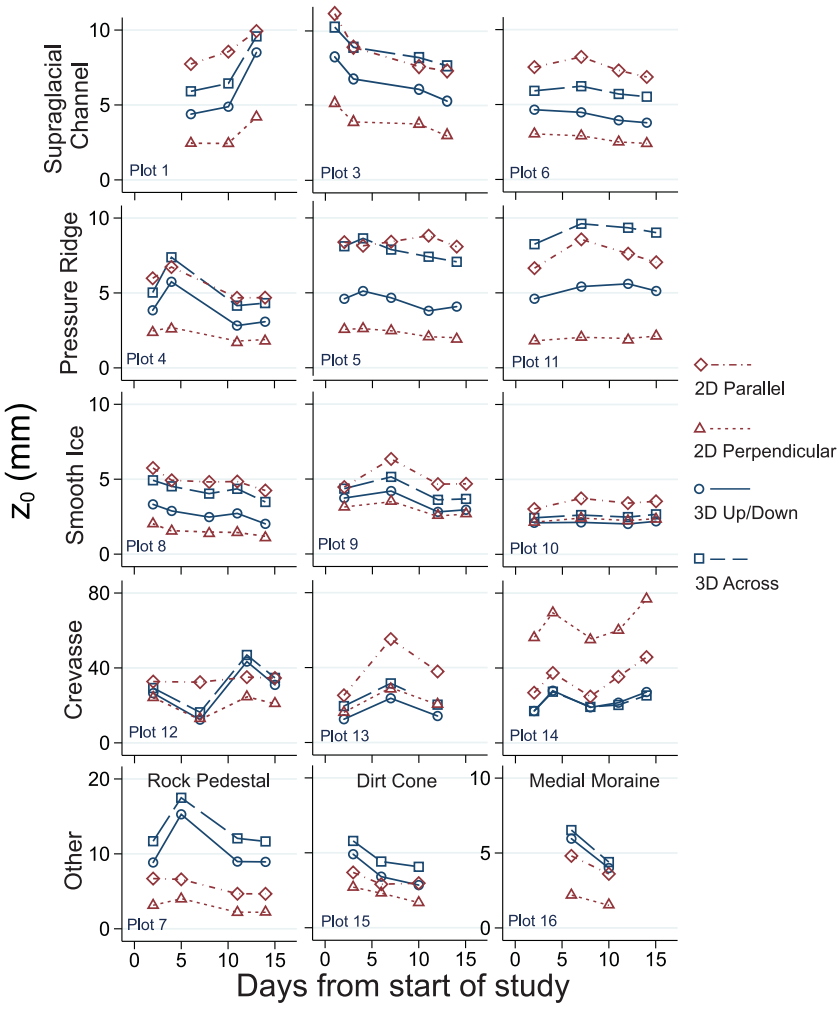

Fig. 6. Temporal change of z_0 for plots with multiple surveys. Each row displays a different surface type. Axes scales are variable to allow for a clearer display of temporal trends for Crevasse and Other sites.

The observed changes in z_0 estimates for Crevasse plots (12, 13 and 14) were more extreme with changes occurring at rates of >5.0 mm d^{-1}. These results are most likely to reflect difficulties in consistently data modelling the complex terrain present at Crevasse plots. Both the Dirt Cone (15) and Dirty Ice (16) plots showed a clear decrease in z_0 over the field campaign indicating a surface smoothing. The Rock Pedestal plot (7) displayed two different trends: the 2-D z_0 exhibited a gentle decline through the survey period, while the 3-D z_0 value showed greater variability with an initial rapid rise in z_0 followed by a decline back to the original value.

3.3 Distributed z_0 estimates at the glacier scale

TLS survey point density for the lower and upper glacier was ~15 and 20 points m^{-2}, respectively (Fig. 7a). Ice facies exhibited similar relative values for both TLS σ_d and SfM derived z_0 estimates (cf. Fig. 5 and Fig. 7). An ANOVA test indicated a statistically significant difference between the groups, while post-hoc Fisher tests showed that Crevasse plots were statistically significantly different from all other plots ($p < 0.001$) and Smooth Ice plots were significantly different from Supraglacial Channels ($p = 0.002$). Though not statistically significant ($p = 0.051$), a difference also appears

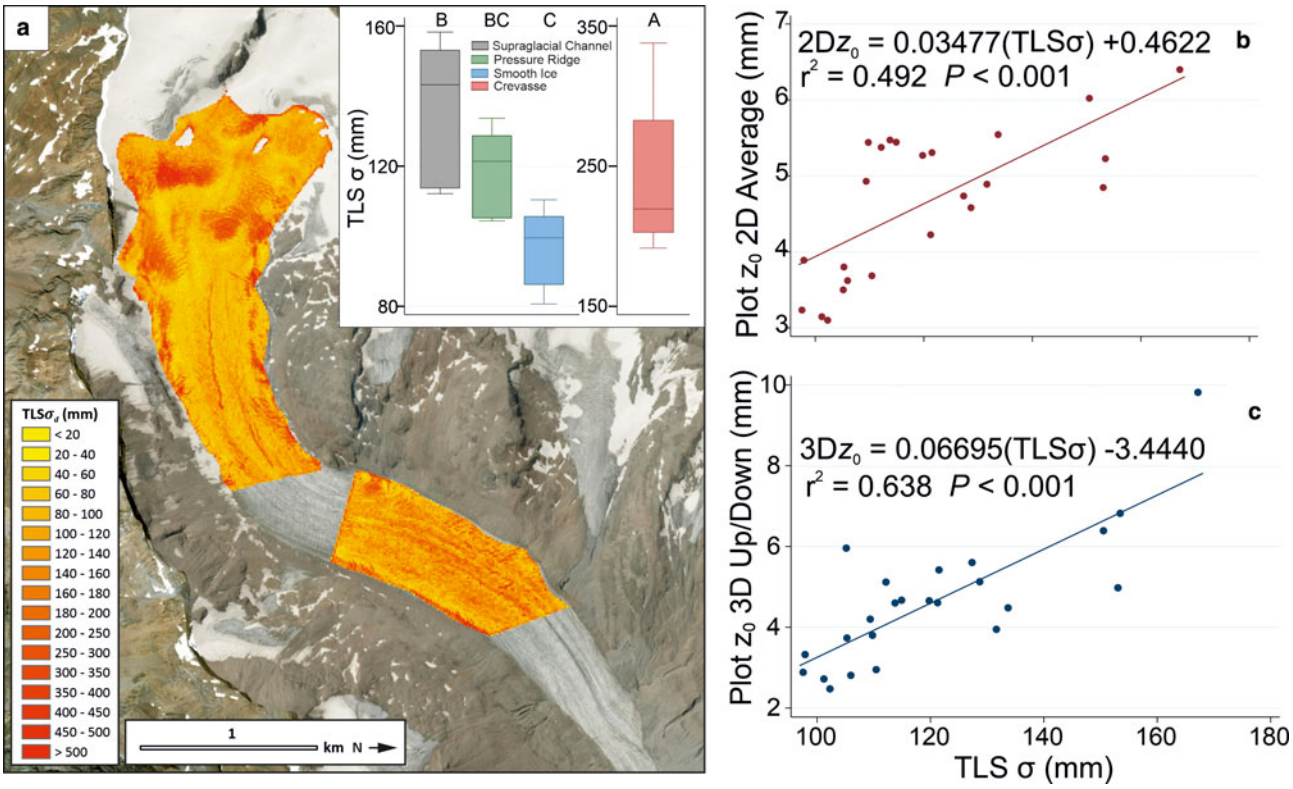

Fig. 7. (a) Glacier-wide TLS σ_d from 3 August with inset distributions for each ice surface facies (groupings from Fisher pairwise comparisons are displayed above boxes). (b) Linear regressions for 2-D and (c) 3-D estimates of z_0.

Table 3. Comparison of TLS z_0 predictions and SfM z_0 estimates for plots withheld from regression analysis

Surface type	SfM z_0 (mm)	TLS z_0 (mm)	Error (mm)
		3-D estimates	
Supraglacial Channel (Plot 1)	6.45	7.07	0.62
Pressure Ridge (Plot 4)	4.80	3.97	0.83
Smooth Ice (Plot 10)	2.12	2.59	0.47
Rock Pedestal (Plot 7)	11.03	14.46	3.43
Crevasse (Plot 14)	20.99	12.22	8.77
		2-D estimates	
Supraglacial Channel (Plot 1)	6.08	5.92	0.16
Pressure Ridge (Plot 4)	4.01	4.31	0.30
Smooth Ice (Plot 10)	2.86	3.58	0.72
Rock Pedestal (Plot 7)	4.18	9.76	5.58
Crevasse (Plot 14)	45.66	8.60	37.06

to exist between TLS σ_d values for Smooth Ice and Pressure Ridge plots.

Linear regression between TLS σ_d and both 2-D and 3-D SfM plot-scale z_0 estimates showed a reasonable fit ($r^2 = 0.49$ and 0.64, respectively) (Fig. 7c) and were used to produce glacier-scale distributed maps of z_0. Validation of the relationships using withheld data points is presented in Table 3. TLS-based estimates were particularly accurate for Supraglacial Channel, Pressure Ridge and Smooth Ice surfaces with values falling within 1 mm of SfM values. They performed less well for Rock Pedestal and Crevasse plots which were not used to inform the regression relationships.

Spatially distributed maps of TLS-estimated z_0 are displayed in Figure 8. The highest predicted values of z_0 (typically >20 mm) were located towards the margins of the glacier and in its upper reaches where the presence of crevasses led to locally high values of z_0. However, these values were most uncertain given that the regression relationships on which they are based did not perform well for these facies (Table 3). The lowest values of z_0 (0–4 mm) were located in areas of the upper glacier where snow cover was present and towards the centre of the upper glacier scan where Smooth Ice plots were surveyed. Such low values of z_0 were much less common at the lower glacier where the majority of the surface was characterised by $z_0 > 4$ mm. Maps created from both 2-D and 3-D relationships show a high level of spatial variation in z_0 over Hintereisferner; however, the use of the 3-D z_0 relationship predicted a larger range of values in z_0 arising from the higher gradient term in the linear regression relationship. For example, on the 16 August, the range in 2-D-derived z_0 estimates was 56.45 mm compared to 106.35 mm for 3-D-derived estimates.

In contrast to plot-scale trajectories, a gradual and consistent increase in TLS derived z_0 estimates was observed for both the mean glacier 2-D (0.05 mm d^{-1}) and 3-D (0.10 mm d^{-1}) estimates (Fig. 8), though glacier-scale median values exhibit a notably slower increase. Between 3 August and 16 August, z_0 estimates over Hintereisferner changed markedly in a number of areas (Fig. 8a–c). Over the crevasses at the true left margin of the glacier and in its upper reaches z_0 can be seen to increase considerably. The smooth surfaces characterised by low z_0 that surround the crevasses in the upper reaches also appeared to increase in roughness, as did the true left margin of the lower glacier. The use of a geographical coordinate system defining the TLS survey cell extents means that the down-glacier progression of surface features during the field campaign may result in local increases and decreases in roughness as features pass from cell to cell. However, the 10 m cell size means that such an effect would be limited over these time scales and this localised variability has no impact on the glacier-scale changes reported above.

The space-for-time substitution lends further support to the notion of a progressive increase in z_0 (Fig. 9). Dated snow lines, areas of the glacier surfaces classified by exposure date and histograms of TLS z_0 estimates within each section are presented in Figure 9. Ice exposed for <2 weeks had a mean and median z_0 value of less than half of ice exposed for >8 weeks. The rate of

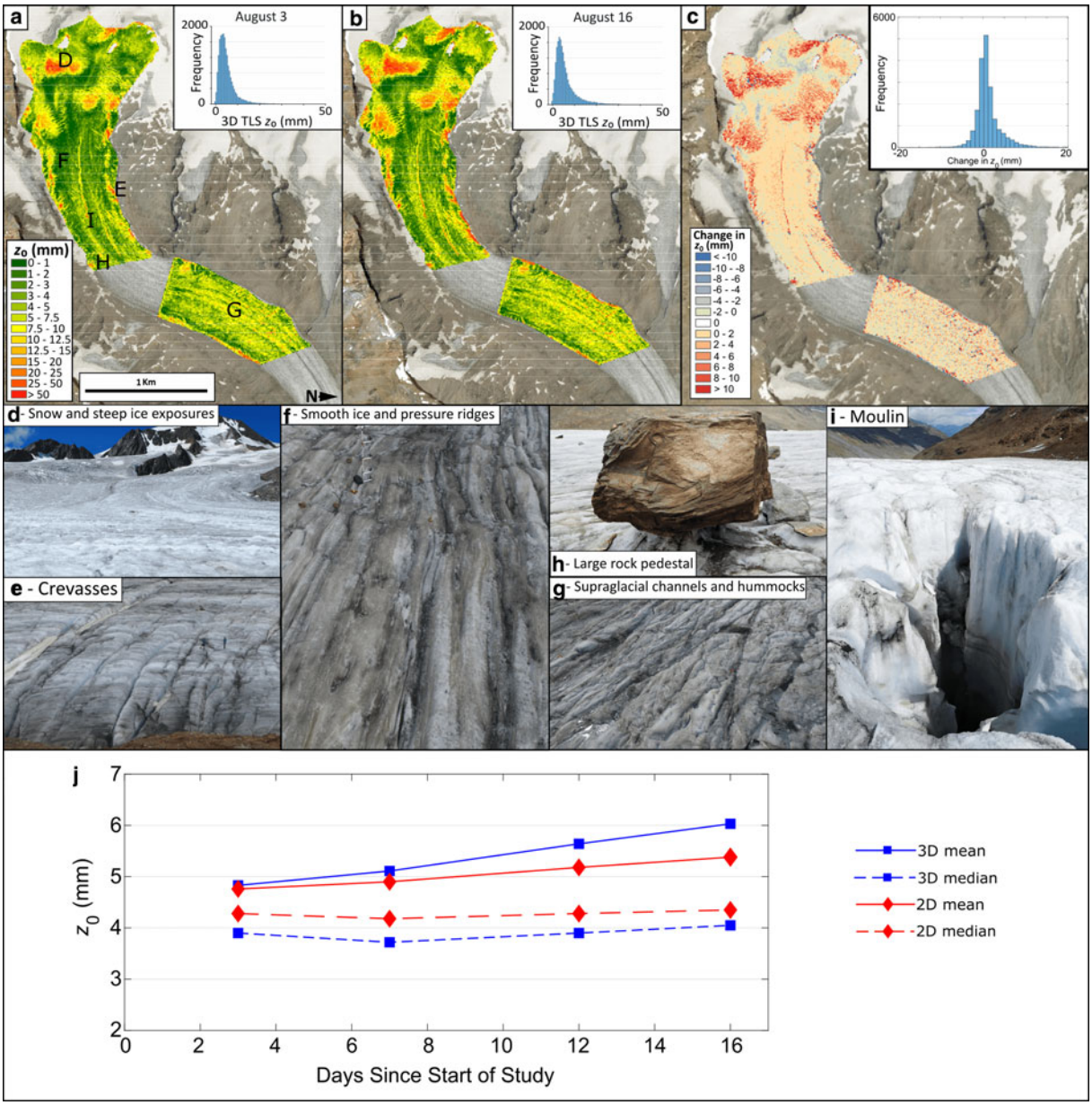

Fig. 8. Map of estimated 3-D z_0 for the 3rd (a) and 16th (b) day of study, and change in z_0 between the two dates (c). Frequency distributions for each map are inset. See online Supplementary Fig. S2 for equivalent figures for 2-D z_0. Example imagery (d–i) from the field of the different facies observed within close proximity of the areas indicated by letters in (a). Mean, median and standard deviation of glacier-scale TLS derived z_0 estimates (j).

increase was ~0.07 mm d^{-1} and appears to be relatively constant for mean values. The rate of increase in z_0 was more variable in median values, with the greatest rates of change occurring between 25 and 37 d of exposure.

Rates of change for each of the classified exposure zones were also calculated for the study period, by differencing z_0 values from the repeat TLS scans from the 3 and 16 August (Table 4). Zones which had been exposed most recently (i.e. farthest up-glacier) experienced the greatest increases in z_0 (1.46 mm). In zones that had been exposed for longer, the ice surface displayed smaller changes until >36 d (for both methods) when changes started to stabilise.

4. Discussion

4.1 Estimating z_0 from microtopographic data

The successful generation of dense point clouds for multiple surface types over Hintereisferner attests to the already recognised potential of SfM for generating microtopographic data for glacial surfaces (e.g. Irvine-Fynn and others, 2014; Chambers and others, 2019). However, the application of SfM was most challenging over Crevasse plots and over Rock Pedestal plots; gaps in the point clouds within the deep vertical crevasse walls and steep faces of rock pedestals were observed and are likely to be a consequence of imperfect image capture (given safety concerns) and unavoidable shadowing. While caution is required when interpreting microtopographically-derived z_0 values over such surfaces, this impact is limited for upscaling owing to their relatively small area at the glacier scale.

2-D and 3-D z_0 estimation methods displayed differing levels of agreement for different surface types. For surfaces devoid of large protruding roughness elements, the methods give similar results; where such roughness elements were present, there was less agreement between the two methods. Over Dirt Cone and Rock Pedestal plots 3-D z_0 estimates were typically greater than their 2-D counterparts. These findings corroborate those of Smith and others (2016) over Kårsaglaciären in northern Sweden and Quincey and others (2017) who observed that for

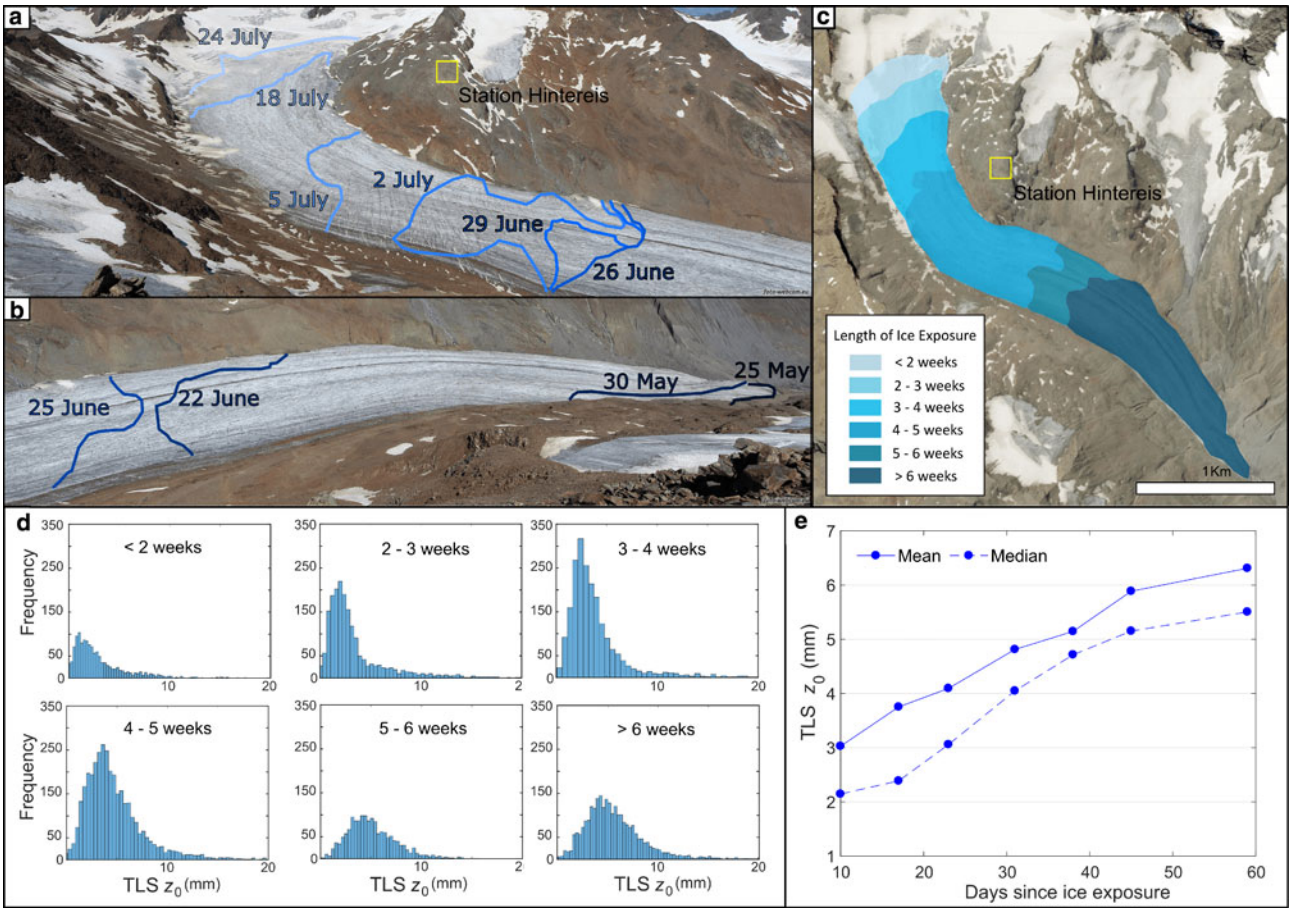

Fig. 9. (a) and (b) Digitised snow lines from time lapse cameras for upper and lower glacier, respectively. Imagery from www.foto-webcam.eu. (c) Polygons classifying glacier ice areas into zones of exposure length. (d) 3-D TLS z_0 estimates for each classified exposure zone. Estimates are made using the 3 August TLS survey. (e) Mean and median values of z_0 for areas of ice exposed to ablation for varying lengths of time.

debris-covered ice in the Himalaya, with $z_0 \gg 5$ mm, 3-D estimates of z_0 far exceeded 2-D estimates. Conversely, at Crevasse plots, 2-D z_0 estimates were larger than the 3-D estimates, as also observed by Smith and others (2016).

The difference in 2-D and 3-D z_0 estimates for different surface types most likely arises from the different way in which each method calculates frontal area. The 3-D method partially accounts for sheltering by ignoring all roughness elements below the detrended plane; the influence of this calculation step was most pronounced for Crevasse plots which contained extremely deep negative extensions below this plane. In contrast, the 2-D method included every point within a given transect and thus incorporated the effect of the deep crevasse as far as it was surveyed. As such, the 2-D method would generate the same value for an inverted crevasse transect as a regular crevasse. The approach of the 3-D method and its account for sheltering, therefore, seems reasonable given that a roughness element extending positively above the surface will likely impede the flow of air considerably more than a roughness element of the same size extending below the surface. Therefore, for plots with large roughness elements that extend above the detrended plane (e.g. Rock Pedestal and Dirt Cone) 3-D estimates exceed 2-D estimates and where roughness elements extended negatively below the detrended plane (e.g. Crevasses) 2-D estimates exceed 3-D estimates. Overall, the more sophisticated representation of sheltering possible and the increased availability of topographic data sufficient for 3-D z_0 estimates indicates that 3-D topographic methods will likely provide the source of z_0 values for use in distributed melt models.

Table 4. Mean change in 3-D z_0 over the period 3–16 August of classified exposure zones

Number of days exposed:	Change in 3-D z_0 (mm)
<2 weeks	1.46 [2.22]
2–3 weeks	1.40 [2.63]
3–4 weeks	0.74 [2.52]
4–5 weeks	0.56 [3.30]
5–6 weeks	0.42 [2.79]
>6 weeks	0.44 [3.31]

Standard deviation is in square brackets. See online Supplementary Table S2 for 2-D z_0 changes.

4.2 Plot-scale z_0 variability at Hintereisferner

The lowest values of z_0 recorded over Hintereisferner were between 1 and 5 mm for Smooth Ice, Dirty Ice and Compound surface types. These z_0 values are greater than some estimates of z_0, which for particularly smooth ice surfaces can be <1 mm (e.g. Grainger and Lister, 1966; Arnold and Rees, 2003; Giesen and others, 2009); yet, the values seem reasonable given that even the smoothest surfaces observed were visibly degraded and exhibited topographic variability. Indeed, the range of z_0 values observed over Hintereisferner compares more favourably with degraded and melting glacial ice surfaces in the literature (e.g. Greuell and Smeets, 2001; Sun and others, 2014; Guo and others, 2018). Pressure Ridge and Supraglacial Channel plots exhibited elongated roughness elements with z_0 ranging between 3 and 10 mm; estimates within the literature of z_0 over elongated glacier

ice hummocks range between 0.7 and 6.9 mm (e.g. Munro, 1989; Fitzpatrick and others, 2019), suggesting the values presented here are robust. Estimates of z_0 for Rock Pedestal and/or Dirt Cone plots have hitherto not been made; however, given the scale of roughness elements the larger estimates of z_0 of >10 mm predicted by 3-D methods seem reasonable. The most topographically variable surfaces over Hintereisferner were present at Crevasse plots, as reflected in high z_0 estimates for both 2-D and 3-D methods which are typically >20 mm. Smith and others (2016) recorded similarly large values over crevassed plots at Kårsaglaciären, while over very rough ice surfaces comparable values have been recorded (e.g. Obleitner, 2000; Smeets and van den Broeke, 2008; Azam and others, 2014).

Notably, our estimates of z_0 over Hintereisferner are typically larger than those obtained from similar studies utilising SfM imagery over bare ice surfaces (e.g. Irvine-Fynn and others, 2014; Smith and others, 2016). These higher z_0 values are likely a function of scale; the 10 m × 10 m plots utilised in this study are ~25× greater in area compared to the 2 m × 2 m plots utilised in these previous applications of the 2-D and 3-D z_0 estimation methods. Microtopographic estimations of z_0 have been found to show scale dependence, with z_0 increasing with plot size (Chambers and others, 2019). Therefore, when compared to the z_0 estimates of Irvine-Fynn and others (2014) and Smith and others (2016), higher values of z_0 for a similar surface should be expected. We assume herein that, despite this recognised scale dependence of z_0 values, their temporal evolution is relatively consistent within the length scale ranges of these plot-focused studies.

4.3 Upscaling z_0 estimates using TLS surveys

An assessment of the TLS z_0 estimates over a variety of different ice facies is presented in Figure 8. The map correctly identifies high and low values of z_0 for the steep ice exposures that contained crevasses and the smooth snow surfaces, respectively (d). Areas of the glacier with smooth ice surfaces and pressure ridges (f) are characterised by a z_0 ranging from ~2 to 7.5 mm throughout the upper glacier. Crevasses towards the edges of the glacier are particularly well highlighted (e) and are represented by z_0 values generally >12.5 mm and in some cases >50 mm. Relatively small, yet extreme, topographic features are also highlighted by high values of z_0 such as an area containing extensive debris cover, large rock pedestals (h), a large moulin (i) and the deep supraglacial channel network feeding it in the centre of the upper glacier. Due to a longer exposure of the ice surface, values of z_0 (ranging between 4 and 12.5 mm) over the lower glacier were typically greater than those over the upper glacier, characterising the topographic variability of the extensive network of supraglacial channels and hummocky ice present (g).

Surface roughness measured from the TLS surveys exhibited a stronger relationship with SfM estimated z_0 values than those achieved previously (e.g. Smith and others, 2016). This was potentially due to the larger plot size used over Hintereisferner, allowing for TLS scans to better reflect topographic variability when compared to the 2 m × 2 m plots studied by Smith and others (2016). The utility of TLS σ_d as a proxy for z_0 was further demonstrated by the finding that TLS σ_d values for separate ice facies fall into distributions similar to more detailed plot-scale z_0 estimates. The maps of z_0 estimates derived from TLS data facilitate clear visualisation of the variability of z_0 across Hintereisferner. Previous z_0 maps over bare ice surfaces have typically represented spatial variability by extrapolating point data (e.g. Brock and others, 2006). The maps presented here offer a step forward and could be readily applied in distributed melt SEB models. It should be noted, however, that model performance was weaker over Crevasse plots, especially for 2-D estimates, though this is perhaps related to the sheltering and SfM model quality issues mentioned above. Certainly, the approach demonstrated herein provides a more robust representation of z_0 than a constant value, as adopted by some SEB models (e.g. van As, 2011; Fausto and others, 2016*b*).

4.4 A scale-dependent model of the temporal variability of z_0

Several studies have reported considerable variation in z_0 over the course of an ablation season (e.g. Guo and others, 2011; Sicart and others, 2014; Fitzpatrick and others, 2019). Much of this variability is accounted for by differences in both wind speed and direction; however, the development of surface microtopography through time also has a significant effect. The effect of evolving topography on z_0 is to date relatively poorly understood and the literature shows multiple contrasting trends in the evolution of z_0 through time (e.g. Smeets and others, 1999; Smeets and van den Broeke, 2008; Smith and others, 2016). In an effort to unify these different perspectives, we adapted the three-stage model of Guo and others (2011) to propose a new scale-dependent theoretical model for predicting the evolution of z_0 throughout an ablation season.

Our model separates the temporal z_0 evolution model of Guo and others (2011) into five stages (Fig. 10a). Stage 1 details the transition of the surface from fresh snow cover, to a mixed snow and ice surface, at which z_0 reaches its first peak (as per Guo and others, 2011). Stage 2 maps the transition of the surface from this mixed cover to a bare ice surface and can take several trajectories depending on the roughness of the underlying ice surface (the suggested range of which is noted as grey dashed lines in Fig. 10a). Guo and others (2011) observed a decreasing z_0 as a flat ice surface was gradually exposed; conversely Smeets and van den Brooke (2008) noted an increase in z_0 at this stage at the Greenland ice sheet as ice hummocks were exposed. No observations were made of these two stages at Hintereisferner; however, the relatively rough underlying ice observed in the field indicates that a substantial decrease in z_0 during stage 2 is unlikely. Our field observations begin at stage 3 which represents a period of time between ice exposure and the clear development of surface features, during which only small channels are present in the surface and ice hummocks are yet to develop. In stage 4 z_0 rapidly increases, as surface features are established and are pronounced by increasing melt rates and the development of a complex meltwater channel network. During stage 5, z_0 approaches its peak value beyond which the density of some smaller-scale roughness elements will reach values where wake-interference and skimming flow are initiated thereby decreasing z_0.

To inform the development of the theoretical model, each plot (excluding Rock Pedestal and Crevasse plots) was placed on the proposed model and a simplification of the z_0 trajectory indicated (Fig. 10b). Following the space-for-time substitution in Figure 9, plots located towards the lower end of the glacier, over which the ice surface had been exposed for a longer time period, appear further along the transition model. Field observations of the ice surface were used to guide the overall positioning along the theoretical curve. The trajectory of z_0 values within the plots rarely followed the anticipated trajectory. Indeed, the theoretical model predicts an increasing value of z_0; contrastingly, plot-scale z_0 estimates showed highly variable trajectories with an overall decrease in z_0 for the majority of plots, despite the existence of pronounced surface features. Two of the Smooth Ice (P8 and P9) plots, which would be expected to be characterised by a relatively constant z_0, demonstrated a variable value of z_0 which decreased over the course of observation. Overall, only three

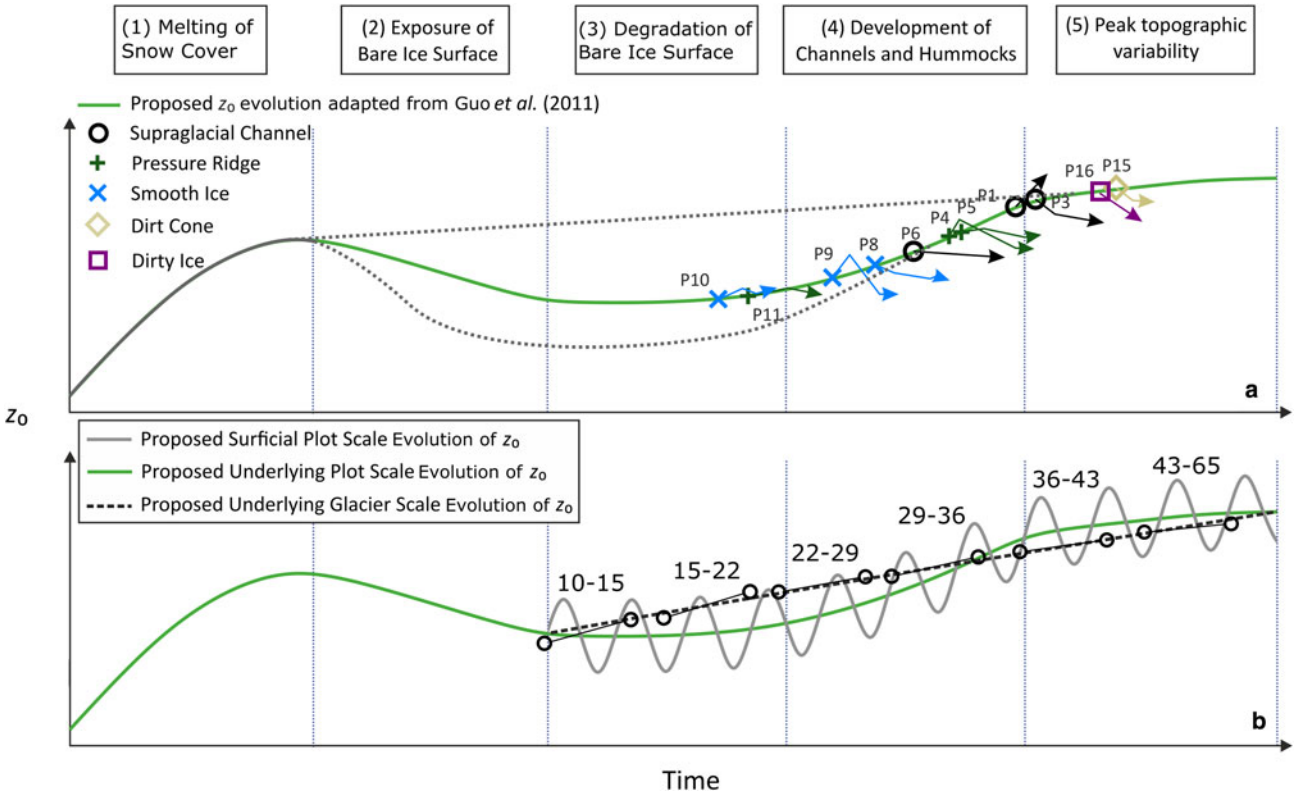

Fig. 10. (a) Initial, five-stage theoretical model for z_0 development during the ablation season (developed from Guo and others (2011) where stages 2–4 were grouped together). Temporal evolution of the ice facies observed over Hintereisferner is also indicated (excluding Compound, Rock Pedestal and Crevasse plots). (b) Proposed scale-dependent theoretical models with indications of where observed changes to each exposure zone over study duration would fall on model, based on field observation.

plots (P10, P11 and P1) exhibited the expected evolution of z_0 anticipated from the model.

Here we argue that scale plays an important role in determining how the temporal evolution of z_0 is observed. At the plot scale, the complex interaction of preferential melt and meltwater channel development controls the microtopography of the surface at Hintereisferner. The simple model proposed in Figure 10a is certainly inadequate and cannot represent the variability of z_0 due to these processes. The variability in the trajectory of z_0 is high and is unlikely to reveal any underlying progressive evolution of z_0 ice surfaces except over long time periods. Plot-scale trajectories of z_0 appear to be relatively unpredictable and independent of the ice facies, contrasting the findings of Smith and others (2016). Other studies suggest that the diversity of plot-scale z_0 trajectories is most pronounced following the initial melt of the snow surface. At the plot scale, Fitzpatrick and others (2019) measured z_0 over the course of an entire ablation season using sonic anemometers and observed an initial rise in z_0 as snow cover melts to form sun cups, supporting the underlying plot-scale evolution of z_0. Following the initial rise, they recorded a period of 60 d with no trend in z_0, potentially reflecting the relatively stable behaviour of z_0 through late stage 2 to early stage 4. Similarly, Brock and others (2006) recorded wind profile and microtopographic estimations of z_0 across the course of the 1993 and 1994 ablation seasons of Haut Glacier D'Arolla, Switzerland. Although their z_0 observations over snow surfaces support the progression proposed in stage 1, they observed a number of different temporal trends in the evolution of z_0 values over exposed ice surfaces, including a declining value of z_0 towards the end of the ablation season.

The underlying progression of z_0 can only be revealed through observations of greater spatial scales, over which the unpredictable behaviour of individual plot values are aggregated into a more predictable trajectory. Figure 10b presents a visual representation of this theoretical z_0 evolution model. At the glacier scale, TLS derived z_0 estimates display a constant and relatively linear increase in mean z_0 at a rate of ~0.10 mm d^{-1}, over the 15 d observation period (Fig. 10b). The space-for-time substitution of Figure 9 lends further support to the notion of a progressive increase in z_0 over a 50 d period, with a slightly slower increase in the mean z_0 of ~0.07 mm d^{-1}. Observed changes in z_0 within exposure zones (Table 4) indicate a more-or-less linear increase during the study period. While older exposed surfaces experience smaller increases than more recently exposed surfaces, the reduction in gradient is not as pronounced as suggested in the underlying theoretical model. This theoretical glacier-scale behaviour is supported by the spatially distributed maps of z_0 presented in Brock and others (2006), who over six periods throughout the melt season, observed a clear increase in glacier-scale z_0 with the onset of melt, continuing until snowfall at the end of the ablation season, at which point a lowering of z_0 is observed at a number of sites.

4.5 Further work

Both 2-D and 3-D z_0 estimates have been demonstrated to reasonably approximate aerodynamically derived z_0 values (Quincey and others, 2017; Chambers and others, 2019); yet, further consideration of the drag coefficient (Quincey and others, 2017), the influence of sheltering effects and scale dependencies of microtopographically derived z_0 would give estimates a stronger theoretical foundation.

The proposed scale-dependent trajectories of z_0 outlined in Figure 10 infers the behaviour of z_0 over an entire ablation season. Yet, plot-based estimates of z_0 observed at Hintereisferner had a maximum measurement period of 14 d, with some plots being observed over shorter time periods and glacier-scale TLS-based

estimates spanning 13 d only. Although the time period was extended to ~50 d using a space-for-time substitution, the results of which supported a progressive increase in z_0, the conclusions presented herein are limited by the short duration over which observations were made. The space-for-time substitution should be treated with some caution, given the potential for longitudinal glacier interactions, notably the downstream transfer of meltwater, which may influence the signal observed. Certainly, a longer observation period would allow for a clearer assessment of the accuracy of the theoretical model proposed.

Finally, with a larger number of plot-scale observations, a more objective classification of ice surface facies becomes possible, potentially based on observed roughness metrics from glacier-scale surveys. Such distributed maps of ice surface type could then better inform the production of distributed z_0 maps via individual regression relationships for each surface type. The incorporation of such z_0 maps into a distributed SEB model represents the key focus for further research, though there remains the question of how much detail of z_0 variability in both space and time is required to have a substantial impact on turbulent flux estimation.

5. Conclusions

This research adds to a growing literature (e.g. Brock and others, 2006; Smeets and van den Broeke and others, 2008; Guo and others, 2011; Smith and others, 2016; Quincey and others, 2017; Fitzpatrick and others, 2019) that emphasises the need to more comprehensively represent z_0 in SEB models to reduce errors in estimates of ablation. Specifically, the assumption of a constant z_0 value over ice surfaces, commonly 1 mm (e.g. van As, 2011), requires improvement. Representing z_0 more accurately in SEB models is especially important given the increasing contribution of turbulent fluxes to glacier SEB as the climate becomes wetter, windier and warmer.

The recent proliferation of high-resolution topographic data acquisition techniques has advanced the potential for estimations of z_0 and enabled effective relationships to be developed to upscale plot results to the glacier scale. The use of 3-D methods to estimate z_0 makes the best use of this available data. Plot scale estimates of z_0 demonstrated substantial variability in both space and time, ranging from $z_0 < 3$ mm to $z_0 > 40$ mm. z_0 over such surfaces can change at rates in excess of 0.25 mm d^{-1} as the surface melts and can be due to complex interactions between meltwater channel development and preferential melt. At the glacier scale, spatial variability in z_0 values was >2 orders of magnitude but a consistent increase in z_0 of 0.07–0.10 mm d^{-1} was observed.

Our findings indicate that glacier scale topographic datasets can usefully capture the variability in ice surface roughness that is relevant for the estimation of z_0. While a TLS was available for this study, airborne laser scanning or even satellite-derived datasets that are more widely available may provide sufficient topographic information to estimate z_0 variability in space and time to the extent that is required by distributed melt models.

Overall, we contend that by interpreting the temporal trends in z_0 as a function of the spatial scale over which they are observed, our theoretical z_0 model goes some way towards unifying a variety of contrasting temporal trends observed within the wider literature. The interpretation presented here is that plot scale trends in z_0 are stochastic in the short term but by extending either the length of observation or the spatial scale underlying trends in z_0 are revealed. Further work into theoretical scale-dependent behaviour of z_0 through time is required. If such work supports a progressive increase in z_0, constraining the rate of this increase may pave the way for representation of the temporal development of z_0 in SEB models.

Supplementary material. The supplementary material for this article can be found at https://doi.org/10.1017/jog.2020.56

Acknowledgements. Fieldwork was funded by an INTERACT transnational access grant awarded to MWS under the European Union H2020 Grant Agreement No. 730938. The TLS facility is financed by the University of Innsbruck and jointly operated by the Department of Geography and the Department of Atmospheric and Cryospheric Research. JRC is supported by a NERC PhD studentship (NE/L002574/1). IS was funded by Austrian Science Fund (FWF) grant T781-N32. The authors acknowledge Matt Westoby and Andy Baird and two anonymous reviewers for constructive comments on this work. The authors declare that they have no conflicts of interest.

References

Ambach W (1961) Die Bedeutung des aufgefrorenen Eises für den Massen- und Energiehaushalt der Gletscher. *Zeitschrift für Gletscherkunde und Glazialgeologie* **4**, 169–189.

Anslow FS, Hostetler S, Bidlake WR and Clark PU (2008) Distributed energy balance modeling of South Cascade Glacier, Washington and assessment of model uncertainty. *Journal of Geophysical Research: Earth Surface* **113**(F2), F02019. doi:10.1029/2007JF000850.

Arnold NS and Rees WG (2003) Self-similarity in glacier surface characteristics. *Journal of Glaciology* **49**(167), 547–554. doi:10.3189/172756503781830368.

Azam MF and 6 others (2014) Processes governing the mass balance of Chhota Shigri Glacier (western Himalaya, India) assessed by point-scale surface energy balance measurements. *The Cryosphere* **8**(6), 2195–2217. doi:10.5194/tc-8-2195-2014.

Behrens H, Bergmann H, Moser H, Ambach W and Jochum O (1975) On the water channels of the internal drainage system of the Hintereisferner, Ötztal Alps, Austria. *Journal of Glaciology* **14**(72), 375–382. doi:10.3189/S0022143000021900.

Belart JMC and 9 others (2017) Winter mass balance of Drangajökull ice cap (NW Iceland) derived from satellite sub-meter stereo images. *The Cryosphere* **11**, 1501–1517.

Bintanja R and van den Broeke MR (1995) Momentum and scalar transfer coefficients over aerodynamically smooth Antarctic surfaces. *Boundary-Layer Meteorology* **74**(1-2), 89–111. doi:10.1007/BF00715712.

Blümcke A and Hess H (1899) Untersuchungen am Hintereisferner. *Wissenschaftliche Ergänzungshefte zur Zeitschrift des Deutschen und Österreichischen Alpenvereins* **1**(2), 1–87.

Brasington J, Vericat D and Rychkov I (2012) Modeling river bed morphology, roughness, and surface sedimentology using high resolution terrestrial laser scanning. *Water Resources Research* **48**, W11519. doi: doi:10.1029/2012WR012223.

Bravo C, Loriaux T, Rivera A and Brock B (2017) Assessing glacier melt contribution to streamflow at Universidad Glacier, central Andes of Chile. *Hydrology and Earth System Sciences* **21**(7), 3249–3266. doi:10.5194/hess-21-3249-2017.

Brock BW, Willis IC and Sharp MJ (2006) Measurement and parameterization of aerodynamic roughness length variations at Haut Glacier d'Arolla, Switzerland. *Journal of Glaciology* **52**(177), 281–297. doi:10.3189/172756506781828746.

Brock BW, Willis IC, Sharp MJ and Arnold NS (2000) Modelling seasonal and spatial variations in the surface energy balance of Haut Glacier d'Arolla, Switzerland. *Annals of Glaciology* **31**, 53–62. doi:10.3189/172756400781820183.

Carrivick JL and 7 others (2015*a*) Decadal-scale changes of the Ödenwinkelkees, central Austria, suggest increasing control of topography and evolution towards steady state. *Geografiska Annaler: Series A, Physical Geography* **97**(3), 543–562. doi:10.1111/geoa.12100.

Carrivick JL, Smith MW and Carrivick DM (2015*b*) Terrestrial laser scanning to deliver high-resolution topography of the upper Tarfala valley, arctic Sweden. *GFF* **137**(4), 383–396. doi:10.1080/11035897.2015.1037569.

Chambers J and 5 others (2019) Glacial aerodynamic roughness estimates: uncertainty, sensitivity and precision in field measurements. *Journal of Geophysical Research: Earth Surface* **125**(2). doi:10.1029/2019JF005167.

Conway JP and Cullen NJ (2016) Cloud effects on surface energy and mass balance in the ablation area of Brewster Glacier, New Zealand. *The Cryosphere* **10**(1), 313–328. doi:10.5194/tc-10-313-2016,, 2016.

Cuffey KM and Paterson WSB (2010) *The Physics of Glaciers*, 4th ed. Oxford: Butterworth-Heinemann.

Deschamps-Berger C and 7 others (2020) Snow depth mapping from stereo satellite imagery in mountainous terrain: evaluation using airborne lidar data. *The Cryosphere Discussions* doi:10.5194/tc-2020-15.

Ebrahimi S and Marshall SJ (2016) Surface energy balance sensitivity to meteorological variability on Haig Glacier. *Canadian Rocky Mountains. The Cryosphere* **10**(6), 2799–2819. doi:10.5194/tc-10-2799-2016.

Escher-Vetter H, Kuhn M and Weber M (2009) Four decades of winter mass balance of Vernagtferner and Hintereisferner, Austria: methodology and results. *Annals of Glaciology* **50**(50), 87–95. doi:10.3189/172756409787769672.

Fausto RS and 5 others (2016*a*) The implication of nonradiative energy fluxes dominating Greenland ice sheet exceptional ablation area surface melt in 2012. *Geophysical Research Letters* **43**(6), 2649–2658. doi:10.1002/2016GL067720.

Fausto RS, van As D, Box JE, Colgan W and Langen PL (2016*b*) Quantifying the surface energy fluxes in south Greenland during the 2012 high melt episodes using in-situ observations. *Frontiers in Earth Science* **4**, 82. doi:10.3389/feart.2016.00082.

Favier V and 5 others (2011) Modelling the mass and surface heat budgets in a coastal blue ice area of Adelie Land, Antarctica. *Journal of Geophysical Research: Earth Surface* **116**(F3), F03017. doi:10.1029/2010JF001939.

Fischer A (2010) Glaciers and climate change: interpretation of 50 years of direct mass balance of Hintereisferner. *Global and Planetary Change* **71**(1–2), 13–26. doi:10.1016/j.gloplacha.2009.11.014.

Fischer A, Seiser B, Stocker Waldhuber M, Mitterer C and Abermann J (2015) Tracing glacier changes in Austria from the Little Ice Age to the present using a lidar-based high-resolution glacier inventory in Austria. *The Cryosphere* **9**(2), 753–766. doi:10.5194/tc-9-753-2015.

Fitzpatrick N, Radić V and Menounos B (2019) A multi-season investigation of glacier surface roughness lengths through in situ and remote observation. *The Cryosphere* **13**(3), 1051–1071. doi:10.5194/tc-13-1051-2019.

Franco B, Fettweis X and Erpicum M (2013) Future projections of the Greenland ice sheet energy balance driving the surface melt. *The Cryosphere* **7**(1), 1–18. doi:10.5194/tc-7-1-2013.

Geist T and Stotter J (2007) Documentation of glacier surface elevation change with multi-temporal airborne laser scanner data--case study: Hintereisferner and Kesselwandferner, Tyrol, Austria. *Zeitschrift fur Gletscherkunde und Glazialgeologie* **41**, 77–106.

Giesen RH, Andreassen LM, Oerlemans J and van den Broeke MR (2014) Surface energy balance in the ablation zone of Langfjordjøkelen, an arctic, maritime glacier in northern Norway. *Journal of Glaciology* **60**(219), 57–70. doi:10.3189/2014JoG13J063.

Giesen RH, Andreassen LM, van den Broeke MR and Oerlemans J (2009) Comparison of the meteorology and surface energy balance at Storbreen and Midtdalsbreen, two glaciers in southern Norway. *The Cryosphere* **3**, 57–74. doi:10.5194/tc-3-57-2009.

Grainger ME and Lister H (1966) Wind speed, stability and eddy viscosity over melting ice surfaces. *Journal of Glaciology* **6**(43), 101–127. doi:10.3189/S0022143000019109.

Greuell W (1992) Hintereisferner, Austria: mass-balance reconstruction and numerical modelling of the historical length variations. *Journal of Glaciology* **38**(129), 233–244. doi:10.3189/S0022143000003646.

Greuell W and Genthon C (2004) Modelling land-ice surface mass balance. In Bamber JL and Payne AJ (eds), *Mass Balance of the Cryosphere: Observations and Modelling of Contemporary and Future Changes*. Cambridge: Cambridge University Press, pp. 117–168. doi:10.1017/S0016756805251701.

Greuell W and Smeets P (2001) Variations with elevation in the surface energy balance on the Pasterze (Austria). *Journal of Geophysical Research: Atmospheres* **106**(D23), 31717–31727. doi:10.1029/2001JD900127.

Gromke C, Manes C, Walter B, Lehning M and Guala M (2011) Aerodynamic roughness length of fresh snow. *Boundary-Layer Meteorology* **141**(1), 21–34. doi:10.1007/s10546-011-9623-3.

Guo X and 7 others (2011) Critical evaluation of scalar roughness length parametrizations over a melting valley glacier. *Boundary-layer Meteorology* **139**(2), 307–332. doi:10.1007/s10546-010-9586-9.

Guo S and 10 others (2018) Simple parameterization of aerodynamic Roughness lengths and the turbulent heat fluxes at the Top of midlatitude August-One Glacier, Qilian Mountains, China. *Journal of Geophysical Research: Atmospheres* **123**(21), 12–66. doi:10.1029/2018JD028875.

Hock R and Holmgren B (2005) A distributed surface energy-balance model for complex topography and its application to Storglaciären, Sweden. *Journal of Glaciology* **51**(172), 25–36. doi:10.3189/172756505781829566.

Hoffman MJ, Fountain AG and Liston GE (2008) Surface energy balance and melt thresholds over 11 years at Taylor Glacier, Antarctica. *Journal of Geophysical Research: Earth Surface* **113**(F4), F04014. doi:10.1029/2008JF001029.

Irvine-Fynn T, Sanz-Ablanedo E, Rutter N, Smith M and Chandler J (2014) Measuring glacier surface roughness using plot-scale, close-range digital photogrammetry. *Journal of Glaciology* **60**(223), 957–969. doi:10.3189/2014JoG14J032.

Ishikawa N, Owens IF and Sturman AP (1992) Heat balance characteristics during fine periods on the lower parts of the Franz Josef Glacier, South Westland, New Zealand. *International Journal of Climatology* **12**(4), 397–410. doi:10.1002/joc.3370120407.

James MR, Robson S, d'Oleire-Oltmanns S and Niethammer U (2017*b*) Optimising UAV topographic surveys processed with structure-from-motion: ground control quality, quantity and bundle adjustment. *Geomorphology* **280**, 51–66. doi:10.1016/j.geomorph.2016.11.021.

Klug C and 8 others (2018) Geodetic reanalysis of annual glaciological mass balances (2001–2011) of Hintereisferner, Austria. *The Cryosphere* **12**(3), 833–849. doi:10.5194/tc-12-833-2018.

Koelemeijer R, Oerlemans J and Tjemkes S (1993) Surface reflectance of Hintereisferner, Austria, from Landsat 5 TM imagery. *Annals of Glaciology* **17**, 17–22. doi:10.3189/S0260305500012556

Kuhn M and 5 others (1999) Measurements and models of the mass balance of Hintereisferner. *Geografiska Annaler: Series A. Physical Geography* **81**(4), 659–670. doi:10.1111/1468-0459.00094.

Kutzbach JE (1961) *Investigations of the modification of wind profiles by artificially controlled surface roughness*. (Ph.D. thesis, University of Wisconsin)

Lambrecht A and Kuhn M (2007) Glacier changes in the Austrian Alps during the last three decades, derived from the new Austrian glacier inventory. *Annals of Glaciology* **46**, 177–184. doi:10.3189/172756407782871341.

Lettau H (1969) Note on aerodynamic roughness-parameter estimation on the basis of roughness-element description. *Journal of Applied Meteorology* **8**(5), 828–832. doi:10.1175/1520-0450(1969)008<0828:NOARPE>2.0.CO;2.

Lewis KJ, Fountain AG and Dana GL (1998) Surface energy balance and meltwater production for a Dry Valley glacier, Taylor Valley, Antarctica. *Annals of Glaciology* **27**, 603–609. doi:10.3189/1998AoG27-1-603-609.

Marti R and 5 others (2016) Mapping snow depth in open alpine terrain from stereo satellite imagery. *The Cryosphere* **10**, 1361–1380.

Miles ES, Steiner JF and Brun F (2017) Highly variable aerodynamic roughness length (z0) for a hummocky debris-covered glacier. *Journal of Geophysical Research: Atmospheres* **122**(16), 8447–8466. doi:10.1002/2017JD026510

Morris EM (1989) Turbulent transfer over snow and ice. *Journal of Hydrology* **105**(3–4), 205–223. doi:10.1016/0022-1694(89)90105-4.

Munro DS (1989) Surface roughness and bulk heat transfer on a glacier: comparison with eddy correlation. *Journal of Glaciology* **35**(121), 343–348. doi:10.3189/S0022143000009266

Nicholson LI, Petlicki M, Partan B and MacDonell S (2016) 3D Surface properties of glacier penitentes over an ablation season, measured using a Microsoft Xbox Kinect. *Cryosphere* **10**(5), 1897–1913. doi:10.5194/tc-10-1897-2016.

Obleitner F (1994) Climatological features of glacier and valley winds at the Hintereisferner (Ötztal Alps. Austria). *Theoretical and Applied Climatology* **49**(4), 225–239. doi:10.1007/BF00867462.

Obleitner F (2000) The energy budget of snow and ice at Breidamerkurjökull, Vatnajökull, Iceland. *Boundary-layer Meteorology* **97**(3), 385–410. doi:10.1023/A:1002734303353.

O'Connor J, Smith MJ and James MR (2017) Cameras and settings for aerial surveys in the geosciences: optimising image data. *Progress in Physical Geography* **41**(3), 325–344. doi:10.1177/0309133317703092.

Patzelt G (1970) Die Längenmessungen an den Gletschern der österreichischen Ostalpen 1890–1969. *Zeitschrift für Gletscherkunde und Glazialgeologie* **6**(1–2), 151–159.

Patzelt G (1980) The Austrian glacier inventory: status and first results. *International Association of Hydrological Sciences* **126**, 181–183.

Quincey D and 5 others (2017) Evaluating morphological estimates of the aerodynamic roughness of debris covered glacier ice. *Earth Surface Processes and Landforms* **42**(15), 2541–2553. doi:10.1002/esp.4198.

Radić V and 5 others (2017) Evaluation of different methods to model near-surface turbulent fluxes for a mountain glacier in the Cariboo Mountains, BC, Canada. *The Cryosphere* **11**(6), 2897–2918. doi:10.5194/tc-11-2897-2017.

Rees WG and Arnold NS (2006) Scale-dependent roughness of a glacier surface: implications for radar backscatter and aerodynamic roughness modelling. *Journal of Glaciology* **52**(177), 214–222. doi:10.3189/172756506781828665.

RIEGL (2019) *Data Sheet RIEGL VZ*-6000. [Online]. [Accessed 23 July 2019]. Available from: http://www.riegl.com/uploads/tx_pxpriegldownloads/RIEGL_VZ-6000_Datasheet_2019-05-28_01.pdf.

Schmidt LS and 7 others (2017) The importance of accurate glacier albedo for estimates of surface mass balance on Vatnajökull: evaluating the surface energy budget in a regional climate model with automatic weather station observations. *The Cryosphere* **11**(4), 1665–1684. doi:10.5194/tc-11-1665-2017.

Shaw TB, Gascoin S, Mendoza PA, Pellicciotti F and McPhee J (2020) Snow depth patterns in a high mountain Andean catchment from satellite optical tristereoscopic remote sensing. *Water Resources Research* **56**, e2019W, R024880.

Shean DE and 5 others (2020) A systematic, regional assessment of high mountain Asia Glacier mass balance. *Frontiers in Earth Science* **7**, 363.

Sicart JE, Litt M, Helgason W, Tahar VB and Chaperon T (2014) A study of the atmospheric surface layer and roughness lengths on the high-altitude tropical Zongo glacier, Bolivia. *Journal of Geophysical Research: Atmospheres* **119**(7), 3793–3808. doi:10.1002/2013JD020615.

Sicart JE, Wagnon P and Ribstein P (2005) Atmospheric controls of the heat balance of Zongo Glacier (16 S, Bolivia). *Journal of Geophysical Research: Atmospheres* **110**(D12), D12106. doi:10.1029/2004JD005732.

Smeets CJPP, Duynkerke PG and Vugts HF (1999) Observed wind profiles and turbulence fluxes over an ice surface with changing surface roughness. *Boundary-Layer Meteorology* **92**(1), 99–121. doi:10.1023/A:1001899015849.

Smeets CJPP and van den Broeke MR (2008) Temporal and spatial variations of the aerodynamic roughness length in the ablation zone of the Greenland ice sheet. *Boundary-Layer Meteorology* **128**(3), 315–338. doi:10.1007/s10546-008-9291-0.

Smith MW (2014) Roughness in the earth sciences. *Earth-Science Reviews* **136**, 202–225. doi:10.1016/j.earscirev.2014.05.016.

Smith MW and 6 others (2016) Aerodynamic roughness of glacial ice surfaces derived from high-resolution topographic data. *Journal of Geophysical Research: Earth Surface* **121**(4), 748–766. doi:10.1002/2015JF003759.

IPCC (2013) Information from paleoclimate archives. In Stocker TF, Qin D, Plattner GK, Tignor M, Allen SK, Boschung J, Nauels A, Xia Y, Bex V and Midgley PM (eds), *Climate Change 2013: The Physical Science Basis. Contribution of Working Group I to the Fifth Assessment Report of the Intergovernmental Panel on Climate Change*. Cambridge, United Kingdom and New York, NY, USA: Cambridge University Press, pp. 383–464. doi:10.1017/CBO9781107415324.

Strasser U and 10 others (2018) The Rofental: a high Alpine research basin (1890–3770 m asl) in the Ötztal Alps (Austria) with over 150 years of hydrometeorological and glaciological observations. *Earth System Science Data* **10**(1), 151. doi:10.5194/essd-10-151-2018.

Sun W and 9 others (2014) Ablation modeling and surface energy budget in the ablation zone of Laohugou glacier No. 12, western Qilian mountains, China. *Annals of Glaciology* **55**(66), 111–120. doi:10.3189/2014AoG66A902.

Sun W and 6 others (2018) The response of surface mass and energy balance of a continental glacier to climate variability, western Qilian Mountains, China. *Climate Dynamics*. **50**(9–10), 3557–3570. doi:10.1007/s00382-017-3823-6.

van As D (2011) Warming, glacier melt and surface energy budget from weather station observations in the Melville Bay region of northwest Greenland. *Journal of Glaciology* **57**(202), 208–220. doi:10.3189/002214311796405898.

van den Broeke MR and 5 others (2008) Partitioning of melt energy and meltwater fluxes in the ablation zone of the west Greenland ice sheet. *The Cryosphere* **2**(2), 179. doi:10.5194/tc-2-179-2008.

van den Broeke MR, Smeets CJPP and van de Wal RSW (2011) The seasonal cycle and interannual variability of surface energy balance and melt in the ablation zone of the west Greenland ice sheet. *The Cryosphere* **5**(2), 377–390. doi:10.5194/tc-5-377-2011.

van de Wal RSW, Oerlemans J and van der Hage JC (1992) A study of ablation variations on the tongue of Hintereisferner, Austrian Alps. *Journal of Glaciology* **38**(130), 319–324. doi:10.3189/S0022143000002203.

Vincent C and 9 others (2017) Common climatic signal from glaciers in the European Alps over the last 50 years. *Geophysical Research Letters* **44**(3), 1376–1383. doi:10.1002/2016GL072094.